



Avalanche Studies and model Validation in Europe, SATSIE

3. Annual report

20021048-11

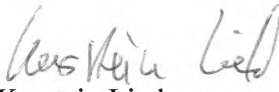
1 December 2005

Client: **European Commission**

Contact person: Denis Peter
Contract reference: Contract of 2002.12.18

For the Norwegian Geotechnical Institute

Project Manager:


Karstein Lied

Report prepared by:

Dieter Issler

Work also carried out by:

Participating
organisations

Postal address:
Street address:
Internet:

P.O. Box 3930 Ullevaal Stadion, N-0806 OSLO, NORWAY
Sognsveien 72, OSLO
<http://www.ngi.no>

Telephone: (+47) 22 02 30 00
Telefax: (+47) 22 23 04 48
e-mail: ngi@ngi.no

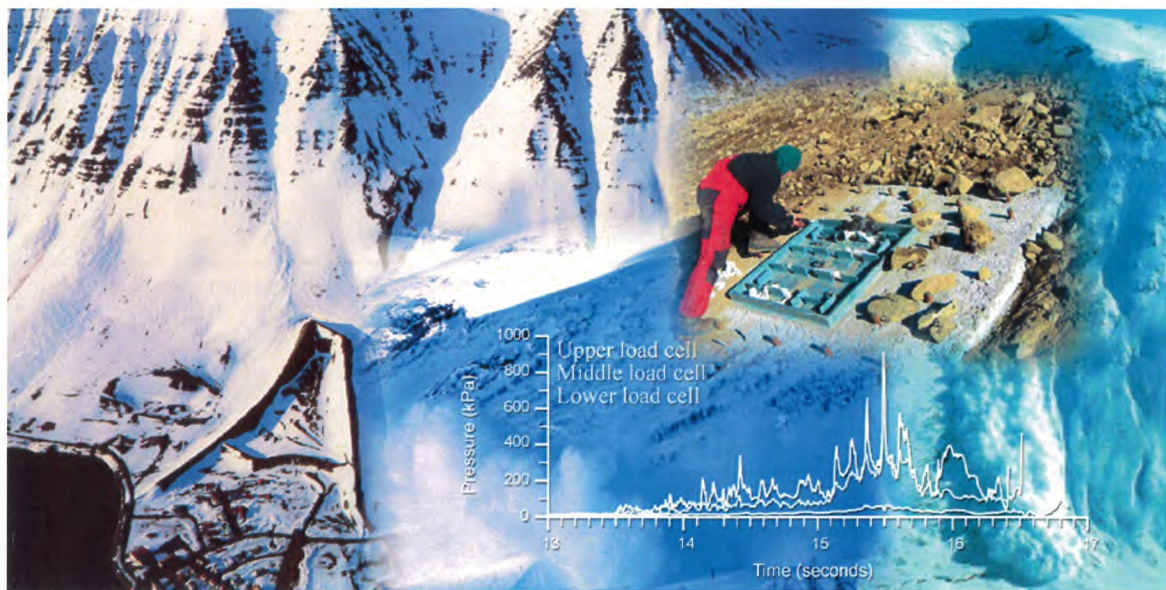
Postal account: 0814 51 60643
Bank account: 5096 05 01281
Business No. 958 254 318 MVA

European Commission — *Fifth Framework Programme*

SATSIE

Avalanche Studies and Model Validation in Europe

EU Contract no. EVG1-CT2002-00059



Third Annual Report

Contains Sections 1–4

Deliverable D16

Reporting period: 1 October 2004 – 30 September 2005

Coordinator: Karstein Lied, Norwegian Geotechnical Institute

Project home page: <http://www.leeds.ac.uk/satsie>

Contents

1	Management Progress Report 01/05–30/09/2005	1
1.1	Objectives of the reporting period	1
1.2	Scientific/technical progress in the Work Packages	1
1.2.1	WP 1 – Sensor development	1
1.2.2	WP 2 – Data analysis techniques	2
1.2.3	WP 3 – Instrumentation of selected facilities	2
1.2.4	WP 4 – Measurement campaigns	2
1.2.5	WP 5 – Model development	3
1.2.6	WP 6 – Data sharing and dissemination of results	3
1.3	Milestones and deliverables	4
1.4	Deviations from the work plan or/and time schedule	7
1.5	Coordination and communication	7
1.6	Encountered management and coordination difficulties	7
2	Executive Summary 01/10/2004–30/09/2005	11
3	Scientific Progress Report 01/10/2004–30/09/2005	17
3.1	WP 1 – Sensor development	17
3.1.1	Objectives for the reporting period	17
3.1.2	Scientific achievements during the reporting period	17
3.1.3	Plan and objectives for the next period	19
3.2	WP 2 – Data analysis techniques	20
3.2.1	Objectives for the reporting period	20
3.2.2	Scientific achievements during the reporting period	20
3.2.3	Plan and objectives for the next period	21
3.3	WP 3 – Instrumentation of selected facilities	22
3.3.1	Objectives for the reporting period	22
3.3.2	Scientific achievements during the reporting period	22
3.3.3	Plan and objectives for the next period	22

3.4	WP 4 – Measurement campaigns	23
3.4.1	Objectives for the reporting period	23
3.4.2	Scientific achievements during the reporting period	24
3.4.3	Plan and objectives for the next period	29
3.5	WP 5 – Model development	30
3.5.1	Objectives for the reporting period	30
3.5.2	Scientific achievements during the reporting period	30
3.5.3	Plan and objectives for the next period	33
3.6	WP 6 – Data sharing and dissemination of results	34
3.6.1	Objectives for the reporting period	34
3.6.2	Achievements during the reporting period	34
3.6.3	Plan and objectives for the next period	35
3.7	Socio-economic relevance and policy implications	36
3.8	Contributions by the consortium partners	38
3.9	Discussion and conclusion	40
A	Reprinted Papers and Reports 2004–2005	45
A.1	Published, Peer-Reviewed Paper (1)	45
A.2	Published, Peer-Reviewed Paper (2)	57
A.3	Published Paper without Peer-Review (1)	67
A.4	Published Paper Without Peer-Review (2)	79
A.5	Paper Submitted to Peer-Reviewed Journal(1)	87
A.6	Paper Submitted to Peer-Reviewed Journal (2)	125
A.7	Paper Submitted to Peer-Reviewed Journal (3)	139
A.8	Manuscript to Be Submitted to Peer-Reviewed Journal (1)	155
A.9	Unpublished Report(1)	173
A.10	Unpublished Report(2)	241

List of Figures

3.1	The concentric-cylinder rheometer.	18
3.2	First tests with snow: shear bands appear near the inner cylinder.	18
3.3	Map of the Ryggfonn test site with avalanches recorded in winter 2004/2005. . .	24
3.4	Avalanche 20050416 15:00: Snapshot of avalanche descent	25
3.5	Avalanche 20050416 15:00: Velocity and acceleration vs. location along the lower track	27
3.6	Avalanche 20050416 15:00: ρC_D vs. position within the avalanche	28
3.7	Example image showing a granular flow interacting with a forward-facing step. The flow direction is from left to right.	28

List of Tables

1.1	Project planning and time table – List of milestones (starting date 01.10.2002)	5
1.2	List of deliverables.	6
1.3	Gantt diagram, updated per 30/09/2005.	8
1.4	WPM table for the third year, 01/10/2004–30/09/2005.	9
3.1	Avalanche classification	23
3.2	Overview of archived measurements at the Ryggfonn test site during the winter season 2004/2005.	23
3.3	Overview table of contributions of the consortium partners to each work package.	39

No.	Partner	Contact person	Address	Telephone / Fax	E-mail
1	NGI	Karstein Lied	NGI, P. O. Box 3930 Ullevaal Stadion, N-0806 Oslo, Norway	T +47 2202 3074 F +47 2223 0448	kl@ngi.no
2	IMOR	Tómas Jóhannesson	IMOR, Bústaðavegi 9, IS-150 Reykjavík, Iceland	T +354 522 6000 F +354 522 6001	tj@vedur.is
3	SGUL	Chris Keylock	University of Leeds, School of Geography, Woodhouse Lane, Leeds LS2 9JT, England	T +44 113 343 3307 F +44 113 343 3308	c.j.keylock@leeds.ac.uk
4	DAMTP	Jim McElwaine	Department of Applied Mathematics and Theoretical Physics, Centre for Mathematical Sciences, Wilberforce Road, Cambridge CB3 0WA, England	T +44 1223 337 858 F +44 1223 765 900	J.N.McElwaine@damtp-cam.ac.uk
5	AIATR	Lambert Rammer	Inst. für Lawinen- und Wildbachforschung, Hofburg, Rennweg 1, A-6020 Innsbruck, Austria	T +43 512 573933 5105 F +43 512 573933 5250	lambert.rammer@uibk.ac.at
6	INW	Helmut Schreiber	University of Technology, Dept. of Communications and Wave Propagation, Inffeldgasse 12, A-8010 Graz, Austria	T +43 316 873 7443 F +43 316 463 697	helmut@radar.tu-graz.ac.at
7	ETNA	Mohammed Naaim	Cemagref, Érosion torrentielle, neige et avalanches, BP 76, F-38402 St-Martin-d'Hères cedex, France	T +33 476 762 722 F +33 476 513 803	mohamed.naaim@cemagref.fr
8	DIIA	Massimiliano Barbolini	University of Pavia, Hydraulics and Environmental Engineering Dept., Via Ferrata 1, I-27100 Pavia, Italy	T +39 0382 985 308 F +39 0382 985 589	m.barbolini@unipv.it
9	DGG	Emma Suriñach	Universitat de Barcelona, Dept. de Geodinàmica i Geofísica, Martí i Franqués s/n, E-08028 Barcelona, Spain	T +34 93 402 1386 F +34 93 402 1340	emma.surinach@ub.edu

Address list of participants

LIST OF TABLES

Chapter 1

Management Progress Report 01/05–30/09/2005

1.1 Objectives of the reporting period

Sensor development and installation: Determine and correct reason(s) for malfunctioning of FMCW radars during the winter of 2004/2005, reinstall repaired radars in Ryggfonn. Improve the seismic data acquisition system.

Development of data analysis methods: Improve existing analysis methods for seismic signals, in particular for the determination of avalanche velocities at Ryggfonn. Begin study of analysis methods for high-time-resolution load-cell measurements from the Vallée de la Sionne test site (in collaboration with SLF).

Experiments and data analysis: Conduct further experiments on the rheology of rapidly flowing granular materials and on entrainment/deposition at the granular chute in Pavia. Analyse data from Ryggfonn and from granular chutes.

Development of new dynamical models: Continue development, validation and documentation of ETNA's MN2L model. Understand density dependence of the stresses in sheared granular material, formulate the governing equations for NGI's new density-changing flow model. Continue the study of shock formation in the impact of a granular flow against obstacles.

Dissemination of results: Outline of Handbook on dam design, detailed planning of work. Planning of the European Summer University advanced course on snow avalanche modelling (to be held after the conclusion of SATSIE). Maintenance of website. Data archiving.

1.2 Scientific/technical progress in the Work Packages

1.2.1 WP 1 – Sensor development

- The four new frequency-modulated continuous-wave (FMCW) profiling radars were retrieved from Ryggfonn and thoroughly tested. Their malfunctioning was mainly due to progressive corrosion of contacts. The necessary repairs and changes were largely finished in the reporting period, reinstallation in Ryggfonn will take place in November 2005.
- The improvement of ETNA's annular snow rheometer was completed. Tests with snow will be carried out during the winter 2006 at Col du Lac Blanc.

- The damaged air-pressure sensors at Vallée de la Sionne were modified and will be tested again during the winter 2006.

1.2.2 WP 2 – Data analysis techniques

- The algorithms for front tracking in video recordings have been improved so that they are capable of stabilising shaking videos. The video material available from SATSIE experiments has been processed.
- An agreement has been reached between DAMTP and SLF on further developing the analysis algorithms for high-frequency pressure measurements and analysing respective data from Vallée de la Sionne during the next reporting period.

1.2.3 WP 3 – Instrumentation of selected facilities

- As noted above under WP 2, the four FMCW radars were retrieved from Ryggfonn for testing and repairing. They will be reinstalled in November 2005.
- The necessary maintenance work was carried out at the Ryggfonn test site. Replacement of the data and power cables had to be postponed for financial reasons.

1.2.4 WP 4 – Measurement campaigns

- A measurement campaign with artificial release was carried out at Ryggfonn in mid-April. Data were obtained from video cameras, geophones, load plates at four locations, and the new Doppler radar. AIATR's Doppler radar and all four FMCW radars malfunctioned.
- The Ryggfonn data from 2004/2005 as well as selected events from earlier winters were thoroughly analysed, emphasising cross-comparison between different types of measurements. It was corroborated that dry-snow avalanches are preceded by a fluidised head of high velocity but low density. The velocity along the avalanche body diminishes at least linearly from the head to the tail.
- Analysis of the April 2005 Ryggfonn data showed that pressures from slow-moving wet-snow avalanches can be much higher than commonly believed.
- Correlation of measured runout distances and approach velocities at the Ryggfonn dam revealed a linear relationship between initial specific kinetic energy and overrun length from the dam, with an effective friction coefficient of 0.4. If corroborated by further measurements, this will be a result of great practical usefulness.
- Various impact experiments were conducted at the granular chute in Pavia and the snow chute at Col du Lac Blanc. Obstacles included deflecting dams, shallow steps and high mast-like objects. The granular flows had very high Froude numbers and exhibited shock formation or jets shooting off at the sides of the obstacle.
- In contrast, the snow-chute experiments with a deflecting dam had much lower (yet supercritical) Froude numbers and an oblique shock did not always form. The run-up height may exceed traditional estimates based only on kinetic energy. Theoretical analysis of these experiments is ongoing.
- Dedicated experiments have been started at the Pavia chute to study entrainment and the consequent modification of the velocity profile. They can be used to test recent theoretical work (see below) and will be continued throughout the next reporting period.

1.2.5 WP 5 – Model development

- The MN2L two-layer model was distributed to professionals of the Service RTM in France who are in charge of hazard mapping in mountain areas. To this end, the model code was embedded in a standard spreadsheet with macros providing input masks and visualising the simulation results. The package also contains a manual in French (an English translation is in preparation). The package gives the user the choice of three different models: a simple centre-of-mass model, a one-layer variant of MN2L and the full two-layer code. User response to the model has been very positive.
- In the study of flow-regime changes in the Criminale-Ericksen-Filbey rheology, it was appreciated that a well-defined density response to changes in slope and thus to the ratio of shear and normal stresses is possible only if the dispersive shear stresses grow more slowly with density than the normal stresses. revealed that the existing NIS model needs to be extended with an additional dispersive-pressure term to avoid inconsistencies at high shear rates and that the parameters have to satisfy certain inequalities. The model has the potential to describe the transition to a fluidised flow regime at high shear rates, but it is suspected that such a transition requires excess pore pressures due to the air flow around the avalanche body unless the terrain is extremely steep.
- The mathematical theory of the flow about and inside a gravity-current head was developed further and extended so as to be better applicable to powder-snow avalanches. In order to test the theory, data from the improved air-pressure sensors installed at Vallée de la Sionne (Switzerland) was expected but not obtained due to sensor failure. Publications to be submitted to peer-reviewed journals are in preparation.
- The problem of the interaction of snow avalanches with catching and deflecting dams was approached from different angles. The chute measurements made in Bristol can be very well reproduced by the theory of hydraulic jumps applied to granular flows; several interesting new results were obtained. The merits and limitations of earlier Russian work on compression effects in avalanche impacts were discussed in a report. Back-calculations of naturally deflected avalanches with several different models revealed the benefits of making deflecting dams curved and showed the limitations of present models in the modelling of impacts onto dams.

1.2.6 WP 6 – Data sharing and dissemination of results

- The *SATSIE homepage* was kept up-to-date.
- *Archiving* of new experimental data using CDF as the data format was continued.
- *Handbook on dam design*: An outline of the entire document and drafts of some sections have been produced. The remaining work has been assigned to project participants and deadlines for writing contributions, reviewing and finalizing have been set.
- *European Summer University, advanced course on avalanche modelling*: The course will be held in Grenoble in September 2006. The Pôle Grenoblois Risques Naturels will take care of administrative matters. A preliminary budget has been elaborated and the list of instructors established, pending some financial uncertainties. A general outline of the course has been agreed upon.

1.3 Milestones and deliverables

Note: The “Status” column in Table 1.1 reflects the status of the milestones at the end of the reporting period: 3 – achieved; 2 – nearing completion; 1 – not yet near completion.

The following milestones were reached during the 6th semester of SATSIE:

M0.6: The 3rd Management Progress Report was delivered to the Commission on time.

M1.13, M2.5: The report documenting sensor development and data analysis software is completed, but an agreement between DAMTP and SLF makes it possible to analyse high-frequency impact pressure data from Vallée de la Sionne. Report delivery has been postponed so that a description of the techniques to be developed and the concomitant software can be included in the report.

M4.8, M4.9: A comprehensive presentation of the results obtained at Ryggfonn in the winter 2005 is given in an NGI report. The highlights of both the chute experiments and the Ryggfonn measurements were presented in four talks at the 2005 General Assembly of the EGU in Vienna (April 2005). Several papers corresponding to these talks have been submitted to a peer-reviewed journal (Cold Regions Science and Technology).

M6.4, M6.4: Archiving of the experimental data from SATSIE up to the winter 2005 has been completed.

Status of the deliverables due during the reporting period:

D9 3rd Management Progress Report: delivered to the Commission in time.

D6 Report on sensor development and data analysis techniques: As stated above, this report is completed but held back so that an important additional development can be included.

D8 Updated report on European test sites: This deliverable is based on a report produced by the EU RTD project SAME in 1998. Its completion has been delayed because the editing team had underestimated the effort when deciding to transfer this complex document from the L^AT_EX document processing system to Microsoft Word format. By the end of the reporting period, however, the report has been submitted to review by the consortium members.

D10 Documentation of sensor installation work: Completed, but still in the process of internal reviewing. As D8, it will definitely be ready for delivery before the end of 2005.

Status of deliverables due within the next reporting period:

D11 Summary publication on results from small and large-scale experiments: The second draft of a comprehensive review paper has been circulated among team members. Work on the publication is progressing. Towards the end of the winter 2006, it will have to be decided whether submission of the article can proceed as planned or important new findings from the 2006 campaign require it to be held back until mid-2006.

D12 Summary publication on avalanche / dam interaction measurements: A scientific paper analysing all data from Ryggfonn of sufficient quality has been submitted to a peer-reviewed journal, thus this deliverable is considered achieved. Depending on the outcome of laboratory experiments and full-scale measurements at Ryggfonn, further publications may follow.

Table 1.1: Project planning and time table – List of milestones (starting date 01.10.2002)

No.	Date	Content	Tasks	Status
M0.1	30.04.2003	Deliverable D1 (Management Progress Report #1)		3
M0.2	30.11.2003	Deliverable D3 (1st Annual Report)		3
M0.3	30.04.2003	Deliverable D4 (Management Progress Report #2)		3
M0.4	30.10.2004	Deliverable D5 (Midterm review meeting)		3
M0.5	30.11.2004	Deliverable D7 (2nd Annual Report)		3
M0.6	30.04.2005	Deliverable D9 (Management Progress Report #3)		3
M0.7	30.11.2005	Deliverable D16 (3rd Annual Report)		2
M0.8	31.03.2006	Deliverable D17 (Technology Implementation Plan)		2
M0.9	30.04.2006	Deliverable D19 (Final Report)		1
M1.1	31.08.2002	Shear/normal stress plates ready for tests	T1.5	3
M1.2	31.10.2002	Prototype LED sensors ready for tests	T1.4	3
M1.3	31.10.2003	Snow rheometer ready for tests	T1.6	3
M1.4	30.09.2003	Video locations and recording strategies selected	T1.2	3
M1.5	31.12.2003	Seismic equipment ready for tests	T1.7	3
M1.6	15.12.2003	Prototype frequency-stepping radar ready for first tests	T1.1	3
M1.7	31.10.2003	Prototype pulsed Doppler radar ready for basic testing	T1.1	3
M1.8	30.09.2002	Shear/normal stress plates ready for installation	T1.5	3
M1.10	31.12.2002	LED sensor arrays ready for installation	T1.4	3
M1.11	30.10.2004	Improved design of frequency-stepping radar	T1.1	3
M1.12	30.06.2004	Prototype pulsed Doppler radar ready for operational use	T1.1	3
M1.13	30.11.2004	Deliverable D6 (together with WP 2)	T1.1-1.7	3
M2.1	31.12.2002	Review of current techniques, proposals for improvements	T2.1-2.6	3
M2.2	31.05.2003	Beta software and algorithms for data analysis completed	T2.1-2.6	3
M2.3	31.07.2003	Review of data analysis with proposals for improving measurements	T2.1-2.6	3
M2.4	31.05.2004	Version 1 of software and algorithms for data analysis completed	T2.1-2.6	3
M2.5	30.11.2004	Deliverable D6 (together with WP 1)	T2.1-2.6	2
M2.6	31.07.2004	Review of data analysis, proposals for improving measurements	T2.1-2.6	3
M2.7	31.05.2005	Version 2 of software and algorithms for data analysis completed	T2.1-2.6	3
M3.1	30.09.2003	Inventory of needed measurements and existing instrumentation	T3.1-3.5	3
M3.2	30.09.2003	Inventory of the existing laboratory facilities	T3.4-3.5	3
M3.3	30.09.2003	Plan for extended instrumentation of the Ryggfonn site	T3.1-3.5	3
M3.4	31.10.2003	Instrumentation maintenance after winter 2003	T3.1-3.3	3
M3.5	31.10.2004	Instrumentation maintenance after winter 2004	T3.1-3.3	3
M3.6	30.11.2004	Installation of instrumentation at Ryggfonn completed	T3.1-3.5	3
M3.7	30.11.2004	Deliverable D8: Updated overview of European test sites	T3.1-3.5	2
M3.8	31.08.2005	Deliv. D10: Documentation of installation work	T3.1-3.5	2
M3.9	30.09.2005	Instrumentation maintenance after winter 2005	T3.1-3.3	2
M4.1	31.05.2003	Summary of experiments during winter 2003	T4.1-4.4	3
M4.2	31.07.2003	Preliminary analysis and comparison of updated experimental plan	T4.1-4.4	3
M4.3	30.11.2004	Exp. data from winter 2003 processed and archived	T4.1-4.3	3
M4.4	30.10.2004	Chute experiments 2003 summarised, processed and archived	T4.4	3
M4.5	31.05.2004	Summary of experiments during winter 2004	T4.1-T4.3	3
M4.6	31.07.2004	Preliminary analysis and comparison – updated experimental plan	T4.1-4.4	3
M4.7	30.11.2004	Exp. data from winter 2004 processed and archived	T4.1-4.3	3
M4.8	30.05.2005	Chute experiments 2004 processed and archived	T4.4	3
M4.9	31.05.2005	Summary of experiments during winter 2005	T4.1-4.3	3
M4.10	31.03.2006	Deliverables D11, D12	T4.4-4.5	2
M4.11	31.12.2005	Chute experiments 2005 processed and archived	T4.4	2
M4.12	31.05.2006	Summary of experiments during winter 2006	T4.1-T4.3	1
M5.1	30.06.2004	Preliminary reports on model development	T5.1-5.4	3
M5.2	31.12.2004	Updated reports on model development	T5.1-5.4	2
M5.3	31.03.2006	Summary report on the validation of the new models	T5.5	1
M5.4	31.03.2006	Deliverable D13 (new models of specific processes)	T5.1-5.4	1
M6.1	31.01.2003	Deliverable D1: SATSIE web site established	T6.3	3
M6.2	31.03.2004	Data format for SATSIE data archive defined	T6.1	3
M6.3	30.11.2004	Preprocessed data from winter 2003 archived	T6.2	3
M6.4	30.11.2004	Preprocessed data from winter 2004 archived	T6.2	3
M6.5	30.11.2005	Preprocessed data from winter 2005 archived	T6.2	3
M6.7	31.03.2006	Deliverable D14: Handbook on design of protection dams	T6.4	2
M6.8	31.03.2006	Deliv. D15: User manuals for advanced models	T6.5	2

Table 1.2: List of deliverables.

Deliverable No.	Responsible partner	Deliverable title	Due date (month)	Nature	Dissemination level
1	SGUL, DAMTP	Web site and meta-data archive	6	Da	PU/CO
2	NGI	Management progress report #1	7	Re	CO
3	NGI	1st Annual scientific report and related materials	14	Re	CO
4	NGI	Management progress report #2	19	Re	CO
5	NGI	Mid-term review meeting	25	Meeting	
6	ETNA, DAMTP	Summary publication on sensor design and data analysis techniques	26	Re	RE
7	NGI	2nd Annual scientific report and related materials	26	Re	CO
8	DIHA	Updated report on European avalanche test sites	26	Re	PU
9	NGI	Management progress report #3	31	Re	CO
10	DIHA	Documentation of instrumentation scheme and installation work at the selected sites	35	Re	PU
11	SGUL	Summary publication on results from small and large-scale experiments	42	Re, Da	PU
12	SGUL	Summary publication on avalanche / dam interaction measurements	42	Re, Da	PU
13	IMOR, ETNA, NGI, DIHA, SGUL, DAMTP	Models of specific processes in avalanche flow and sample modules for inclusion in numerical codes	42	Re, Th, De	PU/CO
14	IMOR	Handbook on deflection and catching dam design	42	Re	PU
15	IMOR, NGI, ETNA, DIHA, SGUL, DAMTP	User manuals for advanced models in avalanche hazard mapping	44	Re	PU
16	NGI	3rd Annual scientific report and related materials	38	Re	CO
17	NGI	Technology Implementation Plan	42	Re	CO
18	DIHA, ETNA	European Summer University 2004 on avalanche hazard mapping	24	O	PU
19	NGI	Final scientific report and related materials	46	O	PU

D13 Models of specific processes in avalanche flow and sample modules for inclusion in numerical codes: ETNA's new model (MN2L) has been completed, and it has been introduced in practice in France. Work at NGI on a variant of the original NIS model for strongly curved paths and on a flow-regime-changing model has met with several technical difficulties, but solutions appear to have been found and rapid progress is expected.

D14 Handbook on deflection and catching dam design: By the end of the reporting period, an outline was agreed upon and drafts of several sections written. Completion of the handbook will be a challenge to the consortium because some important open questions remain and the financial resources are very limited (the personnel resources as well for some partners). Nevertheless, work has been progressing largely as planned since the conclusion of the reporting period.

D17 Technology Implementation Plan: A draft of the eTIP was submitted to the Commission with the 2nd Annual Report. Some further results will be added and the entire eTIP reviewed. No delays are expected.

1.4 Deviations from the work plan or/and time schedule

Below we list the deviations from the work plan (in its revised form with adjustments for the project prolongation) and list of milestones and deliverables:

Deliverables D8 and D10: Drafts of the documents are finished, delays were incurred only with certain last-minute adjustments and the reviewing process. There is no impact on the project as no other work or deliverables depend on them.

M3.9: Investigation of the malfunctioning FMCW radars and their repair were not yet completed at the end of the reporting period. Reinstallation of the radars has been scheduled for November.

Model development: Development of NGI's new models describing flow-regime changes has progressed more slowly than anticipated. Further delays would negatively affect deliverables D13 and D15 as well as the planned advanced course on snow avalanche modelling. Therefore, NGI has allocated additional funding (from sources outside the project SATSIE) to further this work.

1.5 Coordination and communication

The third (and last) annual project meeting was held in Seyðisfjörður, Iceland from 1st to 3rd September, preceded by a workgroup meeting covering the handbook on dam design in Reykjavík on 31 August. As the earlier project meetings, this meeting was informative and effective as all project partners sent representatives, the results of the past year could be communicated and discussed, and decisions were taken concerning the finalisation of the deliverables. In addition, partners' ideas and preferences for future research directions and possible collaborations were discussed.

The active participation of the Scientific Officer following up on SATSIE, Mr. Denis Peter, was much appreciated. His brief presentation and his contributions to the discussion were very helpful for understanding the goals of the upcoming 7th Framework Programme. It was decided that the consortium would write a memorandum proposing research priorities in the field of snow and avalanches. (This document was sent to the Commission at the end of September 2005 after having been discussed and accepted by all team members.)

1.6 Encountered management and coordination difficulties

No particular difficulties have been encountered in coordinating the project and communicating among the project members or with outside institutions. As mentioned in earlier reports, managing a project with nine partners is more time-consuming than originally hoped, but the accumulated experience helps to streamline procedures.

An overview showing planned and used manpower in Personnel Months (PM), and "Other costs" (in Euro), is presented in Table 1.4.

SATSIE: Resource use (personnel / O. costs)

Reporting period: April 1, 2005 – September 30, 2005

PM: Personnel months

O. costs: Other costs in Euro

Partner		1	NGI	2	IMOR	3	DAMTP	4	SGUL	5	AIATR	6	INW	7	ETNA	8	DIIA	9	DGG	Tot. pers.	Total
		PM	O.costs	PM	O.costs	PM	O.costs	PM	O.costs	PM	O.costs	PM	O.costs	PM	O.costs	PM	O.costs	PM	O.costs	months	O. costs
Coor- dination	<i>planned</i>	0,50	1500,00	0,00	0,00	0,00	0,00	0,00	0,00	0,00	0,00	0,00	0,00	0,00	0,00	0,00	0,00	0,00	0,00	0,50	1500,00
	<i>used</i>	0,47	3330,96	0,00	0,00	0,00	0,00	0,00	0,00	0,00	0,00	0,00	0,00	0,00	0,00	0,00	0,00	0,00	0,00	0,47	3330,96
	<i>Diff.</i>	-0,03	1830,96	0,00	0,00	0,00	0,00	0,00	0,00	0,00	0,00	0,00	0,00	0,00	0,00	0,00	0,00	0,00	0,00	-0,03	1830,96
WP 1	<i>planned</i>	0,00	0,00	0,00	0,00	0,00	0,00	0,00	0,00	0,00	0,00	0,00	0,00	1,00	0,00	0,00	0,00	0,50	517,00	1,50	517,00
	<i>used</i>	0,40	1259,18	0,00	0,00	0,00	0,00	0,00	0,00	0,00	0,00	0,00	0,00	1,00	0,00	0,00	0,00	1,00	575,00	2,40	1834,18
	<i>Diff.</i>	0,40	1259,18	0,00	0,00	0,00	0,00	0,00	0,00	0,00	0,00	0,00	0,00	0,00	0,00	0,00	0,00	0,50	58,00	0,90	1317,18
WP 2	<i>planned</i>	0,00	0,00	0,00	0,00	0,00	0,00	0,00	0,00	0,00	0,00	1,50	2000,00	0,00	0,00	0,00	0,00	4,50	4649,00	6,00	6649,00
	<i>used</i>	0,00	0,00	0,00	0,00	0,00	0,00	0,00	0,00	0,00	0,00	0,50	2000,00	0,00	0,00	0,00	0,00	4,00	2310,00	4,50	4310,00
	<i>Diff.</i>	0,00	0,00	0,00	0,00	0,00	0,00	0,00	0,00	0,00	0,00	-1,00	0,00	0,00	0,00	0,00	0,00	-0,50	-2339,00	-1,50	-2339,00
WP 3	<i>planned</i>	0,80	0,00	0,25	0,00	0,00	0,00	0,00	0,00	0,00	0,00	0,00	0,00	1,50	0,00	1,00	2500,00	0,50	517,00	4,05	3017,00
	<i>used</i>	0,74	9413,50	0,25	0,00	0,00	0,00	0,00	0,00	0,00	0,00	0,00	0,00	1,50	0,00	1,10	3500,00	0,50	290,00	4,09	13203,50
	<i>Diff.</i>	-0,06	9413,50	0,00	0,00	0,00	0,00	0,00	0,00	0,00	0,00	0,00	0,00	0,00	0,10	1000,00	0,00	-227,00	0,04	10186,50	
WP 4	<i>planned</i>	1,30	5200,00	0,25	0,00	0,00	0,00	0,00	0,00	1,50	7540,00	0,00	0,00	0,00	0,00	1,17	1750,00	0,50	517,00	4,72	15007,00
	<i>used</i>	3,12	7602,05	0,25	0,00	0,00	0,00	0,00	2891,91	2,40	8762,55	0,00	0,00	0,00	0,00	1,27	4500,00	0,50	290,00	7,54	24046,51
	<i>Diff.</i>	1,82	2402,05	0,00	0,00	0,00	0,00	0,00	2891,91	0,90	1222,55	0,00	0,00	0,00	0,00	0,10	2750,00	0,00	-227,00	2,82	9039,51
WP 5	<i>planned</i>	2,20	2000,00	0,75	0,00	0,00	0,00	0,00	0,00	0,00	0,00	0,00	0,00	0,00	0,00	1,83	250,00	0,00	0,00	4,78	2250,00
	<i>used</i>	1,93	2187,68	0,75	0,00	0,00	0,00	0,00	0,00	0,00	0,00	0,00	0,00	0,00	0,00	2,00	1500,00	0,00	0,00	4,68	3687,68
	<i>Diff.</i>	-0,27	187,68	0,00	0,00	0,00	0,00	0,00	0,00	0,00	0,00	0,00	0,00	0,00	0,00	0,17	1250,00	0,00	0,00	-0,10	1437,68
WP 6	<i>planned</i>	1,30	0,00	0,75	0,00	0,00	0,00	0,00	0,00	0,50	1000,00	0,00	0,00	0,00	0,00	0,50	500,00	0,00	0,00	3,05	1500,00
	<i>used</i>	0,67	0,00	0,75	2397,00	0,00	0,00	0,00	0,00	0,75	800,00	0,00	0,00	0,00	0,00	0,55	0,00	0,00	0,00	2,72	3197,00
	<i>Diff.</i>	-0,63	0,00	0,00	2397,00	0,00	0,00	0,00	0,00	0,25	-200,00	0,00	0,00	0,00	0,00	0,05	-500,00	0,00	0,00	-0,33	1697,00
Total	<i>planned</i>	6,10	8700,00	2,00	0,00	0,00	0,00	0,00	0,00	2,00	8540,00	1,50	2000,00	2,50	0,00	4,50	5000,00	6,00	6200,00	24,60	30440,00
	<i>used</i>	7,33	23793,37	2,00	2397,00	0,00	0,00	0,00	2891,91	3,15	9562,55	0,50	2000,00	2,50	0,00	4,92	9500,00	6,00	3465,00	26,40	53609,83
	<i>Diff.</i>	1,23	15093,37	0,00	2397,00	0,00	0,00	0,00	2891,91	1,15	1022,55	-1,00	0,00	0,00	0,00	0,42	4500,00	0,00	-2735,00	1,80	23169,83

Table 1.4: WPM table for the third year, 01/10/2004-30/09/2005.

There is overall good agreement between planned and used resources concerning manpower, as the total used manpower is only about 7% higher than planned. The “Other costs” are considerably higher than planned, that is 76% higher. This excess consumption is mainly caused by partner No. 1, where the extra expenditures are due to:

- the expensive coordination meeting in Iceland,
- costs caused by the malfunctioning of the FMCW radars in Ryggfonn (WP1 and WP3),
- the repair of pressure transducers at the steel pylon in Ryggfonn (WP3), and
- expensive field tests in Ryggfonn (WP4).

Apart from this discrepancy there is good agreement between planned and used costs in the reporting period.

Chapter 2

Executive Summary

01/10/2004–30/09/2005

Contract no.	EVG1-CT2002-000590	Reporting period	01/10/2004 – 30/09/2005
Title	SATSIE – Avalanche Studies and Model Validation in Europe		
Main objectives: <ul style="list-style-type: none">• Improve design of new sensors where necessary.• Measurement campaigns at Ryggfonn, several series of chute experiments at Col du Lac Blanc, in Pavia and Davos.• Theoretical studies and modelling of flow-regime transitions, entrainment, powder-snow avalanche flow and seismic signals generated by avalanches.• Continue studies of shock formation in avalanche–dam interactions.• Outline of handbook on dam design, begin writing. Planning for advanced course on avalanche modelling (European Summer University 2006).			
Scientific achievements: <ul style="list-style-type: none">• One combined dry and wet-snow avalanche artificially released at Ryggfonn site, velocity measurement with new Doppler radar. Refined analysis of this and older data from Ryggfonn revealed a fairly simple correlation between approach velocity at the dam and overrun length that needs to be tested further..• FMCW radar systems at Ryggfonn and air-pressure sensors at Vallée de la Sionne failed due to corrosion and freezing problems, other sensors worked. The problems have been analysed and the instrument designs improved.• Chute experiments at Col du Lac Blanc and Pavia refined earlier experiments and corroborated their findings (velocity profiles, entrainment rates and mechanisms, etc.). New series of chute experiments with granular matter and snow on avalanche–obstacle interaction confirm shock theory at high Froude numbers and may show deviations from theory in snow flows at Froude numbers around 3.• ETNA’s new avalanche model MN2L introduced to French practitioners. Progress in extending the NIS model to describe flow-regime transitions.• Work on dissemination of results intensified.			

Socio-economic relevance and policy implications:

After the successful European Summer University 2004, dissemination of project results to the interested public (government agencies, avalanche practitioners) will largely occur through the deliverables due at the end of the prolonged project in mid 2006. An exception is the new French avalanche model MN2L, which is already being distributed to the Service Réstitution Terrains en Montagne in France.

Work during the final phase of SATSIE will be strongly directed towards synthesis of the new results and application to products with socio-economic relevance, i. e., improved models for avalanche hazard mapping, a practical handbook for improved dam design, and dissemination of our results. After the closing date of SATSIE, an advanced European Summer University course on the use of the new models in avalanche hazard mapping will be offered in 2006.

Conclusions:

In its third year, SATSIE has again produced a wealth of important results, even though the new FMCW radar systems were damaged by corrosion and did not deliver data. The necessary steps were taken to ensure their proper functioning in the winter 2006. The prolongation of the project opens the perspective of collecting data from Ryggfonn that is more comprehensive than hitherto and will serve to test the new numerical models and the proposed shock theory of avalanche–dam interactions. The valorisation of the project results has begun, with intense work scheduled for the handbook on dam design, a number of reports and scientific publications, and the preparations for an advanced summer course in 2006.

Keywords:

Snow avalanches, mitigation, hazard mapping, avalanche monitoring, handbook on dam design, radar, full-scale experiments, chute experiments, flow regimes, entrainment, shock formation, powder-snow avalanches.

Peer-reviewed articles

- Barbolini, M., A. Biancardi, F. Cappabianca, L. Natale and M. Pagliardi. 2005. Experimental study of erosion processes in snow avalanches. *Cold Regions Science and Technology* **43** (1–2), 1–9; doi:10.1016/j.coldregions.2005.01.007.
- Barbolini, M., A. Biancardi, L. Natale and M. Pagliardi. 2005. A low cost system for the estimation of concentration and velocity profiles in rapid dry granular flows. *Cold Regions Science and Technology* **43** (1–2), 49–61; doi:10.1016/j.coldregions.2005.05.003.
- Barbolini, M., F. Cappabianca and F. Savi. 2003. Risk assessment in avalanche prone areas. *Annals of Glaciology* **38**, 115–122.
- Barbolini, M., F. Cappabianca and F. Savi. 2003. A new method for the estimation of avalanche exceedance probabilities. *Surveys in Geophysics*, **24** (5–6), 587–601.
- Bouchet, A., M. Naaim, F. Ousset, H. Bellot and D. Cauvard. 2003. Experimental determination of constitutive equations for dense and dry avalanches: presentation of the set-up and first results. *Surveys in Geophysics* **24** (5–6), 525–541.
- Eglit, M. E., and K. S. Demidov. 2005. Mathematical modeling of snow entrainment in avalanche motion. *Cold Regions Science and Technology* **43** (1–2), 10–23; doi:10.1016/j.coldregions.2005.03.005. (Elaboration of this paper was funded by a NATO fellowship linked to SATSIE.)
- Faug, T., M. Naaim, D. Bertrand, P. Lachamp and F. Naaim-Bouvet. 2003. Varying dam height to shorten the run-out of dense avalanche flows: developing a scaling law from laboratory experiments. *Surveys in Geophysics* **24** (5–6), 555–568.
- Faug, T., M. Naaim and F. Naaim-Bouvet. 2004. Experimental and numerical study of granular flow and fence interaction. *Annals of Glaciology* **38**, 135–138.
- Faug, T., M. Naaim and F. Naaim-Bouvet. 2004. An equation for spreading length, centre of mass and maximum run-outs shortenings of avalanche flows by obstacle. *Cold Regions Science and Technology* **39**, 141–151.
- Gauer, P., and D. Issler. 2004. Possible erosion mechanisms in snow avalanches. *Annals of Glaciology* **38**, 384–392.
- Hákonardóttir, K. M., A. J. Hogg, J. Batey and A. W. Woods. 2003. Flying avalanches. *Geophysical Research Letters* **30** (23), art. no. 2191.
- Hákonardóttir, K. M., A. J. Hogg, T. Jónsson, M. Kern and F. Tiefenbacher. 2003. Large-scale avalanche braking mound and catching dam experiments with snow: A study of the airborne jet. *Surveys in Geophysics* **24** (5–6), 543–554.
- Hákonardóttir, K. M., A. J. Hogg, T. Jóhannesson and G. G. Tómaasson. 2003. A laboratory study of the retarding effects of braking mounds on snow avalanches. *Journal of Glaciology* **49** (165), 191–200.
- Issler, D. 2003. Experimental information on the dynamics of dry-snow avalanches. In K. Hutter and N. Kirchner (eds.): *Dynamic Response of Granular and Porous Materials Under Large and Catastrophic Deformations*. Lecture Notes in Applied and Computational Mechanics 11, Springer, Berlin, pages 109–160.
- Kern, M. A., F. Tiefenbacher and J. N. McElwaine. 2004. The rheology of snow in large chute flows. *Cold Regions Science and Technology* **39**, 181–192.
- Keylock, C. J. 2005. An alternative form for the statistical distribution of extreme avalanche runout distances. *Cold Regions Science and Technology* **42**, 185–193.

- McElwaine, J. N., and F. Tiefenbacher. 2003. Calculating internal avalanche velocities from correlation with error analysis. *Surveys in Geophysics* **24** (5–6), 499–524.
- McElwaine, J. N. 2004. Calculation of Two-Dimensional Avalanche Velocities From Opto-Electronic Sensors. *Annals of Glaciology* **38**, 139–144.
- McElwaine, J. N. 2005. Rotational flow in gravity current heads. *Philosophical Transactions of the Royal Society of London, Series A* **363**, 1603–1623; doi:10.1098/rsta.2005.1597.
- McElwaine, J. N., K. Sugiura and N. Maeno. 2004. The splash function for snow from wind-tunnel measurements. *Annals of Glaciology* **38**, 71–78.
- McElwaine, J. N., and B. Turnbull. 2005. Air pressure data from the Vallée de la Sionne avalanches of 2004. *Journal of Geophysical Research* **110**, F03010; doi:10.1029/2004JF000237.
- Naaïm, M., T. Faug and F. Naaïm-Bouvet. 2003. Dry granular flow modelling including erosion and deposition. *Surveys in Geophysics* **24** (5–6), 569–585.
- Naaïm, M., F. Naaïm-Bouvet, T. Faug and A. Bouchet. 2004. Dense snow avalanche modeling: flow, erosion, deposition and obstacle effects. *Cold Regions Science and Technology* **39**, 193–204.
- Naaïm-Bouvet, F., M. Naaïm and T. Faug. 2004. Dense and powder avalanches. Momentum reduction generated by a dam. *Annals of Glaciology* **38**, 373–378.
- Naaïm-Bouvet, F., S. Pain, M. Naaïm and T. Faug. 2003. Numerical and physical modelling of the effect of dam on powder avalanche motion: Comparison with previous approaches. *Surveys in Geophysics* **24** (5–6), 479–498.
- Primus, M., F. Naaïm-Bouvet, M. Naaïm and T. Faug. 2004. Physical modelling of the interaction between mounds or deflecting dams and powder snow avalanches. *Cold Regions Science and Technology* **39**, 257–267.
- Sampl, P., F. Naaïm-Bouvet and M. Naaïm. 2004. Interaction between dams and powder avalanches: determination of simple friction laws for shallow-water avalanche models. *Cold Regions Science and Technology* **39**, 115–131.
- Suriñach, E., I. Vilajosana, G. Khazaradze, B. Biescas, G. Furdada, and J. M. Vilaplana. 2005. Seismic detection and characterization of landslides and other mass movements. *Natural Hazards and Earth System Sciences* **5**, 791–798; SRef-ID: 1684-9981/nhess/2005-5-791.

Articles submitted to peer-reviewed journals

- Bouchet, A., and M. Naaïm. 2004. Clustering in dense snow flows. Submitted to *Journal of Rheology*.
- Faug, T., M. Naaïm and A. Fourrière. 2005. Dense snow flowing past a deflecting obstacle: an experimental investigation. Submitted to *Cold Regions Science and Technology* (EGU 2005 special issue).
- Gauer, P., D. Issler, K. Lied, K. Kristensen, H. Iwe, E. Lied, L. Rammer, and H. Schreiber. 2005. On avalanche full-scale measurements at the Ryggfonn test site, Norway. Submitted to *Cold Regions Science and Technology* (EGU 2005 special issue).
- Hauksson, S., M. Pagliardi, M. Barbolini and T. Jóhannesson. 2005. Laboratory measurements of impact forces of granular flow against mast-like obstacles. Submitted to *Cold Regions Science and Technology* (EGU 2005 special issue).
- Keylock, C. J. 2005. Constrained surrogate time series with preservation of the mean and variance structure. Submitted to *Physical Review E*.

- Natale, L., M. Barbolini, and C. J. Keylock. 2005. A critical assessment of the *alpha-beta* statistical model for estimating extreme avalanche runout. Submitted to *Arctic, Antarctic and Alpine Research*.
- Vilajosana, I., G. Khazaradze, E. Suriñach, E. Lied and K. Kristensen. 2005. Snow avalanches speed determination using seismic methods. Submitted to *Cold Regions Science and Technology* (EGU 2005 special issue).

Non-refereed publications and reports

- Barbolini, M., F. Cappabianca, D. Issler, P. Gauer, M. E. Eglit, M. Naaim and R. Sailer. October 2003. *Erosion and deposition processes in snow avalanche dynamics: Report on the state of the art*. SATSIE report. Dipartimento d'Ingegneria Idraulica e Ambientale, Università degli Studi di Pavia, Pavia, Italy.
- Barbolini, M. and M. Pagliardi. October 2003. *Experiments with granular materials at Pavia chutes*. SATSIE project report. Dipartimento d'Ingegneria Idraulica e Ambientale, Università degli Studi di Pavia, Pavia, Italy.
- Barbolini, M., F. Cappabianca and R. Sailer. 2004. Empirical estimate of vulnerability relations for use in snow avalanche risk assessment. In: C. A. Brebbia (ed.), *Risk Analysis IV*. WIT press. Pages 533–542.
- Gauer, P. and K. Kristensen. 2005a. Ryggfonn measurements. Winter 2004/2005. NGI Report 20021048–8. Norges Geotekniske Institutt, Oslo, Norway.
- Gauer, P. and K. Kristensen. 2005b. Ryggfonn measurements. Overview and dam interaction. NGI Report 20021048–10. Norges Geotekniske Institutt, Oslo, Norway.
- Hákonardóttir, K. M. March 2004. The Interaction Between Snow Avalanches and Dams. PhD thesis, School of Mathematics, University of Bristol, Bristol, England. xxi + 142 pages.
- Hákonardóttir, K. M., A. Hogg and T. Jóhannesson. November 2003. A laboratory study of the interaction between supercritical, shallow flows and dams. Report 03038, Veðurstófa Íslands, IS-150 Reykjavík, Iceland.
- Issler, D. February 2003. *Notes on the Criminale–Ericksen–Filbey fluid as a candidate rheology for snow avalanches*. SATSIE memo. Norges Geotekniske Institutt, Oslo, Norway.
- Issler, D., M. Barbolini, F. V. De Blasio, C. B. Harbitz, G. Khazaradze, K. Kristensen, K. Lied, J. N. McElwaine, A. I. Mears, A. Moe, M. Naaim and R. Sailer. In preparation. Simulations of dry-snow avalanches observed in the full-scale test site Ryggfonn, Norway.
- Issler, D., C. B. Harbitz, K. Kristensen, K. Lied, A. S. Moe, M. Barbolini, F. V. De Blasio, G. Khazaradze, J. N. McElwaine, A. I. Mears, M. Naaim and R. Sailer. 2005. Comparison of avalanche models as applied to dry-snow avalanches observed in the full-scale test site Ryggfonn, Norway. In: K. Senneset, K. Flaate and J. O. Larsen (eds.), *Landslides and Avalanches. ICFL 2005 Norway*. Proc. 11th Intl. Conf. and Field Trip on Landslides, Norway, 1–10 Sept. 2005. Taylor & Francis/Balkema, Leiden, The Netherlands. Pages 173–179.
- Jóhannesson, T. January 2003. *SATSIE Work Package 5 Meeting in Leeds on 16–18 January 2002. Thoughts to start discussion about model development and validation*. Memo TóJ-2003–02, Icelandic Meteorological Office, Reykjavík, Iceland.
- Naaim, M., T. Faug, F. Naaim-Bouvet and A. Bouchet. 2004. Modélisation des avalanches de neige sèche intégrant l'érosion, le dépôt et les effets d'une digue. *La Houille Blanche* no. 1/2004.

Planned publications

A substantial number (ten or more) of scientific publications in refereed international journals, several reports as well as various contributions to conference proceedings are expected to flow directly from project work. The major works will be a comprehensive review of experimental results in snow avalanche research and their implications, several papers on the results from Ryggfonn and the chute experiments with respect to flow regimes and entrainment, and on the extension of the NIS avalanche model. Another major publication, directed towards practical use by engineers, will be the handbook on dam design (Deliverable D14).

Chapter 3

Scientific Progress Report 01/10/2004–30/09/2005

3.1 WP 1 – Sensor development

3.1.1 Objectives for the reporting period

Task 1.1 – Radar techniques: Determine reasons for malfunctioning of the FMCW radars during the winter 2005 and repair the systems.

Task 1.6 – Snow rheometer: Implement external pressurising system to prevent formation of shear bands.

Task 1.7 – Seismic sensors: Modify data acquisition system for better reliability.

3.1.2 Scientific achievements during the reporting period

Task 1.1: Radar techniques: The four FMCW radars that had malfunctioned during the winter 2005 were retrieved from their caverns underneath 4–10 m of avalanche deposits and thoroughly investigated in Oslo and Graz. The main problem was found to be corrosion of contacts inside the systems under the harsh and humid conditions they were exposed to for several months. In addition some other design weaknesses that degrade radar performance to some degree were also identified. One was fixed, the impact of the remaining do not justify the large effort of redesigning several components of the system at this point. They can, however, be corrected if a future series of radars is built. Another weakness that could not be studied in detail and cannot presently be corrected for financial reasons is the cables between the instrument shed and the sensors: 22 conductor pairs, carrying both radar power and communication, are united in single cable of over 500 m length. Experience has shown a relatively high frequency of noise spikes in the data lines. Some of these spikes generated false avalanche trigger signals leaving the radars in a full power mode. This problem is now fixed by radar software modification, but a relatively high bit error rate in data transfer from the radar to the controlling PC in the shed remains.

The repaired radars will be reinstalled in Ryggfonn in late November or early December 2005.

Task 1.6: Snow rheometer: In order to determine the constitutive equation of the dense flowing snow, Cemagref installed a large concentric-cylinder rheometer (see Fig. 3.1) at Col du



Figure 3.1: The concentric-cylinder rheometer.



Figure 3.2: First tests with snow: shear bands appear near the inner cylinder.

Lac Blanc. This system will serve to characterise the snow properties just before running the chute experiments. The inter-cylinder distance is 20 cm and the total volume is 0.5 m^3 . The rotation velocity can be varied between 0 and 60 r.p.m.

After the analysis of a series of unsuccessful tests with snow (shear localisation, see Fig. 3.2), the following adaptations were made in order to avoid the formation of shear bands:

- A lateral load is applied thanks to an inflatable membrane.
- A vertical boundary condition is applied using a lid made of Plexiglas to control the total volume and enable visual observations of the experiment.

The modified rheometer will be used during experimental campaigns in the winter 2005/2006.

Task 1.7: Adaptation of seismic instrumentation to the conditions encountered in avalanche paths: During the 2004-2005 winter season the seismic Data Acquisition System (DAS) REFTEK 130 experienced several problems, mainly due to hardware errors related to the malfunctioning of the internal logger's communications card. For this reason, at the end of February the DAS was replaced with a new unit temporarily lent by the manufacturer.

Unfortunately, this instrument also developed similar problems. These technical problems with the data logger have been solved for the next season by the dealer. The new equipment was installed in Ryggfonn in October 2005. For the coming winter season, the UB seismometers were placed at the same locations as in the last two campaigns (see 2nd Annual Report). The configuration of the logger remains largely the same as in previous years, even though some parameters have been changed. Specifically, to trigger the equipment, an external trigger is now used instead of the level trigger used during the last campaigns. The main reason for this change is that the E–W component of the sensor near the hut has been repaired and cannot be used as the level trigger channel anymore. The trigger signal is now the same as that used by NGI's system.

3.1.3 Plan and objectives for the next period

Sensor design within SATSIE is completed. The performance of the repaired FMCW radar system during the winter 2006 will be closely monitored, but no repairs or further adaptations of the systems will be possible before the end of the project (the radars can be retrieved from their caverns only in the summer).

The report on sensor design and analysis techniques (deliverable D6) is also completed but is held back pending development of further data analysis tools.

3.2 WP 2 – Data analysis techniques

3.2.1 Objectives for the reporting period

Task 2.1 – Data-analysis techniques for radars: Completion and testing of the programs for Doppler and FMCW radars.

Task 2.3 – Air pressure sensor analysis: Investigate and possibly correct the reason for the failure of the air-pressure sensors at Vallée de la Sionne.

Task 2.5 – Impact pressure analysis: Improvement of the analysis technique proposed by (Schaer and Issler, 2001) if and when SLF makes high-frequency measurements from Vallée de la Sionne available.

Task 2.6 – Seismic signal analysis techniques: Further development of technique for determining avalanche front speed. Search for criteria to detect avalanche type and size from seismic signals.

3.2.2 Scientific achievements during the reporting period

All but two tasks in this work package are complete. Analysis of data is performed as it arrives. Deliverable 2 “Summary publication on sensor design and data analysis techniques” has been written. Further additions to this are expected.

Task 2.1 – Data-analysis techniques for radars: Development of the analysis programs for both the Doppler and FMCW radars was finished during the reporting period. Data from the April 2005 avalanche allowed successful testing of the Doppler program. The FMCW program will be adapted if necessary when data from snow avalanches becomes available.

Task 2.2 – Video analysis: As mentioned in the previous report this task is essentially finished. New videos will be analysed as they are filmed. A video from Ryggfjonn 2005 has been obtained, but was not filmed from a tripod, so the images had considerable shake and global motion. Software was written to track features between each frame and thus build up trajectories for the image sequence. Homographies were then calculated to map all the images to a standard reference frame thus stabilising the image sequence. This work is being added to Deliverable 2 on data analysis. The next stage is to calculate the camera parameters from this and map the avalanche onto the digital terrain map.

Task 2.3 – Air pressure sensors: The two new air pressure sensors from Vallée de la Sionne with five transducers have been examined. The transducers were all sent back to the manufacturer who reported that they had all been destroyed. The most likely explanation for this is as follows. Each transducer was connected by a very short tube to the outlet on sensor, which had a heating element to keep it ice free. If the heating elements were powerful enough to heat the outlet to a higher relative temperature than the transducer, a gradient in water vapour would be set up, resulting in a flux of water vapour into the transducer. In all likelihood, the transducer temperature remained sub-zero so that this water vapour gradually accumulated in the transducer on the membrane, eventually destroying it through overpressure. To correct this, the new design will heat the transducers directly and not the outlets so that the transducers will always be warmer than the rest of the sensor and the outlets, directing the water vapour flux away from the sensors.

Task 2.5 – Impact pressure analysis: Data from high-frequency impact pressure recordings at Vallée de la Sionne has been obtained from SLF and analysis work has begun. This will be completed over the winter 2006 when J. McElwaine returns to SLF.

Task 2.6 – Seismic signal analysis techniques: At the beginning of this period preliminary results on the dependence of the shape of seismic signals on the snow type were presented to the consortium in October 2004. At the EGU General Assembly (Vienna) in April 2005, final results were presented in two separate talks.

Application of seismic techniques to NGI's geophone data from 11 avalanches of different types and sizes that occurred in Ryggfonn yielded promising avalanche speed estimates (Vilajosana and others, 2006). The seismically determined speed estimates were compared with independent measurements from CW-Radar (IMOR) and load plates (NGI). Agreement between the different instruments is good. Profiles of front speed vs. distance and time were elaborated. Two distinct behaviours have been observed in the speed vs. position representation, which are attributed to two different snow types. Specifically, we obtain linearly decreasing speeds for dense avalanches and acceleration for dry/mixed avalanches. The detailed comparison of instruments reveals differences between radar and geophone speed estimations that relate to the instruments detecting distinct parts of the avalanche. In addition, an interesting characteristic in the time–frequency domain representation of avalanche seismic signals has been revealed also in other mass movements such as landslides (Suriñach and others, 2005). In consequence, part of the measurement and analysis techniques could be applied to other mass movements.

Development continues focusing on new techniques of avalanche location; at the same time, data from pre-SATSIE measurements needs to be analysed.

Task 2.7 – Correlation Methods: This task is essentially complete. As additional data becomes available it will be analysed with the software developed earlier in the project.

3.2.3 Plan and objectives for the next period

Task 2.1 – Data-analysis techniques for radars: Testing of the program for FMCW radars.

Task 2.5 – Impact pressure analysis: Improvement of earlier analysis techniques with high-frequency impact data from Vallée de la Sionne.

Task 2.6 – Seismic signal analysis techniques: Develop techniques for tracking avalanches along the path. Further search for criteria to detect avalanche type and size from seismic signal.

3.3 WP 3 – Instrumentation of selected facilities

3.3.1 Objectives for the reporting period

3.3.2 Scientific achievements during the reporting period

Task 3.1 – Full-scale avalanche test site Ryggfonn (Norway): Maintenance work at Ryggfonn included the replacement of two load cells at the pylon that were probably destroyed by lightning. All four FMCW radars were retrieved for repair (see Sect. 3.1.2).

In December 2004, the seismic system developed communication problems with Barcelona. Both the modem and ethernet communication were lost. Therefore data were not stored during the first part of the winter season and no seismic data from the avalanche of 6/1/2005 were obtained. In February 2005, DGG's logger was replaced with a new one lent by the dealer. This equipment recorded the artificially released avalanche in the middle of April. When DGG's logger was returned to Barcelona from the United States, different laboratory tests were performed to find the most stable configuration for the equipment. During the first week of October 2005, DGG's instrumentation was reinstalled in Ryggfonn. For this campaign, the data acquisition system was set up as in previous campaigns (see 2nd Annual Report). With the new configuration all the instruments will have a common base of time. Communication with Barcelona will be carried out through regular modem connection.

Task 3.2 – Protection dam system in Taconnaz (France): No new instrumentation was installed at the Taconnaz dam during the reporting period.

Task 3.3 – Protection dam system in Flateyri (Iceland): A continuous-wave C-band Doppler radar for measuring the speed of avalanches was installed on the easternmost Flateyri deflecting dam in October 2004. The radar has worked without problems, but no avalanches progressed into the range of the radar during the winter 2004/2005.

Task 3.4 – Snow chute at Col du Lac Blanc: The modified snow rheometer (see Sect. 3.1.2) has been installed at Col du Lac Blanc.

Task 3.5 – Chutes in Pavia: A new chute has been installed at the Pavia laboratory (referred to as chute C). The chute is completely made of Plexiglas, has rectangular shape and is 10 cm wide and 30 cm high. The total length is 6 m, including 1 m of reservoir. The main purpose of the chute is the study of bed erosion and deposition processes, and interaction of granular flows with obstacles and deflecting dams.

Task 3.6 – Chutes in Bristol: No new instrumentation was installed in the Bristol chutes during the reporting period.

3.3.3 Plan and objectives for the next period

No further installation work is planned for the last eight months of the project. Deliverables D8 and D10 will be finalised after review by the consortium.

3.4 WP 4 – Measurement campaigns

3.4.1 Objectives for the reporting period

Task 4.1 – Full-scale measurements at Ryggfonn: Continue measurements of spontaneous and artificially triggered avalanches.

Task 4.3 – Chute measurements: At the Col du Lac Blanc snow chute, perform focused measurements of the bottom shear layer and infer properties of snow-particle aggregates. Complement chute experiments with rheometer measurements. At the granular chutes in Pavia, perform experiments with quasi-steady flow and study impact on various types of obstacles. Extend erosion experiments to other materials in a new chute.

Task 4.4 – Analysis and cross-comparison of results at different sites: Compare avalanche structure, velocity profiles, over-all force balance and entrainment/deposition rates between full-scale events and chute flows. Comparison between interactions of avalanches with deflecting dams in nature and in the laboratory if data becomes available.

Task 4.5 – Elaboration of final reports on experimental results: Continue documentation of all performed experiments and full-scale measurements in two reports on avalanche processes and on avalanche-dam interactions. Write review article of experimental knowledge of avalanche dynamics.

Table 3.1: Avalanche classification

Date yyyymmdd hh:mm	Size ¹	Deposit (10 ³ m ³)	Classification (ICSI) ²										Speed (m s ⁻¹)	
			A	B	C	D	E	F	G	H	J	LC4-LC1 ³	LC1-LP1 ⁴	
													101 m	218 m
20041207 17:00	NA	NA	3	2	1	2	7	3	2	1	1	NA	NA	
20050107 04:16	4	NA	3	2	1	1	7	3	2	1	1	30	17	
20050107 04:16 b	4	NA	3	2	1	1	2	3	2	1	1	NA	5	
20050415	NA	NA	7	/	1	2	/	/	1	1	1	NA	NA	
20050416 15:00	4	NA	4	7	1	2	7(2)	2	7	3	4	30	5	

¹According to Canadian avalanche size classification, cf. (McClung and Schaerer, 1993)

²According to International Avalanche Classification (Avalanche Atlas (UNESCO, 1981), also in (McClung and Schaerer, 1993))

³The estimated average speeds are calculated between the steel tower and the concrete structure,

⁴and between the concrete structure and the foot of the dam, respectively.

Table 3.2: Overview of archived measurements at the Ryggfonn test site during the winter season 2004/2005.

Date yyyymmdd hh:mm	geophone (GF)1 2 3 4 5 6 H1	load cell (LC)4 5 1 2 3	load plate (LP)1 2	radar P-DR	field obs.	maps
20041207 17:00	X O O O O O O	U X O O O	O O	-	-	X
20050107 04:16	X X X X X X X	X X X X X	X X	-	-	X
20050415	-----	-----	--	-	-	X
20050416 15:00	X X X X X X X	B X X X X	X X	X	X	X

Codes: X -data; P -sensor partly buried; B -sensor buried; O -data, but no measured signal (did not reach sensor); - -no data; U sensor status unknown

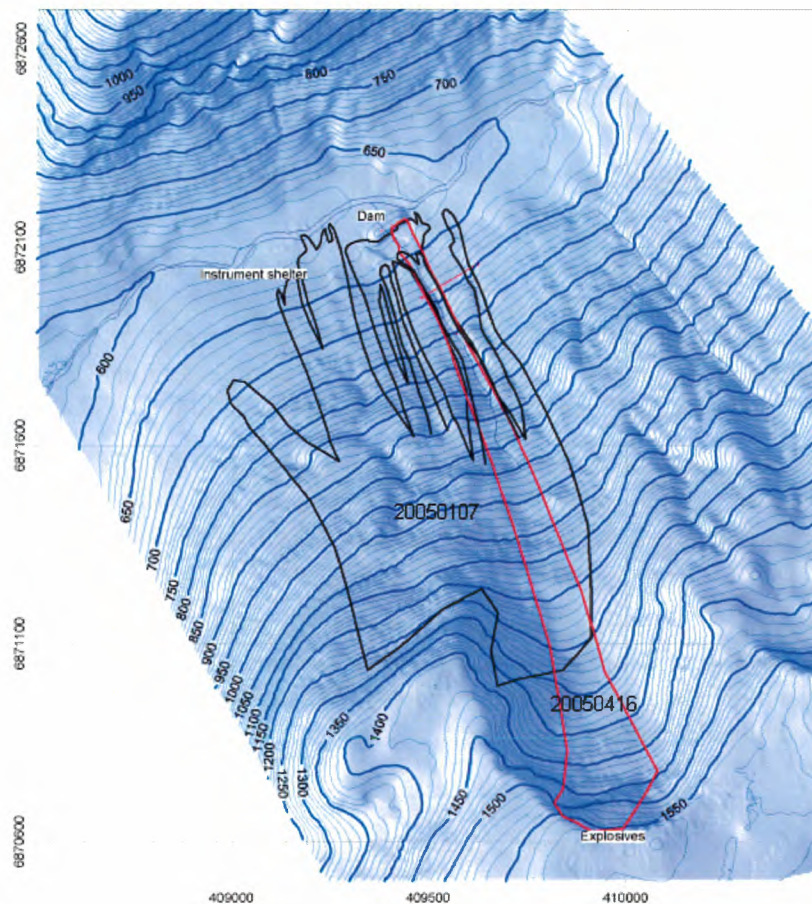


Figure 3.3: Map of the test site with the avalanches recorded in the winter 2004/2005. The red line indicates the artificially released avalanche on 16 April 2005 and the black line the avalanche on 7 January 2005.

3.4.2 Scientific achievements during the reporting period

Ryggfonn full-scale experiments (NGI)

Besides NGI staff, team members from the Department of Geology and Geophysics of the University of Barcelona, and from the Austrian Institute for Avalanche and Torrent Research participated in this task. Despite the anomalous functioning of the data logger, the DGG seismic equipment recorded one artificially released avalanche (16/4/2005). The same event was also captured on video by I. Vilajosana from DGG.

In the winter 2004/2005, three avalanche events were recorded, two of which were natural releases and one avalanche was artificially released. (A fourth event did not trigger the recording equipment.) Table 3.1 provides an overview and short classification of the different events and Figure 3.3 shows the approximate outline of the two major events. Table 3.2 summarizes the conducted measurements for the individual events and gives an estimation on the sensor status during the event.

Results After nearly two months of stable weather and snow conditions there was a period of snowfall and SW winds in the first part of April. On the 16th the main Ryggfonn avalanche was released by detonating 150 kg of explosives buried in the top cornice. The weather was sunny and calm with 25 cm of fresh snow from the preceding days. At 1420 m a.s.l. the air temperature

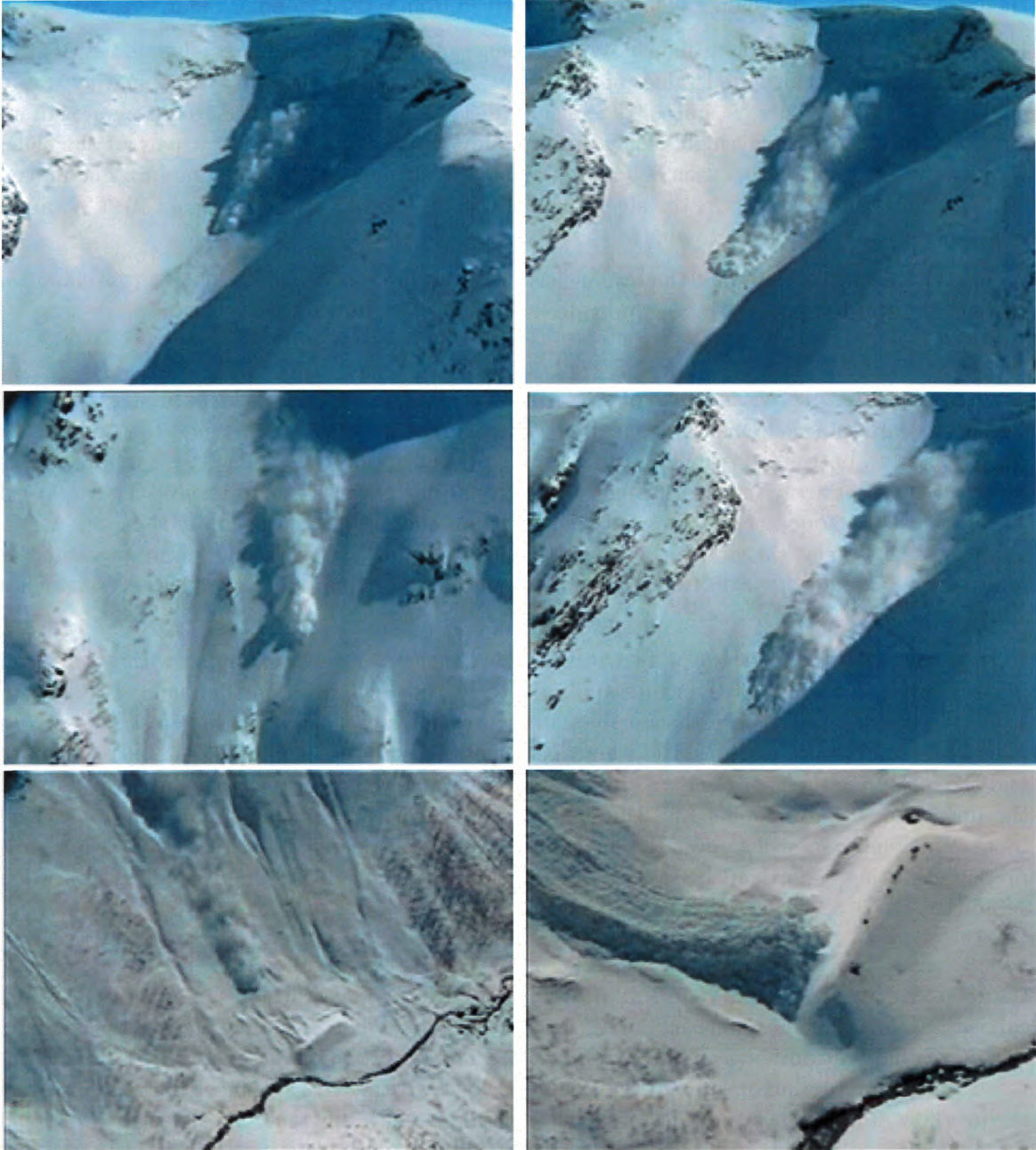


Figure 3.4: Avalanche 20050416 15:00: Snapshot of avalanche descent, taken from the video by K. Kristensen.

20021048-11

was -2.5°C , with high temperatures of -1.5°C during the preceding 24 hours. Southwesterly winds of 2 m s^{-1} , with gusts up to 5 m s^{-1} . In the runout zone the temperature was 5.1°C at the time of release. Figure 3.4 depicts snapshots from this avalanche release.

Figure 3.5 shows the velocity and acceleration (deceleration) data of this event along the lower part of the track derived from the available measurements for six instants in time. In addition, the front velocity is also shown. The data are derived from pulsed Doppler radar measurements.

How the flow regime or the avalanche type influences the forces on an obstacle is illustrated in Figure 3.6. It plots calculated values of $\rho C_D = 2P/U^2$ and shows also the corresponding values of the measured pressure, P , and of the velocity distribution, U . The measured pressures of up to 800 kPa are surprisingly high. They are probably related to the wet-snow part of the slide. If one assumes a density between 300 and 500 kg m^{-3} within the slowly moving tail, one finds a C_D of approximately 4 to 8 at the steel tower (LC4). At the concrete wedge (LC2), C_D values might be even as high as 20 to 40.

A more detailed description of the avalanches of the winter season 2004/2005 can be found in (Gauer and Kristensen, 2005b, see appendix).

Chute experiments with snow at Col du Lac Blanc At the snow chute at Col du Lac Blanc, the earlier measurements were extended to a larger variety of snow types, focusing on the rapidly sheared bottom layer and on the role of aggregates of particles. The latest modifications of the LED sensor arrays for measuring the velocity profile gave very good results. They allowed to resolve the bottom layer and to show that it is not sliding, but very rapidly sheared. A new analysis of clusters at the surface confirmed the first results. The new results were presented as oral presentation at the 2005 EGU General Assembly and submitted to Cold Regions Science and Technology (CRST).

In the winter 2004/2005, the Col du Lac Blanc avalanche chute was extended with an inclined plane located at the end of the chute and a deflecting obstacle fixed on the plane. It allows to study the interaction between the steady-state dense snow flows and deflecting obstacles. Three main parameters were varied during the experiments: the chute inclination, the mass flow rate and the deflecting angle of the dam. Image processing allowed to quantify the influence of both the upstream Froude number and the deflecting angle in terms of maximum run-up reached by the stationary snow flow over the deflecting dam. A poster reporting these new results was presented during the avalanche session of the 2005 EGU General Assembly and a publication submitted to CRST (Faug and others, 2006).

Chute experiments with granular materials in Pavia Several series of experiments were carried out in November 2004 in the 7.5 m long chute in Pavia (usually referred to as “chute B”) in a collaboration between IMOR and DIIA. The objective of the experiments was to investigate the interaction of supercritical granular flows with wedges and mast-like obstacles and the overflow of granular avalanches over deflecting dams with different side slopes. A report on these experiments is in preparation. The results of the experiments investigating the pressure on mast-like obstacles were presented at the EGU–2005 conference in Vienna in April 2005; a manuscript describing these results has been submitted to a scientific journal (Hauksson and others, 2005). In 2005 a series of new experiments was carried out in a newly constructed chute (referred to as “chute C”), with the aim of investigating erosion processes in granular flows. Of particular interest is the modification of velocity profiles during the erosion phase as this allows to test some of the conclusions arrived at in the theoretical study by NGI and IMOR. This research activity is still in progress.

In collaboration with the team at Pavia, SGUL undertook experiments on the interaction be-

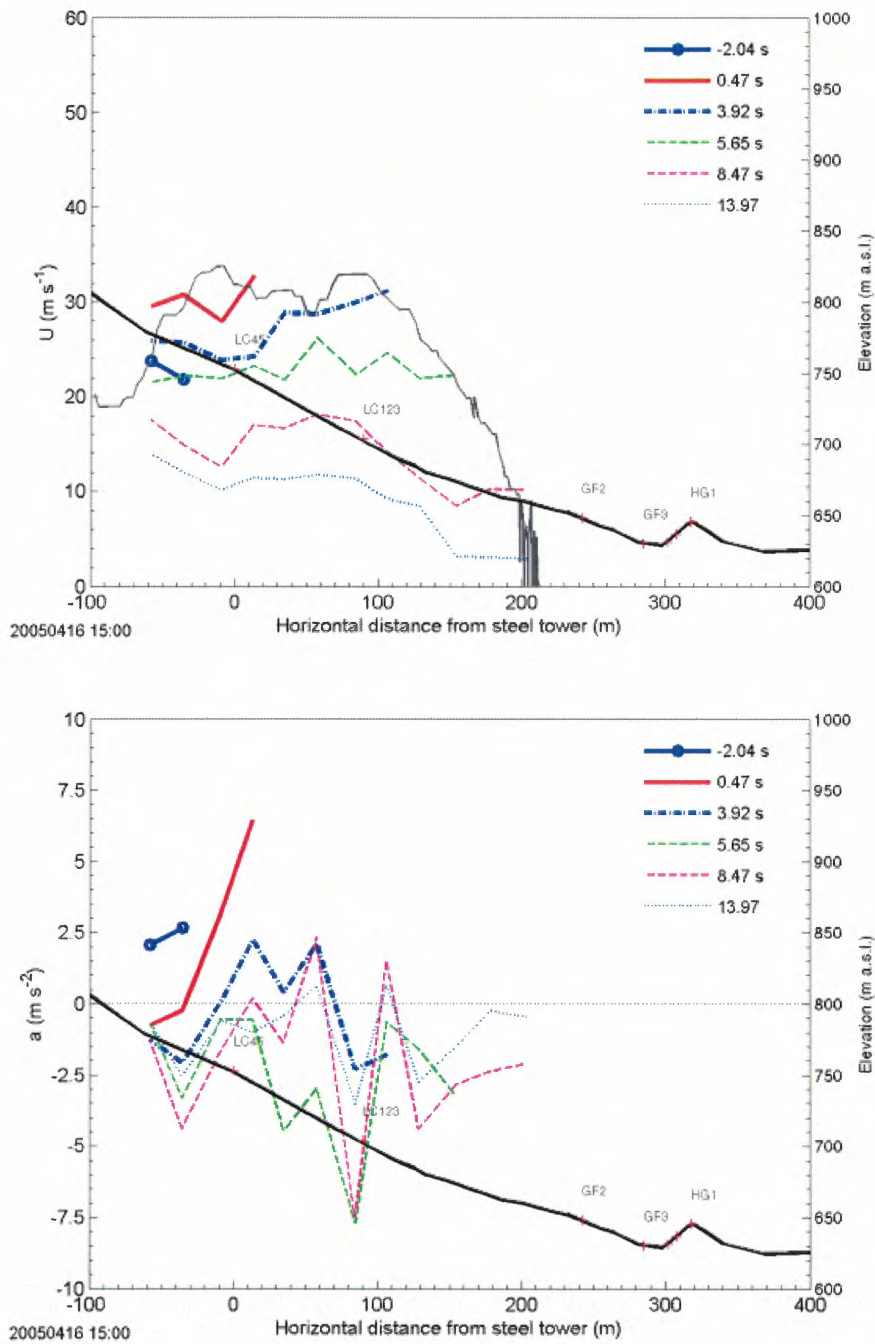


Figure 3.5: Avalanche 20050416 15:00: Velocity and acceleration vs. location along the lower track for six instants in time. The upper panel shows the averaged velocity and the lower panel the acceleration derived from the respective pair of adjoining range gates of the Doppler radar. In addition, the thin solid line in the upper panel shows the front velocity. The thick solid line gives the path profile in the lower part of the track.

20021048 - 11

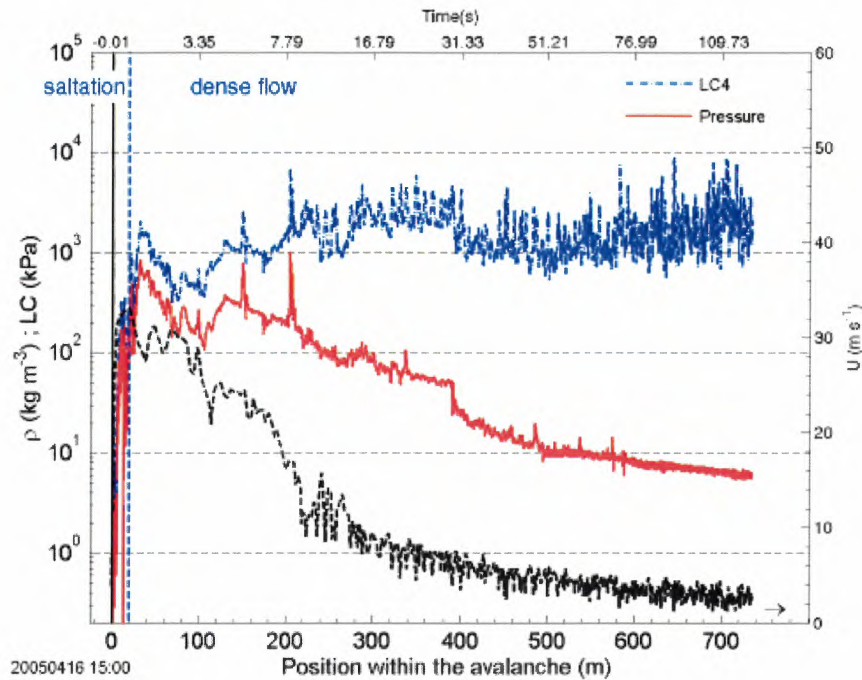


Figure 3.6: Avalanche 20050416 15:00: ρC_D vs. position within the avalanche (dash-dotted line). The full lines represent the measured impact pressure as the running mean taken over 5 m. Note the logarithmic scaling of the left ordinate. The black dashed lines show the corresponding velocity profiles. The panel gives measurements from the steel tower (LC4) at the Ryggfonn test site.

tween granular flows and topographic obstacles in the spring of 2005. These studies investigated a physical situation that differs from those studied by IMOR in Bristol and Pavia; there is no transition from supercritical to subcritical Froude number, the flow remains supercritical. Hence, such experiments are more pertinent to the study of the interaction of a granular flow with smaller topographic discontinuities. An example image from one experiment is shown in Fig. 3.7.

Current work involves developing effective image processing algorithms for automatically tracking the grains through the flow field over a series of images. From this we intend to elucidate the controls on the flapping frequency of the flow as it passes over the step. This instability

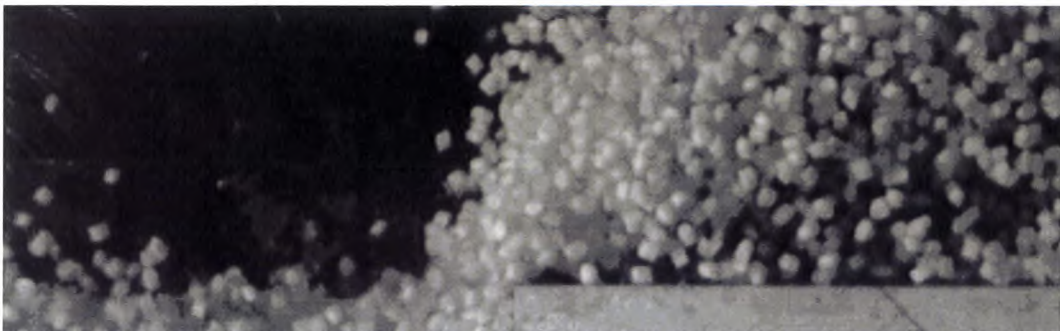


Figure 3.7: Example image showing a granular flow interacting with a forward-facing step. The flow direction is from left to right.

appears to be controlled by changes in the grain configuration at the step. Hence, the physics of this problem are complex as they involve the interaction between a rapid flow and a more static granular arrangement.

3.4.3 Plan and objectives for the next period

Task 4.1 – Full-scale measurements at Ryggfonn: Continue measurements of spontaneous and artificially triggered avalanches.

Task 4.3 – Chute measurements: At the Col du Lac Blanc snow chute, perform further focused measurements of the bottom shear layer and infer properties of snow-particle aggregates. Complement chute experiments with rheometer measurements. At the granular chutes in Pavia, perform experiments with quasi-steady flow and study impact on various types of obstacles. Extend erosion experiments to other materials in a new chute.

Task 4.4 – Analysis and cross-comparison of results at different sites: Compare avalanche structure, velocity profiles, over-all force balance and entrainment/deposition rates between full-scale events and chute flows. Comparison between interactions of avalanches with deflecting dams in nature and in the laboratory if data becomes available.

Task 4.5 – Elaboration of final reports on experimental results: Complete the documentation of all performed experiments and full-scale measurements in two reports on avalanche processes and on avalanche–dam interactions. Submit review article on experimental knowledge of avalanche dynamics.

3.5 WP 5 – Model development

3.5.1 Objectives for the reporting period

The goal of the model development work package is to improve the physical basis of currently operational snow avalanche models. The objectives of WP 5 within the reporting period were to finalise the interpretation and reporting of laboratory and full-scale experiments that were carried out in the first phase of the project, continue with the implementation of improved model physics and numerical methods in numerical models, and decide which of these developments will be used as the basis of improved design criteria for avalanche dams, which will be described in the Satsie handbook to be written in Work Package 6.4. The objectives of each task within the work package are:

Task 5.1 – Flow regimes: Further development and validation of the two-layer depth-integrated MN2L snow avalanche model. Further work on constitutive equations for 2D depth-integrated avalanche flow that allows for transition from dense to fluidised flow, based on an extension of the Criminale–Ericksen–Filbey rheology, including the implementation of these equations into a numerical model. Molecular-dynamics simulations for studying the influence of cohesion and shear rate on the stress state of granular snow.

Task 5.2 – Snow entrainment and mass balance: Finalise interpretation of chute experiments to study the micro-physics of entrainment in granular flows. Investigate the effect of entrainment on the vertical velocity profile in avalanche flow using laboratory experiments.

Task 5.3 – Powder snow avalanches: Investigate the dynamics of air flow near the head of a powder snow avalanche using a combination of field observations and theoretical analysis. Also, analyse the internal flow dynamics near the head of powder snow avalanches using experimental results from chute experiments and theoretical analysis based on fluid dynamics for incompressible flow.

Task 5.4 – Interactions with dams, impact loads: Analysis of data obtained from natural snow avalanches in order to verify theoretical ideas and computational models for avalanche-dam interactions that have been derived during the project and previous research projects. Further analysis of shock dynamics with a focus on avalanche flow over dams.

Task 5.5 – Validation of new models: The compilation of a report on validation of new models takes place during the last phase of the project. Therefore, the objective of this task during the reporting period was mainly to gather information that will be used during the next reporting period.

Work meetings were held in Vienna, Austria, on 27 April 2005 and in Seyðisfjörður, Iceland, on 1–3 September 2005. In addition to SATSIE members, Xinjun Cui (Dept. of Mathematics, University of Manchester), Margarita E. Eglit (Mechanics and Mathematics Department, Moscow State University), and Betty Sovilla (Swiss Federal Inst. for Snow and Avalanche Research, Davos) attended the meeting in Seyðisfjörður. Various issues regarding energy loss in avalanche flow over dams, formation of shocks in the interaction of avalanches with obstacles and numerical and computational aspects of a new model were considered.

3.5.2 Scientific achievements during the reporting period

Task 5.1 – Flow regimes of snow avalanches: Work continued on the interpretation of the results of chute experiments with snow by ETNA in terms of the rheology of full-scale

snow avalanches and on the further development of the MN2L model based on these results. Granular particle models are also being utilised at Cemagref in order to gain understanding of the micro-dynamics of avalanche flow, in particular on the formation and effect of ephemeral particle chains.

Using molecular dynamics simulations, plane shear flow of an assembly of slightly polydisperse disks was studied at controlled pressure and shear rate, without gravity. Biperiodic boundary conditions were used to avoid wall perturbations. A cohesive force of the Van der Waals type enhanced the usual interaction term (elasticity, friction and dissipation). The properties of this system depend on two dimensionless numbers. The first is related to the shear state imposed on the material. The second characterises the cohesion. In steady homogeneous shear flows, the variations of the solid fraction and of the effective friction were measured as a function of these two numbers, from which a visco-plastic constitutive law could be derived. Moreover, the grains agglomerate into transient clusters when the cohesion number increases. The analysis of the space and time correlations shows a structural transition when the cohesion force becomes larger than the confinement force.

In the next step, the molecular dynamics simulations were applied to the flow of a bidisperse assembly of frictional cohesionless disks down a rough inclined plane. The particle assembly is characterised by the size ratio and the proportion of large grains. The study was restricted to steady uniform flows, once a stable segregation had developed inside the flowing layer. The material segregated into three layers: a basal layer made of small grains, a superficial layer made of large grains, and a mixed layer in the center. In a certain range of parameters of the mixture, this structure leads to localisation of the shear near the rough bed. Moreover, as for slightly polydisperse assemblies, an approximately linear increase of the effective friction as a function of the ratio of the Froude number and the height of the flowing layer was measured. These results were compared with the predictions of a simple two-layer model.

For each of these two investigations, a publication was accepted and an oral presentation given at Powders & Grains 2005 on 18–22 July 2005 in Stuttgart, Germany.

During this period, the original NIS rheological and numerical model for snow avalanche dynamics has been thoroughly revised. An extra isotropic dispersive pressure term was added to avoid that lateral pressure vanishes as the shear rate approaches the critical value for fluidisation. Additional inertia is introduced to avoid that centrifugal forces cause immediate and unphysical displacement and run-up during avalanche deflection. Curvilinear coordinates following the path are introduced instead of Cartesian ones to handle large curvature (*e. g.* at the upstream bend of a catching dam). A paper on the theoretical basis of the NIS model and some examples of numerical simulations of avalanches in strongly curved paths is nearing completion (Irgens and others, 2006). During his second stay at the University of Manchester from May to July 2005, Ph.D. student Arne Moe worked on the shock-capturing numerical scheme for the new model under the supervision of Nico Gray and Xinjun Cui.

The study of flow-regime transitions in the framework of an extended NIS rheology at NGI showed that the air-pressure distribution at the head must play a decisive role in the onset of fluidisation and in limiting the expansion of the fluidised material. A suitable description of these processes is being sought to complete the formulation of the new model. The main question to be understood is whether and to which degree the density dependences of the shear and normal stresses differ, both in the collisional and grain-inertial regimes. Such a difference is crucial for establishing a new equilibrium density in the flow after a slope change. The present state of development was presented in a talk at the EGU-2005 conference in Vienna in April 2005.

Task 5.2 – Snow entrainment and mass balance: Experimental laboratory study of the erosion processes has progressed. The experiments carried out in Chute B in Pavia, mainly designed to investigate erosion mechanisms and the mixing process of the eroded material in the avalanche flow, have been completed; a paper describing the main results has been published in a scientific journal (Barbolini and others, 2005).

A theoretical paper studying the application of different entrainment models to an idealised avalanche path also appeared in print (Eglit and Demidov, 2005). A new study of the proper formulation of entrainment terms in depth-averaged gravity mass flow models was carried out in a collaboration between NGI and IMOR (with additional funding from the Swiss National Science Foundation through a grant to D. Issler). The results were presented as a poster at the EGU–2005 conference in Vienna in April 2005. A manuscript describing the results is nearly ready for submission to a scientific journal.

New experiments, performed in a newly installed chute in Pavia (Chute C), have been started, with particular attention paid to measurements of velocity profiles before, during and after the erosion phase. These experiments intend to test some of the theoretical conclusions proposed in the study by NGI and IMOR. This research activity is still in progress.

Task 5.3 – Analysis of the generation of powder snow avalanches: Work continued on the interpretation of chute experiments with snow on steep slopes at SLF that are described in the Second Annual Report, and on the application of some of the ideas from this work to full-scale avalanches at Vallée de la Sionne. Two papers previously accepted for publication have appeared in print (McElwaine and Turnbull, 2005; McElwaine, 2005). Three more papers are shortly to be submitted.

Task 5.4 – Interaction of avalanches with obstacles: An interpretation of available data about flow of avalanches in Ryggfonn over the 16 m high catching dam at the foot of the slope was carried out at NGI as a part of this task (Gauer and Kristensen, 2005a), following up on earlier work (Lied and others, 2002). The new results have considerable practical value in terms of a formulation of improved guidelines for the design of catching dams. The data may be used to evaluate the shortening of avalanche run-out as a consequence of the impact with a dam, which is partly overrun by the avalanche. These results are the first reported field observations that may be used to evaluate reduction in avalanche hazard below catching dams in a quantitative manner.

A study of the overflow of avalanches over deflecting dams is being carried out as a part of the interpretation of the chute experiments in Pavia in November 2004 (see Sect. 3.4.2). Results of previous studies within the project about the interaction of granular avalanches with obstacles (see the last annual report) are being compared to traditional theories and incorporated into the handbook about dam design that will be produced in WP 6. A paper describing some of the results of these previous studies was published in a scientific journal during the reporting period (Hákonardóttir and Hogg, 2005).

Interpretation of laboratory experiments to study the impact of supercritical granular flow with mast-like obstacles was completed in the reporting period. The experiments were carried out in Pavia in November 2005 in a collaboration between IMOR and DIIA. The results were presented at the EGU–2005 conference in Vienna in April 2005 and a manuscript describing the results has been submitted to a scientific journal (Hauksson and others, 2005).

A study of shock waves connected with the compressibility of the flowing material at the impact against obstacles was continued by Margarita Eglit at the University of Moscow. A publication summarising previous Russian research in this field, clarifying the basic assumptions and

proposing some corrections, is ready for submission to a scientific journal (Eglit, 2005).

Task 5.5 – Report on the validation of new models: This task will be carried out in the last reporting period of the project.

3.5.3 Plan and objectives for the next period

The main objectives of WP 5 during the next and final period of SATSIE are to:

- finalise the theoretical description of the new flow-regime-changing model, implement it in the advanced shock-capturing numerical scheme developed in collaboration with the University of Manchester and test the new model,
- complete the investigation of the effects of entrainment on the velocity profile and compare the predictions with chute measurements carried out in Pavia,
- determine the range of validity of the hydraulic-jump model of avalanche–dam interactions by detailed analysis of the snow-chute experiments at moderate Froude numbers,
- report on the validation of the improved model physics using data obtained from chute experiments and field observations.

A joint SATSIE/SLF work meeting about dam–avalanche interaction and dam design will be held in early 2006 as part of the preparations for the handbook to be produced in WP 6.

3.6 WP 6 – Data sharing and dissemination of results

3.6.1 Objectives for the reporting period

The following list of objectives corresponds to the goals set for the completion of the project at the end of the third year and does not reflect the changes made in connection with the prolongation until 31 May 2006. See Sect. 3.6.2 for the adjustments made.

Task 6.2 – Database maintenance and data back-up: Archive all new experimental data.

Task 6.3 – Maintenance of project website: Keep the website up-to-date and informative.

Task 6.4 – Handbook on dam design: Completion of handbook.

Task 6.5 – User manuals for new numerical models: Completion of user manuals.

Task 6.6 – European Summer University 2006, advanced course: First preparatory steps, such as definition of targeted audience, course outline, selection of location, preliminary list of instructors for additional course in 2006.

3.6.2 Achievements during the reporting period

After the first peak of activity at the beginning of the project, less work was to be done in the middle phase. The third year has seen concentrated work on some of the key deliverables (handbook on dam design, description of new avalanche models, European Summer University course). However, not all objectives set for the third year could be achieved in time, partly due to delays in other tasks that are prerequisite to these, partly due to some of the main contributors lacking sufficient time.

Task 6.1 – Database on experimental results: Completed earlier.

Task 6.2 – Database maintenance and data back-up: More data has been archived from Ryggfonn for 2005 and 2004, including impact pressures, radar, seismic data and videos. The latest series of experiments on chute flows at SLF (air pressure data and videos) has been converted to the archive format and added to the data archive.

Task 6.3 – Maintenance of project website: The SATSIE web site <http://www.leeds.ac.uk/satsie/> has continued to expand as research results have appeared and meetings have taken place. It has now been visited some 3150 times since March 2003. Major developments since last year include a division of the research publications area into “by topic” and “by institution” lists and the addition of a page for the third annual meeting in Seyðisfjörður, <http://www.leeds.ac.uk/satsie/seydis.html>. From this page one can access images from the field illustrating the practical consequences of some of the theoretical research undertaken during SATSIE. In addition, in the private area one can access minutes from meetings as well as slides from presentations that took place at these meetings (<http://www.leeds.ac.uk/satsie/private/seydimeeting.html>).

We will continue to develop the web page throughout the remaining life time of the project and thereafter.

Task 6.4 – Handbook on dam design: The working title of the handbook is “The design of avalanche protection dams: Practical and theoretical developments and results”. The first draft of the introduction and overview has been written. An outline of its structure has been agreed upon: Examples of catching dams and deflecting dams will be given as well

as laws and regulations relating to design and hazard zoning beneath structures. Recommendations for the necessary height of deflecting and catching dams etc. will be based on supercritical flow theory using traditional and shock-based approaches. Additional design issues such as face steepness and curvature will be discussed for deflecting dams. Catching dams are considered to be less well understood than deflectors. The key uncertainty is ensuring that a shock forms. Recommendations for the design of wedges for the protection of single buildings will be based on those given in the Swiss guidelines. Probably mast-like structures will not be covered by the handbook. The complex avalanche defense systems at Neskaupstaður (Iceland) and Taconnaz (France) will serve as examples in a discussion of combined measures. A section on powder snow avalanches will be followed by a brief review of the state-of-the-art of numerical modelling of avalanche flow around obstacles. An overview of geotechnical issues encountered in dam design will also be given.

Task 6.5 – User guides for new numerical models: The user manuals for three models developed by ETNA, namely the centre-of-mass, shallow-water dense avalanche, and shallow-water two-layer (MN2L) models are available in French and translation into English has been started. The two-dimensional version of MN2L will be first distributed to the French service RTM. The user manuals for NGI's new flow-regime-changing model can be written only when the model is operational and has been used in practical work.

Task 6.6 – European Summer University course: It was decided to organise an advanced course on snow avalanche modelling in September 2006, as a specialised follow-up to the European Summer University course on avalanches in Courmayeur, Italy, in September 2004. The new models developed during SATSIE will be presented together with the experimental findings that motivated them. Following the proposals and preliminary budget elaborated by ETNA, the consortium opted for Grenoble as the main course location and decided to entrust the Pôle Grenoblois Risques Naturels to organise the logistic aspects of the course, which will last four or five days. The course instructors will be members of the SATSIE team; SLF has indicated interest to also participate. Since this course is outside the contractual obligations and duration of SATSIE and the budget will be used up by the originally scheduled project work, additional financing will have to be found by the members of the consortium. As of now, sufficient resources have been secured to allow the course to be offered, but more funding is being sought to assure participation of instructors notably from NGI, IMOR and DIHA.

3.6.3 Plan and objectives for the next period

During the prolongation period of SATSIE, the data archiving and website maintenance will continue as before (Tasks 6.2, 6.3). In parallel with the testing of the new models (Task 5.5), user guides will be translated into English at ETNA and written at NGI (Task 6.5, Deliverable D15). The main activity will, however, focus on the elaboration of Deliverable D14 (Handbook on dam design, Task 6.4), involving mostly IMOR, NGI, ETNA and AIATR. All partners will take an active role in the reviewing process. As far as possible, the SATSIE handbook will be coordinated with a similar handbook for Switzerland under elaboration by SLF. The working group for the 2006 European Summer University course (Task 6.6) will meet and elaborate detailed course contents, schedules and instructor lists as well as oversee PGRN's organisation of the logistic aspects. Instructors will be trained in the use of all models to be presented at the course.

3.7 Socio-economic relevance and policy implications

Due to the fundamental role that full-scale experiments with snow—which can only be conducted in the winter and crucially depend on unpredictable weather conditions—play in SATSIE, the synthesis work producing results useful to the end-users is concentrated in the last phase of the project. Consequently, results of socio-economic relevance and with significant policy implications will emerge mostly at the end of the project and thereafter. However, certain trends and opportunities begin to become visible already now and deserve a brief discussion.

Doppler and FMCW radar for monitoring and alarm systems: Doppler radar systems have been used for several years in the monitoring of avalanche paths that threaten pass roads in Austria. The new Doppler range-gating radar developed by INW boasts higher performance at a lower price than the predecessor designs. The latter aspect increases the number of sites where such a system might be profitably used. This would be beneficial mostly for traffic safety whereas the economic impact remains small due to the restricted number of systems. Furthermore, Doppler systems without range-gating capabilities are, and will remain, significantly cheaper than the high-performance system developed by INW; they may be sufficient for many alarm systems.

In many cases, information about the development of the snow cover over time is even more important for the safety responsibilities of road services or towns. The FMCW radar developed jointly by NGI and INW is an attractive instrument because it allows such information to be obtained directly from the starting area. Commercialisation will first require a proof of concept in the form of high-quality measurements at Ryggfonn, and then some additional development work geared towards a less sophisticated, but cheaper system. Unfortunately, the failure of all systems before the release of the first avalanche of the winter 2005 has prevented us from demonstrating the performance of the design; we therefore await the next winter with much anticipation. The size of the market for such an instrument is difficult to estimate because yet unforeseen applications in other situations might increase it significantly. These possibilities will be pursued vigorously after tests in real avalanches have been successful.

Improved knowledge on dam design: The joint work of IMOR and the University of Bristol on shock formation in the impact of granular materials on various types of obstacles represents a breakthrough in our understanding of the functioning of catching and deflecting dams as well as braking mounds. Even though many questions need to be studied in more detail still, it is clearly visible that the presently used, very crude dimensioning criteria will be superseded by a more complete theory. Fortunately, the new insights do not completely invalidate the design of existing dams, but they will allow a more thorough assessment of the hazard reduction achieved by such measures and help in optimizing the design of future dams. The societal benefit of these results lies not in their commercialisation, but in the added safety and the potentially lower costs of optimised designs.

A similar initiative, albeit at a somewhat smaller scale, has been taken in Switzerland by SLF. Due to contractual obligations of SLF, it will not be possible to completely merge the two efforts, but both the SATSIE partners and SLF agree that every effort should be made to exchange knowledge and experience on the topic and to strive for compatibility between the SATSIE handbook and the Swiss guidelines. This paves the way for a common European handbook (or guidelines) in the future.

Improved avalanche dynamics models: The recognition of different flow regimes in the dynamics models under development is expected to lead to a more detailed view of the pressure distribution along avalanche paths. While it is too early to draw conclusions, there

is the possibility that pressures in the distal areas of avalanches are lower than hitherto assumed on the basis of calculations with older models. If so, constructible areas may be increased or protection requirements lowered in many mountain villages, resulting in an increase of property value or a decrease of construction costs. The beneficial economic impact in those areas may be considerable. Furthermore it is to be expected that the models developed in SATSIE for snow avalanches may be use in the development of models for other types of slides, in particular debris flows and rock avalanches.

Increased competence of the consortium partners: The SATSIE project in general and the workshops and meetings in particular are designed to contribute to the professional formation of the team members beyond their specific research field. As most of these institutions are involved in practical avalanche work (hazard zoning, warning and other mitigation measures, education) in their home countries, their increased competence brings about many benefits that are not easily quantifiable but nevertheless important. The intense collaboration also increases the mutual understanding of different approaches towards avalanche protection taken in different countries—a valuable basis for future attempts towards harmonising avalanche-related procedures and standards in Europe.

Improved education of avalanche professionals: More than half of the instructors in the 2004 session on avalanches of the European Summer University were members of the SATSIE consortium. The organisers consider this course as perhaps the most successful of all avalanche sessions held so far, thanks to the quality of the instructors. In 2006, after the official conclusion of the project, the SATSIE consortium will organise a follow-up course focusing on numerical modelling, in which the most up-to-date results from SATSIE research will be introduced in practical work. Discussions have started within the consortium on how to facilitate future collaboration in the education of European avalanche professionals.

3.8 Contributions by the consortium partners

Table 3.3 gives an overview of the main activities of the partners in each work package. More detail can be found in Sections 3.1–3.6. In the third year of SATSIE, experiments and model development were continued at the same or higher level as in the second year. Work on disseminating the results from the project—the main goal of WP 6—has been intensified, and will continue to be intensified during the prolongation period from October 2005 through May 2006.

All the partners have maintained their high level of activity in the project. AIATR, after a year of forced inactivity due to unusual snow conditions in western Norway, could bring their Doppler radar to the site for one campaign, even if only late in the winter season. (Unfortunately, temporary malfunctioning of the hard disk prevented acquisition of data.) In contrast, malfunctioning of the four FMCW radar systems kept INW active in the project beyond the expected date.

Table 3.3: Overview table of contributions of the consortium partners to each work package.

Partner	WP 1	WP 2	WP 3	WP 4	WP 5	WP 6
1 NGI	Debugging of FMCW radar		Installation of FMCW, Doppler radars at Ryggfonn	Meas. of spont. aval. at Ryggfonn, 1 campaign with artificial release	NIS2. Flow-regime changes. Entrainment dynamics	Preliminary work for handbook on dam design
2 IMOR				Chute experiments with obstacles in Pavia	Shocks in granular flows. Entrainment dynamics	Planning of handbook on dam design, outline.
3 SGUL		Methods for analysis of time series from experiments		Experiments at Pavia chute. Review paper 2nd draft	Work on statistical analysis of runout data	Maintenance of SAT-SIE website
4 DAMTP	Improved design of air pressure sensor	Preliminary work on analysis of impact sensor data	Improved chute for flows on very steep slopes	Exp. on powder snow avalanches. Air pressure at VdIS	Theory of powder snow clouds on steep slopes	Maintenance of SAT-SIE data archive
5 AIATR				1 campaign at Ryggfonn		Drawings for handbook on dam design
6 INW	Debugging of FMCW radar			Analysis of Doppler radar data		
7 ETNA	Redesign of snow rheometer			Snow chute experiments.	Further development and testing of N2L, rheological studies	Work on handbook on dam design
8 DIIA		Video analysis techniques	New chute for entrainment studies	Chute exp. on flow regimes, entrainment, impacts		First Italian university course on snow and avalanches
9 DGG	Improvements of data acquisition system	Seismic methods for velocity measurements		Measurement, analysis of seismic signals at Ryggfonn		

3.9 Discussion and conclusion

Much of what was said in the corresponding section of the second Annual Report is still valid today and will not be repeated here. Instead we focus on the new developments that have taken place, and the changes in the assessment of achieved results and open questions.

In the area of sensor development, the project suffered two setbacks in that both the new FMCW radar systems and the air-pressure sensors failed early in the winter and did not produce the eagerly awaited data. In both cases there is no indication of basic design flaws, but corrosion or freezing in critical parts must be prevented. There is thus a good chance that the prolongation of SATSIE will allow us to collect important new data. Whether meaningful rheological tests can be performed on snow with the cylindrical rheometer is still an open question. If the planned tests prove successful, an important gap in our options for studying avalanching snow will be filled.

Until the FMCW radars deliver data of good quality, the open questions concerning the corresponding data analysis techniques cannot be answered; new measurements from Ryggfonn are therefore eagerly awaited. In the meantime, DAMTP's high degree of competence in data analysis has prompted SLF to collaborate with DAMTP and to grant access to the high-frequency impact-pressure data from their test site at Vallée de la Sionne; this work will refine the crude analysis made earlier (Schaer and Issler, 2001). These data are expected to give very important information on the density profile, particle-size and velocity distribution in the fluidised layer of dry-snow avalanches. They will represent the most direct test of NGI's new multi-regime avalanche model. It may be hoped that this collaboration can be extended to SLF's extensive collection of radar data, which has never been adequately analysed.

The chute experiments at Col du Lac Blanc, in Pavia, Bristol, Reykjavík and Davos were again continued in the reporting period and once more were very successful. On the granular chutes in Pavia, some limitations of the first series of experiments were circumvented and the newly constructed chute and inlet allow a more direct comparison of these measurements with the snow experiments at Col du Lac Blanc. This should enable us to eventually understand the notable differences between the velocity profiles in the two settings and to obtain a hint as to the correct extrapolation to real snow avalanches.

A common theme at both chutes was the interaction of the flow with obstacles. The granular-flow experiments in Pavia were carried out at very high Froude numbers ($Fr \approx 13$) and confirmed the experimental results obtained earlier in Bristol and the theoretical predictions based on the theory of hydraulic jumps. Interestingly though, the snow-chute experiments were limited to lower Froude numbers ($Fr \approx 3$) that seem to be close to those estimated in the body of dense avalanches. An important observation from the snow experiments is that the oblique shocks at deflecting dams form only under more restricted conditions than predicted by the new theory. This point needs more investigation because of its immediate importance for the handbook on dam design. Analysis of the results from the full-scale measurements at Ryggfonn had long been hampered by the lack of velocity data at the dam itself; use of the newly developed seismic techniques (Vilajosana and others, 2006) enabled us to obtain these velocities from geophone data for a substantial number of events in the past. A strikingly simple correlation was found between the kinetic energy at approach to the dam and the overrun length (Gauer and Kristensen, 2005a), and a similar correlation may also apply to the laboratory measurements with granular materials. It remains to be analysed in detail how this empirical correlation relates to the approach developed in (Faug and others, 2003, 2004).

Painstaking analysis of pressure patterns and comparison with the few available measurements with a range-gating Doppler radar (Rammer and others, 1998; Schreiber and others, 2001; Gauer and others, 2006) finally allowed to estimate the rate of decrease of the internal velocity

with the distance from the head, seen in all analysed dry-snow avalanches at Ryggfonn as well as in several humid ones. The density in the head could be determined semi-quantitatively and was found to be quite low, typically well below 100 kg m^{-3} . The head thus seems to be in a fluidised flow regime, as we had conjectured from other observations; incidentally, this finding strongly supports the assumptions made in the development of the new multi-flow-regime model. A rather disconcerting finding, however, was that slow wet-snow avalanches may exert much higher pressures (up to 800 kPa) than had been generally thought possible (Gauer and Kristensen, 2005b). Clearly, this must be due to cohesion effects, and dedicated experimental and numerical studies are needed for a more complete understanding that allows to assess the potential impact on hazard-mapping procedures. The extension of the project until May 2006 allows measurements to be carried out during an additional winter, and these data will in all likelihood be most important.

While ETNA's new numerical avalanche model (Naaïm and others, 2003, 2004), MN2L, has already found wide-spread acceptance and use among French practitioners, progress on NGI's new model was slower than expected and a concentrated effort is being made to bring it to operational status before the end of the project. At the theoretical level, the principal difficulty is to determine the density dependence of the different components of the stress tensor because neither direct measurements nor a comprehensive theory applicable to snow are available. In this situation, general inferences from full-scale and chute experiments as well as cautious extrapolation of the properties of highly simplified theories of granular flows guide the formulation of the new model. Once operational, it will be an important tool for exploring the consequences of the new insight into the layered structure of avalanches in hazard mapping.

The present intensive work on the handbook on dam design highlights the advantages of tackling such a challenge at a European level: Experience from observations and consulting work, from experiments and theoretical investigations can be pooled, leading to a document of much better quality than if it came from a single institution, and the resulting product will have a wide audience. It is encouraging that SLF, who started work on similar guidelines in response to a request from the Swiss authorities, want to coordinate their work and document as much as possible with the SATSIE initiative. SLF have also expressed interest to participate in the advanced European Summer University course 2006 on avalanche modelling. This would bring together all European institutions active in this field and would represent yet another step towards the main goals of this project.

Bibliography

- Barbolini, M., A. Biancardi, F. Cappabianca, L. Natale, and M. Pagliardi. 2005. Experimental study of erosion processes in snow avalanches. *Cold Regions Sci. Technol.*, **43**(1–2), 1–9; doi:10.1016/j.coldregions.2005.01.007.
- Eglit, M. E. 2005. Impact of a snow avalanche against an obstacle. Formation of shock waves. *To be submitted*, .
- Eglit, M. E. and K. S. Demidov. 2005. Mathematical modeling of snow entrainment in avalanche motion. *Cold Regions Sci. Technol.*, **43**(1–2), 10–23; doi:10.1016/j.coldregions.2005.03.005.
- Faug, T., M. Naaim, D. Bertrand, P. Lachamp, and F. Naaim-Bouvet. 2003. Varying dam height to shorten the run-out of dense avalanche flows: developing a scaling law from laboratory experiments. *Surveys Geophys.*, **24**, 555–568.
- Faug, T., M. Naaim, and A. Fourrière. 2006. Dense snow flowing past a deflecting obstacle: an experimental investigation. *Cold Regions Sci. Technol.*, **submitted**.
- Faug, T., M. Naaim, and F. Naaim-Bouvet. 2004. An equation for spreading length, center of mass and maximum run-out shortenings of dense avalanche flows by vertical obstacles. *Cold Regions Sci. Technol.*, **39**, 141–151.
- Gauer, P., D. Issler, K. Lied, K. Kristensen, H. Iwe, E. Lied, L. Rammer, and H. Schreiber. 2006. On avalanche full-scale measurements at the Ryggfonn test site, Norway. *Cold Regions Sci. Technol.*, **submitted**.
- Gauer, P. and K. Kristensen. 2005a. Ryggfonn measurements. Overview and dam interaction. NGI Report 20021048–10. Norges Geotekniske Institutt.
- Gauer, P. and K. Kristensen. 2005b. Ryggfonn measurements. Winter 2004/2005. NGI Report 20021048–8. Norges Geotekniske Institutt.
- Hákonardóttir, K. M. and A. J. Hogg. 2005. Oblique shocks in rapid granular flows. *Phys. Fluids*, **17**, 177101.
- Hauksson, S., M. Pagliardi, M. Barbolini, and T. Jóhannesson. 2005. Laboratory measurements of impact forces of granular flow against mast-like obstacles. *Cold Regions Sci. Technol.*, **submitted**.
- Irgens, F., A. S. Moe, and D. Issler. 2006. Simplified simulation model of dense snow avalanches and landslides. *Can. Geotech. J.*, **to be submitted**.
- Lied, K., A. Moe, K. Kristensen, and D. Issler. 2002. Ryggfonn. Full scale avalanche test site and the effect of the catching dam. NGI Report 581200–35. Postboks 3930 Ullevål Stadion, N–0806 Oslo, Norway, Norges Geotekniske Institutt.

- McClung, D. and P. Schaerer. 1993. *The Avalanche Handbook*. 1011 SW Klickitat Way, Seattle, Washington 98134, The Mountaineers.
- McElwaine, J. N. 2005. Rotational flow in gravity current heads. *Phil. Trans. Royal Soc. London, Series A*, **363**, 1603–1623.
- McElwaine, J. N. and B. Turnbull. 2005. Air pressure data from the Vallée de la Sionne avalanches of 2004. *J. Geophys. Res.*, **110**(F3), F03010; doi:10.1029/2004JF000237.
- Naaïm, M., T. Faug, and F. Naaïm-Bouvet. 2003. Dry granular flow modelling including erosion and deposition. *Surveys Geophys.*, **24**, 569–585.
- Naaïm, M., F. Naaïm-Bouvet, T. Faug, and A. Bouchet. 2004. Dense snow avalanche modeling: flow, erosion, deposition and obstacle effects. *Cold Regions Sci. Technol.*, **39**, 193–204.
- Rammer, L., K. Kristensen, K. Lied, H. Schreiber, and W. L. Ranau. 1998. Radar measurements of snow avalanche full scale experiment in ryggfonn. In Hestnes, E., editor, *25 Years of Snow Avalanche Research, Voss, 12–16 May 1998*. Postboks 3930 Ullevaal Stadion, N-0806 Oslo, Norway, Norges Geotekniske Institutt, pages 215–219.
- Schaer, M. and D. Issler. 2001. Particle densities, velocities, and size distributions in large avalanches from impact-sensor measurements. *Annals Glaciol.*, **32**, 321–327.
- Schreiber, H., W. L. Ranau, H. Schaffhauser, and L. Rammer. 2001. Avalanche dynamics measurement by pulsed Doppler radar. *Annals Glaciol.*, **32**, 275–280.
- Suriñach, E., I. Vilajosana, G. Khazaradze, B. Biescas, G. Furdada, and J. M. Vilaplana. 2005. Seismic detection and characterization of landslides and other mass movements. *Nat. Haz. Earth Systems Sci.*, **5**, 791–798; SRef-ID 1684–9981/nhess/2005–5–791.
- UNESCO, . 1981. *Avalanche Atlas*. UNESCO/International Commission on Snow and Ice of the International Association of Hydrological Sciences, IAHS.
- Vilajosana, I., G. Khazaradze, E. Suriñach, E. Lied, and K. Kristensen. 2006. Snow avalanches speed determination using seismic methods. *Cold Regions Sci. and Technol.*, **submitted**.

Appendix A

Reprinted Papers and Reports 2004–2005

A.1 Published, Peer-Reviewed Paper (1)

Keylock, C. J. 2005. An alternative form for the statistical distribution of extreme avalanche runout distances. *Cold Regions Science and Technology* **42**, 185–193.



An alternative form for the statistical distribution of extreme avalanche runout distances

C.J. Keylock*

Earth and Biosphere Institute and School of Geography, University of Leeds, Woodhouse Lane, Leeds, LS2 9JT, UK

Received 20 May 2004; accepted 17 January 2005

Abstract

There are two main approaches in the avalanche literature for the statistical characterisation of extreme avalanche runout and these are known as the alpha-beta and runout ratio methods. Recent work suggests that the latter method is a more robust approach. This paper examines the statistical reasoning behind the selection of the Extreme Value Type I or Gumbel distribution used to characterise the runout distribution in the runout ratio method. On the basis that a threshold is often applied to the distribution of extreme avalanches used in analysis, it is proposed that the Generalised Pareto distribution is an appropriate candidate distribution based on theoretical arguments. Such a proposal is tested against data on extreme avalanches in Iceland for both the largest events on specific paths and for all events exceeding a threshold. The latter is a peaks-over-threshold approach that potentially allows more robust distribution estimation due to the increase in data availability.

© 2005 Elsevier B.V. All rights reserved.

Keywords: Avalanches; Snow; Statistical analysis; Statistical distributions; Peaks over threshold; Iceland

1. Introduction

Hazard zoning schemes for snow avalanches tend to require information on expected damage and impact pressures, as well as the probable return period of different events. Traditional statistical modelling of avalanche runout distances involves fitting a distribution function to an avalanche runout distance dataset, where events from different avalanche paths are

‘normalised’ based on a topographic parameter. These methods have an important role to play in hazard zoning in some countries (Lied and Bakkehøi, 1980) and have been used for indirect calibration of the coefficients in deterministic models (Barbolini et al., 2000) and also to derive impact pressure estimates for risk analysis (Keylock and Barbolini, 2001).

This paper considers the appropriate form of the statistical distribution that underpins one of these models. More specifically, it examines the runout ratio approach of McClung and Lied (1987), which has been applied to a variety of avalanche paths (McClung et al., 1989) and has been modified to

* Tel.: +44 113 3433307; fax: +44 113 3433308.

E-mail address: c.keylock@geog.leeds.ac.uk.

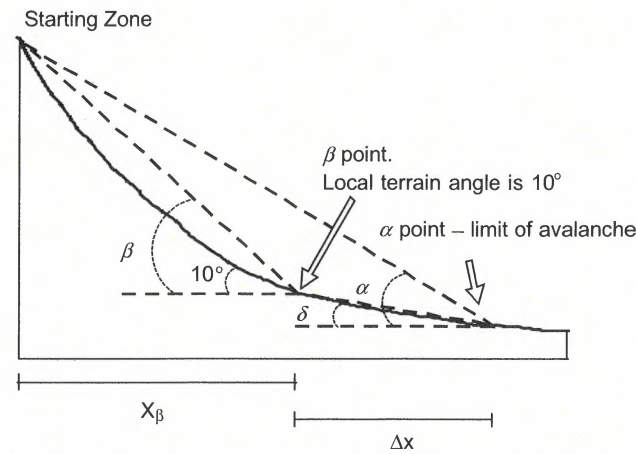


Fig. 1. The terrain and avalanche properties used to define the various properties of the different methods for extreme avalanche runout analysis.

analyse rockfall behaviour (Keylock and Domaas, 1999). This technique may be contrasted with the alpha-beta approach of Lied and Bakkehøi (1980), which has also been tested on various avalanche paths (Martinelli, 1986; Barbolini et al., 2000) and compared to the runout ratio method (Jóhannesson, 1998; McClung, 2001). This paper demonstrates that one of the common operational decisions made when using the runout ratio method invalidates the theoretical rationale for the selection of the Gumbel distribution as an appropriate probability density function for extreme runout. The Gumbel distribution may still provide a very good fit to the data, but theoretically the Generalised Pareto Distribution (GPD) is a preferred choice in these circumstances.

2. The runout ratio and extreme value distributions

The procedure for calculating the runout ratio is illustrated in Fig. 1. This diagram also shows the α and β angles that are related using least-squares regression in the alpha-beta model. The runout ratio also incorporates the average angle of the runout zone (δ) as can be seen from its definition:

$$\frac{\Delta x}{X_\beta} = \frac{\tan\beta - \tan\alpha}{\tan\alpha - \tan\delta} \quad (1)$$

McClung (2001) uses a statistical analysis to show that although δ is not a significant predictor of α ,

because the runout ratio method takes δ into account, a strong dependence of the exceedance probability of the runout distance upon δ is removed, resulting in more robust results with respect to the alpha-beta model. Hence, it would seem that the runout ratio method is the preferable technique for characterising avalanche runout distances statistically.

The form of the cumulative distribution function (CDF) generally used to describe extreme avalanche runout from a given mountain region is the Gumbel distribution (Gumbel and von Schelling, 1950):

$$P_n(x_i) = \exp\left[-\exp\left(-\frac{x_i - a}{b}\right)\right] \quad (2)$$

where x_i represents a particular runout ratio, P_n is the non-exceedance probability and a and b are the location and scale parameters of the distribution, respectively. Two other important extreme value distributions are the Fréchet Eq. (3) and Weibull Eq. (4) distributions:

$$P_n(x_i) = 0 \quad x_i \leq a$$

$$= \exp\left[-\left(\frac{x_i - a}{b}\right)^{-\omega}\right] \quad x_i > a \quad (3)$$

$$P_n(x_i) = \exp\left[-\left(\frac{x_i - a}{b}\right)^\omega\right] \quad x_i < a$$

$$= 1 \quad x_i \geq a \quad (4)$$

where ω is a distribution parameter. All three of these distributions are special cases of the Generalised Extreme Value Distribution (GEV):

$$P_n(x_i) = \exp\left\{-\left[1 + \xi\left(\frac{x_i - a}{b}\right)\right]^{-1/\xi}\right\} \quad (5)$$

where the shape parameter $\xi=0$ for the Gumbel, $\xi>0$ for the Fréchet and $\xi<0$ for the Weibull.

The distributions given by Eqs. (2)–(4) are the possible families that can be obtained for the maximum M_H of H independent random variables with a common CDF F , as $H \rightarrow \infty$ and following a linear renormalization where the scale parameters $b_H > 0$:

$$\frac{M_H - a_H}{b_H} \leq x_i \quad (6)$$

That is, if there are sequences of location a_H and scale b_H parameters such that $Pr[(M_H - a_H)/b_H \leq x_i] \rightarrow P_n(x_i)$ as $H \rightarrow \infty$, and $P_n(x_i)$ is an appropriate distribution function, then $P_n(x_i)$ must be of a form given by Eqs. (2)–(4) and hence, Eq. (5). Because the GEV Eq. (5) is a limiting case independent of the form for F , it can be considered to have certain similarities with the derivation of the normal distribution from the central limit theorem. Thus, it is not surprising that analyses based upon these distributions have been applied to many extreme-value problems including wind speeds (Sinton and Jones, 2002), flooding (Kim and Heo, 2002) and rainfall (Yue, 2000).

One difficulty in assuming Eq. (2) to hold a priori is that errors can be introduced into analysis because Eqs. (2)–(4) are all possible candidate distributions for the type of extreme-value problem described above. Hence, perhaps a preferable procedure is to assume the GEV to hold and to then choose between the possible candidates using an appropriate formal method such as a likelihood ratio test. In the avalanche literature, it is generally assumed that Eq. (2) holds and the fitting procedure then adopted follows the original work of McClung and Lied (1987). Inspection of Eq. (2) shows that suitable rearrangement gives:

$$b\{-\ln - \ln[P_n(x_i)]\} + a = x_i \quad (7)$$

Hence, it is possible to determine values for a and b using least-squares regression with runout ratio (x)

as the dependent variable and the transformed probability $-\ln - \ln [P_n(x_i)]$ as the independent variable. Various probability plotting formulae can be used to assign probabilities to individual runout ratios based on a ranked list of values. Commonly used formulae include those of Hazen (1930), Weibull (Gumbel, 1958), Kimbal (1960) and Gringorten (1963). These are all of a general form given by Blom (1958) Eq. (8), where q is a parameter, r_i is the rank of the value x_i based on an ascending order of ranking and N is the total number of values x_i . McClung and Mears (1991) also employed $P_n(x_i) = (r_i - 0.4)/N$. Cunnane (1978) showed that for the Gumbel distribution, the Gringorten formula is preferable, where the value for q is 0.44.

$$P_n(x_i) = \frac{r_i - q}{N + 1 - 2q} \quad (8)$$

It should be noted that the least-squares procedure is identical to a maximum likelihood estimator when the residuals are independent, Gaussian distributed and homoscedastic. If these assumptions are not met then this method will be biased relative to maximum likelihood methods (Cunnane, 1989).

3. A Generalised Pareto Distribution for avalanche runout

The motivation for this paper comes from the observation that in several studies, the extreme avalanche runout distances appear to fit the Gumbel distribution better when the data are censored at a particular runout ratio (Nixon and McClung, 1993; Smith and McClung, 1997). This is particularly apparent in the data from the Canadian Rockies and Purcells presented in Fig. 2 of McClung and Mears (1991). Jóhannesson (1998) found that there were only small changes to the nature of the fit when this threshold was adjusted from the value of $\Delta x/X_\beta = 0$. However, the derivation of the extreme value distributions presented above, takes place without the inclusion of a threshold. Consequently, although there may well be very good pragmatic reasons for choosing these distributions based on the quality of fit, from a theoretical perspective, the justification for choosing the Gumbel distribution in this situation needs reconsidering.

The Generalised Pareto Distribution (GPD) was introduced by Pickands (1975) as the limit distribution for exceedances over a high threshold. Further work upon this distribution was undertaken by Davison (1984) and Smith (1984, 1985) and it has recently been shown to be very useful for analysing the statistical properties of natural phenomena such as storm volume statistics (Salavadori and De Michele, 2004). It is proposed in this paper that this may be an appropriate candidate distribution for the study of extreme avalanche runout ratios where censoring of the data has taken place, as appears to be common in practice.

If X_1, X_2, \dots are a set of independent and identically distributed random variables, each with a CDF F , and RR represents the threshold runout ratio, then the behaviour of a particular extreme event X^* can be written as a conditional probability:

$$Pr[X^* > RR + \psi | X^* > RR] = \frac{1 - F(RR + \psi)}{1 - F(RR)} \quad (9)$$

where ψ is a positive increase in the avalanche runout given by $X_i - RR$. Recalling that if M_H is the maximum of H independent random variables with the same CDF F , the GEV is the limiting distribution as $H \rightarrow \infty$, appropriate substitution of Eq. (5) into Eq. (9) gives:

$$Pr[X^* > RR + \psi | X^* > RR] = \frac{1 - \exp\left\{-\left[1 + \xi\left(\frac{RR + \psi - a}{b}\right)\right]^{-1/\xi}\right\}}{1 - \exp\left\{-\left[1 + \xi\left(\frac{RR - a}{b}\right)\right]^{-1/\xi}\right\}} \quad (10)$$

Taking logarithms of Eq. (5), the CDF for the GEV may be written as

$$\log F(RR) = -\left[1 + \xi\left(\frac{RR - a}{b}\right)\right]^{-1/\xi} \quad (11)$$

If runout ratios are extreme then the non-exceedance probability $F(RR)$ will take a high value. A Taylor series expansion of $\log F(RR)$ can be written as:

$$\begin{aligned} \log F(RR) &= \log\{1 + [F(RR) - 1]\} \\ &= [F(RR) - 1] - \frac{1}{2}[F(RR) - 1]^2 \\ &\quad + \frac{1}{3}[F(RR) - 1]^3 - \frac{1}{4}[F(RR) - 1]^4 \dots \end{aligned} \quad (12)$$

For high values of $F(RR)$ the first term on the right-hand side will dominate and a suitable approximation is that

$$\log F(RR) \approx F(RR) - 1 \equiv -[1 - F(RR)] \quad (13)$$

Hence, Eq. (11) may be replaced by

$$1 - F(RR) \approx \left[1 + \xi\left(\frac{RR - a}{b}\right)\right]^{-1/\xi} \quad (14)$$

and Eq. (10) may be simplified to

$$\begin{aligned} Pr[X^* > RR + \psi | X^* > RR] &= \frac{\left[1 + \xi\left(\frac{RR + \psi - a}{b}\right)\right]^{-1/\xi}}{\left[1 + \xi\left(\frac{RR - a}{b}\right)\right]^{-1/\xi}} \\ &= \left[1 + \xi\frac{\psi}{b}\right]^{-1/\xi} \end{aligned} \quad (15)$$

where

$$\tilde{b} = b + \xi(RR - a) \quad (16)$$

Therefore, the CDF for the generalised Pareto distribution (GPD) is

$$P_n(\psi) = 1 - \left[1 + \xi\frac{\psi}{\tilde{b}}\right]^{-1/\xi} \quad (17)$$

This distribution is a special case of the Wakeby distribution (Houghton, 1978; Landwehr et al., 1979). One advantage of adopting such an approach in avalanche studies is that it may increase the amount of available data—there may be more events exceeding a threshold runout ratio than the total number of avalanche paths in the dataset. Hence, confidence in the statistical model fitted to the data may be enhanced if the increase in the total number of avalanches outweighs any effect of bias towards particular paths.

4. Fitting statistical distributions to data

The likelihood function for N different values x_i that are believed to be independently drawn from a PDF f with parameters θ is given by

$$L(\theta) = \prod_{i=1}^N f(x_i, \theta) \quad (18)$$

or may be expressed as a log likelihood

$$\ell(\theta) = \log L(\theta) = \sum_{i=1}^N \log f(x_i, \theta) \quad (19)$$

The maximum likelihood approach to distribution fitting involves the selection of values for the parameters that maximise either Eq. (18) or Eq. (19). Using the log likelihood, the maximum likelihood equations for the GPD are given by (Coles, 2001):

$$\ell(\tilde{b}, \xi) = -N \log \tilde{b} - (1 + 1/\xi) \times \sum_{i=1}^N \log \left(1 + \xi \frac{\psi_i}{\tilde{b}} \right) \quad \xi \neq 0$$

$$\ell(\tilde{b}, \xi) = N \log \tilde{b} - \frac{1}{\tilde{b}} \sum_{i=1}^N \psi_i \quad \xi = 0 \quad (20)$$

These equations need to be treated numerically and Grimshaw (1993) gave an algorithm for the maximum likelihood estimation of the GPD. Various alternative estimators exist in the literature including probability weighted moments (Greenwood et al., 1979; Hosking and Wallis, 1987), L-moments (Hosking, 1990), linear order statistics (Salvadori, 2003) and Bayesian methods (Coles and Tawn, 1996). While the issue of the most appropriate methodology for distribution fitting is an important one, it is not the primary focus of this paper, which intends to demonstrate the utility of the GPD for analysing extreme avalanches. Consequently, this paper makes use of the generally applicable max-

Table 1
GPD fits at various thresholds using MLE for all 45 events in the Icelandic extreme avalanche database

Threshold runout ratio	N	\tilde{b}	ξ	Standard errors	Negative log likelihood
-0.05	44	0.4276	-0.7903	0.0745, 0.1547	-28.158
0.00	40	0.3693	-0.7487	0.0734, 0.1696	-29.788
0.05	33	0.3607	-0.8203	0.0576, 0.1525	-27.715
0.10	30	0.2956	-0.7523	0.0718, 0.2127	-29.130
0.15	27	0.2231	-0.6319	0.0595, 0.2207	-30.569
0.20	19	0.2497	-0.8660	0.0188, 0.0883	-23.816

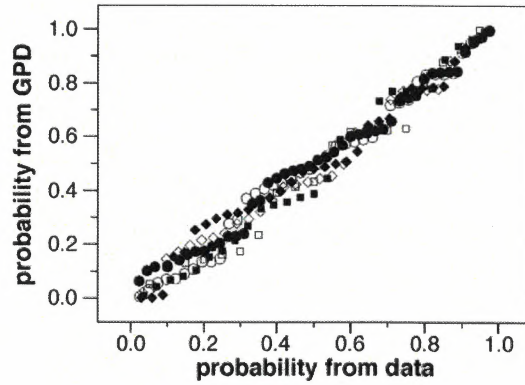


Fig. 2. GPD models fitted to the data for different values of the threshold. The ordinate is the non-exceedance probability derived from the fitted distribution, while the values on the abscissa are given by the Weibull fitting procedure. Dark circles are for a threshold runout ratio of -0.05, with circles, dark diamonds, diamonds, dark squares and squares represent thresholds of 0.0, 0.05, 0.10, 0.15 and 0.20, respectively.

imum likelihood method and the least-squares methods commonly used in avalanche studies.

5. The distribution of extreme avalanches

Table 1 shows maximum likelihood fits of the GPD to the Icelandic maximum runout dataset of Jóhannesson (1998) at various thresholds. These fits were obtained using R software routines written by Alec Stephenson (<http://www.maths.lancs.ac.uk/~stephena/software.html>), based on the S-Plus functions developed by Stuart Coles (Coles, 2001). The probability

Table 2
Fitting the Gumbel and GEV distributions to the Icelandic extreme avalanche dataset

Fitting method	A	b	ξ	Standard errors	Negative log likelihood
Hazen	0.1168	0.1136	-	0.0361	-
Weibull	0.1137	0.1243	-	0.0295	-
Kimball	0.1159	0.1167	-	0.0340	-
Gringorten	0.1163	0.1152	-	0.0350	-
MLE Gumbel	0.1110	0.1237	-	0.0195, 0.01463	-23.335
MLE GEV	0.1224	0.1323	-0.1660	0.0240, 0.0185, 0.1713	-23.731

20021048-11

Table 3
Extreme value distributions fitted to the Icelandic extreme avalanche dataset censored at a runout ratio of zero

Fitting method	A	b	ξ	Standard errors	Negative log likelihood
Weibull	0.1429	0.1167	–	0.0273	–
MLE Gumbel	0.1403	0.1172	–	0.0196, 0.01456	–23.203
MLE GEV	0.1536	0.1264	–0.2049	0.0237, 0.0180, 0.1647	–23.829

plot in Fig. 2 shows that the quality of the fitted model is reasonably robust to the choice of threshold, in accordance with the results of Jóhannesson (1998) and this is supported by the low variation in the log likelihoods for runout ratios less than 0.15 in Table 1. Extreme value distribution fits to the Icelandic dataset are given in Tables 2 and 3, where the standard error quoted for the equation fitting method is that derived from a least-squares regression fit to the data. Fig. 3 compares distributions fitted to the data censored at a runout ratio of 0.0. A likelihood ratio test based on the log likelihoods quoted in Table 3 and approximating the deviance function by the chi-squared distribution yields no significant difference between the GEV and the Gumbel distribution, suggesting that the two parameter Gumbel model is more parsimonious.

One clear advantage of the GPD model can be seen in Fig. 3. Because the distribution is pinned at

the left to the value of the threshold, unrealistic values for the runout ratio at low non-exceedance probabilities cannot be attained, which is a deficiency of both the GEV and Gumbel models. The lack of a shape parameter in the Gumbel model dramatically reduces the standard error for the fitted parameters. However, this enhanced precision can be dangerous if the Gumbel distribution is not the appropriate model for the data. This is because the narrow confidence intervals will give an unjustified faith in the model. The theoretical analysis presented above suggests that the GPD model is at least as justifiable for exceedances over a threshold as the Gumbel model. Although the Gumbel distribution gives a more conservative fit to the low frequency part of the distribution in this particular example, for alternative datasets in the literature this is not the case. Fig. 4 shows Gumbel and GPD fits to the Colorado data presented by McClung and Mears (1991). A mean residual life plot gave a value for the threshold for the GPD model of 0.2 (Fig. 5) and this was supported by the value for the negative log likelihoods at various runout ratios (Table 4). The distributions were fitted to the data exceeding this threshold (105 avalanche runout distances). The GPD model fits the Colorado data more effectively than the Gumbel model and gives a more conservative estimate of the probability of a particular runout ratio at low exceedance probabilities. That is, as well as not having any spurious behaviour for more

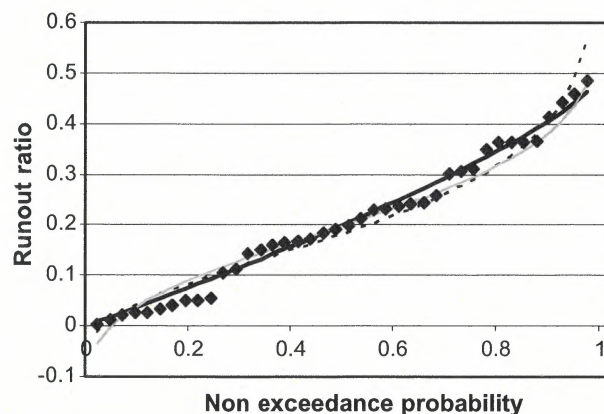


Fig. 3. Comparison of the GEV, Gumbel and GPD models fitted to the Icelandic runout ratio data censored at a runout ratio of 0.0. The diamonds are the recorded avalanches, the dotted line is the fitted Gumbel distribution (the parameter values from MLE and from Weibull plotting positions were indistinguishable on the plot), the dark line is the fitted GPD model, while the grey line is the GEV model. The plotting positions on the abscissa use the Weibull formula.

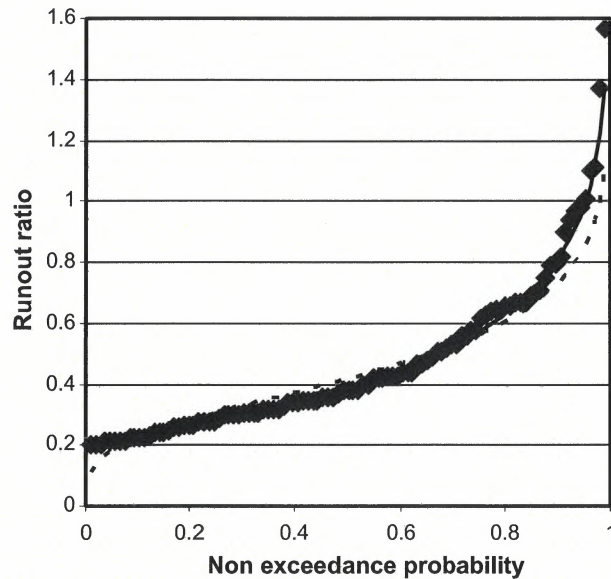


Fig. 4. Maximum likelihood fits of the Gumbel distribution (dotted line) and the GPD distribution (solid line) to the Colorado data from McClung and Mears (1991) censored at a runout ratio of 0.2.

frequent events on the left-hand side of the plot, the GPD provides a safer estimate of the runout distance of the larger extreme avalanches (right-hand side of the plot).

In any given mountain range there are likely to be more events that exceed the threshold than the maximum event on each path. Based on the derivation of the GPD provided above, a fairer test of this model is to apply it to all avalanches that exceed a threshold rather than just the largest events on particular paths

that exceed the threshold. This is the peaks-over-threshold approach and potentially allows a more precise estimate of the distribution of extreme avalanches due to an expansion of the number of records available. Using data collected as part of the work described in Keylock et al. (1999), the GPD was fitted to all events in the Icelandic database that were known about at that time. Table 5 indicates that a runout ratio of -0.05 is an appropriate choice of threshold and the fit to the Icelandic data based on this

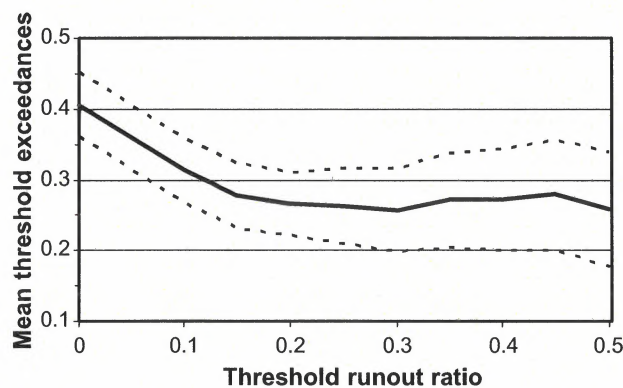


Fig. 5. Mean residual life plot for the Colorado runout ratio data. The values plotted on the ordinate are given by $\frac{1}{N(RR)} \sum_{i=1}^{N(RR)} x_i - RR$ where $N(RR)$ is the number of values exceeding the threshold RR and x_1, x_2, \dots, x_{N_T} are the avalanche events exceeding the threshold RR .

20021048-11

Table 4
Generalised Pareto Distributions fitted to the Colorado extreme avalanche dataset

Threshold runout ratio	Number of avalanches	Parameters	Standard errors	Negative log likelihood
0.0	130	0.509, -0.283	0.0497, 0.0499	5.3
0.1	127	0.363, -0.159	0.0400, 0.0669	-22.0
0.2	105	0.276, -0.038	0.0386, 0.1005	-34.1
0.3	74	0.260, -0.011	0.0456, 0.1313	-26.4
0.4	48	0.300, -0.100	0.0605, 0.1417	-14.6

Table 5
Generalised Pareto Distributions fitted to the Icelandic avalanche database

Threshold runout ratio	Number of avalanches	Parameters	Standard errors	Negative log likelihood
-0.15	199	0.390, -0.614	0.0320, 0.0597	-110.4
-0.10	189	0.317, -0.527	0.0280, 0.0629	-127.6
-0.05	174	0.251, -0.425	0.0250, 0.0726	-140.8
0.00	141	0.229, -0.424	0.0262, 0.0853	-126.6
0.05	103	0.246, -0.545	0.0320, 0.1007	-97.8
0.10	81	0.231, -0.590	0.0348, 0.1208	-85.4

model is given in Fig. 6. The GPD appears to describe the data well.

6. Conclusion

The Generalised Pareto Distribution has been introduced as a candidate distribution for extreme

avalanche runout. It is theoretically the preferable choice if one is examining exceedances over a threshold and appears to provide a good fit to extreme avalanches. By analogy to the hydrological literature, the standard extreme value methods used in the avalanche literature (the runout ratio and alpha-beta methods) have a certain resemblance to the analysis of annual event series. If the mountain range is the river then the analysis of the population of largest events on particular paths is similar to the study of the annual event series. The approach used at the end of this paper (the fitting of the distribution to all events larger than a threshold) is analogous to the peaks-over-threshold method in hydrology. This method has the advantage that it increases the amount of data available and hence, reduces the uncertainty attached to fitting a particular model. However, care would be needed in applying such a method in mountain areas where the number of recorded avalanches is heavily biased towards one or two paths. An approach based on the GPD and the peaks-over-threshold method has the potential to be extended to path-specific analyses based on a regional GPD fit and the path-specific frequency of threshold exceedance.

Acknowledgements

I am grateful to Tomas Jóhannesson for providing me with the data presented in Figs. 2 and 3.

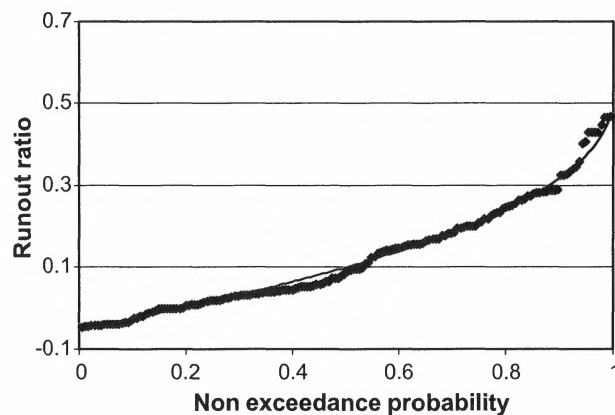


Fig. 6. The Generalised Pareto Distribution fitted to the Icelandic avalanche database using a threshold runout ratio of 0.2.

References

- Barbolini, M., Gruber, U., Keylock, C.J., Naaim, M., Savi, F., 2000. Application and evaluation of statistical and hydraulic-continuum dense-snow avalanche models to five real European sites. *Cold Reg. Sci. Technol.* 31, 133–149.
- Blom, G., 1958. *Statistical Estimates and Transformed Beta Variables*. John Wiley and Sons, New York.
- Coles, S., 2001. *An Introduction to Statistical Modeling of Extreme Values*. Springer, London. 208 pp.
- Coles, S., Tawn, J., 1996. A Bayesian analysis of extreme rainfall data. *Appl. Stat. J. Roy. St. C* 45, 463–478.
- Cunnane, C., 1978. Unbiased plotting positions—a review. *J. Hydrol.* 37, 205–222.
- Cunnane, C., 1989. *Statistical Distributions For Flood Frequency Analysis*, WMO Operational Hydrology Report no. 33, 118 pp.
- Davison, A.C., 1984. Modelling excesses over high thresholds, with an application. In: Tiago de Oliveira, J. (Ed.), *Statistical Extremes and Applications NATO ASI Series*. D. Reidel, Dordrecht, p. 692.
- Greenwood, J.A., Landwehr, J.M., Matalas, N.C., Wallis, J.R., 1979. Probability weighted moments: definition and relation to parameters of the several distributions expressible in inverse form. *Water Resour. Res.* 15, 1049–1054.
- Grimshaw, S.D., 1993. Computing maximum likelihood estimates for the generalized Pareto distribution. *Technometrics* 35, 185–191.
- Gringorten, I.I., 1963. A plotting rule for extreme probability paper. *J. Geophys. Res.* 68, 813–814.
- Gumbel, E.J., 1958. *Statistics of Extremes*. Columbia University Press, New York.
- Gumbel, E.J., von Schelling, H., 1950. The distribution of the number of exceedances. *Ann. Math. Stat.* 21, 247–262.
- Hazen, A., 1930. *Flood Flows, A Study of Frequencies and Magnitudes*. John Wiley and Sons, New York.
- Hosking, J.R.M., 1990. L-moments: analysis and estimation of distributions using linear combinations of order statistics. *J. R. Stat. Soc., Ser. B* 52, 105–124.
- Hosking, J.R.M., Wallis, J.R., 1987. Parameter and quantile estimation for the Generalized Pareto distribution. *Technometrics* 29, 339–349.
- Houghton, J.C., 1978. Birth of a parent: the Wakeby distribution for modeling flood flows. *Water Resour. Res.* 14, 1105–1110.
- Jóhannesson, T., 1998. Icelandic avalanche runout models compared with topographic models used in other countries. 25 years of Snow and Avalanche Research. Voss 12–16 May 1998, Norwegian Geotechnical Institute Publication, vol. 203, pp. 43–52.
- Keylock, C.J., Barbolini, M., 2001. Snow avalanche impact pressure—vulnerability relations for use in risk assessment. *Can. Geotech. J.* 38, 227–238.
- Keylock, C.J., Domaas, U., 1999. Evaluation of topographic models of rockfall travel distance for use in hazard applications. *Arct. Antarct. Alp. Res.* 31, 312–320.
- Keylock, C.J., McClung, D.M., Magnússon, M.M., 1999. Avalanche risk mapping by simulation. *J. Glaciol.* 45, 303–314.
- Kim, K.D., Heo, J.H., 2002. Comparative study of flood quantiles estimation by nonparametric models. *J. Hydrol.* 260, 176–193.
- Kimbal, B.F., 1960. On the choice of plotting positions on probability paper. *J. Am. Stat. Assoc.* 55, 546–560.
- Landwehr, J.M., Matalas, N.C., Wallis, J.R., 1979. Estimation of parameters and quantiles of Wakeby distributions. *Water Resour. Res.* 15, 1361–1379.
- Lied, K., Bakkehøi, S., 1980. Empirical calculations of snow-avalanche run-out distance based on topographic parameters. *J. Glaciol.* 26 (94), 165–177.
- Martinelli, M., 1986. A test of the avalanche runout equations developed by the Norwegian Geotechnical Institute. *Cold Reg. Sci. Technol.* 13, 19–33.
- McClung, D.M., 2001. Extreme avalanche runout: a comparison of empirical models. *Can. Geotech. J.* 38, 1254–1265.
- McClung, D.M., Lied, K., 1987. Statistical and geometrical definition of snow avalanche runout. *Cold Reg. Sci. Technol.* 13, 107–119.
- McClung, D.M., Mears, A.I., 1991. Extreme value prediction of snow avalanche runout. *Cold Reg. Sci. Technol.* 19, 163–175.
- McClung, D.M., Mears, A.I., Schaerer, P.A., 1989. Extreme avalanche run-out: data from four mountain ranges. *Ann. Glaciol.* 13, 180–184.
- Nixon, D.J., McClung, D.M., 1993. Snow avalanche runout from two Canadian mountain ranges. *Ann. Glaciol.* 18, 1–6.
- Pickands, J., 1975. Statistical inference using extreme order statistics. *Ann. Statist.* 3, 119–131.
- Salvadori, G., 2003. Linear combinations of order statistics to estimate the quantiles of generalized Pareto and extreme value distributions. *Stoch. Environ. Res. Risk Assess.* 17, 116–140.
- Salvadori, G., De Michele, C., 2004. Analytical calculation of store volume statistics involving Pareto-like intensity–duration marginals. *Geophys. Res. Lett.* 31, L04502.
- Sinton, D.S., Jones, J.A., 2002. Extreme winds and windthrow in the western Columbia river gorge. *Northwest Sci.* 76, 173–182.
- Smith, R.L., 1984. Threshold methods for sample extremes. In: Tiago de Oliveira, J. (Ed.), *Statistical Extremes and Applications NATO ASI Series*. D. Reidel, Dordrecht. 692 pp.
- Smith, R.L., 1985. Maximum likelihood estimation in a class of non-regular cases. *Biometrika* 72, 67–90.
- Smith, M.J., McClung, D.M., 1997. Characteristics and prediction of high-frequency avalanche runout. *Arct. Alp. Res.* 29, 352–357.
- Yue, S., 2000. The Gumbel logistic model for representing a multivariate storm event. *Adv. Water Resour.* 24, 179–185.

A.2 Published, Peer-Reviewed Paper (2)

Suriñach, E., I. Vilajosana, G. Khazaradze, B. Biescas, G. Furdada, and J. M. Vilaplana. 2005. Seismic detection and characterization of landslides and other mass movements. *Natural Hazards and Earth System Sciences* **5**, 791–798; SRef-ID: 1684-9981/nhess/2005-5-791.

Seismic detection and characterization of landslides and other mass movements

E. Suriñach, I. Vilajosana, G. Khazaradze, B. Biescas, G. Furdada, and J. M. Vilaplana

Grup d'Allaus (RISK-NAT Research Group), Dept. Geodinàmica i Geofísica, Fac. de Geologia, Universitat de Barcelona, Martí i Franquès s/n, 08028 Barcelona, Spain

Received: 1 August 2005 – Revised: 28 September 2005 – Accepted: 29 September 2005 – Published: 25 October 2005

Part of Special Issue “Documentation and monitoring of landslides and debris flows for mathematical modelling and design of mitigation measures”

Abstract. Seismic methods used in the study of snow avalanches may be employed to detect and characterize landslides and other mass movements, using standard spectrogram/sonogram analysis. For snow avalanches, the spectrogram for a station that is approached by a sliding mass exhibits a triangular time/frequency signature due to an increase over time in the higher-frequency constituents. Recognition of this characteristic footprint in a spectrogram suggests a useful metric for identifying other mass-movement events such as landslides. The 1 June 2005 slide at Laguna Beach, California is examined using data obtained from the Caltech/USGS Regional Seismic Network. This event exhibits the same general spectrogram features observed in studies of Alpine snow avalanches. We propose that these features are due to the systematic relative increase in high-frequency energy transmitted to a seismometer in the path of a mass slide owing to a reduction of distance from the source signal. This phenomenon is related to the path of the waves whose high frequencies are less attenuated as they traverse shorter source-receiver paths. Entrainment of material in the course of the slide may also contribute to the triangular time/frequency signature as a consequence of the increase in the energy involved in the process; in this case the contribution would be a source effect. By applying this commonly observed characteristic to routine monitoring algorithms, along with custom adjustments for local site effects, we seek to contribute to the improvement in automatic detection and monitoring methods of landslides and other mass movements.

1 Introduction

Seismic detection in real or quasi-real time of natural events associated with mass movements such as landslides, debris flows, rock falls and snow avalanches can provide timely warnings to people, reducing the associated risk. Detection even in remote, uninhabited areas can be helpful in characterizing return periods. Moreover, the seismic characterization of these phenomena can serve to remove them as “noise” events, masking other potentially important seismic signals such as earthquakes or volcanic and man-made explosions of interest.

In addition to the most common application of seismology to the discrimination and analysis of assumed stationary, point-source phenomena such as explosions and earthquakes, these methods have also been applied to the study of mass movements. Landslide signals recorded by seismometers were investigated in the early 20th century; two of the eminent researchers in this area were Galitzin (1915) and Jeffreys (1923). More recent analyses have been carried out by Norris (1994) and Wiechert et al. (1994), on rockfalls and landslides, respectively. Uhira et al. (1994) studied seismic waves excited by pyroclastic flows in erupting volcanoes in an attempt to clarify the source mechanism of seismic waves. Most of these studies have been based on time series obtained with seismometers.

Snow avalanches were first investigated seismologically by Lawrence and Williams (1976). Suriñach et al. (2000) demonstrated that seismology can be successful in detecting and determining the characteristics of snow avalanches. Seismic sensors have also been used for debris flows (e.g. Arattano, 2003; Arattano and Marchi, 2005). Additional sensors such as microphones, hydrophones or accelerometers have also been used in the study of mass movements (e.g. Van Lancker and Chritin, 1991; Hagerty et al., 2000; Itakura et al., 2000; Huang et al., 2004).

Correspondence to: E. Suriñach
(emma.surinach@ub.edu)

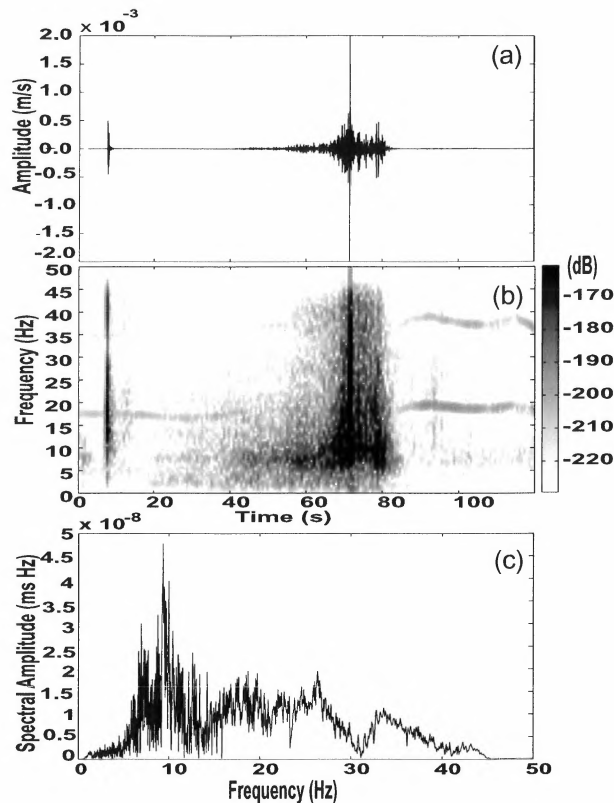


Fig. 1. (a) E-W component seismogram (100 sps) of La Sionne (Switzerland) artificially released dry/mixed avalanche on 20 February 2000, 09:40 UTC recorded at station C (Fig. 4c). (b) Running spectra with a 128-sample window and 50% overlap. (c) Total spectrum of the avalanche signals (excluding the explosion).

In general, the recorded seismic time series of these phenomena are complex since the wave field obtained at a point receiver is composed of many phase arrivals. This results from the existence of moving multi-seismogenic sources and from the complexity of the wave propagation in heterogeneous media and the rugged topography that usually accompanies the phenomena. Energy attenuation through internal frictional losses (anelasticity) and geometrical spreading with distance must also be taken into account.

Although the mass movements stated above are different in nature and have, in general, different characteristics, they can all be regarded as moving seismogenic sources because the material propagation down slope due to gravity produces ground vibration. This vibration can be recorded and separated from the seismic ambient noise if this is sufficiently energetic. It is in this regard that these phenomena are considered in the present paper.

The snow avalanche team of the Universitat de Barcelona (UB) has been studying the characteristics of snow avalanches since 1994, using seismic methods (Sabot et al., 1998; Suriñach, 2004). We have studied the seismic signals of avalanches that occurred in the valleys of Boí Taüll and Núria (Catalan Pyrenees), Vallée de La Sionne (Swiss Alps)

and at the test site in Ryggfonn (Norway). Our aim is to contribute to a better understanding of the dynamics of avalanche propagation. The detection of snow avalanches is also within our scope.

During our experiments different types of snow avalanches (flow and size) were recorded at several distances. Avalanches were triggered by explosives experts by dropping explosives from a helicopter or by detonating them on land. In addition to the seismic signals we also analyzed information obtained simultaneously from video images and field observations including cartography, type of flow and deposits. These data allowed us to identify general and specific characteristics of the seismic signals of the different types of avalanches in the time and frequency domains. The evolution in time of the frequency content (running spectra or spectrogram) of the signals provided valuable information on the snow avalanches (Biescas et al., 2003). Similar methods are used routinely to complement the time signal analyses in the seismic monitoring of volcanic areas in order to distinguish the different types of seismic events produced by volcanoes (e.g. Ibañez et al., 2000; Del Pezzo, 2003). Spectrograms are also useful as a complement in locating pyroclastic flows (Jolly et al., 2002). Information contained in spectrograms is also included in the design of algorithms of detection and classification of seismic events by means of neural networks (Wang and Teng, 1995; Scarpetta et al., 2005). Nevertheless, none of the above studies had considered in detail the specific characteristic shapes of the calculated spectrograms associated with various types of mass movements, which is the main subject of our paper. Specifically, we describe the results obtained in our earlier studies of snow avalanches and discuss their applicability to other types of mass movements.

2 Methods and results

Seismic records from avalanches were obtained with different types of seismometers. All were three-component geophones with eigenfrequencies of 0.2, 1, and 2 Hz, respectively and a cut-off of 40 Hz. Data were recorded with different sampling rates (100, 200 and 400 sps). All data were homogenised converting the amplitude of the signals to ground motion (m/s) using the corresponding transfer function of the equipment and then filtered using an order 4 Butterworth band pass filter. Time series, total spectrum (TS) and spectrogram (RS) of all the records were analysed. Figure 1 shows the E-W component of the avalanche signal obtained at Vallée de la Sionne (site C, Fig. 4c). This was a triggered dry/mixed avalanche that descended a 2500 m long path and reached the recording station at ~ 70 s. The time series in Fig. 1a at 7.4 s shows the signal of the explosion that triggered the avalanche. After this signal, at ~ 40 s, the increased signal-to-noise ratio allows visual detection of the avalanche arrival. The TS of the portion of the signal corresponding to the avalanche is shown in Fig. 1c plotted on a linear scale. In Fig. 1b the RS shows the evolution of the frequencies and their partitioning. In our RS representation the

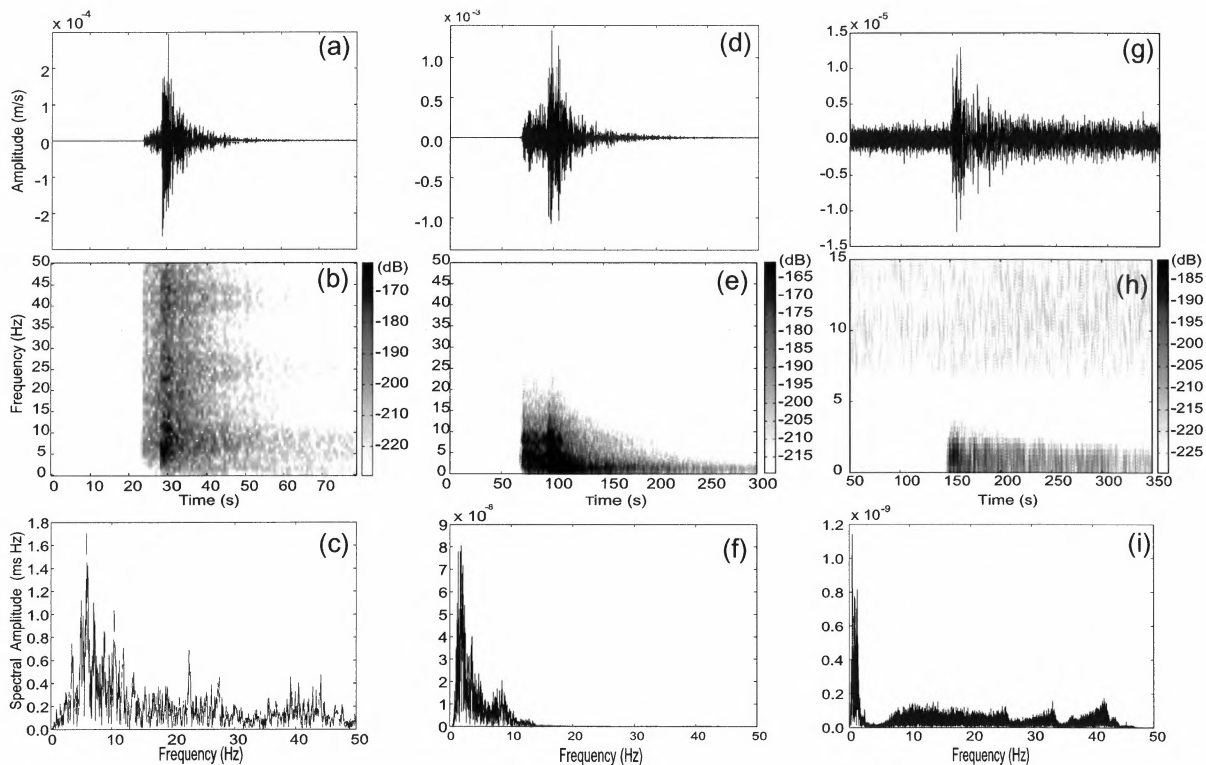


Fig. 2. E-W component seismogram (100 sps) recorded at station C in La Sionne, Switzerland (Fig. 4c). Top: seismograms. Middle: spectrograms. Bottom: full spectra. (a) Local (52.8 km), ML 2.0 earthquake of 10 April 2002, 13:6:29.2 UTC at Zermat, Switzerland. (b) Regional earthquake (228.2 km), ML 5.1, 11 April 2003, 09:26:57.6 UTC in northern Italy. (c) Teleseismic recording (6931.6 km) of ML 6.7 event of 17 April 2003, 00:48:46.8 UTC in Qinghai, China. All running spectra with a 128-sample window and 50% overlap.

spectral amplitudes are given in a grey shade scale; the darkest colours correspond to the maximum amplitudes in dB. The sharp band of high spectral amplitude at ~ 7 s covering all the frequencies corresponds to the explosion. Two bands at ~ 18 and ~ 35 Hz oscillating in time affect the whole RS. These bands correspond to harmonics associated with the helicopter flying over the area. The RS facilitates the detection of the onset of the avalanche signal because of the coherent signal behaviour. The gradual increase in frequencies and amplitudes with time is evident at ~ 18 s, which indicates a detection of the avalanche that is earlier than in the time series.

One result of our earlier studies that is worth highlighting concerns the running spectra (RS) of the signals produced by snow avalanches. The reproducibility of these was observed and discussed by Biescas et al. (2003). One constant characteristic observed in the RS of the studied avalanches is an increase in the high frequency content (and amplitude) of the signal with time when the avalanche approaches the sensor, which is responsible for the triangular shape observed in the RS (Fig. 1b). This feature seems to be peculiar to the signals of snow avalanches and is not observed in other natural or artificial seismogenic sources such as helicopters, explosions or earthquakes. For the sake of comparison, Fig. 2 shows the time series (E-W component), RS and total spectrum (TS) of three different type earthquakes: local, regional

and teleseism that were recorded at the same station at Vallée de la Sionne (site C, Fig. 4c) as the avalanche of Fig. 1. Further characteristics of these earthquakes are given in the caption of Fig. 2. In all these cases, regardless of the frequency range, the shape of the time series and TS functions is similar to those of the avalanches (Figs. 1 and 3). However, the shape of the RS is different. In the RS of earthquakes high spectral amplitudes in all frequencies suddenly appear at the same time (earthquake arrival time), and no triangular shape is observed, indicating that the evolution of frequencies in this case is completely different from avalanches. Likewise, for the explosions (Figs. 1 and 3) the initial shape of the RS does not resemble the triangle. In Fig. 3 the seismic signals of avalanches recorded at two more sites (Núria, and Ryggfönn) are presented. In both cases the general tendency of the functions is analogous to that of Fig. 1, although the slope of the triangles in the RS and the characteristics of the total spectra are different. Figures 3a–3c correspond to an avalanche recorded at Núria triggered by explosives. This was a small size dense/wet avalanche that stopped 40 m up slope the seismic station. The length of the path was 150 m. Figures 3d–3f show the signal of a large dry/mixed artificially released avalanche recorded at the Ryggfönn site. This avalanche travelled 2100 m down the path and passed over the sensor at ~ 76 .

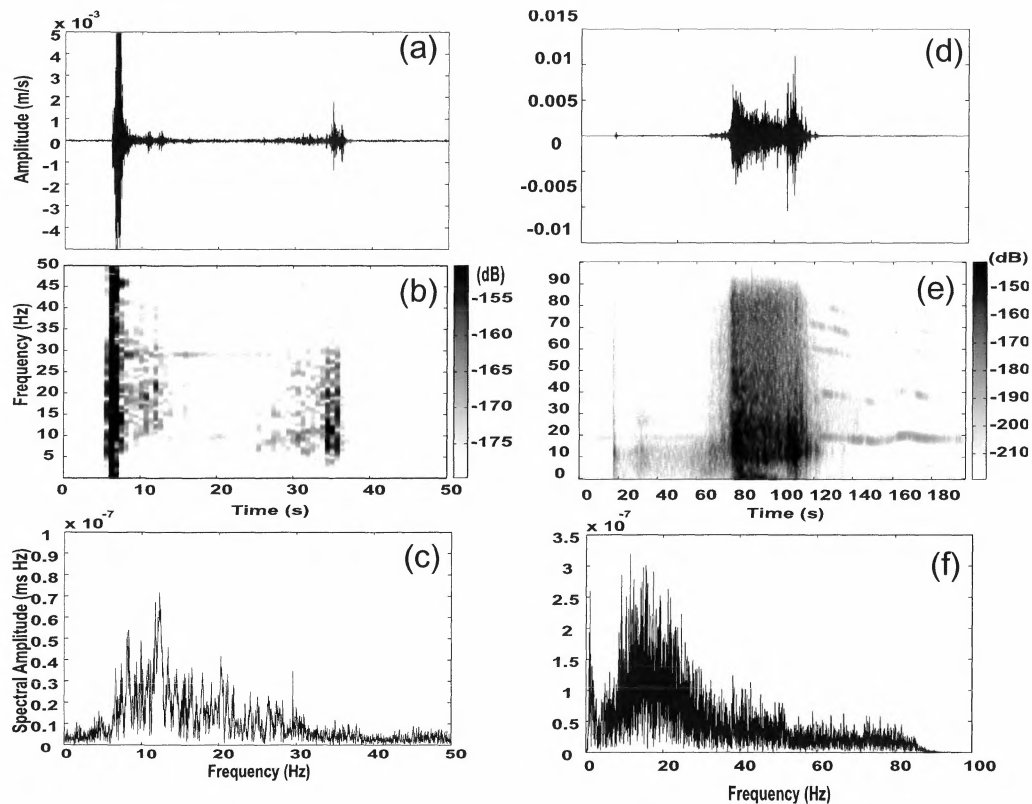


Fig. 3. Núría and Ryggfjonn avalanche signals. Top: seismograms; Middle: spectrograms (RS); Bottom: full spectra (TS). (a) E-W component seismogram (100 sps) of the Núría (Spain) artificially released wet snow avalanche on 1 February 1996. (b) N-S component seismogram (200 sps) of the Ryggfjonn site (Norway) artificially released dry-mixed snow avalanche on the 28 February 2004. Running spectra with a 128-sample window and 50% overlap.

In the light of our findings, we can conclude that the triangular shape observed in the RS of avalanche seismic signal is a general and independent characteristic of these phenomena, regardless of the site and type of flow. This triangular shaped increase in high frequency contents observed in the RS could not be attributed to Doppler Effect (Biescas, 2003). In fact, experimental data and numerical simulations of the seismic wave field caused by moving sources show the triangular behaviour of the spectrogram (RS) when the velocity of the moving source approaching the sensor is lower than the wave propagation speed regardless of the scale (Almendros et al., 2002; Anderson et al., 2004; Ketcham et al., 2005). These findings support our proposal that the triangular shape observed in the RS is produced by a moving mass approaching the sensor, i.e. the snow avalanche.

Possible explanations for the triangular shape characteristics are 1) the anelastic attenuation with distance of the seismic waves that propagate in the earth, which is frequency dependent. High frequencies attenuate faster than low frequencies (Aki, 1980; Lay and Wallace, 1995); and/or 2) the increase in the energy involved in the avalanche due to the snow entrainment when the avalanche propagates down the path (Gauer and Issler, 2004) resulting in an increase in the amplitude of the signal.

In support of this hypothesis we present a case where the avalanche departs from the sensor. Figure 4 shows the signals corresponding to the same avalanche presented in Fig. 1 but recorded at sensor A (Fig. 4c). The avalanche reaches the sensor at 5–6 s. The increase in frequencies before the avalanche reaches the sensor is abrupt because of the short distance between the releasing zone of the avalanche and the recording site. After 5–6 s the spectrogram shows a decrease in frequencies as the avalanche departs from the sensor causing an inverted triangular shape in the RS. In the same figure, at 12 s, an increase in the amplitudes and frequencies is observed, which we attributed to the entrainment of snow. A physical justification of this statement is presented below: a) the amplitude of a seismogram is proportional to the force transmitted into the ground (Aki and Richards (1980), b) for a moving mass this force is proportional to the mass involved and dependent on the angle of the slope (i.e. Brodsky et al., 2003, Eq. 1). Thus, in a first approximation, any mass increase in the moving flow is converted into an increase in the net force applied to the ground and, hence, into an increase of the amplitude of the seismogram. This amplitude increase produces a bias of the amplitudes in all frequencies to higher values (i.e. Jolly et al., 2002, Eq. 1), which can be observed in the RS representation. Consequently, the sudden increase

in the amplitudes in all the frequencies observed in the RS in Fig. 4 at approx. 12 s could be attributed to the incorporation of the mass in the flow as observed in the video images.

3 The case of a landslide (Laguna Beach)

In order to confirm our hypothesis that the increase in frequencies and amplitudes with time in snow avalanche seismic records is related to the mass movement, and that this increase can be observed in other types of mass movements, corroboration by seismic data from such events is necessary. On 1 June 2005, at approx. 06:51 a.m./PDT (13:51 UTC) a significant landslide occurred in the Bluebird Canyon near the town of Laguna Beach in southern California (Tran et al., 2005) (Fig. 5). Considerable landslides have been reported in this area since 1978 (Miller et al., 1979). A 121.405 m² piece of 15 to 18 m deep hillside broke free and slid downwards, destroying dozens of multi-million dollar houses. Since this landslide occurred in an area with a dense state-of-the-art Caltech/USGS Regional Seismic Network (CI), we expected that some of these stations had recorded the seismic signal associated with the landslide. We downloaded seismic data from the 10 closest broadband stations of the CI network from the Southern California earthquake data centre (SCEDC, www.data.scec.org) (Fig. 5). We examined a 24-hour section of 3-component, continuous ground motion (m/s) data recorded at 20 sps, and we realised that only stations SDD and LLS, 9 and 23 km respectively from the slide, recorded the signal. However, the SDD signal was barely perceptible. Unfortunately, station STG, close to the event, which could have been of help, seemed to be out of order at the time of the landslide. There were no local earthquakes that could have disturbed our study during the 24 h corresponding to our time window.

The instruments at SDD and LSS have an eigenfrequency of 1 Hz and a cut-off frequency of 30 Hz. The time-series, together with their RS of both stations is shown in Fig. 5. We only present the E-W component of the ground motion since the two other components are similar. The initial time in both time series is 12:00 UTC (approx. 2 h before the occurrence of the landslide). Although, the highest amplitudes in the LLS time series that last approx. 11 h are observed at 14:02:15 (7335 s), first energetic arrivals appear at 13:25:55 (5155 s), which we interpreted as the onset of the landslide (Fig. 5a). The time series from the SDD station exhibits only a small increase in the amplitudes during the landslide and no first arrival can be identified (Fig. 5c). The significantly lower signal-to-noise ratio observed at this station with respect to the LLS, was somewhat unexpected, since SDD is located closer to the landslide. This effect could be produced by characteristics of the seismometer, the site and/or the directivity of the wave propagation. To test the significance of these effects, we examined the time series of a local earthquake recorded at SDD and LSS, which showed a small difference in the amplitudes of the recorded signals. In consequence, we suspect that the differences observed in the land-

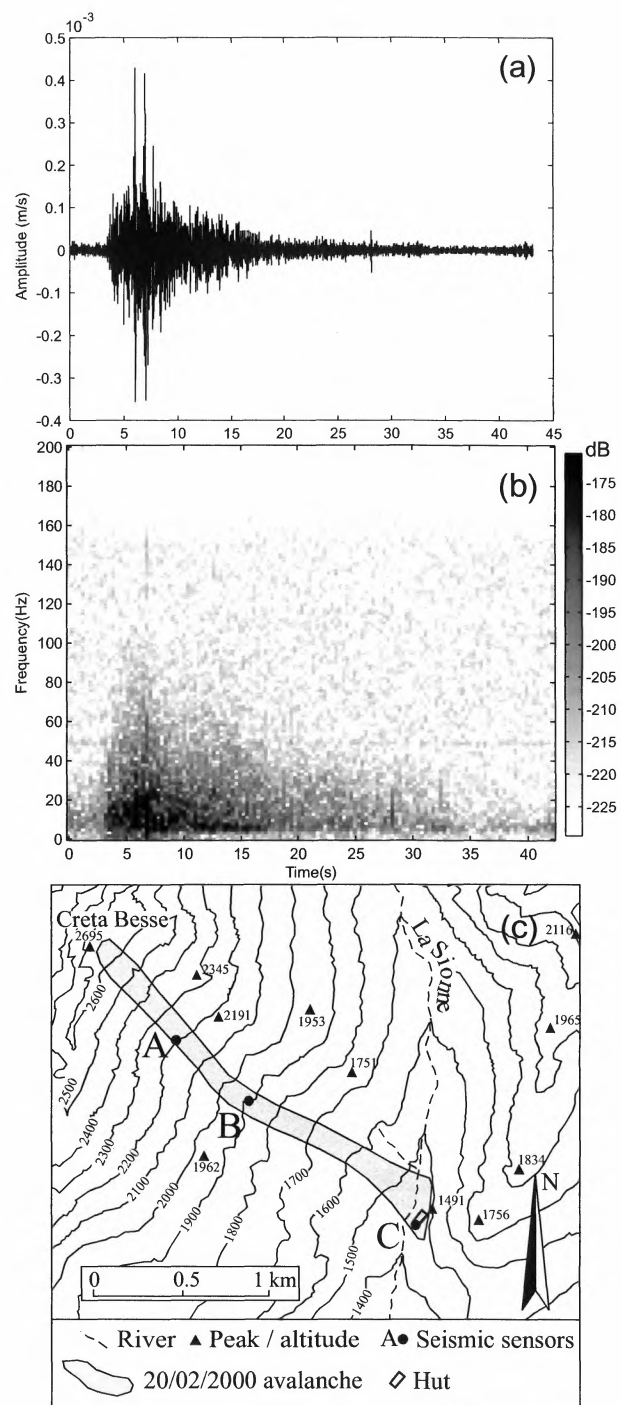


Fig. 4. (a) E-W component seismogram (400 sps) of La Sionne (Switzerland) artificially released dry/mixed avalanche of 20 February 2000 09:40 UTC, recorded at station A. (b) Running spectra with a 128-sample window and 50% overlap. (c) Cartography of the avalanche; A, B, C locations of the seismic sensors.

slide records are independent of the stations and are probably caused by other effects (e.g. directivity).

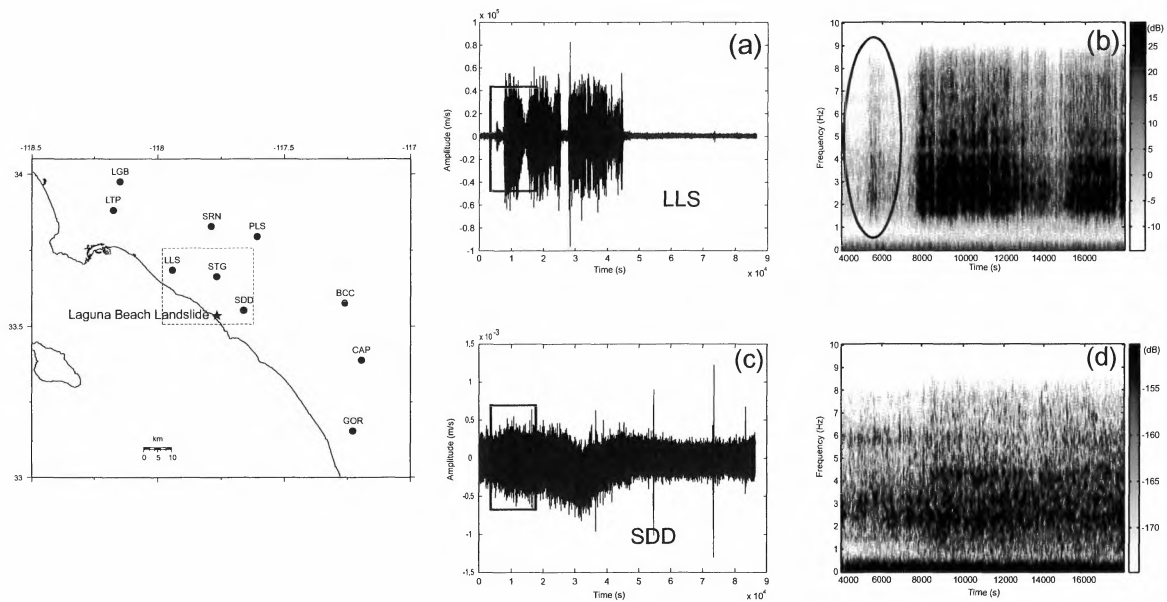


Fig. 5. Left: Map showing the Laguna Beach landslide (Star) and 10 closest seismic stations of Caltech/USGS Regional seismic network (CI). Centre: E-W component seismograms (20 sps) recorded at stations (a) LLS (23 km from landslide); (c) SDD (9 km from landslide); (b) and (d) spectrograms (RS) of (a) and (c) respectively with a 128-sample window and 50% overlap.

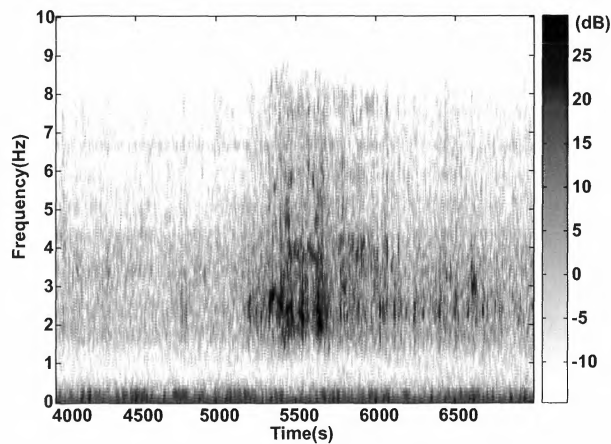


Fig. 6. Detail of the first part of the Laguna Beach landslide running spectra of station LLS indicated in Fig. 5b.

Figures 5b and 5d shows the RS corresponding to the interval indicated in the time series for both stations. Spectra of both time series are limited to 8–9 Hz, although the Nyquist frequency is 10 Hz and data were not filtered. Regardless of the scale, the shape of the RS is similar to those of the avalanches. An increase in the frequencies and energy through time also results in a triangular shape. This is more evident at station LLS (Fig. 5b). A detail of the RS in the 5500–6800 s interval is presented in Fig. 6. At approx. (4800 s, 3 Hz) an increase in the amplitudes and frequencies involving all frequencies at 5300 s with a nucleus of high amplitude centred at (5500 s, 2–4 Hz) is observed. Amplitudes

in higher frequencies decrease at ~ 6100 s. High amplitude in low frequencies (~ 2 –4 Hz) still persists. This behaviour is also observed in the RS of the second part of the LLS signal at ~ 7800 s (Fig. 5b). At station SDD the triangular shape can also be observed between 6500–8000 s, although it is less clear owing to the compressed scale of time and the low signal-to-noise ratio. We attribute the energy observed from 8000 s with a duration of approx. 11 h to a large movement of mass of origin different (plug flow) from that of a turbulent mechanism such as an avalanche or a pyroclastic flow.

4 Discussion and conclusions

The preliminary analysis of the landslide seismic data seems to support our hypothesis that the increase in the frequencies and amplitudes with time in the spectrograms is associated with the mass movements on the surface. Although we compared only one landslide to snow avalanches, this is not the only case where similar effects can be observed. For example, Jolly et al. (2002) present the RS of pyroclastic flows for stations within 1–2 km range at La Soufrière Hills Volcano (Montserrat), where it is possible to identify a triangular shape. Although, these authors did not specifically focus on this feature, it seems that the directivity effect was present. As in our experiments with snow avalanches, the RS triangular shape is clearer when the flow approaches the recording station. In addition, a typical triangular shape can also be observed in the spectrograms obtained during the laboratory studies of debris flows using hydrophones in a flume (Huang et al., 2004). However, this shape is observed only when the

grain size is large enough to produce sufficient energy to be detected before the flume material arrives at the sensor.

In the light of the examples discussed in this paper, which covers a wide range of distances and energy scales, we conclude that a characteristic triangular shape appears in the RS representation when the seismic signal of the moving source is recorded at a sensor located in the direction of its propagation. This suggests the existence of a general physical mechanism that is responsible for the observed increase in frequency content with time in the RS: the anelastic attenuation of frequencies and the mass (i.e. energy) incorporation. Greater distances between source and receiver will produce more low-frequency energy in the spectrogram because of the intrinsic attenuation for high frequency signals. As the source approaches the sensor and the path is shortened, a greater proportion of high frequency energy will be observed as the overall amplitudes increase. Moreover, entrainment of additional material into the moving mass will serve to increase overall amplitudes. These factors combine to generate the triangular shape observed in the spectrogram for instruments in the path of an approaching mass. Although more work on the influence of site characteristics and other variables is warranted, our findings may prove useful in refining algorithms designed to monitor the occurrence of mass movements.

Acknowledgements. This study is supported by the grants of the Ministry of Education and Science of Spain (MiCYT REN2002-12779-E/RIES and RyC for G. Kh.), the government of Catalonia (RISKMAT PIGC: 2001SGR00081) and the EU (SATSIE EVG1-CT-2002-00059). Field experiments were carried out with the support of Ferrocarrils de la Generalitat de Catalunya, Swiss Federal Institute of Snow and Avalanche Research (SLF) and the Norwegian Geotechnical Institute (NGI). We are indebted to F. Dufour, D. Issler, K. Kristensen, E. Lied, D. Paret, Q. Sabata, F. Sabot and X. Vilajosana for their useful discussions and support in the field. We are also very grateful to C. Rowe for her constructive and helpful comments.

Edited by: M. Arattano

Reviewed by: C. Rowe

References

- Aki, K.: Attenuation of shear-waves in the lithosphere for frequencies from 0.05 to 25 Hz, *Phys. Earth Planet. Inter.*, 21, 50–60, 1980.
- Aki, K. and Richards, P. G.: *Quantitative Seismology*, W. H. Freeman and Company, New York, USA, 557 pp., 1980.
- Almendros, J., Chouet, B., and Dawson, P.: Array detection of a moving source, *Seismol. Res. Lett.*, 73, 153–165, 2002.
- Anderson, T. S., Moran, M. I., Ketcham, S. A., and Lacombe, J.: Tracked vehicle simulations and seismic wavefield synthesis in seismic sensor systems, *Comp. Sci and Eng.*, 224, 22–28, 2004.
- Arattano, M.: Monitoring the presence of the debris-flow front and its velocity through ground vibration detectors, in *Debris Flow hazard Mitigation: Mechanics, Prediction and Assessment*, edited by Rickenmann and Chen, Millpress, Rotterdam, 2003.
- Arattano, M. and Marchi, L.: Measurements of debris flow velocity through cross-correlation of instrumentation data, *Nat. Hazards Earth Syst. Sci.*, 5, 137–142, 2005, **SRref-ID: 1684-9981/nhess/2005-5-137**.
- Biescas, B.: *Aplicación de la sismología al estudio y detección de los aludes de nieve*, Ph.D. Thesis, Universitat de Barcelona, Barcelona, Spain (ISBN: B. 46927-2003 / 84-688-3758-X), 1–130 pp., <http://www.tdx.cesca.es/TDX-1010103-084042>, 2003.
- Biescas, B., Dufour, F., Furdada, G., Khazaradze, G., and Suriñach, E.: Frequency content evolution of snow avalanche seismic signals, *Surv. Geophys.*, 24, 447–464, doi:10.1023/B:GEO.0000006076.38174.31, 2003.
- Brodsky, E. E., Gordeev, E., and Kanamori, H.: Landslide basal friction as measured by seismic waves, *Geophys. Res. Lett.*, 30, 2236, 1–5, doi:10.1029/2003GL0184852236, 2003.
- Del Pezzo, E., Esposito, A., Giudiciopietro, F., Marinaro, M., Martini, M., and Scarpetta, S.: Discrimination of earthquakes and underwater explosions using neural networks, *Bull. Seismol. Soc. Am.*, 93, 215–223, 2003.
- Galitzin, P. B.: Sur le tremblement de terre du 18 de février 1911, *Comptes Rendus Acad. Sc. de Paris*, 160, 810–813, 1915.
- Gauer, P. and Issler, D.: Possible erosion mechanisms in snow avalanches, *Ann. Glaciol.*, 38, 384–392, 2004.
- Hagerty, M. T., Schwartz, S. Y., Garces, M. A., and Protti, J. M.: Analysis of seismic and acoustic observations at Arenal Volcano, Costa Rica, *J. Volcanol. Geo. Res.*, 101, 27–65, 2000.
- Huang, C., Shieh, C., and Yin, H.: Laboratory study of the underground sound generated by debris flows, *J. Geophys. Res.*, 109, F01008, doi:10.1029/2003JF000048, 2004.
- Ibañez, J. M., Del Pezzo, E., Almendros, J., La Rocca, M., Alguacil, G., Ortiz, R., and Garcia, A.: Seismovolcanic signals at Deception Island Volcano, Antarctica; wave field analysis and source modeling, *J. Geophys. Res.*, 105, 13 905–13 931, 2000.
- Itakura, Y., Fujii, N., and Sawada, T.: Basic characteristics of ground vibration sensors for the detection of debris flow, *Phys. Chem. Earth*, 25, 717–720, 2000.
- Jeffreys, Sir H.: The Pamir earthquake of 18 February 1911, in relation to the depths of earthquake foci, *Monthly Notices of the Royal Astr. Soc. Geophys.*, Supplement 1, 22–31, 1923.
- Jolly, A. D., Thompson, G., and Norton, G. E.: Locating pyroclastic flows on Soufrière Hills volcano, Montserrat, West Indies, using amplitude signals from high dynamic range instruments, *J. Volcan. Geother. Res.*, 118, 299–317, 2002.
- Ketcham, S. A., Moran, M. L., Lacombe, J., Greenfield, R. J., and Anderson, T. S.: Seismic Source Model for Moving Vehicles, *IEEE Trans. Geosci. Remote Sens.*, 43, 248–256, 2005.
- Lawrence, W. S. and Williams, T. R.: Seismic signals associated with avalanches, *J. Glaciol.*, 17, 521–526, 1976.
- Lay, T. and Wallace, T. C.: *Modern Global Seismology*, Academic Press, San Diego, California, 521 pp., 1995.
- Miler, Russell V., and Tan, S. S.: Bluebird Canyon landslide of 2 October 1978, Laguna Beach, California, *California Geology*, 32, 1, 5–7, 1979.
- Norris, R. D.: Seismicity of rockfalls and avalanches at three Cascade Range volcanoes; implications for seismic detection of hazardous mass movements, *Bull. Seismol. Soc. Am.*, 84, 1925–1939, 1994.
- Sabot, F., Naaim, M., Granada, F., Suriñach, E., Planet, P., and Furdada, G.: Study of the Avalanche Dynamics by means of Seismic Methods, Image Processing Techniques and Numerical Models, *Ann. Glaciol.*, 26, 319–323, 1998.

- Scarpetta, S., Giudicepietro, F., Ezin, E. C., Petrosino, S., Del, P. E., Martini, M., and Marinaro, M.: Automatic classification of seismic signal at Mt. Vesuvius Volcano, Italy, using neural networks, *Bull. Seismol. Soc. Am.*, 95, 185–196, 2005.
- Suriñach, E.: Spanish avalanche research: Experimental sites and seismic measurements, in: *Snow and Avalanche Test Sites*, edited by: Naaim, M. and Naaim-Bouvet, F., Cemagref, 71–183, 2004.
- Suriñach, E., Sabot, F., Furdada, G., and Vilaplana, J. M.: Study of Seismic Signals of Artificially Released Snow Avalanches for Monitoring Purposes, *Phys. Chem. Earth*, 25, 721–727, 2000.
- Suriñach, E., Furdada, G., Sabot, F., Biescas, B., and Vilaplana, J. M.: On the characterization of seismic signals generated by snow avalanches for monitoring purposes, *Ann. Glaciol.*, 32, 268–274, 2001.
- Tran, M., Lobdell, W., and Hanley, C.: Laguna Beach Homes Destroyed in Slide, in: *Los Angeles Times*, edited, Los Angeles, USA, 2005.
- Uhira, K., Yamasato, H., and Takeo, M.: Source mechanism of seismic waves excited by pyroclastic flows observed at Unzen Volcano, Japan, *J. Geophys. Res.*, 99, 17 757–17 773, 1994.
- Van Lancker, E. and Chritin, V.: Des avalanches sous bonne surveillance, *Neige et avalanches*, 96, 10–14, 2001.
- Wang, J. and Teng, T. I.: Artificial neural network-based seismic detector, *Bull. Seismol. Soc. Am.*, 85, 308–319, 1995.
- Weichert, D., Horner, R. B., and Evans, S. G.: Seismic signatures of landslides; the 1990 Brenda Mine collapse and the 1965 Hope rockslides, *Bull. Seismol. Soc. Am.*, 84, 1523–1532, 1994.

A.3 Published Paper without Peer-Review (1)

Barbolini, M., F. Cappabianca and R. Sailer. 2004. Empirical estimate of vulnerability relations for use in snow avalanche risk assessment. *In: C. A. Brebbia (ed.), Risk Analysis IV*. WIT press. Pages 533–542.

Empirical estimate of vulnerability relations for use in snow avalanche risk assessment

M. Barbolini¹, F. Cappabianca¹, R. Sailer²

¹*Department of Hydraulic and Environmental Engineering,
University of Pavia, Italy.*

²*Austrian Institute for Avalanche and Torrent Research, Austria.*

Abstract

Formal risk analysis may be considered a promising method for evaluating the danger to people from avalanches and for introducing proper land-use regulation in the hazard prone areas. According to the Committee on Risk Assessment of the Working Group on Landslides of the International Union of Geological Sciences (IUGS,[1]) quantitative risk analysis involves expressing the risk as a function of the hazard, the elements at risk and the vulnerability. Vulnerability is defined as the degree of loss to a given element or set of elements at risk within the area affected by avalanches. It is expressed on a scale of 0 (no loss) to 1 (total loss). For property, the loss will be the value of the property, and for persons it will be the probability that a particular life (the element at risk) will be lost, given the person is affected by the avalanche. A relevant limit of all the current procedures for avalanche risk calculation is the lack of knowledge on how avalanche impact damage structures and cause fatalities. In this study data from two catastrophic avalanches occurred in the Austrian Alps are analysed in a way to define vulnerability relations suitable for alpine buildings, as well as for people inside them. On the base of data on avalanche accidents occurred during outdoor winter activities over the Italian Alps in the last 20 years also a vulnerability relation for people directly exposed to avalanches is tentatively proposed. The empirical curves found in this study express the vulnerability as a function of avalanche dynamical parameters, such as velocity and flow depth, and can be easily implemented in a risk-analysis framework. However, more data on catastrophic avalanches are crucial to assess the validity of the result presented.

Keywords: snow avalanches, risk, vulnerability, study cases.

1 Introduction

Only very recently approaches based on formal risk analysis have emerged for analysing the potential effects of snow avalanches on mountain communities. A review of the various methods proposed for avalanche risk assessment is given in Barbolini *et al.* [2]. Regardless from the method adopted, two ingredients are essential for the estimation of avalanche risk: the hazard and the vulnerability, see [1]. The hazard component of risk can be calculated by different methods, based either on dynamical simulation models [3] or statistical analysis of historical data [4]. Conversely, the vulnerability component of risk is more difficult to assess, because of the paucity of suitable data to evaluate the effects of avalanches on people and properties.

Vulnerability relations for different categories of buildings are given in Whilelm [5], where susceptibility of buildings to damage is related to the avalanche extent (expressed in kNm^{-2}); however, the derivation of these curves is not supported by data from real avalanche accidents.

Concerning the vulnerability of people inside buildings Jónasson *et al.* [6] on the base of the data from the 1995 catastrophic avalanches at Sudavik and Flateyri, Iceland, proposed a relation between the survival probability inside a building and the avalanche speed. Using the same data set Keylock and Barbolini [7] and Barbolini *et al.* [2] proposed alternative vulnerability relations. These relations are suitable for Icelandic type of building, fairly weak timber or concrete houses with relatively large windows facing the mountain side, but their validity is questionable with respect to other types of buildings, such as the alpine ones.

The data on the avalanche victims outside buildings are few and poorly detailed. Some authors [8, 9] presented studies on the victims caused by avalanches during outdoor winter sports in which are reported the number of accidents that involved people, the number of victims and of injured people and their degree of burial under the snow. However, no vulnerability relations are inferred.

In this paper, on the basis of the data from two catastrophic avalanche events occurred in the Austrian Alps in 1988 and 1999, we derive two vulnerability relations to be used to estimate the risk for alpine buildings and for people inside them, respectively. Using the available data from literature we also attempt to formulate a vulnerability relation for people outside buildings.

2 The Data Set

2.1 The Wolfsgruben and Galtuer Avalanches

In the West Tyrol, Austria, in 1988 and 1999, two extraordinary events affected the villages of St. Anton and Galtuer, respectively (Figure 1).

The Wolfsgruben avalanche occurred on March 13th 1988 and reached the eastern part of St. Anton. The avalanche started on the NNW exposed slope of the Zwölferkopf at an altitude of about 2450 m a.s.l. The release mass was

approximately 52 kt. This avalanche was characterised by a predominant powder part that caused the major destruction [10]. Seven person were killed and 31 buildings damaged (Figure 2), two of them completely destroyed.

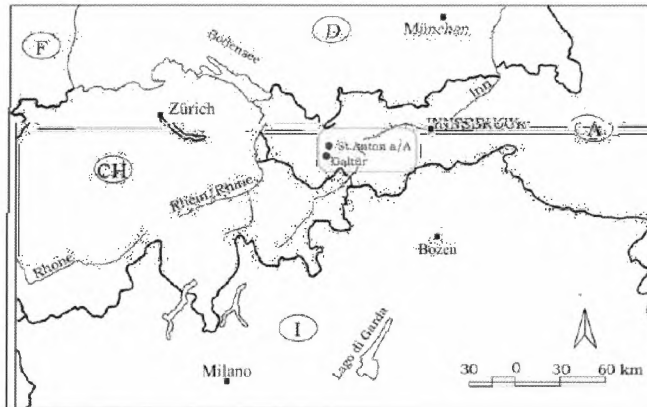


Figure 1: Geographical setting of the investigation area.



Figure 2: Deposit and damages caused by the Wolfsgruben avalanche.

A huge dry-snow slab avalanche affected the village of Galtuer on February 23rd 1999 [11]. The upper fracture line reached an altitude of 2700 m a.s.l. with a totally released mass of approximately 100 kt. About 60 persons were buried or thrown down by the avalanche, 31 persons were killed and 22 injured. The avalanche affected 24 buildings, among which 6 were completely destroyed and 7 heavily damaged (Figure 3).

The data used in this study have been made available by the Austrian Institute for Avalanche and Torrent Research. In particular, for both the avalanche events were known: (i) the buildings hit by the avalanche (in particular their structural features and the degree of damages suffered); (ii) the number of people inside each building; (iii) the number of victims and injured people (see Table 2).



Figure 3: A building destroyed by the Galtuer avalanche (Photo: WLV Tyrol).

2.2 Avalanche accidents in the Italian Alps

In Italy the data concerning the avalanche accidents to people are collected by different offices that operate at regional level in the Alps, whose tasks are mainly prevention of mountain accidents and rescue activities. Between 1983 and 2003 529 avalanches were documented; 1423 people were involved and 388 people lost their life [9] (Table 1).

Table 1: Summary of mountain avalanche accidents in Italy in the last 20 years, according to different degree of burial.

Degree of burial	No. people affected	No. of victims
Completely buried	498	322
Partly buried	398	66
Not buried	527	0

3 Vulnerability relations

3.1 Relations for buildings and people inside building

Among the numerous factors that may contribute to the vulnerability of a building affected by an avalanche and, as a consequence, of the people inside it, the structural features of the building and the dynamical features of the avalanche acting on it are the most important. Since the buildings of the two villages affected by the Wolfsgruben and Galtuer avalanches as a first approximation

may be considered to be of the same type (i.e. partly reinforced buildings), in this study attention is paid to the effect of the avalanche impact pressure on the degree of damage. In order to relate the dynamical characteristic of the events to the damages caused, the two events have been back-calculated with the avalanche simulation model SAMOS [12, 13], and the impact pressure of the avalanches at each affected building have been estimated (see Table 2).

The model simulation doesn't account for the mutual position of buildings and consequently for the "shielding" effect, that is the velocity and pressure decrease induced by the impact of the avalanche on a row (or more successive rows) of houses. Consequently, on the base of the mutual position of the affected houses, we have corrected some of the impact pressure values given by the simulations (Italic font in Table 2); a velocity reduction of 7.5 ms^{-1} per house row was adopted, according to the proposal of Jónasson *et al* [6]. The degree of damage (DD) of each building has been obtained from official Police reports and has been expressed in a scale 1-4, according to the definition of Table 3.

Table 2: Data considered in the study. No: building number, DD: degree of damage, Pimp: (powder component) impact pressure. Some of the affected houses are not reported in the Table, see text.

No.	DD	Pimp (kPa)	People inside building	Victim	No.	DD	Pimp (kPa)	People inside building	Victim
St.Anton buildings									
1a	4	21.1	16	5	25	1	<i>3.6</i>	16	0
1b	4	22.0	15	0	26	2	<i>4.2</i>	20	0
2	4	17.8	18	1	27	2.5	<i>11.2</i>	17	0
3	3	13.9	18	0	28	2.5	19.4	5	0
5	3	22.6	18	0	29	1.5	<i>5.8</i>	16	0
6	2	16.8	36	0	Galtuer buildings				
7	2	11.0	18	0	26	2.5	16.0	1	0
8	3	21.7	0	0	27	4	21.0	1	0
9	2.5	13.7	3	0	28	4	22.0	3	3
10	2	<i>4.1</i>	11	0	29	2.5	22.0	4	0
11	2	<i>4.6</i>	23	0	40	3.5	22.5	4	0
12	1	<i>4.2</i>	9	0	41	2	<i>5.8</i>	2	0
13	1	6.8	unknown	0	42	2	2.7	20	0
19	2.5	26.0	80	0	45	2.5	19.0	0	0
21	2	<i>11.8</i>	4	0	47	2.5	14.0	2	2
22	1.5	<i>15.7</i>	9	0	53	2.5	<i>8.8</i>	1	0
23	1	10.9	11	0	56	2	<i>8.6</i>	1	0
24	2	10.9	15	0	57	2	<i>3.5</i>	4	0

Table 3: Scale used for the degree of damage of buildings.

DD	Phenomena observed
4 (complete)	Partial or complete failure of the building
3 (heavy)	Heavy damage to structural elements
2 (medium)	Failed chimneys, attics or gable walls; damage or collapse of roof
1 (moderate)	No visible damage to structural elements, damage to frames, windows, etc.

20021048-11

The Galtuer Avalanche was a “mixed” avalanche: some of the buildings were hit both by the dense and by the powder component, some other only by the powder part. Where the dense-flow part reached the buildings the damages were due to the impact of both the powder and dense part, and it is very hard to distinguish between the two effects. For this reason, in this study (and in Table 2) we have considered the buildings of Galtuer affected by the powder component alone. Also in the case of the Wolfsgruben avalanche some damaged building have not been considered in the analysis, because they were located behind a dam whose protecting effect was not accounted for in the simulation, nor easily estimable by other ways.

3.1.1. Buildings

The vulnerability of buildings is defined as the ratio between the cost of repair and the building value, in the following referred as specific loss, SL . According to the proposal of Keylock *et al.* [14] the following relation between degree of damage (DD) and specific loss (SL) has been introduced:

$$SL = \frac{4DD^2}{64} \quad (1)$$

To obtain the vulnerability curve the buildings of Table 2 have been divided in five classes according to five pressure ranges (0-5 kPa, 5-10 kPa, 10-15 kPa, 15-20 kPa, >20 kPa) and an average value of SL has been estimated for each class. The average impact pressure and the average SL for each class have been plotted (Figure 4) and the points obtained have been fitted by a linear least square regression (the intercept term was found to be insignificant at a 5% level), obtaining the following relation:

$$SL = \begin{cases} 0.0297P_{imp} & \text{if } P_{imp} \leq 34 \text{ kPa} \\ 1 & \text{if } P_{imp} > 34 \text{ kPa} \end{cases} \quad (2)$$

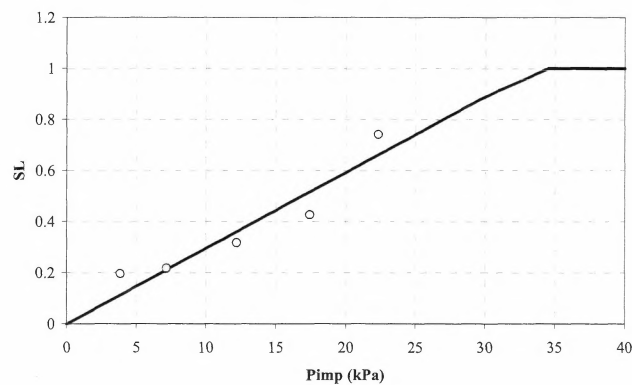


Figure 4: Vulnerability of buildings versus (powder) avalanche impact pressure: empirical values and best fitting line.

The vulnerability relation gives a SL that linearly increase from 0 to 1 as the impact pressure increase from 0 to 34 kPa. Reasonably, there is not a lower impact pressure threshold, that is even a very small impact pressure is considered able to produce some limited damage to the building. The upper threshold, corresponding to the destruction of the building, is found to be equal to about 34 kPa. This value is in good agreement with the value suggested by Wilhelm [5] as “destruction limit” for concrete reinforced buildings.

3.1.2. People inside buildings

The vulnerability for people inside buildings, in the following D_{in} , is defined as the probability of being killed by an avalanche if one stays inside a building when the accidents occurs. D_{in} has been calculated for each building dividing the number of victims by the number of people inside it (Table 2). The data have been divided in five classes according to the pressure ranges previously indicated (§ 3.1.1), and an average value of vulnerability has been calculated for each class. The average impact pressure and the average D_{in} for each class have been plotted (Figure 5), and the points obtained have been fitted by a linear last square regression, obtaining the following relation:

$$D_{in} = \begin{cases} 0 & \text{for } P_{imp} \leq 5 \text{ kPa} \\ 0.0094P_{imp} - 0.0508 & \text{for } 5 \text{ kPa} < P_{imp} < 34 \text{ kPa} \\ 0.27 & \text{for } P_{imp} > 34 \text{ kPa} \end{cases} \quad (3)$$

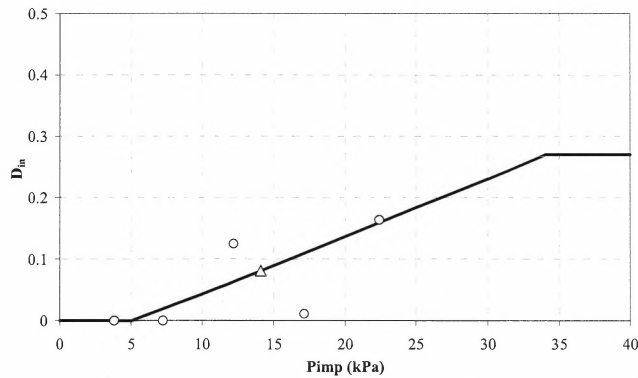


Figure 5: Vulnerability for people inside buildings versus (powder) avalanche impact pressure: empirical values and best fitting line (the triangle indicates the value of D_{in} obtained grouping the pressure classes 10-15 kPa and 15-20 kPa).

Concerning vulnerability of people inside buildings a lower threshold is obtained (5 kPa), which indicates the maximum value of impact pressure on the building according to which people inside it may be considered safe. This result is in accordance with the proposal of Barbolini *et al.* [2], who indicates zero

vulnerability for avalanche velocity lower than 3.5 ms^{-1} , and of Keylock *et al.* [14] who gives a null vulnerability for the smallest avalanche size (1 and 2 according to the Canadian Avalanche size Classification). The upper impact pressure threshold is set on the base of the one obtained for buildings (34 kPa): the destruction of the building should in fact led to the maximum value of vulnerability for people inside it. In this way a maximum value of D_{in} of about 0.3 is obtained; a person inside a destroyed house has a survival chance equal to about 70%. Wilhelm [5] suggested a probability of death lower than one for people inside a destroyed house, but gives a survival chance lower than ours (about 55%).

The vulnerability relations for people inside building available in literature refer to Icelandic type of buildings, which have characteristics different from the alpine one; moreover, they are obtained for dense-flow avalanches. Consequently, a comparison with our results is of doubtful meaning.

3.2 Relation for people outside buildings

To obtain a vulnerability relation for people outside buildings the idea is of relating the probability of being killed by an avalanche to the degree of burial, even conscious that the factors that bring to death are manifold (duration of burial, kind of snow, etc.). The degree of burial is then tentatively related to flow depth of the avalanche (h in the following).

Using the data of Table 1, the death probability outside buildings (in the following D_{out}) is calculated for each degree of burial class as the ratio between the number of death and the number of people involved in the accidents (see Table 4). The avalanche flow depths proposed for different degree of burial are given in Table 4. In particular we fixed: a flow depth equal to 2 m in the case of complete burial of people, assuming that for this to occur the flow depth should be at least as high as a person; a flow depth equal to 1 m (half of the previous depth) for people partially buried; a flow depth of 30 cm for people not buried, considering that even in the worst case this snow depth is insufficient to bury the head of a person.

Table 4: Probability of death for people outside buildings (D_{out}) versus avalanche flow depth (h)

Degree of burial	h (cm)	D_{out}
completely buried	200	0.65
partially buried	100	0.17
not buried	30	0

The vulnerability relation obtained by a linear last square regression through the point of Figure 6 was the following:

$$D_{out} = \begin{cases} 0 & \text{if } h \leq 40 \text{ cm} \\ 0.0039h - 0.1546 & \text{if } 40 \text{ cm} < h < 210 \text{ cm} \\ 0.65 & \text{if } h > 210 \text{ cm} \end{cases} \quad (4)$$

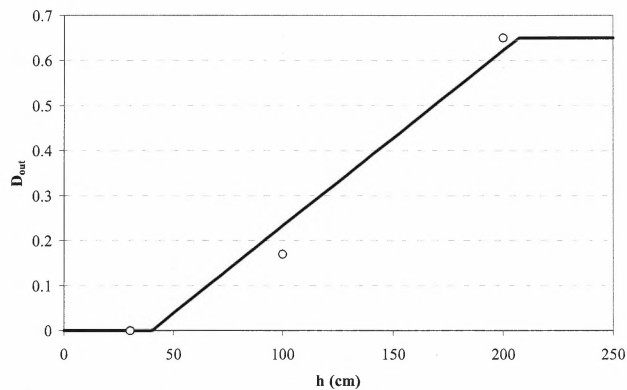


Figure 6: Vulnerability for people outside buildings versus avalanche flow depth.

4 Conclusions

In this paper empirical vulnerability relations have been derived on the base of data from real avalanche accidents. The curves proposed express the vulnerability (of buildings and people inside and outside buildings) as a function of avalanche dynamical parameters (impact pressure, flow depth), and can be easily implemented in the procedures for risk calculation in avalanche prone areas.

Relations proposed for buildings and people inside them are the first referring to alpine-type of buildings based on real avalanche. However, they have been obtained only with respect to powder avalanches. Despite the great practical relevance this type of avalanche has in alpine countries (especially in Austria and Switzerland), this fact represent a partial limitation of this work.

Moreover, vulnerability relations for people (either inside or outside buildings) are based on a limited amount of data and to some degree on subjective assumptions (such as the relation proposed between burial depth and avalanche flow depth). Furthermore, the survival probability of a person affected by an avalanche (either directly exposed or inside a building) is inherently influenced by fortuitous factor, that would need a proper statistical treatment.

Therefore, more data are needed to validate the results of our study as well as to extend the analysis to dense-flow avalanches; the availability of a larger data set will allow also the inclusion of uncertainties in the vulnerability analysis.

References

- [1] IUGS (International Union of Geological Sciences) Working Group on Landslides, Committee on Risk Assessment. Quantitative risk assessment for slopes and landslides - the state of the art. *Proc. Int. Workshop on Landslide Risk Assessment*, 19-21 February 1997, Honolulu, Hawaii, U.S.A. Cruden D.M. & R. Fell Ed., A.A. Balkema, Rotterdam, pp. 3-12, 1997.
- [2] Barbolini, M., Cappabianca, F. & Savi, F. Risk assessment in avalanche prone areas. *Annals of Glaciology*, In Press.
- [3] Barbolini, M., Cappabianca, F., & Savi, F. A New Method for Estimation of Avalanche Distance Exceeded Probabilities. *Surveys in Geophysics* **24**(5-6), pp. 587-601, 2003.
- [4] Barbolini, M. & Cappabianca, F. Determinazione della relazione tra distanze di arresto e tempi di ritorno delle valanghe: un nuovo metodo basato sull'analisi statistica dei dati storici. *Neve e Valanghe* **46**, pp. 12-20, 2002.
- [5] Wilhelm, C. Quantitative risk analysis for evaluation of avalanche protection projects. *Proc. of 25 Years of Snow Avalanche Research at NGI*, Voss 12-16 May 1998, Hestness, E. Ed., NGI Publications 203, Oslo, pp. 288-293, 1998.
- [6] Jónasson, K., Sigurdson, S. & Arnalds, P. Estimation of Avalanche risk. *Vedurstofu Islands* n. R99001-UR01, 1999.
- [7] Keylock, C.J. & Barbolini, M. Snow avalanche impact pressure/vulnerability relations for use in risk assessment. *Can. Geotech. J.*, **38**, pp. 227-238, 2001.
- [8] Tschirky F., Brabec, B. & Kern, M. Avalanche rescue system in Switzerland: experience and limitation. *Proc. Int. Snow Science Workshop*, Blue Sky, MT, USA, 1-6 October 2000, pp. 369-376, 2000.
- [9] Valt, M., Cagnati, A. & Crepaz, A. Gli incidenti da valanghe in Italia. *Neve e Valanghe* **49**, pp. 9-13. 2003.
- [10] Gabl, K. Das Lawinenereignis im März 1988 in St. Anton am Arlberg aus meteorologischer Sicht. In *FBVA Berichte. Schriftenreihe der Forstlichen Bundesversuchsanstalt*, Wien, pp. 97-107, 1992.
- [11] Heumader, J. The catastrophic avalanche disaster of Galtuer and Valzur on the 23rd and 24th of February 1999 in the Paznaun Valley, Tyrol. In *Proc. Int. Workshop on Hazard Mapping in Avalanching Areas*, 2-7 April 2000, St. Christoph, Tyrol, Austria, IUFRO Div. 8, pp.179-187, 2000.
- [12] Sailer, R. Case studies with SAMOS - Comparison with observed avalanches. *AVL - Advanced Simulation Technologies, International User Meeting 2003*, 2003.
- [13] Sampl, P. & Zwinger, T. A simulation model for dry snow avalanches. *Proc. XXVIII IAHR Congress*, 22-27 August, 1999, Graz, Austria, 1999.
- [14] Keylock, C.J., McClung, D.M. & Magnússon, M.M. Avalanche risk mapping by simulation. *J. Glaciol.*, **45**(150), pp. 303-314, 1999.

A.4 Published Paper Without Peer-Review (2)

Issler, D., C. B. Harbitz, K. Kristensen, K. Lied, A. S. Moe, M. Barbolini, F. V. De Blasio, G. Khazaradze, J. N. McElwaine, A. I. Mears, M. Naaïm and R. Sailer. 2005. Comparison of avalanche models as applied to dry-snow avalanches observed in the full-scale test site Ryggfonn, Norway. *In*: K. Senneset, K. Flaate and J. O. Larsen (eds.), *Landslides and Avalanches. ICFL 2005 Norway*. Proc. 11th Intl. Conf. and Field Trip on Landslides, Norway, 1–10 Sept. 2005. Taylor & Francis/Balkema, Leiden, The Netherlands. Pages 173–179.

A comparison of avalanche models with data from dry-snow avalanches at Ryggfonn, Norway

D. Issler, C. B. Harbitz, K. Kristensen, K. Lied & A. S. Moe

Norwegian Geotechnical Institute, P.O. Box 3930 Ullevål Stadion, N-0806 Oslo, Norway

M. Barbolini

Univ. of Pavia, Hydraulics and Environmental Engineering Dept., Via Ferrata 1, I-27100 Pavia, Italy

F. V. De Blasio

*Inst. for Geosciences, University of Oslo, P.O. Box 1047 Blindern, N-0316 Oslo, Norway and
International Centre for Geohazards, c/o NGI, P.O. Box 3930 Ullevål Stadion, N-0806 Oslo, Norway*

G. Khazaradze

Univ. of Barcelona, Dept. of Geodynamics and Geophysics, c/ Martí i Franquès s/n, E-08028 Barcelona, Spain

J. N. McElwaine

*Dept. of Applied Mathematics and Theoretical Physics, Centre for Mathematical Sciences,
Cambridge University, Wilberforce Road, Cambridge, CB3 0WA, UK*

A. I. Mears

555 County Road 16, Gunnison, Colorado 81230, USA

M. Naaim

CEMAGREF, Division ETNA, 2 rue de la Papeterie, F-38402 St-Martin-d'Hères, France

R. Sailer

Austrian Institute for Avalanche and Torrent Research, Hofburg, Rennweg 1, A-6020 Innsbruck, Austria

ABSTRACT: Twelve well-documented dry-snow avalanches from the instrumented Ryggfonn path in western Norway were selected for back-calculations with several dynamical avalanche models. In each case, the run-out distance, the front velocity in the lower track, the extent of the deposits and the depth profile along a line are known. A 16 m high and 100 m wide retention dam in the run-out zone is often overflowed by avalanches but retains a considerable fraction of their mass. The tested models comprise a quasi-analytic block model, two 1D hydraulic models, a particle model with entrainment, and SAMOS, an advanced 2D/3D two-layer model. For each model, a wide range of friction parameters was needed to reproduce the twelve events, and none of the models matches the deposit distributions of all avalanches with fair accuracy. Explicit representation of the intermediate-density layer in dry-snow avalanches and accurate numerical schemes are expected to improve the modelling of dam interactions.

1 INTRODUCTION

As a geotechnical material, snow has striking similarities with other soil types, especially clay, but also several decisive differences. Compared to landslides, snow avalanches are a very frequent phenomenon, yet the return period of extreme avalanches is beyond individual memory and the traces of avalanches are not as clearly preserved as e.g. debris-flow deposits. Protection of settlements by means of land-use planning therefore usually requires extrapolation from a short observation period to return periods of several hundred years. Technical measures like catching and deflecting dams are sometimes cost-effective protection schemes but dimensioning them optimally also depends on sound knowledge of the dynamical properties of extreme avalanches. A multitude of dy-

namical avalanche models have been developed over the past 50 years (Harbitz 1998) and measurements on full-size avalanches and laboratory flows carried out for 40 years. With many open questions still remaining in avalanche dynamics, current work aims at a deeper understanding of the basic avalanche processes through detailed measurements in the field and the laboratory, and at improving models on this basis. Among other things, the latter should be capable of realistically simulating the interaction with dams.

As part of co-ordinated efforts at the European level, NGI operates a full-scale instrumented test site in the Ryggfonn avalanche path in western Norway, which features a 16 m high and 100 m wide catching dam in the run-out zone. In order to assess the capabilities and limitations of existing models in a re-

alistic context, we selected twelve well-documented dry-snow avalanches from the 1983–2000 Ryggfonn data and five avalanche models that are currently in use for hazard mapping and represent different levels of complexity. For each of the models and each of the twelve avalanches, we determined the optimum friction parameters for simulating the measured run-out distance and velocity. The same initial conditions and parameters were then used to obtain the model predictions for the run-out distance and deposit geometry if there were no dam. Obviously, we do not know Nature’s “true” answer, but the differences in the impact behaviour of the five models are clearly highlighted.

2 MAIN FEATURES OF THE MODELS

The earliest avalanche models described the motion of a point of mass M on a slope $z(x)$ according to Newton’s equation $Ma = Mg \sin \phi - F_f$, where $a = dv/dt$ is the acceleration along the slope, g the gravitational acceleration, ϕ the local slope angle and F_f the friction force, which needs to be specified in terms of M , g , v and ϕ . A simple extension is the *Flexible Sliding Block* (FSB) model that considers an avalanche as a perfectly flexible slab of fixed length l . Its centre of mass obeys formally the same equation of motion, but ϕ , F_f (and the curvature κ , see below) are to be considered means over the path segment presently occupied by the avalanche. The FSB model includes dry friction proportional to the apparent weight (taking into account centrifugal forces) and “turbulent” friction or drag:

$$F_f = \text{sgn}(v)M \left[\mu \cdot \left(g \cos \phi + \kappa v^2 \right) + \frac{v^2}{\Lambda} \right]. \quad (1)$$

The drag term is assumed proportional to the avalanche mass and $\Lambda = \mathcal{O}(10^3 \text{ m})$ is the length scale over which the kinetic energy decays due to drag. The solution of the equation of motion can be expressed in terms of quadratures.

One-dimensional hydraulic models like VARA-1D (Natale et al. 1994) and NIS (Norem et al. 1989) are the most frequently used in practical applications today. The depth-integrated mass and momentum balance equations have the structure

$$\frac{\partial h}{\partial t} + \frac{\partial(hu)}{\partial s} = w_e, \quad (2)$$

$$\frac{\partial(hu)}{\partial t} + \frac{\partial(fh u^2)}{\partial s} = gh \sin \phi + \frac{\partial(h\tilde{\sigma}_s)}{\partial s} - \tilde{\tau}_b. \quad (3)$$

where s is the distance along the curved path, h is the flow height, u the depth-averaged velocity, w_e the snow-entrainment rate per unit density (neglected in most models). The Boussinesq coefficient f depends on the velocity profile; $f = 1$ in VARA-1D

and $f = 5/4$ in NIS. Many models, like VARA-1D, assume the depth-averaged longitudinal stress per unit density to be hydrostatic, $\tilde{\sigma}_s = -(h/2)g \cos \phi$. Various formulations have been proposed for the bed shear stress τ_b . In VARA-1D, the usual Coulomb dry-friction term is accompanied by a drag term proportional to the velocity squared; note that it is not proportional to the flow depth, in contrast to the FSB model (1):

$$\tilde{\tau}_b = \text{sgn}(u)(\mu gh \cos \phi + ku^2), \quad (4)$$

where $k \sim 5 \cdot 10^{-3}$ is an adjustable parameter.

The NIS model recognizes the granular nature of avalanches and represents the bed-normal stress as the sum of effective and dispersive stresses; it is assumed that the latter is proportional to the square of the shear rate. Besides the Coulomb friction proportional to the effective normal stress (including centrifugal effects), there is also a dispersive contribution to the shear stress. In practical applications, only a restricted implementation of the full NIS model is used; the bottom shear stress then reduces to (Lied et al. 2004, pages 33–37))

$$\tilde{\tau}_b = \text{sgn}(v) \left(\mu gh \cos \phi + \left(\frac{\alpha_2}{h^2} + \kappa \mu h \right) u^2 \right), \quad (5)$$

and the longitudinal normal stress is not hydrostatic:

$$\tilde{\sigma}_s = (1 - (\tan \phi - \mu)\alpha_1) \frac{h}{2} g \cos \phi. \quad (6)$$

Typical parameter values are $\mu \sim 0.3$, $m \sim \alpha_2 \sim 10^{-3} \text{ m}^2$ and $\alpha_1 \sim 10$.

The PLK model (Perla et al. 1984) describes avalanches as collections of snow blocks, each of which obeys the equation of motion

$$\frac{dv}{dt} = g \sin \phi - \text{sgn}(v) \left(\mu g \cos \phi + \frac{v^2}{\Lambda} \right) \pm bv. \quad (7)$$

The last term, with the sign chosen stochastically, represents interaction of a block with its neighbours, b being a measure of the collision frequency. A user-determined number of particles per unit length is added to the system as the front advances. An (ad hoc) assumption important in connection with dam impacts is that, at concave slope changes, the original momentum component normal to the new slope is lost.

SAMOS (Sampl & Zwinger 2004) combines a 2D depth-averaged dense-flow model with a 3D powder-snow avalanche model. The dense part of the flow is a Lagrangean implementation of the Savage–Hutter model (Savage & Hutter 1991) at low velocities; above a threshold determined by the dispersive stresses a drag term replaces the dry-friction term. Snow entrainment and the effect of path curvature on dry friction are taken into account. In contrast to the other models, a digital terrain model was used in the simulations.

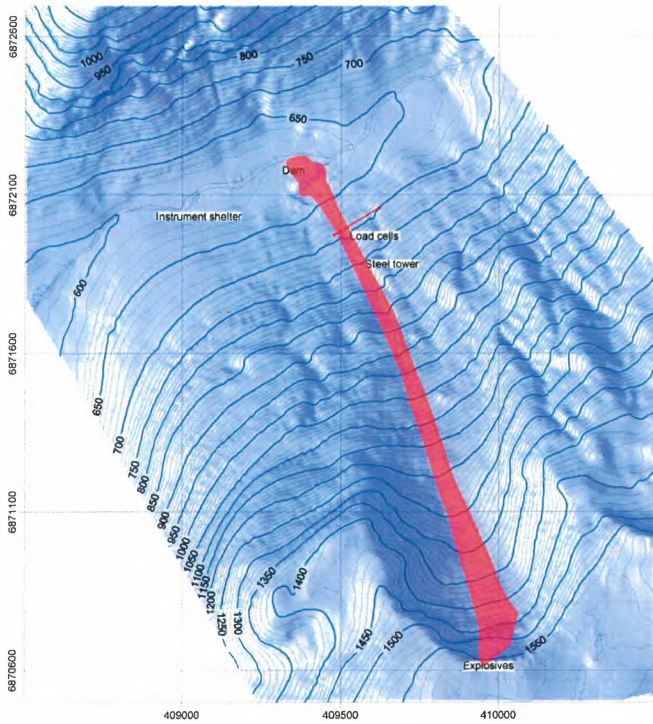


Figure 1: Overview map of the Ryggfonn avalanche path with the dam and deposit area of the avalanche event 3. The co-ordinates at the left and bottom sides are in meters, north is towards the top of the figure.

3 THE RYGGFONN AVALANCHES

Located near Stryn in western Norway at an altitude from 1500 to 600 m a.s.l., the Ryggfonn full-scale avalanche test site (Figure 1) has been in operation since 1980. Avalanches starting in the bowl-shaped release zone are channelled in the track before they begin to spread laterally on an alluvial fan and impact on a 100 m wide and 16 m high catching dam in the run-out zone after a horizontal travelling distance of approximately 1600 m. The deposit volume of observed avalanches ranges from 10,000 m³ to 500,000 m³, the maximum velocities reach up to 60 m s⁻¹. From the avalanche arrival times at two pressure-measurement locations 320 and 230 m upstream from the dam, the front velocity can be determined, albeit with some uncertainty because sensors of different sensitivity were used prior to 2002.

For the present study, we selected twelve dry-snow avalanches for which surveys providing estimates of the release area, fracture depth, runout length, deposit area and volume had been carried out (Table 1). All the selected avalanches hit the dam, and either were stopped by it or over-topped it. The snow density in the release area was extrapolated from NGI's snow measurement station at Fonnbu, located a few kilometers away at an elevation of 920 m a.s.l. The initial conditions for the simulations are thus known with reasonable accuracy.

Some of the avalanches occurred after earlier

Table 1: Ryggfonn avalanches used in the numerical simulations. The over-run length is measured from the downstream base of the dam, with estimated values for the thick deposits in parentheses. The avalanche volume refers to the estimated release volume.

No.	Overrun (m) all	Overrun (m) core	Freebd. (m)	Volume (10 ³ m ³)	Velocity (m s ⁻¹)
1	148	?	14	100	46
2	-22	-22	13	45	23
3	48	?	16	20	34
4	203	-20	14	70	48
5	23	-20	16	40	38
6	38	38	15	75	31
7	48	-20	15	30	43
8	151	?	6	20	35
9	29	-5	16	40	33
10	58	?	15	20	35
11	173	70	5	100	45
12	311	150	5	80	49

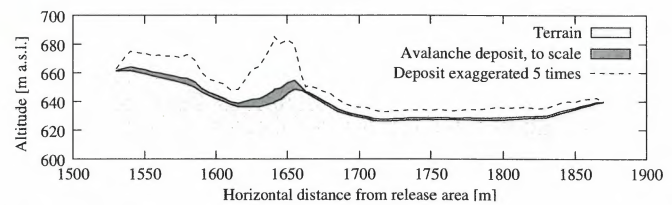


Figure 2: Deposit profile of the avalanche event 12 drawn to scale (shaded) and five times exaggerated (dashed line).

avalanches had partially filled up the retention volume upstream of the dam. On the one hand, this made it easier for the next avalanche to overtop the dam, but on the other hand the friction on the old deposit may have been significantly increased. Table 1 records the freeboard for each event, i.e. the vertical distance between the snow surface at the dam foot and the top of the dam. With release volumes from 20,000 m³ to 100,000 m³ and front velocities from 23 m s⁻¹ to 49 m s⁻¹, the selected avalanches span a wide range of sizes.

Important information about the behaviour of a model at the dam is contained in the deposit distribution. For each of the twelve avalanches, the deposit depth was measured along a line crossing the dam, and the edges of the deposits were mapped (Figures 1 and 2); all maps and profiles are presented in (Lied et al. 2004, pages 25–98). Many of the profiles show deep deposits (up to 18 m) only to a certain point—most often the dam—and a rather abrupt decrease to 2 m or even much less just downstream from that point. This deposit structure may indicate the presence of two different flow regimes in these avalanches, namely a dense, relatively slow core preceded by a dilute, fluidised layer moving at much higher speed (Schaerer & Salway 1980; Schaer & Issler 2001). (The deposits from the suspension layer were not mapped.) The deep deposits of avalanches

20021048-11

Table 2: Optimum parameter values for simulating the twelve Ryggfonn avalanches. The drag terms were transformed to a canonical form with a dimensionless coefficient k by dividing by appropriate powers of the release height. The much higher k -value for SAMOS reflects the fact that this model switches between dry friction and “turbulent” drag according to the local dispersive pressure.

No.	FSB		VARA-1D		NIS		PLK		SAMOS	
	μ	10^3k	μ	10^3k	μ	10^3k	μ	10^3k	μ	10^3k
1	0.35	1.7	0.39	0.2	0.40	1.5	0.25	1.9	0.34	22
2	0.26	6.1	0.17	2.3	0.39	3.3	0.25	4.1	0.49	22
3	0.35	2.6	0.41	0.3	0.28	3.4	0.20	3.0	0.36	22
4	0.25	1.9	0.20	0.5	0.25	1.3	0.30	3.6	0.29	22
5	0.49	0.5	0.41	0.3	0.33	2.1	0.30	2.8	0.42	22
6	0.32	3.6	0.42	0.3	0.42	2.8	0.25	3.2	0.45	22
7	0.51	0.1	0.41	0.3	0.42	0.8	0.30	3.2	0.45	22
8	0.20	3.1	0.28	0.5	0.24	3.0	0.25	2.4	0.27	22
9	0.38	2.4	0.41	0.1	0.32	2.5	0.25	3.0	0.40	22
10	0.34	2.4	0.42	0.2	0.38	2.2	0.25	3.5	0.36	22
11	0.28	1.8	0.28	0.5	0.32	1.6	0.25	2.4	0.36	22
12	0.06	3.1	0.10	0.6	0.18	2.0	0.25	1.0	0.19	22
Average	0.32	2.4	0.33	0.5	0.33	2.2	0.26	2.8	0.37	22
Standard deviation	0.12	1.5	0.12	0.6	0.08	0.8	0.03	0.8	0.09	0

11 and 12 extend to the river and to the foot of the opposite slope, respectively. The corresponding over-run lengths are about 70 m instead of 173 m and 150 m instead of 311 m, respectively. Present-day models do not distinguish these flow regimes, therefore the run-out distance of the fluidised layer was used in calibrating the models in this study. Reanalysis of pressure data from Ryggfonn indicates that the density in the head of dry-snow avalanches tends to be below 100 kg m^{-3} and that the velocity decays steadily after passage of the head while the density increases (P. Gauer, pers. comm.).

The mapped outlines of the avalanches presented in (Lied et al. 2004) show that the lateral spreading of the avalanche debris around the dam differs considerably between events. This is not very surprising because it is expected to depend on a number of highly variable factors like the location and width of the release area, the flow velocity, the snow properties and earlier deposits. Among the compared models, only the 2D code SAMOS is in principle able to take these effects into account. No simple relation between speed, volume, runout and spread-out ratio has been found so far. As an example, avalanche 1 with a volume of $100,000 \text{ m}^3$, velocity 46 m s^{-1} and over-run length of 148 m showed almost no spread whereas avalanche 11, which had about the same volume, over-run length and velocity, doubled its width over the last 150 m. The extreme case is avalanche 4, whose width increased nearly four-fold.

4 SIMULATION RESULTS

For each of the five models and each of the twelve avalanches, we determined the best combination of

friction parameters for matching the observed run-out distance and front velocity. With these values, the run-out distance on a modified path profile with the freeboard of the dam removed was calculated. The details of the simulation procedure varied somewhat between models due to differences in their input requirements and resource needs. For the quasi-analytic FSB model, the dry-friction coefficient μ was obtained in terms of the dimensionless drag coefficient k for each avalanche. One thousand simulations per avalanche were performed with VARA-1D. With NIS, the parameter space was scanned as well, but with fewer simulations. In the PLK runs, the parameters were optimised starting from their values used in practical hazard mapping. SAMOS requires very substantial computational resources so that only a few simulations could be carried out for each avalanche; the internal friction angle and the dynamic friction coefficient were kept fixed at $\phi = 35^\circ$ and $k = 0.022$, respectively, and only the base friction angle $\delta = \arctan \mu$ was varied. The SAMOS simulations represent mixed dense-flow/powder-snow avalanches, but only the dense part was considered for velocities, run-out distances and parameter optimisation.

In order to allow (semi-quantitative) comparison of the optimum parameters between models (Table 2), the drag terms were transformed to have the same structure, with a non-dimensional drag coefficient k , by scaling them with the appropriate power of the release depth. The parameter sets that best reproduce the observed events at Ryggfonn are much less pessimistic than the parameters recommended for predicting extreme avalanches in Switzerland using a model quite similar to VARA-1D (Bartelt et al. 1999). We cannot conclusively explain this discrepancy but

Table 3: Observed and simulated deposit distributions: Estimated percentage of mass stopped above the downstream foot of the dam. For each model the numbers in the right column refer to simulations with the same model parameters, but without a dam.

No.	Meas. (%)	FSB		VARA-1D		NIS		PLK		SAMOS	
		(%)	(%)	(%)	(%)	(%)	(%)	(%)	(%)	(%)	(%)
1	67	0	0	23	6	16	11	57	5	20	16
2	100	100	62	100	95	100	83	100	10	100	95
3	87	55	39	70	53	44	30	9	9	70	50
4	79	0	0	16	9	0	0	65	11	14	11
5	91	80	56	85	76	95	90	100	7	99	86
6	87	65	46	70	60	72	62	61	5	85	84
7	90	9	0	64	56	34	31	93	9	90	84
8	64	0	0	27	21	0	0	16	8	26	18
9	94	74	55	75	60	94	89	95	8	92	67
10	75	45	30	54	38	36	28	97	7	88	68
11	65	0	0	8	4	0	0	14	7	38	25
12	38	0	0	11	9	0	0	11	11	4	3

note that (i) except for the largest avalanches in our sample, the return periods are less than five years, and (ii) the dissipative effect of the dam is underestimated in these models (except by PLK), so higher friction values along the entire path must be used to compensate for this deficiency.

Except for the very highly fluidised avalanche 12, the observed run-out distances could generally be matched fairly well by all models. Significant discrepancies occurred for the front velocity, with deviations as large as 10 m s^{-1} in some cases. Unfortunately, the front velocity data are not precise enough to blame only the models for the discrepancies. The average dry-friction coefficient over all twelve avalanches was close to 0.32 with a standard deviation between 0.08 and 0.12 for most models. In the case of the calibration of the PLK model, the parameters were chosen as close as possible to those found in extensive consulting experience. This fact explains the somewhat lower value of μ together with an elevated value of k as well as the smaller range of both these parameters in the PLK model. (This choice reflects itself also in a poorer match of the velocity compared to the other models.) It is likely that the parameter range of the other models could also be reduced if similar preferences were imposed during calibration.

From Table 3 it is apparent that most simulations underestimated the retention ratio, i.e. the fraction of avalanche mass stopped upstream of the downstream foot of the dam, even though the run-out distance and the velocity in the lower track were tuned to the measured values. About 30% of the simulations gave a mass distribution close to the observed one, in 10% of the cases the retention ratio was overestimated, and it was too small in about 60%. For six of the twelve avalanches, at most one estimate was correct, all others being too low. The only readily recognizable trend in the discrepancies between model results and obser-

Table 4: Shortening of simulated run-out distances due to the presence of the dam. For each event and model, the same parameters were used as in the corresponding optimized simulation with the dam.

No.	Freebd. (m)	FSB (m)	VARA-1D (m)	NIS (m)	PLK (m)	SAMOS (m)
1	14	-2	0	39	222	30
2	13	63	15	57	129	25
3	16	16	10	40	171	15
4	5	-4	0	59	13	55
5	16	24	40	1	71	105
6	14	19	20	28	136	5
7	14	11	15	36	88	40
8	5	-15	0	36	46	15
9	16	19	15	4	164	20
10	15	14	10	39	106	35
11	5	-6	0	44	34	0
12	5	-5	0	36	36	0
Avg.		11	10	35	101	29

vations is that FSB, VARA-1D and NIS generally predict too low retention ratios while PLK and SAMOS overestimate them in certain cases. Underestimation of the retention ratio by FSB and NIS may be linked to an underestimation of the longitudinal spreading of the avalanche—since the run-out distance was forced to agree with observations, the deposits were concentrated too far downstream.

After the optimum parameters had been determined for each combination of avalanche event and model, the same parameter set was applied with the same initial conditions, but on a terrain profile from which the freeboard of the dam had been removed (Tables 3 and 4). The “correct” run-out shortening due to the dam is not known, of course, but the tables highlight how differently the models react to a large object in the path.

The energy dissipation due to Coulomb friction is

20021048-11

insensitive to the dam (if the avalanche is fast enough to overtop the dam); also, the drag effects do not differ much with or without the dam. Accordingly, VARA-1D predicts a mere 10 m of run-out shortening on average. The PLK model exhibits very pronounced run-out shortening with about 100 m on average: The ad hoc prescription for momentum reduction in concave bends reduces the kinetic energy to roughly one quarter of its value before the dam. A more physical approach is to account for the centrifugal effects in bends (FSB, NIS, SAMOS); friction increases in the concave bends at the foot of the dam and decreases it in convex ones at the crown, but to a lesser degree because the velocity is smaller there. The net extra dissipation of energy per unit mass at the dam is (Lied et al. 2004, page 50)

$$\Delta E \approx -4\mu g H \alpha = \mathcal{O}(-gH), \quad (8)$$

where the deflection angle α is about 40° and $H \leq 16$ m at Ryggfonn. With $\mu \sim 0.4$, this translates into a run-out shortening of about 40 m in the case of full freeboard. This estimate is reasonably well confirmed by the NIS and SAMOS, but not the FSB calculations.

5 CONCLUSIONS

Several conclusions relevant to avalanche hazard mapping and future model development can be drawn from our restricted study. First, the range of friction and drag parameters needed to reproduce different avalanches in the same track is extremely wide. ‘‘Blind’’ application of models may lead to completely wrong results; automated generation of detailed hazard maps is inadmissible with present-day models.

Second, future models should allow for flow-regime changes in order to describe the fluidised layer observed in front of many if not all dry-snow avalanches. This may both improve the modelling of the pressure distribution in the run-out zone and narrow the range of friction parameters needed for reproducing observations.

Third, the power of current personal computers allows very rapid 1D computations of avalanche flow; hence there is little need to further use block models like FSB. Even though 2D simulations are now also quite feasible on PCs, the effort required for input preparation for the time being still limits their application to situations where an avalanche may split in several branches or chose its path depending on the velocity. e.g. on alluvial fans or in bends of shallow channels.

Finally, so-called conservative formulations of the balance equations should be combined with shock-capturing numerical schemes (Tai et al. 2002) to account for shocks that develop in the impact of granular flows on obstacles (Hákonardóttir et al. 2003). First results from such codes (Gray et al. 2003) appear very promising.

ACKNOWLEDGEMENTS

This work was funded by the European Union 5th Framework Programme through the project SATSIE (EU Contract no. EVG1-CT2002-00059) and by the Norwegian Geotechnical Institute.

REFERENCES

- Bartelt, P., Salm, B. & Gruber, U. (1999). Calculating dense snow avalanche runout using a Voellmy-fluid model with active/passive longitudinal straining. *J. Glaciol.* 45(150): 242–254.
- Gray, J. M. N. T., Tai, Y.-C. & Noelle, S. (2003). Shock waves, dead-zones and particle-free regions in rapid granular free surface flows. *J. Fluid Mech.* 491: 161–181.
- Hákonardóttir, K. M., Hogg, A. J., Jóhannesson, T. & Tómasson, G. G. (2003). A laboratory study of the retarding effects of braking mounds on snow avalanches. *J. Glaciol.* 49(165): 191–200.
- Harbitz, C. (1998). A survey of computational models for snow avalanche motion. NGI Report 581220-1. Oslo, Norway: SAME Collaboration/Norwegian Geotechnical Institute.
- Lied, K., Moe, A., Kristensen, K. & Issler, D. (2004). Ryggfonn. Full scale avalanche test site and the effect of the catching dam. In M. Naaim and F. Naaim-Bouvet (eds), *Snow and avalanches test sites*. Proc. Intl. Seminar on Snow and Avalanches Test Sites in the Memory of Philippe Revol, Grenoble 22–23 November 2001: 25–98. Antony, France: Cemagref Editions.
- Natale, L., Nettuno, L. & Savi, F. (1994). Numerical simulation of snow dense avalanche: an hydraulic approach. In M. H. Hamza (ed.), *Proc. 24th Intl. Conf. on Modeling and Simulations, 2–4 May 1994, Pittsburgh, Pennsylvania*: 233–236. Anaheim, California: IASTED.
- Norem, H., Irgens, F. & Schieldrop, B. (1989). Simulation of snow-avalanche flow in run-out zones. *Annals Glaciol.* 13: 218–225.
- Perla, R., Lied, K. & Kristensen, K. (1984). Particle simulation of snow avalanche motion. *Cold Regions Sci. Technol.* 9: 191–202.
- Sampl, P. & Zwinger, T. (2004). Avalanche simulation with SAMOS. *Annals Glaciol.* 38: 393–398.
- Savage, S. B. & Hutter, K. (1991). The dynamics of avalanches of granular material from initiation to runout. Part I: Analysis. *Acta Mechanica* 86: 201–223.
- Schaer, M. & Issler, D. (2001). Particle densities, velocities, and size distributions in large avalanches from impact-sensor measurements. *Annals Glaciol.* 32: 321–327.
- Schaerer, P. A. & Salway, A. A. (1980). Seismic and impact-pressure monitoring of flowing avalanches. *J. Glaciol.* 26(94): 179–187.
- Tai, Y. C., Noelle, S., Gray, J. M. N. T. & Hutter, K. (2002). Shock-capturing and front-tracking methods for granular avalanches. *J. Comp. Phys.* 175(1): 269–301.

A.5 Paper Submitted to Peer-Reviewed Journal(1)

Gauer, P., D. Issler, K. Lied, K. Kristensen, H. Iwe, E. Lied, L. Rammer, and H. Schreiber. 2005. On avalanche full-scale measurements at the Ryggfonn test site, Norway. Submitted to *Cold Regions Science and Technology* (EGU 2005 special issue).

20021048-11

On avalanche full-scale measurements at the
Ryggfonn test site, Norway

Peter Gauer^{1,2*}, Dieter Issler^{1,2}, Karstein Lied¹,
Krister Kristensen¹, Harald Iwe^{1,2}, Erik Lied¹,
Lambert Rammer³, and Helmut Schreiber⁴

¹Norwegian Geotechnical Institute, Oslo

²International Centre for Geohazards, c/o NGI

³Austrian Institute for Avalanche and Torrent Research, Innsbruck

⁴Institute for Communication Technology and Wave Propagation, TU Graz

June 28, 2005

*Corresponding authors address:

Peter Gauer

Norwegian Geotechnical Institute, Postbox 3930 Ullevål Stadion, N-0806 Oslo, Norway

Tel: ++47 22 02 31 29; Fax: ++47 22 23 04 48; E-mail: pg@ngi.no

ABSTRACT. Avalanche measurements from several winter seasons are analyzed with emphasis on recognizing different flow regimes and estimating flow densities. Measurements include impact pressure readings from load cells mounted at two locations within the track and stress readings from load plates buried in the upstream slope of a catching dam. The combination of pressure measurements and velocity estimates based on cross correlations between the load cell readings and, in several cases, on Doppler radar measurements allowed to gain some insight into the spatial structure of the avalanches. In most cases a saltation (fluidized) layer in front of a more dense part could be identified. Doppler radar measurements confirm a fast moving head, in some instants preceded by a slower snout, and decreasing speed behind the head up-to the tail. Calculated accelerations (decelerations) indicate that the effective friction parameter varies strongly and depends on the flow regime.

Keywords: avalanche, full-scale measurements, impact pressure, shear stress, velocity, acceleration

1 INTRODUCTION

Measurements and observations from full-scale avalanches are indispensable for fully understanding the flow behavior of avalanches. They form the basis for the basis for developing and calibrating models. Full scale measurements provide information on the scaling behavior of avalanches and so they are a control for small scale experiments, like chute or water tank experiments. However, full-scale experiments are expensive and time consuming. Unlike laboratory experiments, they are only controllable to a certain degree. Local topography and varying snowpack properties

are setting the initial and boundary conditions. Their reproducibility is limited, qualitatively as well as quantitatively.

In addition, harsh conditions within an avalanche make measurements a difficult task. Accessibility to the avalanche path prior to a release is usually limited. Sensors have to be placed long a time before an event and might be buried by the time due to previous events. The knowledge of the sensor status is important, a fact that limits the reliability of automatic measurements.

To gain information on the flow behavior, information from different measurements and observations must be combined. This is not always straightforward and might need some subjective interpretation, which leaves some uncertainty.

Previous full-scale measurements were reported, e.g., in (Schaerer and Salway, 1980; McClung and Schaerer, 1985), providing information on impact pressure at load cells and their relation to the front velocity as well as on the flow structure from avalanches at Rogers Pass / British Columbia. Norem and others (1985) presented pressure measurements and front velocities for several avalanches at Ryggfonn. In addition, they report on forces on cables due to the powder part of an avalanche. Radar measurements of velocities from dense flow avalanches are reported in (Gubler, 1987; Schreiber and others, 2001) coming from Lukmanier / Switzerland and Ryggfonn, respectively. Experimental studies on a powder-snow avalanche were performed by Kawada and others (1989) and Nishimura and others (1989) reporting impact pressures and velocities from Kurobe Canyon / Japan. Schaer and Issler (2001) investigated impact pressure readings from the Vallée de la Sionne test site / Switzerland to gain information on particle size distributions and particle velocities within avalanches. Some information on Russian experiments can be found in (Bozhinskiy and Losev, 1998) and references therein. At a medium sized slide path, Somavila and Sovilla (1998) conducted mass balance measurements. For further

information on experimental techniques and sensors, the reader is also referred to (Issler, 2003) and reference therein.

2 CHARACTERISTICS OF TEST SITE, INSTRUMENTATION AND METHODS

2.1 Test site

The Ryggfonn full-scale avalanche test site (61.969° N, 7.275° E) has been in operation since 1980. The test site has a vertical drop of about 900 m and a horizontal length of approximately 2000 m. The inclination of the main track is about 30° and that of the runout 17°. In the runout zone at a horizontal distance of approximately 1675 m a 75 m wide (crown width) and 16 m high catching dam was built. Its slope angle is 40°. Behind this the path crosses a creek and ends in a reverse slope. The path itself is slightly canalized. Figure 1 provides an overview map of the site.

FIGURE 1

Typical observed avalanche size ranges from 10^2 t to 10^4 t corresponding to class 2 and 4, respectively, according to the Canadian snow avalanche size classification, cf. (McClung and Schaerer, 1993). Maximum front velocities are up to 60 ms^{-1} . Measurements include dry and wet snow avalanches from artificial as well as natural releases.

2.2 Instrumentation

The instrumentation of the test site includes five load cells at two locations along the track for impact pressure measurements. Each load cell has an area of $1.2 \times 0.6 \text{ m}^2$ and a maximum load capacity of 833 kPa. Three load cells are mounted on a concrete wedge at a distance of 219 m up-slope from the catching dam. Another

101 m further uphill, two load cells are mounted on a steel tower. In addition to those load cells, a geophone is placed inside the tower, which serves as a triggering device for starting all measurements.

In the uphill side of the dam, two 1 m² large load plates are placed at heights 2 and 8 m above the dam base. The plates are constructed to measure the three stress components: (z) normal to the slope, (x) shear pointing towards the dam crown and (y) shear pointing at a right angle. Each load plate has a maximum measuring range of 400 kPa in normal direction and 200 kPa for the shear components. A detailed description can be found in (SATSIE, 2003).

In addition, several geophones are placed in the ground in the runout zone. However, measurements of those are not considered here, but can be found in (Vilajosana and others, submitted).

All measurements are usually sampled at rate of 150 samples per second and collected at a central data acquisition system. Data can then be download to computer via an ISDN connection.

2.3 Impact pressure measurements

The interpretation of load cell measurements is not straightforward. Commonly, the drag force, F_D , due to a flow around a slender obstacle is expressed in terms of a dimensionless drag factor C_D , i.e.

$$F_D = \frac{1}{2} \rho C_D A_e U_\infty^2 \quad (1)$$

Here, ρ is the density of the fluid, U_∞ the upstream flow velocity, and A_e is the projected area of the obstacle, which is effected. The drag factor itself is a function of the flow regime and depends on factors like the Reynolds number, \mathbf{Re} , Froude number, \mathbf{Fr} , and the geometry of the obstacle. If one considers a granular flow, C_D

might also depend on the particle concentration, size, and restitution coefficient. Depending on the flow regime, C_D can vary by several orders of magnitude. Despite this, the value used for a rectangular cross section in dry flow avalanches is commonly set to 2, cf. (Mellor, 1968). This holds true for the powder part part as well as for the dense part, even if not explicitly stated. In (NGI, 1990), Norem proposed a value of 2.5 for dry snow avalanches and 6.3 for wet snow avalanches.

The authors are not aware of any systematic investigation of drag factors in avalanches. Some considerations can be found in (Bozhinskiy and Losev, 1998, Chapter 5.6). Schaerer and Salway (1980) reported values ranging from 2 to 3.4 for the front part and from 0.86 to 0.96 for the body (values are adapted to the form of (1)). However, they related this value to the front velocity, which probably overestimates the velocity within the body (see below) and so causes underestimation of the C_D values. Some considerations can also be found in (McClung and Schaerer, 1985).

Pfeiff and Hopfinger (1986) conducted laboratory experiments with dense suspensions of polystyrene particles in water. They found good agreement with the classical correlation $C_D(\mathbf{Re})$ that is valid in Newtonian fluids, if they calculated the Reynolds number using the apparent viscosity of the suspension. Gauer and Kvalstad (unpublished) used numerical simulations and experimental results to determine the drag coefficient for mud flows hitting a cylinder. They obtained the relationship $C_D = 24/\mathbf{Re} + 1$ with $\mathbf{Re} = \rho U_\infty^2/k$, where k is the yield stress of the mud in simple shear. Chehata and others (2003) conducted experiments with dense granular flows around an immersed cylinder and found that $C_D \propto \mathbf{Fr}^{-2}$, resulting in a velocity independent drag force. The Froude number was defined by $\mathbf{Fr} = U_\infty/\sqrt{g(D+d)}$, where D is the cylinder diameter and d the particle diameter. The velocities in their experiments were less than 1 m s^{-1} . For similar conditions,

Wieghardt (1975) made experiments moving rods in sand. In his case, the drag factor might be approximated by $C_D \approx 24/5 \mathbf{Fr}^{-2} \sqrt{h/D}$, where h is the flow height and $\mathbf{Fr} = U_\infty/\sqrt{gh}$. Wassgren and others (2003) performed numerical simulations of diluted granular flows around an immersed cylinder. They found that C_D depends on the Knudsen number (ratio between the upstream particle free path length to the cylinder diameter; $\mathbf{Kn} = \pi d/(8c_\infty D)$, where c_∞ is the upstream particle concentration) and the upstream Mach number. Beside this, they conclude that the drag coefficient decreases with decreasing restitution coefficient of the particles. However, for the parameter ranges relevant in dilute dry avalanches, C_D would vary only between 1 and 3 so that 2 seems to be a reasonable approximation for this flow regime.

2.4 Load plate measurements

FIGURE 2

In general, an avalanche transmits stresses due to normal pressure, p , and tangential traction, q , at the contact surface. Thus, any stress within a snowpack is a combination of both contributions, and forces measured by a load plate can be written as

$$\begin{aligned}
 LP_z &= f_z(p, q_x, q_y, \alpha) \\
 LP_x &= f_x(p, q_x, q_y, \alpha) \\
 LP_y &= f_y(p, q_x, q_y, \alpha)
 \end{aligned}
 \tag{2}$$

where α is the angle between the sliding surface and the plane of the load plate. The functions f_x , f_y , and f_z might be defined using the superposition of the Boussinesq solutions for a point load normal and tangential to the contact surface and their integration over the loaded area. If one assumes, for simplicity, the avalanche as

uniform rectangular load, the measured force can then be used to back-calculate the normal stress, p , and the tangential components, q_x and q_y . Assuming an infinite wide avalanche hiding the dam and a Poisson ratio ν equal to 0.5, the stresses at a point A(x,z) (see Fig. 2) within the snow pack might read

$$\sigma'_x = -\frac{2z}{\pi} \int_{-b}^a \frac{p(s)(x-s)^2 ds}{((x-s)^2 + z^2)^2} - \frac{2}{\pi} \int_{-b}^a \frac{q_x(s)(x-s)^3 ds}{((x-s)^2 + z^2)^2} \quad (3a)$$

$$\sigma'_z = -\frac{2z^3}{\pi} \int_{-b}^a \frac{p(s) ds}{((x-s)^2 + z^2)^2} - \frac{2z^2}{\pi} \int_{-b}^a \frac{q_x(s)(x-s) ds}{((x-s)^2 + z^2)^2} \quad (3b)$$

$$\tau'_{xz} = -\frac{2z^2}{\pi} \int_{-b}^a \frac{p(s)(x-s) ds}{((x-s)^2 + z^2)^2} - \frac{2z}{\pi} \int_{-b}^a \frac{q_x(s)(x-s)^2 ds}{((x-s)^2 + z^2)^2} \quad (3c)$$

The stresses in the system of the load plates are then given by

$$\begin{pmatrix} \sigma_x & \tau_{pxz} \\ \tau_{xz} & \sigma_z \end{pmatrix} = \begin{pmatrix} \cos \alpha & -\sin \alpha \\ \sin \alpha & \cos \alpha \end{pmatrix} \cdot \begin{pmatrix} \sigma'_x & \tau'_{pxz} \\ \tau'_{xz} & \sigma'_z \end{pmatrix} \cdot \begin{pmatrix} \cos \alpha & -\sin \alpha \\ \sin \alpha & \cos \alpha \end{pmatrix}^T \quad (4)$$

The angle, α , depends on the snow distribution in front of the dam. For definition of the load functions in three dimensions we refer to, e.g., (Johnson, 2001, Chapter 3.2 and 3.6). Due to the motion of the avalanche, the load functions vary with time. Actually, one should consider a layered system, so the Boussinesq solution has some limitation. Also Poisson ratio ν is less than 0.5 for a snowpack.

2.5 Pulsed Doppler radar measurements

During several avalanche releases, pulsed Doppler radar systems were used to measure the avalanche velocity. A pulsed Doppler radar are based on the principle of a pulsed radar which makes a range-discrimination of the echo-signal possible by sampling the echo-signal at constant time-intervals ("range-gating"). Thus, it is

possible to gain information on the front speed along the track and information on the velocity versus time at a specific location (Schreiber and others, 2001).

Using these latter information it is also possible to translate any measurement in time at a specific location into a measurement versus position within the avalanche, x_{pwa} , i.e., versus the distance behind the front as it is measured by an observer fixed at that location (not noticing any changes downstream) after a given time. This allows one to get a glimpse of the spatial structure of the avalanche. The position can be calculated by

$$x_{pwa} = \int_{t_0}^t u(t) dt \quad (5)$$

where t_0 is the arrival time of the front at the specific location. In addition to the velocity, information on accelerations can be derived. For that the velocity of pair of adjoining range gates, having a width Δx are compared. Starting with an first guess of the average velocity, \bar{u} , between both range gates (either the upstream velocity, $u_1(t_1)$, or another suitable estimate) the required travel time, $\Delta t = \Delta x / \bar{u}$, between the range gates can be calculated. Then, the velocity of the downhill range gate $u_2(t_1 + \Delta t)$ is used to recalculate $\bar{u} = (u_1(t_1) + u_2(t_1 + \Delta t)) / 2$. In this way, the average velocity can be found iteratively. The estimated acceleration is calculated by

$$a = \frac{(u_1(t_1) - u_2(t_1 + \Delta t))}{\Delta t} \quad (6)$$

However, one should keep in mind that the measured velocities are actually only an measure for a speed within the width of the range gate. In the experiments, used range gate widths were 25 and 50 m, respectively.

3 OBSERVATIONS

In the following, data from several avalanches are analyzed. The main focus is on dry snow avalanches, however also some data from dry/wet avalanches are included for comparison. The avalanches are selected with respect to reliability and completeness of the data. Table 1 gives a short characterization of the investigated avalanches. Thereafter, most artificially released avalanches (J4) started as slab (A2,A4), whereas the natural ones (J1) released as loose snow (A1). By almost all occurred a new snow fracture (B2). One showed a mixed type of fracture (B7). Only the 20040204 06:10 event were moist from the start (C7). As already mentioned the Ryggfonn path is slightly canalized (D2). The movement of most avalanches are characterized as dry/mixed (E7), exceptions are the both wet snow event 20040204 06:10 and 20050416 15:00, which showed a dominant flow part (E2). The deposits were coarse with rounded clods (F3), with angular clods (F2), or fine (F4). Many deposits were moist (G7) or totally wet (G2). Generally the deposits were clean (H1). 20000217 13:55 avalanche had structure parts within the deposit (H5). The 20040204 06:10 one had some branches (H4) and the 20050416 15:00 contained some soil (H3).

TABLE 1

3.1 Velocity measurements

The availability of a velocity distribution along the avalanche body is crucial for gaining in-depth understanding of its internal structure. Here, pulsed Doppler radar proof to be very valuable. Figure 3 shows radar measurements from the 20050416 15:00 avalanche. Plotted is the calculated mean velocity between two range gates versus position within the avalanche for a location just below the steel tower. In

this case a range gate width of 25 m was used and the radar was located at R2. The calculated values are based on the velocity values of the maximum radar intensity for the two adjoining range gates. In addition, the corresponding acceleration (deceleration) is also given. Given are running means with 5 m width. The figure shows a short head with nearly constant velocity and then a rapid velocity decrease within the body and tail. Similar behavior can also be seen in the velocity distributions in Figure 7 and 8. Also the wave like structures can be recognized in those plots. This wave like behavior is even more obvious in the acceleration plot, where the frontal part shows a high variability with acceleration from approximately $\pm 7 \text{ m s}^{-2}$. In the tail part, the amplitude of the fluctuations decreases. Similar pictures were found for other range gate pairs in the lower track not shown here. In some instants, a slower moving snout preceded the head. This seems to occur when the head encounters higher flow resistance and slows down rapidly. Causes can be due to change in snowpack properties, change in topography or due to entrainment.

FIGURE 3

Figure 4 presents the velocity and acceleration (deceleration) along the lower part of the track derived from the available measurements for six instants in time. In addition, the front velocity is also shown. Actually, the front velocity of this event and from the 19970417 14:00 avalanche closely resemble each other, cf. (Schreiber and others, 2001). Both avalanches were released during similar snow conditions, i.e., dry snow in the upper part of the track and moist to wet in the valley bottom. Obvious is the acceleration of the front in the range from 70 m before until the steel tower. Then, a more less constant front velocity for about 100 m followed by a rapid deceleration. The deceleration of the front is approximately -5 m s^{-2} . The velocity within the avalanche, here given as the velocity at a specific location for

20021048-11

different points in time, indicate that the head velocity tend to be higher until the avalanche starts to decelerate. The higher front velocity would cause a stretching of the avalanche. As the avalanche decelerates, the velocity is higher in the body which then pushes the frontal part. The picture from the acceleration is not as clear. One can see wide fluctuations and deceleration up to -7 m s^{-2} . Some of this might be cause by the specific topography. However, using those acceleration values indicates that the effective friction parameter varies and depends on the flow regime. Unfortunately, no data are available for further up the track from this event.

FIGURE 4

3.2 Turbulent intensity

The variation of the measured pressure signals can be an indication of changes in the flow regime. If one uses the decomposition of the velocity $\tilde{U} = U + u'$, where U is the spatial mean velocity and u' the fluctuation part and similar for $\tilde{\rho} = \rho + \rho'$ and for the pressure signal \tilde{LC} . Now, we define a turbulent intensity as a measure for the fluctuation

$$I = \left| \frac{\tilde{LC} - LC}{LC} \right| \approx \left| \frac{2u'}{U} + \frac{\rho'}{\rho} \right| \quad (7)$$

FIGURE 5

Figure 5 is a plot of the turbulent intensity versus the position within the avalanche for the 20031217 03:24 event. It is regarded as a medium size dry snow avalanche which ran into a moist snowpack at the valley bottom. The plots show the measured impact pressure, the running mean taken over 5 m, and the turbulent intensity. Due to the large size of the sensors, the measured impact forces repre-

sent already an average value over the impact area. Single impacts might exceed measured values by an order of magnitude. The averaging effect of the large size also causes a damping of the turbulent intensity, cf. discussion in (McClung and Schaerer, 1985; Schaer and Issler, 2001). However, the high turbulent intensity in the frontal part of the avalanche indicates a fluidized flow/saltation layer. In the denser part the turbulent intensity decreases in the lower layer (LC3), but there is still noticeable fluctuation in the parts above. This suggests that the upper layer is still at least partly fluidized, which contradicts the assumption of a plug-like flow common to most dynamical models. The high turbulence intensity in the rear part of LC1 measurements is due to the fact that the load cell is only randomly hit by particles at this time.

For comparison, Figure 6 shows a similar plot for the 20040204 06:10 event. In this case, the snow was humid from the start. Even if it was preceded by a short lightly fluidized front, the fluctuations in the dense part are noticeably less and it seemed to have flowed in a more plug-like manner.

FIGURE 6

3.3 Density estimates based on impact pressure measurements

Figure 7 shows an estimated density distribution versus the position within the avalanche as it passes the concrete wedge for three cases. The velocity distributions are based either on correlations between characteristic pressure signals at the steel tower and at the concrete wedge and a linear interpolation to gain $u(t)$ or the velocity was directly measured using Doppler radar (positioned at R1). Only those part of the respective avalanche was regarded for which a reasonably good estimate of the velocity distribution was available. For example, in the case of the 20000217

13:55 avalanche, the front velocity is calculated from the time lag between the first signal at the steel tower and at the concrete wedge. After 1.7s the steel tower was broken and carried away by the avalanche; it impacted and destroyed parts of the wedge approximately 3s thereafter. This time difference was used to estimate the velocity within the body. The avalanche itself was definitely longer at that location. The velocity distribution of the 19970417 14:00 avalanche is based on Doppler radar measurements with a range gate width of 50 m. The distributions are also plotted in the figure. The comparison of the velocity distributions measured by radar with those based on correlations indicate that the approximated distributions are reasonable. The density estimates are calculated from the force measurements using (1) and setting $C_D = 2$ disregarding possible vertical variation of the velocity. The measured forces are averaged using a running mean over 5 m. We are aware that using a constant factor for C_D may cause some error, nevertheless, it allows to get some idea of the density distribution. Otherwise, multiplying by 2 gives an estimate for ρC_D . Actually, as we disregard the inertia of the steel tower in time estimate for the 20000217 13:55 event, the estimated velocity is probably on the lower side. This gives an overestimate of the density especially in the tailing part of this plot. The profiles give some impression of the vertical distribution of the density. The transition from the saltation (fluidized) regime to the dense flow regime is taken where the density surpasses 100 kg m^{-3} . If one assumes a typical density of 400 kg m^{-3} for a snow clod within the avalanche, the free path length of those clods would still be approximately 1.5 d at 100 kg m^{-3} . From our field experiences, clod density of $400 - 500 \text{ kg m}^{-3}$ are reasonable for dry/slightly moist snow avalanches and also supported by measurements by McClung and Schaerer (1985). In all three cases, one can observe a saltation (fluidized) layer at the front ranging from 40 m up to 90 m in length. The estimated density within the dense flow varies in the

three case between 100 to 300 kg m⁻³. The profiles for the avalanches 19970417 14:00 and 20000217 13:55 show a density inversion. Most likely, this caused by: 1) a partly buried load cell (LC3) in the case of the 20000217 13:55 event, and 2) more important due to the disregarding of a probable velocity profile with lower speed towards the ground. Disregarding this leads to an underestimate of the density, but no reliable information are available to correct for this.

FIGURE 7

3.4 Impact pressure and ρC_D values

How flow regime or avalanche type, respectively, influences the forces on an obstacle is illustrated in Figure 8. It plots calculated values of ρC_D for the 20050416 15:00 avalanche. The avalanche was artificially released and started as a small dry snow avalanche, which triggered in the lower part of the track a wet snow slide. The figure shows also the corresponding values of the measured pressure and of the velocity distribution. The measured pressures values of up to 800 kPa are surprisingly high. They are related to the wet snow slide. If one assumes density between 300 to 500 kg m⁻³ within slow moving tail, one finds a C_D of approximately 20 to 40 for LC2. These values, actually, would agree with calculated values using the approach from Wieghardt (1975). At the far end, the load cell was probably no longer totally covered. Also in this case, the preceding dry part seemed to be fluidized.

FIGURE 8

20021048-11

3.5 Load plate measurements

Only few observed avalanches surpassed the catching dam after installing the load plates in 2002. Hence, only limited data are available. One event that surpassed is the 20040224 22:30 avalanche. Several avalanche reached the foot of the dam earlier in that season, so the foot of the dam was buried by old deposits.

FIGURE 9

Figure 9 shows the traction versus normal stress, back-calculated following the inversion of (2). In this case, the lower load plate LP1 registers basically only the hydrostatic loading. LP2 two shows a more complex behavior. At the arrival of the avalanche, shear stress up to 2 kPa are combined with partly negative normal pressures (pressure drop), which causes a relieve at the load plate. Than, as the normal pressure increases the shear stress stays in a limited range indicating a kind of shear failure. The values of the shear stress at failure corresponds well with values of the shear strength for snow densities of concern, cf. (Jamieson and Johnston, 2001; Mellor, 1974). Finally, also LP2 registers the static loading of the plate. Similar behavior could be observed during several other events not shown here. None of those showed a Coulomb-type relation with constant friction parameter. It is not clear to which extent sliding is involved. However, from the theory of plastic failure, e.g. (Johnson, 2001, Chapter 7), it is know that after failure the effective friction coefficient can be related to the normal stress, p , and the yield stress in shear, k , by

$$\frac{1}{\mu} = \frac{p}{k} \quad (8)$$

FIGURE 10

During some events the concrete wedge was covered by snow and previous deposits. In those cases, a similar approach as described in Section 2.4 for the load plates can be used to recycle at least some information from the load cells. Figure 10 shows a measurement from the 20040228 15:30 event. At this time both load cells, LC2 and LC3, were totally buried and LC1 partially. Obvious in the figure is a drop of normal pressure at the front of the avalanche indicating a possible negative dynamic pressure within the avalanche. The existence of an underpressure could contribute to the fluidization of the snowpack and so to its erosion and entrainment by the avalanche, cf. (Gauer and Issler, 2004). There is a degree of uncertainty in this measurement, as can be seen by some negative shear stress values. One reason for this can be erosion or deposition, respectively, at the contact surface which would change the assumed geometry slightly and so cause some error. Nevertheless, the similar behavior was also seen in other events and is also measured in the powder part of a number of avalanches by McElwaine and Turnbull (2004). The static load at the end agrees with the observed deposition. It would be interesting to combine similar kind of measurements with FMCW radar measurements which allow measurements of the vertical structure of the flow.

4 CONCLUSIONS

The following conclusions are based on the observations and measurements from the Ryggfonn test site. Some measurements might be site specific and influenced by the local topography and snow characteristics. Nevertheless, they are supported by measurements and observations from other full-scale avalanches, e.g. (Schaerer and Salway, 1980; Schaer and Issler, 2001; McClung and Schaerer, 1985; Gauer and Issler, 2004; Sovilla and others, 2001; Somavilla and Sovilla, 1998).

All measurements of dry snow avalanches indicate a spatial structure, horizon-

tally and vertically, with a saltation (fluidized) layer at the front (densities ranging approximately between $30 - 100 \text{ kg m}^{-3}$) followed by a more dense flow (density of approximately $100 - 300 \text{ kg m}^{-3}$ depending on the speed). On top of the latter rides a more fluidized layer, above which snow particles are in suspension. Regrettably, no exact height measurements are available from Ryggfonn.

The maximum speed is usually measured within the head. Its length varies but can reach 100 m and more. After the front passage, the observed velocities rapidly decrease. However, the velocity gradient, $\partial u / \partial x_{pwa}$, might not be the same along the body and varies with the location.

Load plate measurements do not reveal a Coulomb-like friction with a constant friction coefficient. Shear failure seems to occur instead. Some load-cell measurements suggest a underpressure behind the front of the saltation layer.

The calculated acceleration (deceleration) and the load plate measurements indicate that the friction parameters, as they are commonly used in numerical models, are not constant and depend on the flow regime or stage of flow, respectively. They may vary considerably.

With respect to the dimensioning of structures it is important to note that the impact pressure measurements show a dependency of the drag coefficient on the flow regime. This dependency is especially noticeable in moist or wet snow avalanches, where the drag coefficient can vary more than one order of magnitude. A more systematic investigation is desirable (and partly on the way Sovilla, 2005, private communication).

It should be noted, due to the high mobility of the saltation (fluidized) layer it can exceed the runout distance of the dense part to great extent. As the impact pressure therein are also considerable this flow regime is of relevance for hazard mapping.

Summarizing in respect to numerical modeling, models with constant density and friction parameters might miss important flow features. The yield strength of the snowpack might be an important factor for the definition of the surface boundary conditions. Pressure drops during frontal passage and the existence of a saltation layer might be of importance concerning possible erosion mechanism, cf. (Gauer and Issler, 2004). Field observations from the 20050416 15:00 avalanche indicate that substantial erosion due to (saltating) particles occurred.

Still, further work is needed to combine results from different sensors to get an even clearer picture of the avalanche structure. This involves also further development of the interpretation techniques for different kinds of sensors. As some of the observations might be avalanche path specific, cross comparison of these results with measurements from other test sites is also important.

ACKNOWLEDGMENTS

This work was funded through NGI's SIP-program "Avalanche research" and through the EU Program "SATSIE (Avalanche Studies and Model Validation in Europe)" within the 5th Framework Program, EU Contract no. EVG1-CT2002-00059. This is Publication no. 91 from the International Centre for Geohazards.

REFERENCES

- Bozhinskiy, A. N. and K. S. Losev. 1998. The Fundamentals of Avalanche Science. Mitt. Eidgenöss. Inst. Schnee- Lawinenforsch. 55. 280 S.
- Chehata, D., R. Zenit, and C. R. Wassgren. 2003. Dense granular flow around an immersed cylinder. *Physics of Fluids*, **15**(6), 1622–1631.
- Gauer, P. and D. Issler. 2004. Possible erosion mechanisms in snow avalanches. *Annals of Glaciology*, **32**, 384–392.
- Gauer, P. and T. Kvalstad. unpublished.

- Gubler, H.-U. 1987. Measurement and modelling of snow avalanche speeds. In Salm, B. and H.-U. Gubler, editors, *Avalanche Formation, Movement and Effects*, volume 162 of *IAHS Publ.* Wallingford, Oxon OX10 8BB, UK, Int. Assoc. Hydrol. Sci., pages 405–419.
- Issler, D. 2003. *Dynamic Response of Granular Materials under Large and Catastrophic Deformations*, volume 11 of *Lecture Notes in Applied and Computational Mechanics*. Springer, chapter Experimental Information on the Dynamics of Dry-Snow Avalanches, pages 109–160.
- Jamieson, B. and C. Johnston. 2001. Evaluation of the shear strength frame test for weak snowpack layers. *Annals of Glaciology*, **32**, 59–69.
- Johnson, K. L. 2001. *Contact Mechanics*. Cambridge, U.K., Cambridge University Press.
- Kawada, K., K. Nishimura, and N. Maneo. 1989. Experimental studies on a powder-snow avalanche. *Annals of Glaciology*, **13**, 129–134.
- McClung, D. and P. Schaerer. 1993. *The Avalanche Handbook*. 1011 SW Klickitat Way, Seattle, Washington 98134, The Mountaineers.
- McClung, D. M. and P. A. Schaerer. 1985. Characteristics of flowing snow and avalanche impact pressures. *Annals of Glaciology*, **6**, 9–14.
- McElwaine, J. N. and B. Turnbull. 2004. Air pressure data from the Vallée de la Sionne avalanches of 2004. *Journal of Geophysical Research*, , (accepted).
- Mellor, M. 1968. Cold regions science and engineering. Part III: Engineering Section A3: Snow Technology Avalanches. Hanover New Hampshire, Cold Regions Research & Engineering Laboratory.
- Mellor, M. 1974. A review of basic snow mechanics. In *Snow mechanics Symposium*, number 114 in IAHS. International Association of Hydrological Sciences, pages 251–291.
- NGI, . 1990. Ryggonn-prosjektet. Report 581200-16. Sognsveien 72, N-0860 Oslo, Norwegian Geotechnical Institute. (in Norwegian).
- Nishimura, K., H. Narita, N. Maneo, and Kawada. 1989. The internal structure of powder-snow avalanches. *Annals of Glaciology*, **13**, 207–210.

- Norem, H., T. K. Kvistroy, and B. D. Evensen. 1985. Measurements of avalanche speeds and forces: Instrumentation and preliminary results of the Ryggfonn project. *Annals of Glaciology*, **6**, 19–22.
- Pfeiff, C. F. and E. J Hopfinger. 1986. Drag on cylinders moving through suspensions with high solid concentrations. *PhysicoChemical Hydrodynamics*, **7**(2/3), 101–109.
- SATSIE, . 2003. *Avalanche Studies and Model Validation in Europe EU: Management Progress Report*. Coordinator: Norwegian Geotechnical Institute.
- Schaer, M. and D. Issler. 2001. Particle densities, velocities and size distributions in large avalanches from impact-sensor measurements. *Annals of Glaciology*, **32**, 321–327.
- Schaerer, P. A. and A. A. Salway. 1980. Seismic and impact-pressure monitoring of flowing avalanches. *Journal of Glaciology*, **26**(94), 179–187.
- Schreiber, H., W. L. Randeu, H. Schaffhauser, and L. Rammer. 2001. Avalanche dynamics measurement by pulsed Doppler radar. *Annals of Glaciology*, **32**, 275–280.
- Sommavilla, F. and B. Sovilla. 1998. The avalanche monitoring system of Mount Pizzac. In Hestnes, E., editor, *25 Years of Snow Avalanche Research*, volume (NGI Publ. 203). Oslo, Norwegian Geotechnical Institute, pages 268–273.
- Sovilla, B. 2005, private communication.
- Sovilla, B., F. Sommarivilla, and A. Tomaselli. 2001. Measurements of mass balance in dense snow avalanche events. *Annals of Glaciology*, **32**, 230–236.
- UNESCO, . 1981. *Avalanche Atlas*. International Commission on Snow and Ice of the International Association of Hydrological Sciences, IAHS.
- Vilajosana, I., G. Khazaradze, E. Suri nach, E. Lied, and K. Kristensen. submitted. Snow avalanches speed determination using seismic methods. *Cold Region Science and Technology*, **this issue**.
- Wassgren, C. R., J. A. Cordova, R. Zenit, and A. Karion. 2003. Dilute granular flow around an immersed cylinder. *Physics of Fluids*, **15**(11), 3318–3330.
- Wieghardt, K. 1975. Experiments in granular flow. *Annual Review of Fluid Mechanics*, **7**, 89–114.

List of Tables

1	Avalanche characterization	26
---	--------------------------------------	----

List of Figures

- 1 Overview of the Ryggfonn test site (UTM in m). The view shows are the line of the main track and the locations of the load cells (LC45 and LC123) and the placement of the load plate in the dam (LP1 and LP2). In addition two Doppler radar positions are indicated (R1 and R2). 27
- 2 Load plate measurements: schematic illustrating the relation between the coordinates systems adapted to the ground and the snow surface, respectively. 28
- 3 Velocity (solid line) and acceleration (dashed line) vs position within the avalanche (20050416 15:00). Values are calculated for a location approximately 9 m below the steel tower. The mean slope angle at this location is approximately 30° 29
- 4 Velocity and acceleration vs location along the lower track for six instants in time (20050416 15:00). The upper panel shows the averaged velocity and the lower panel the acceleration derived from the respective pair of adjoining range gates. In addition, the thin solid line in the upper panel shows the front velocity. The thick solid line gives the path profile in the lower part of the track. 30
- 5 Turbulent intensity vs position within the avalanche for a dry-snow event (20031217 03:24). The lines present the measured impact pressure (dashed line) and the running mean (full line) taken over 5 m, respectively (left axis). The turbulent intensity is marked with dots (right axis). Top: LC1; middle: LC2; bottom: LC3. 31

20021048-11

6	<p>Turbulent intensity vs position within the avalanche for a wet-snow event (20040204 06:10). The lines present the measured impact pressure (dashed line) and the running mean (full line) taken over 5 m, respectively (left axis). The turbulent intensity is marked with dots (right axis).</p>	32
7	<p>Avalanche density (running mean taken over 5 m) vs position within the avalanche assuming $C_D \approx 2$. Note the logarithmic scaling. Profiles indicate the vertical density distribution showing the mean density over the height of individual plates (ticks mark density steps by 100 kg m^{-3}). The black line shows the corresponding velocity profile (right axis). Top: 19970417 14:00; middle: 20000217 13:55; bottom: 20031217 03:24.</p>	33
8	<p>ρC_D vs position within the avalanche (20050416 15:00; dash-dotted line). The full lines present the measured impact pressure as the running mean taken over 5 m. Note the logarithmic scaling. The black dashed lines show the corresponding velocity profiles. Upper panel gives measurements from the steel tower (LC4) and the lower panel from the concrete wedge (LC2). The double arrow indicates the range where the approach from Wieghardt (1975) could fit the values.</p>	34
9	<p>Shear stress vs normal stress at the sliding surface along the dam slope (20040224 22:30). The upper panel shows LP2 and the lower one LP1. The dashed line in both panels corresponds to the ratio between shear and normal stress in the case of static loading ($-\tan 40^\circ$).</p>	35

10 Normal (solid line) and shear stress (dashed line) vs time at the sliding surface (20040228 15:00). Right axes shows corresponding values of the normal stress related to density times flow height. 36

20021048-11

Table 1: Avalanche characterization

Date yyyymmdd hh:mm	Size ¹	Deposit (10 ³ m ³)	Classification (ICSI) ²										Speed (m s ⁻¹)	
			A	B	C	D	E	F	G	H	J	LC4-LC1 ³	LC1-LP1 ⁴	
19970417 14:00	3	40	2	2	1	2	7	3	7	1	4	34	stopped	
20000217 13:55	4	100	2	2	1	2	7	3	7	5	4	49	36	
20031215 16:40	3	NA	1	2	1	2	7	4	1	1	1	28	22	
20031217 03:24	3	NA	1	2	1	2	7	4	7	1	1	29	stopped	
20040204 06:10	3.5	NA	1	2	7	2	2(7)	3	2	4	1	22	2.8	
20040224 22:30	3	NA	1	2	1	2	7	4	1	1	1	25	29	
20040228 15:30	3.5	NA	1	2	1	2	7	4	7	1	4	31	18	
20050416 15:00	4	NA	4	7	1	2	7(2)	2	7	3	4	30	5	

¹According to Canadian avalanche size classification cf. (McClung and Schaerer, 1993)

²According international avalanche classification (Avalanche Atlas (UNESCO, 1981), also in (McClung and Schaerer, 1993))

³The estimated average speeds are calculated between the steel tower and the concrete structure,

⁴and between the concrete structure and the foot of the dam (before 2002, the arrival time at the dam is derived from geophone data), respectively.

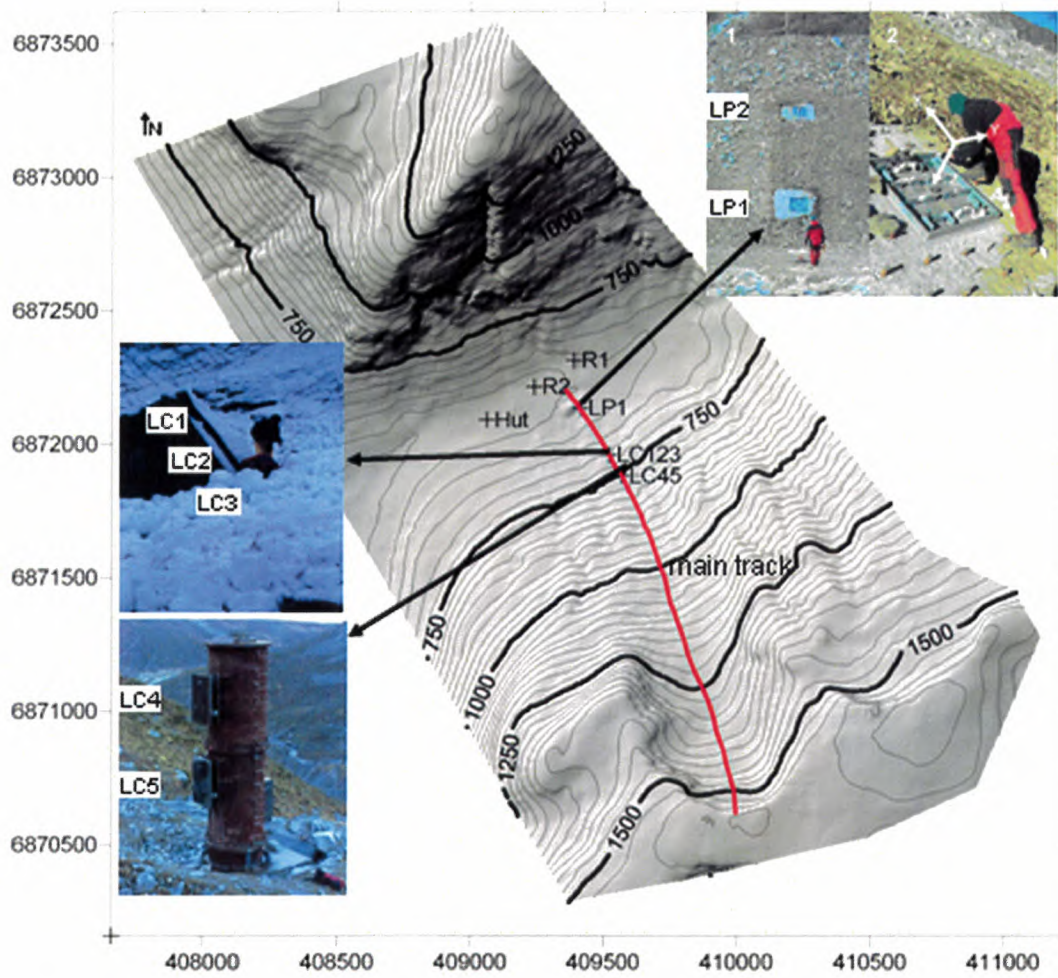


Figure 1: Overview of the Ryggfonn test site (UTM in m). The view shows the line of the main track and the locations of the load cells (LC45 and LC123) and the placement of the load plate in the dam (LP1 and LP2). In addition two Doppler radar positions are indicated (R1 and R2).

20021048-11

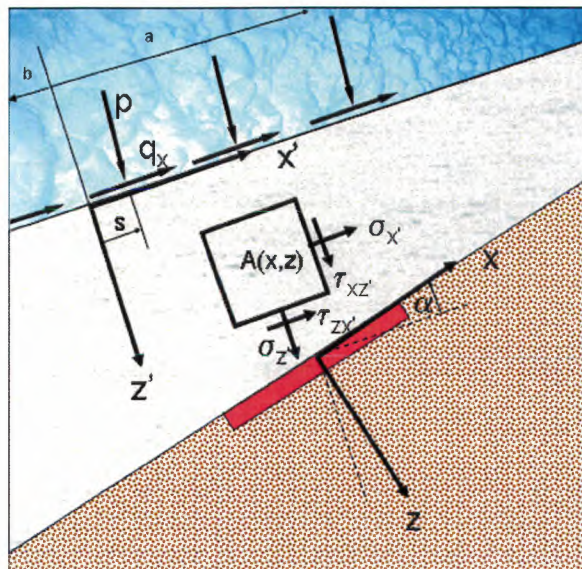


Figure 2: Load plate measurements: schematic illustrating the relation between the coordinates systems adapted to the ground and the snow surface, respectively.

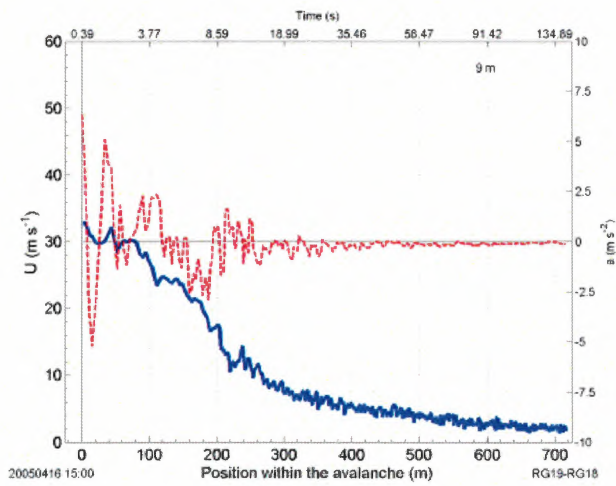


Figure 3: Velocity (solid line) and acceleration (dashed line) vs position within the avalanche (20050416 15:00). Values are calculated for a location approximately 9 m below the steel tower. The mean slope angle at this location is approximately 30°.

20021048-11

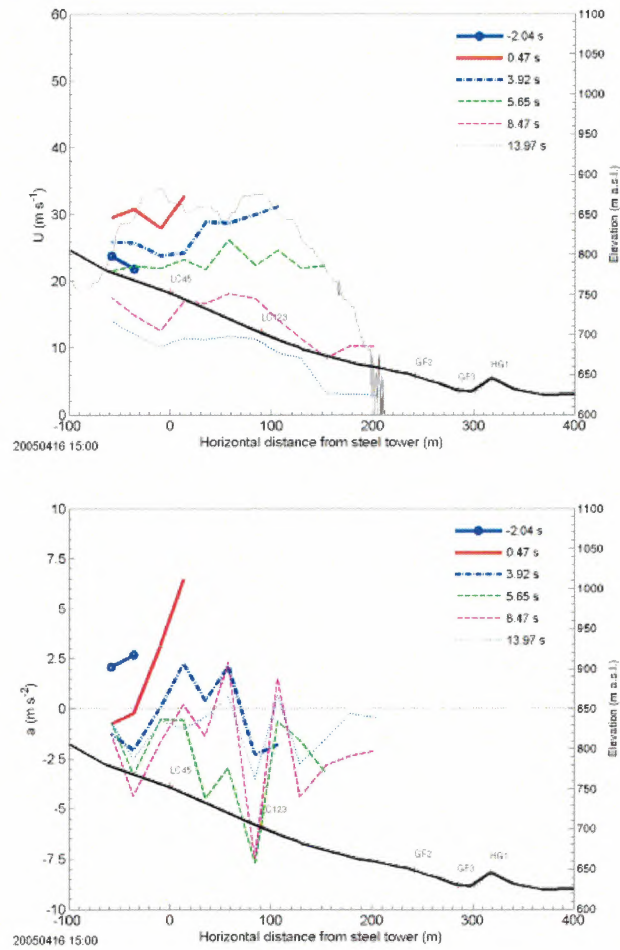


Figure 4: Velocity and acceleration vs location along the lower track for six instants in time (20050416 15:00). The upper panel shows the averaged velocity and the lower panel the acceleration derived from the respective pair of adjoining range gates. In addition, the thin solid line in the upper panel shows the front velocity. The thick solid line gives the path profile in the lower part of the track.

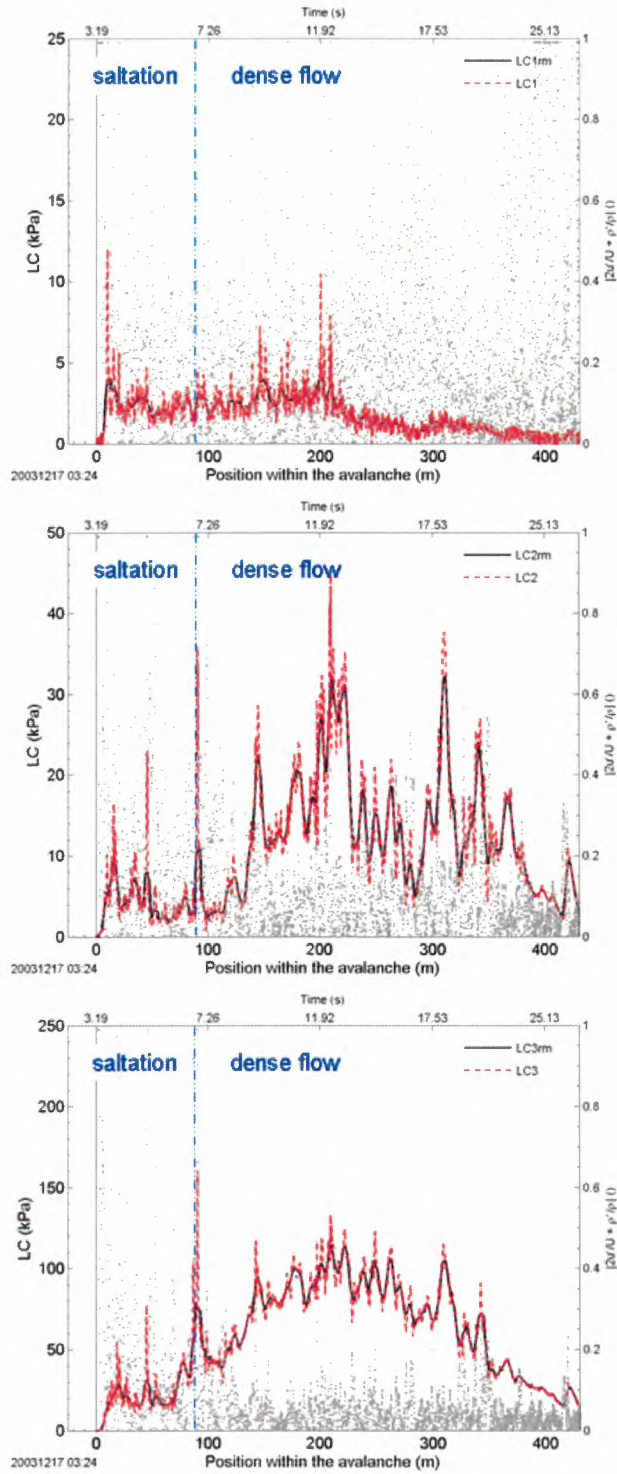


Figure 5: Turbulent intensity vs position within the avalanche for a dry-snow event (20031217 03:24). The lines present the measured impact pressure (dashed line) and the running mean (full line) taken over 5 m, respectively (left axis). The turbulent intensity is marked with dots (right axis). Top: LC1; middle: LC2; bottom: LC3.

20021048-11

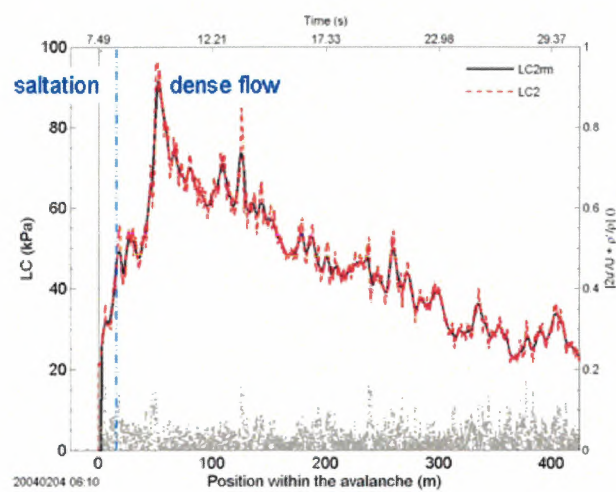


Figure 6: Turbulent intensity vs position within the avalanche for a wet-snow event (20040204 06:10). The lines present the measured impact pressure (dashed line) and the running mean (full line) taken over 5 m, respectively (left axis). The turbulent intensity is marked with dots (right axis).

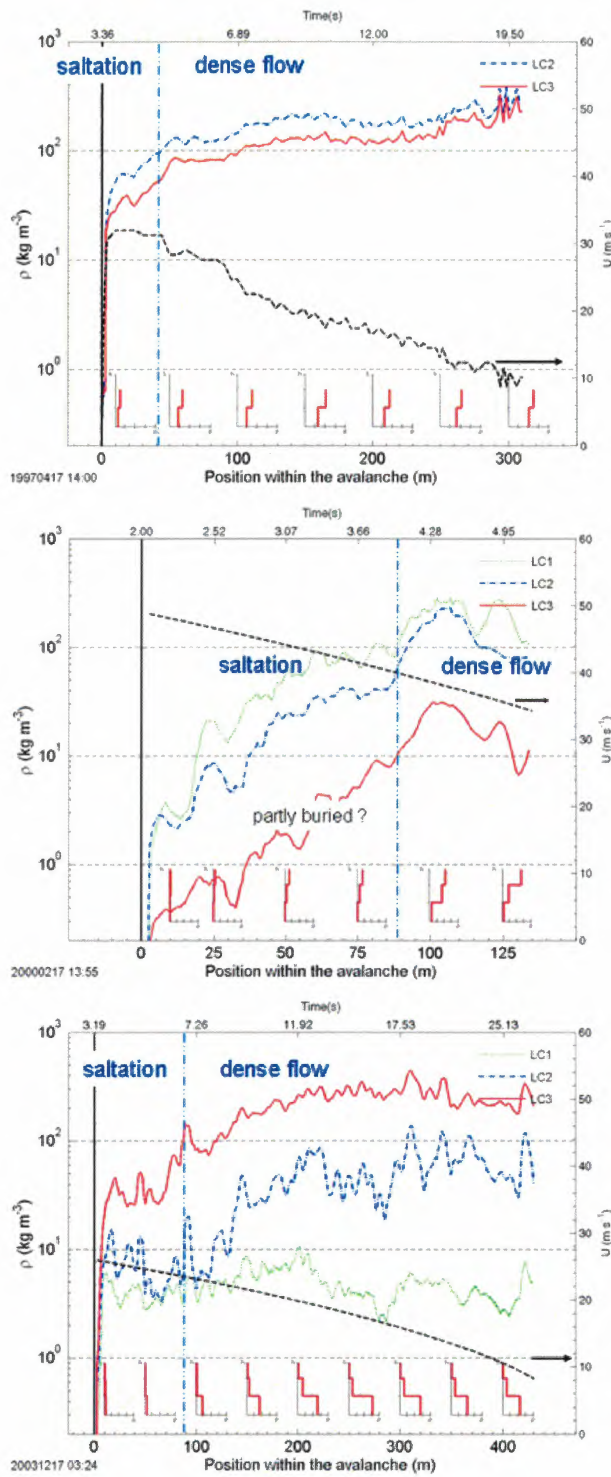


Figure 7: Avalanche density (running mean taken over 5 m) vs position within the avalanche assuming $C_D \approx 2$. Note the logarithmic scaling. Profiles indicate the vertical density distribution showing the mean density over the height of individual plates (ticks mark density steps by 100 kg m^{-3}). The black line shows the corresponding velocity profile (right axis). Top: 19970417 14:00; middle: 20000217 13:55; bottom: 20031217 03:24.

20021048-11

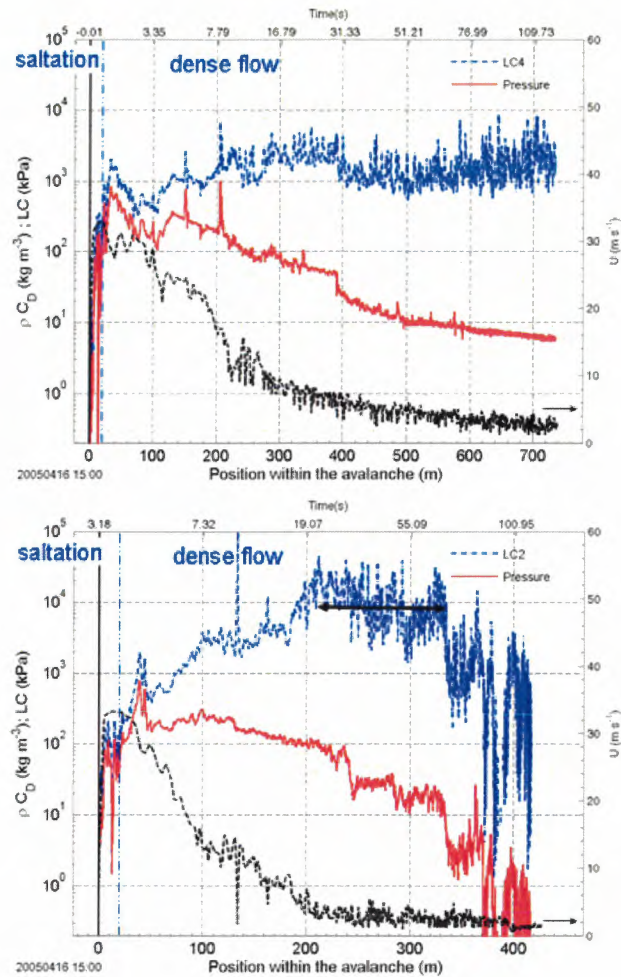


Figure 8: ρC_D vs position within the avalanche (20050416 15:00; dash-dotted line). The full lines present the measured impact pressure as the running mean taken over 5 m. Note the logarithmic scaling. The black dashed lines show the corresponding velocity profiles. Upper panel gives measurements from the steel tower (LC4) and the lower panel from the concrete wedge (LC2). The double arrow indicates the range where the approach from Wieghardt (1975) could fit the values.

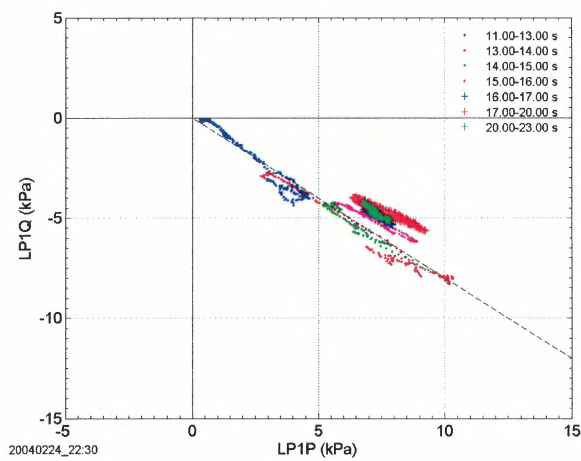
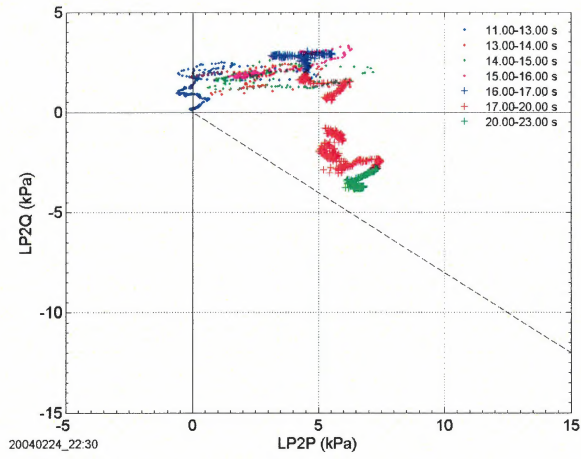


Figure 9: Shear stress vs normal stress at the sliding surface along the dam slope (20040224 22:30). The upper panel shows LP2 and the lower one LP1. The dashed line in both panels corresponds to the ratio between shear and normal stress in the case of static loading ($-\tan 40^\circ$).

20021048-11

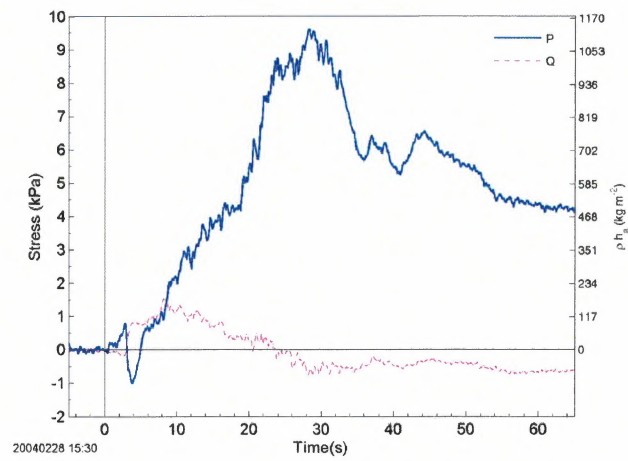


Figure 10: Normal (solid line) and shear stress (dashed line) vs time at the sliding surface (20040228 15:00). Right axes shows corresponding values of the normal stress related to density times flow height.

A.6 Paper Submitted to Peer-Reviewed Journal (2)

Hauksson, S., M. Pagliardi, M. Barbolini and T. Jóhannesson. 2005. Laboratory measurements of impact forces of granular flow against mast-like obstacles. Submitted to *Cold Regions Science and Technology* (EGU 2005 special issue).

Laboratory measurements of impact forces of supercritical granular flow against mast-like obstacles

Sigurjón Hauksson¹, Matteo Pagliardi²,
Massimiliano Barbolini² and Tómas Jóhannesson³

¹VA Consulting Engineers

Kaupvangi 5, IS-700 Egilsstaðir, Iceland

²University of Pavia, Hydraulics and Environmental
Engineering Dept., Via Ferrata 1, I-27100 Pavia, Italy

³Icelandic Meteorological Office,
Bústaðavegur 9, IS-150 Reykjavík, Iceland

29th July 2005

Abstract

Impact forces by snow avalanches on narrow obstacles need to be taken into account in the design of many constructions in avalanche prone terrain, such as masts of electrical power lines, ski lifts and cable cars. An important question in connection with such impact forces on high obstacles that extend through the flow is how they depend on the width and cross-sectional shape of the obstacle for a given velocity and thickness of the

oncoming flow. Widely used engineering guidelines imply that a significant fraction of the dynamic pressure of the avalanche impacts the obstacle simultaneously over a substantial part of the full height range corresponding to the run-up of the avalanche. A series of laboratory experiments was conducted in a 7.5 m long and 0.35 m wide chute in order to investigate impact forces on narrow rectangular and cylindrical obstacles for supercritical granular flow. Obstacle heights varied from about twice the flow depth to more than 20 times the flow depth, which was higher than the observed run-up, and the width of the obstacles varied from about twice the flow depth to about 7 times the flow depth. It was found that the total force on the obstacle did not depend much on the obstacle height for heights that exceeded about 3 flow depths, which is much lower than the run-up on the highest obstacles. For a wide range of obstacle heights exceeding about 3 flow depths, the total force on the rectangular obstacles was of similar magnitude as the dynamic pressure, $\frac{1}{2}\rho_f u^2$, acting over an area corresponding to the width of the obstacle and the upstream depth of the flow. The total force was about 30% lower for cylindrical compared with rectangular obstacles. Our results indicate that measured impact pressure at full-scale avalanche test sites may depend in a complicated manner on obstacle geometry, flow thickness and other such aspects of the flow, in addition to the density and velocity of the oncoming flow. This implies that interpretation of impact pressure measurements in terms of density or other flow characteristics is harder than has perhaps been appreciated before. Impact forces of natural snow avalanches on obstacles are observed to be characterised by some important features that were not analysed in the laboratory experiments described here. In particular, high peaks in the loading are believed to be caused by the impact of large snow clods on the obstacles and even higher impacts may be caused by impacts of rocks, tree trunks and other debris that is advected with the snow in many avalanches. In spite of this, the experiments provide information about the nature of granular flow around obstacles, which may be useful for engineering applications.

Introduction

Masts of electrical power lines, ski lifts and other constructions sometimes need to be built in avalanche paths and must then be designed to withstand the impact of an avalanche (*cf.* Fig. 1).

[Figure 1 about here.]

An important question in connection with impact forces on high obstacles that extend through the flow is how they depend on the width and cross-sectional shape of the obstacle for a given velocity and thickness of the oncoming flow. Widely used engineering guidelines imply that a significant fraction of the dynamic pressure of the avalanche impacts the obstacle simultaneously over a substantial part of the full height range corresponding to the run-up of the avalanche (SLF, 1990). According to Norwegian guidelines based on field experiments in the Ryggfonn avalanche path in western Norway, the dynamic pressure of the avalanche does not affect all this range simultaneously (Norem, 1990). The Norwegian guidelines imply that the avalanche impact is at each point in time limited to a depth range similar in magnitude to the upstream flow depth of the avalanche. In the guidelines from SLF, it is assumed that the full impact pressure affects a depth range corresponding to the upstream flow depth *and* that the impact pressure then decreases linearly to zero at a height corresponding to the run-up of the avalanche on the obstacle.

The experiments reported here were intended to shed light on how the total force on high rectangular and cylindrical obstacles depends on the *width*, *height* and *shape* of the obstacle. They were also intended to study the *height of the run-up* and the *characteristics of the flow* of the material that is thrown sideways and upward by the impact with the obstacle and may hit power lines or other parts of nearby constructions. It is therefore important to understand this aspect of the flow against obstacles in addition to the loading of the obstacle itself.

Measurements of the loading of obstacles that are immersed in a moving fluid or granular material may be expressed in terms of the dynamic drag coefficient, C_D , which is traditionally

defined as

$$C_D = L / (A \rho_f u^2 / 2), \quad (1)$$

where L is the total observed load, A is the area of the projection of the obstacle upon a plane normal to the flow direction, and ρ_f and u are the density and velocity of the oncoming flow, respectively. For thin free-surface flow against a tall obstacle extending through the flow, the projected area A must be defined appropriately. Furthermore, the upstream velocity is not a single uniquely defined number as it may be expected to depend on distance normal to the bed due to bed friction. Here, C_D will be defined as

$$C_D = L / (B h \rho_f \bar{u}^2 / 2), \quad (2)$$

where B is the width of the obstacle, and h and \bar{u} are the thickness and *depth-averaged* velocity of the undisturbed oncoming flow, respectively. This definition in terms of h was chosen because the momentum flux against the obstacle that gives rise to the impact pressure only comes from the upstream flow depth and the run-up on the obstacle does not in principle add to this momentum flux.

The dynamic pressure in a rapidly moving dry-snow avalanche is typically assumed to vary with the density and velocity as $\sim \rho_f \bar{u}^2$ (SLF, 1990; Norem, 1990). This implies a relatively small variation of C_D with velocity if the area affected by the pressure scales with Bh , independent of the velocity. The dynamics of shallow, free-surface gravity flows are characterised by the Froude number

$$\mathbf{Fr} = \frac{\bar{u}}{\sqrt{\cos \psi g h}}, \quad (3)$$

where ψ is the slope of the terrain and g is the acceleration of gravity. The Froude number of the dense core of natural, dry-snow avalanches is on the order of 5–10 (Issler, 2003). Due to the rapid increase of the dynamic pressure with velocity and because of the high velocities that may be reached by dry-snow avalanches, drag forces for high Froude number flow are most important for design criteria for structures that need to withstand the impact of such avalanches.

Granular flow against immersed objects has been studied in a number of laboratory experiments and more recently in numerical simulations in order to obtain data for formulating and validating design criteria for various structures. Wieghardt (1974, 1975) performed a series of experiments with partially immersed rods, which were dragged through sand. He found that the drag force was comparatively independent of the velocity for Froude numbers, $\mathbf{Fr} = u/\sqrt{gh}$, in the range 0–2, where u denotes the velocity with which the rod was dragged through the sand and h denotes the immersion depth. In this case, the drag on the rod is mainly caused by sliding friction interactions, which may be expected to be relatively independent of velocity. In the higher end of the Froude number range considered by Wieghardt, the drag started to rise as $\sim \mathbf{Fr}^2$, indicating a velocity squared dependence in the more inertial flow regime at the higher Froude numbers. For cylindrical rods, his experiments yielded a dynamic drag coefficient $C_D \approx 6$ for $\mathbf{Fr} \approx 2$ (value adapted to the form of (2)). Chahata and others (2003) obtained similar velocity independence for slow frictional flow.

Design criteria for constructions that need to withstand the impact of debris flows have been studied by several authors. Based on Lichtenhahn (1973), some European torrent control authorities recommend that the impact force per unit width on structures in mountain torrents be estimated according to the formula

$$L/B = f \frac{1}{2} \rho_{\text{H}_2\text{O}} g h_{\text{max}}^2, \quad (4)$$

with the factor f in the range 7–11 (or 7–10), where h_{max} is the “maximum surge depth” and $\rho_{\text{H}_2\text{O}}$ is the density of water. Similar criteria are given by Armanini (1997)

$$L/B = f \frac{1}{2} \rho_f g h_{\text{max}}^2, \quad (5)$$

with the factor 7–11 in (5) replaced by 9 (value adapted to the form of (4)), and using the density of the flowing material, ρ_f , rather than that of water, $\rho_{\text{H}_2\text{O}}$. The formulation of Armanini (1997) is based on a flow velocity determined from dam break theory and is, therefore, limited to low Froude number flow, as may also be assumed to be the case for the design criteria

of Lichtenhahn (1973). Scotton and Deganutti (1997) reported the results of laboratory experiments with slurries of water and coal where the maximum impact pressure on a wall perpendicular to the flow direction was found to be in the range $(2.5-7.5)\rho_f g h$ for low Froude number flow with \mathbf{Fr} near 1. It may be noted that Equation (5) may be written

$$L/B = (f/\mathbf{Fr}^2)h_{\max} \frac{1}{2} \rho_f \bar{u}^2, \quad (6)$$

showing that the above expressions for L/B imply that the drag coefficient C_D must vary as $C_D \sim \mathbf{Fr}^{-2}$ in order for equations (2) and (6) to be consistent with each other. These studies are all for wide obstructions to the flow, such as retaining dams, and are, therefore, not directly applicable to narrow obstacles where flow around the obstacle is of importance.

Design criteria where the impact force depends on velocity have been proposed for debris flows with higher velocities. Hungr and others (1984) recommended the formula

$$L = A\rho u^2, \quad (7)$$

where A is the cross sectional area of the flow, for impact on surfaces that are perpendicular to the flow direction. This expression is similar to the formulation of Norem (1990) for dry-snow avalanches. Armanini and Scotton (1993) and Daido (1993) also propose expressions where the impact against a wall is assumed to vary as u^2 .

For high velocities, the drag on obstacles may depend on whether the flow has a free surface or is restricted in the lateral direction as in hoppers or closed channels. It is also important to differentiate between the impact on wide walls, such as catching dams, on one hand, and the drag force on narrow obstacles, such as masts, on the other. Wassgren and others (2003) estimated dynamic drag coefficients for suspended obstacles by numerical simulations for a wide range of conditions for dilute granular flows in the absence of a free surface and found C_D in the range 1–2.5, which is equivalent to a $\sim u^2$ dependence of the drag under these conditions. Buchholtz and Pöschel (1998) obtained similar results from simulations with a high stream velocity, but at lower velocities they found that the drag force varied less rapidly with u .

Recent laboratory experiments with impact forces on debris flow breakers over a very wide range of velocities show that the drag coefficient C_D is a decreasing function of the Froude number, which may be approximated by the empirical formula $C_D = 9 \mathbf{Fr}^{-1.2}$ (value adapted to the form of (2)) for $1 < \mathbf{Fr} < 15$ (Holzinger and others, 2003; Holzinger and Hübl, 2004). This approximation yields C_D in the range 4–6 for $1.5 < \mathbf{Fr} < 2$, in rough agreement with Wieghardt (1974, 1975). It yields C_D in the range 1–2 for $3.5 < \mathbf{Fr} < 6$, which is in agreement with measured and SPH simulated impact forces of a water surge against an obstacle (Gómez-Gesteira and Dalrymple, 2004). This indicates that impact forces in granular flows become more similar to such forces in ordinary fluid flow in the inertial flow regime which may be assumed at higher Froude numbers. For very high Froude numbers, $10 < \mathbf{Fr} < 15$, the empirical formula of Holzinger and Hübl yields C_D in the range 0.35–0.6.

The possible variation of C_D with the Froude number is important for design criteria that are appropriate for constructions in the middle of avalanche paths where impact forces due to dry-snow avalanches with very high velocities need to be taken into account. A downward trend in C_D with increasing Froude number may partly counteract the traditionally assumed variation of the dynamic pressure with the square of the flow velocity, leading to more moderate, or perhaps more appropriately said less extreme, drag forces at very high velocities. The experiments described here were carried out at a high Froude number in order to explore this question.

Design of the experiments

The experiments were carried out in the 7.5 m long chute of the Hydraulics and Environmental Engineering Dept. of the University of Pavia (Figure 2).

[Figure 2 about here.]

The chute is 35 cm wide and has 50 cm high perplex side walls to allow for observations of the flow from the sides. The smooth metal bottom of the chute was lined with plywood plates

for these experiments in order to provide more bottom friction. The uppermost part of the chute was used as a storage compartment for the granular material, which was released down the flow channel with a manual lock gate through a 7 cm high opening. This provided for a relatively steady stream of material with a duration of a few seconds down the lowermost 6 m of the chute. The slope of the chute was $\psi = 34^\circ$ in all the experiments.

The experimental granular material was glass beads (ballotini) with mean particle size $90 \mu\text{m}$, density 2500 kgm^{-3} (bulk density $\approx 1500 \text{ kgm}^{-3}$, estimated density during flow $\rho_f \approx 1380 \text{ kgm}^{-3}$). About 92 kg of the material were release in each experiment, corresponding to a volume of 0.061 m^3 . This is the same material as was used in series of laboratory experiments that have been carried out in recent years for studying the interaction between granular avalanches and obstacles (Hákonardóttir and others, 2003; Hákonardóttir, 2004).

The flow speed was measured by tracking dark tracer particles, 3–5 mm in size, that were mixed with the ballotini, with a high speed video camera with a rate of 240 or 120 frames per sec. Another video camera with a rate of 16 frames per sec. was used to film the experiments from the side or from below depending on the experiment.

The flow depth was measured with an optical distance sensor from Leuze electronic (ODS 96 M/D-5020-600-222) that uses infrared light to measure the distance to a surface. It provides a stream of digital distance measurements at a rate of 51 measurement per sec. and has a resolution of $\leq 0.5 \text{ mm}$ and a light spot diameter of 10 mm.

Square blocks and cylinders with varying width and height were mounted near the lower end of the chute in front of a DS Europe, SERIES 535 QD, load gauge with a sampling rate of 250 measurements per sec. The gauge has a range of 0–118 N and an accuracy of about $\pm 0.04 \text{ N}$ according to the specifications of the manufacturer. The top end of the gauge was located about 20 cm from the lower end of the chute (Fig. 3).

[Figure 3 about here.]

The lowest obstacles were lower than the load cell. A metal bracket was mounted on the load cell in order to protect the load sensor from being affected by material that flowed over the

obstacle in this case (*cf.* Fig. 3, right). Thus, the observed load is in all cases only caused by material that impacts the obstacle itself and is not influenced by material that is thrown sideways or upwards in the impact with the obstacle. This made it possible to investigate in detail how the total load depends on the height of the obstacle beyond the upstream depth of the oncoming flow.

Datum flow

Several experiments were performed to observe the depth and velocity of the flow near the lower end of the chute where the obstacles were located and in order to verify the repeatability of the experiments. The flow front started as a thin sheet that grew rapidly in thickness over 1.5–2 s to a steady level of 10–13 mm that was maintained over 2–2.5 s after which the flow slowed down and thinned out.

The shape of the flow front varied a little from experiment to experiment due to the manual opening of the lock gate. The total volume of material was also slightly variable between experiments depending on a small amount of remaining material in the compartment below the chute where the material accumulated after flowing down the chute. The height of the opening of the storage compartment at the top of the chute was exactly 7 cm in all the experiments and thus the flow rate into the chute during the near-steady flow phase was consistent in all the experiments irrespective of the small variations of the shape of the flow front and in the total volume of the material.

Figure 4 shows depth measurements from 35 experiments (both the experiments with mast-like obstacles that are the subject of this paper and also experiments with other types of obstacles that are not described further here). The measurements from each experiment have been shifted in time so that the times when the depth reaches $0.5h_s$, where h_s is the estimated flow depth during the near-steady flow phase for each experiment, coincide.

[Figure 4 about here.]

The figure also shows a continuous curve determined from all the measurements (thick curve). This curve rises from zero during 1.8 s to a constant flow depth of $h_s = 11.4$ mm, which is maintained for 2.3 s and then subsides exponentially with a time constant of about 1 s.

The surface flow velocity was measured by tracking black 3–5 mm diameter tracer particles that were mixed with the white ballotini material using a high speed video camera operated at a rate of either with 240 or 120 frames per sec. depending on the experiment (Fig. 5). Experiments with the high speed camera filming the flow directly from above for this purpose were carried out on both the first and the last day of the experiments. The flow thickness was measured as a function of time during these experiments as described above.

[Figure 5 about here.]

A 2.5x1 cm grid at the bottom of the chute was filmed with the high speed camera in the same position as in the experiments where the particles were tracked, making it possible to convert a measured shifting between photographs from pixels to absolute distance. The distance was corrected for the small difference in distance between the grid at the bottom of the chute and position of the surface of the flow.

The velocity was estimated as a function of time by computing the cross-correlation function for each pixel row in the downstream direction between successive pairs of photographs, summing all the downstream cross-correlation functions in the direction transverse to the flow.

[Figure 6 about here.]

The cross-correlation computations were done for every image within the time-window considered for each experiment, using the following image in time to form an image pair for experiments that were video-filmed with a rate of 120 frames per sec., and the third next image for experiments that were video-filmed using 240 frames per sec., in order to obtain a larger lag and consequently a better relative accuracy in the velocity estimate. The cross-correlation was computed after a moving average with length of approximately 100 pixels had been subtracted from the signal in the digital 640x198 pixel high speed video images and after

tapering the ends of the resulting time-series with a cosine taper of a corresponding length. An example is shown in Figure 6. Each accumulated cross-correlation function showed a well defined maximum at a spatial lag, which corresponds to the average surface velocity of the flow over the time elapsed between the images.

Figure 7 shows the surface velocity as a function of time for the two datum experiments for which the velocity was estimated.

[Figure 7 about here.]

The figure shows about 800 velocity estimates from each experiment, of which 300–500 are from near-steady flow phase. The measurements from the second experiment stop before the end of the flow is reached because the high speed camera was running at 240 fps in this case and the camera memory holds a maximum of 850 images, which corresponds to about 3.5 sec. Neighbouring spatial lag estimates between the pairs of images in each experiment were quite consistent, rarely varying by more than 1–2 pixels (≈ 0.5 mm) between adjacent pairs. The figure shows that the surface velocity during the near-steady flow phase is approximately equal to $u_t = 4.3 \pm 0.1 \text{ ms}^{-1}$ for both experiments and that the velocity is close to being constant with time during this phase of the flow, except that there seems to be a slight increase in the velocity by about 0.1 ms^{-1} just before the end of the near-steady phase. This indicates that the experiments are repeatable and that there was not a noticeable drift in the material properties over the three day period of the experiments, as is also indicated by the depth measurements.

The Froude number of free-surface flows should be computed from the depth-averaged flow velocity, \bar{u} , rather than the surface flow velocity, u_t . Impact forces should, on the other hand, be computed from a weighted average of the speed over the flow depth, $h\bar{u}_w^2 = \int_{z_b}^{z_t} u^2 dz$, which weights depth ranges with high speeds more than depths with low speeds and is thus slightly higher than \bar{u} in this case. The exact variation of the flow velocity with depth within the flow is not known beyond the surface value, and possibly also the depth-averaged value, which is not accurately known here. A numerical value for \bar{u}_w can, therefore, not be directly computed from available measurements. Assuming that the velocity rises sharply in a very

20021048-11

thin shear layer at the base and rises approximately linearly over most of the rest of the flow depth, one may estimate \bar{u}_w during the near-steady phase as $\bar{u}_w \approx \sqrt{\bar{u}^2 + (u_t - \bar{u})^2/3} \approx \bar{u}$ to two significant digits for values of u_t as given above and rough estimates of \bar{u} from continuity. The value of \bar{u}_w is thus not significantly different from \bar{u} in this case.

Partly based on additional velocity measurements from experiments with deflecting dams that are not described here, the depth-averaged velocity was estimated as $\bar{u} = \bar{u}_w = 4.1 \text{ ms}^{-1}$ for both varieties of the depth-averaged velocity during the near-steady phase of the flow. This estimate is partly based on a subjective evaluation of the available measurements and is considered accurate to $\pm 0.2 \text{ ms}^{-1}$. The density of the granular material during flow was estimated as $\rho_f \approx 1380 \text{ kgm}^{-3}$ based on continuity and the measured variation of the flow thickness and velocity with time. This is slightly lower than the measured bulk density of about 1500 kgm^{-3} for the non-moving material.

The Froude number of the near-steady part of the flow may be estimated from the above estimates of h_s and \bar{u}_s as $\text{Fr} = \bar{u}_s / \sqrt{\cos \psi g h_s} = 13.5$. As mentioned before, the Froude number of the dense core of natural dry-snow avalanches is believed to be on the order of 5–10.

Impact forces against rectangular and cylindrical obstacles

The impact with the obstacle produced a qualitatively similar flow pattern in cases when the obstacle was higher than a few flow thicknesses (Fig. 8).

[Figure 8 about here.]

The granular material was thrown upwards and to the sides, producing an airborne, fan-shaped stream of material, which widened in the downstream direction and maintained a fixed geometry during the near-steady phase of the flow.

Table 1 lists the type, width, B , and height, H , of the obstacles, the run-up at the center of the obstacle, H_r , the maximum bed-perpendicular height of the fan generated by the material that is thrown sideways and upward from the obstacle, H_f , the observed median and maximum

load, L and L_{\max} , and the dynamic drag coefficient, C_D , for each experiment (see also Figs. 10 and 11 where the measured load as a function of time and the median load during the near-steady flow phase are shown for each experiment).

[Table 1 about here.]

The obstacle heights varied from about twice the flow depth to more than 20 times the flow depth, which was higher than the observed run-up, and the width of the obstacles varied from about twice the flow depth to about 7 times the flow depth.

Figure 9 shows a qualitative drawing of the fan generated in the impact of the flow with the obstacle together with the run-up (H_r) and the throw height (H_f) for obstacles with $H \geq 8$ cm, for which the flow is not disturbed by the bracket that was used in the experiments with the lowest obstacles.

[Figure 9 about here.]

It is seen that the run-up and the throw height are both relatively independent of the width and shape of the obstacle. The observed throw height perpendicular to the chute was in the approximate range 15–30 cm, which is about 15–30% of the height corresponding to the kinetic energy of the flow.

[Figure 10 about here.]

[Figure 11 about here.]

Figure 10 shows the measured load on the rectangular blocks and Figure 11 shows the load on the cylinders. Both figures also show the estimated continuous thickness of the datum flow as a function of time (*cf.* Fig. 4). The figures show that the measured load and the estimated flow depth vary with time in a similar manner as expected. The initial rise of the load has a similar form as the rise in the flow depth, which indicates that the speed of the flow front is approximately the same as the speed of the central part of the flow with near-steady depth. The

load during the tail of the flow decreases more rapidly than the flow depth, which indicates that the flow slows down with decreasing flow depth in the tail. A plot of the load divided by the flow depth squared (not shown) demonstrates that this ratio varies by a factor smaller than two in the tail while the load is reduced by more than an order of magnitude, except for the experiment with the largest block where the load was comparatively high near the end of the tail due to a pile of granular material that remained above the block at the end of the experiment.

Figure 12 shows the dynamic drag coefficient, C_D , as tabulated in Table 1, as a function of the mast height, H , normalised with the flow depth, h_s , for blocks and cylinders.

[Figure 12 about here.]

The figure shows that for obstacle heights that exceeded about 3 flow depths, C_D is in the range 0.7–0.85 for blocks and 0.5–0.55 for cylinders, and varies little with the width or height of the obstacle. The drag on the lowest obstacles is much smaller, indicating the effect of the buildup of a stationary wedge near the bottom of the chute, which deflects the flow upwards and to the sides, thereby shielding the obstacle partly from the impact with the flow.

Discussion

The load measurements show that the drag coefficient, C_D , and thus the total force on the obstacle, does not depend much on the obstacle height for heights that exceeded about 3 flow depths, which is much lower than the run-up on the highest obstacles. For a wide range of obstacle heights exceeding about 3 flow depths, the total force on the rectangular obstacles is of similar magnitude as the dynamic pressure, $\frac{1}{2}\rho_f u^2$, acting over an area corresponding to the width of the obstacle and the upstream depth of the flow. The total force was about 30% lower for cylindrical compared with rectangular obstacles, which is similar as found in the numerical simulations of Buchholtz and Pöschel (1998).

The fan-shaped stream of material that is thrown upwards and to the sides by the impact is an important observation that may have practical design implications since the stream may hit power lines or other parts of nearby constructions.

For obstacle heights that exceeded about 3 flow depths, the dynamic drag coefficient C_D was found to be in the range 0.5–0.85 for both rectangular and cylindrical obstacles for the Froude number $\mathbf{Fr} = 13.5$. These values are substantially lower than those found in experiments with granular flow at lower Froude numbers, which are discussed in the Introduction, or values implicitly assumed in traditional design guidelines (SLF, 1990; Norem, 1990), which are based on $C_D = 2$ for rectangular obstacles. Our results are in rough agreement with the experimental results of Holzinger and Hübl (2004) for debris flows at high Froude numbers, although the C_D values obtained here are somewhat higher than those obtained from their empirical formula, which yields $C_D \approx 0.4$ for $\mathbf{Fr} = 13.5$ (see the Introduction).

Our results indicate that the impact load of dry-snow avalanches at very high velocities against small obstacles may be overestimated by assuming that a dynamic pressure equal to $\rho_f \bar{u}^2$, or linearly decreasing to zero from this value over the run-up of the avalanche as assumed by SLF (1990), affects the whole area impacted by the avalanche. Our experiments imply that dynamic pressure on the obstacle in the area above about 3 times the flow depth does not add significantly to the total load exerted on the obstacle.

It should be noted that our results mainly apply to very high speeds that are rarely used as a basis for the design of constructions, except high up in the avalanche path. A snow avalanche traveling at $u = 50 \text{ ms}^{-1}$ with a flow depth $h = 1.5 \text{ m}$ will have a Froude number $\mathbf{Fr} = 13$. It is clearly important to determine whether C_D in this case is about 2, as would be implied by the expression $\rho_f \bar{u}^2$, or in the range 0.5–0.85 as indicated by our results, or even as low as about 0.4, which is indicated by the empirical formula of Holzinger and Hübl. Since the material properties of ballotini and snow are different in many ways and because of the difference in scale between the laboratory chute and natural avalanche paths, it is important to investigate this problem further, in particular by a careful interpretation of the results from full-scale

avalanche test sites.

It is noteworthy that impact pressure measurements from the Ryggfonn full-scale avalanche test site include very fast dry-snow avalanches traveling at 40–50 ms⁻¹, which seem to have similar impact pressures as avalanches traveling at substantially lower speeds around 30 ms⁻¹ (Larsen, 1996). Although this may be partly explained by a lower density of the faster avalanches, it could also indicate a lower drag coefficient at the higher Froude numbers that may be assumed to apply for the faster avalanches. These measurements are not trivial to interpret in this context because they are characterised by very sharp peaks in the loading that may correspond to snow clods impacting the load cells. An appropriate impact pressure level to compare with the laboratory experiments discussed here, would be the pressure that is sustained for a time on the order of a second, which would average out the effect of the snow clods. Often it is the maximum impact pressure that is tabulated in reported results from the full-scale experiments rather than the lower pressure level that is sustained for a longer time interval. Gauer and other (submitted) report very high impact pressures of up to 800 kPa for a wet avalanche in April 2005 at Ryggfonn when the avalanche was traveling with a velocity of 25–30 ms, and surprisingly high impact pressures on the order of 100 kPa in the tail of this avalanche when it was traveling at only about 5 ms⁻¹. These observations are hard to explain unless some variation of C_D with velocity is assumed, but it is also likely that cohesion and bridging in the flow of the wet snow against the obstacle plays a role in the dynamics of this avalanche.

An interesting aspect of this study is that our experiments indicate that interpretation of impact pressure measurements from full-scale experimental sites, for example in Ryggfonn in Norway and Vallée de la Sionne in Switzerland, is far from trivial. If C_D depends on velocity and if the impact, in addition, depends quite a bit on the height of the obstacle/mast, then the measured impact pressure will depend in a complicated manner on obstacle geometry, flow thickness and other such aspects of the flow, in addition to the density and velocity of the oncoming flow. This must mean that interpretation of impact pressure measurements in terms

of density or other flow characteristics is harder than has perhaps been appreciated until now.

Impact forces of natural snow avalanches on obstacles are observed to be characterised by some important features that were not analysed in the laboratory experiments described here. In particular, high peaks in the loading are believed to be caused by the impact of large snow clods on the obstacles and even higher impacts may be caused by impacts of rocks, tree trunks and other debris that is advected with the snow in many avalanches. In spite of this, the experiments provide information about the nature of granular flow around obstacles, which may be useful for engineering applications.

Acknowledgements

This study was carried out with support from the European Commission (the research project *Satsie*, grant EVG1-CT-2002-00059), the Italian Ministry of Instruction, University and Research (contract PRIN 2003) and the Icelandic Avalanche Fund. Assistance from Dario Brivio, Federica Cappabianca and Alice Di Paolo during the execution of the experiments is gratefully acknowledged. We thank Dieter Issler and Peter Gauer for useful discussions about the subject of this paper.

References

- Armanini, A. 1997. On the dynamic impact of debris flows. *In* Armanini A. and M. Masanori, eds., *Recent developments on debris flows*, Lecture notes in earth sciences, **64**, Berlin, etc., Springer Verlag, 208–226.
- Armanini, A. and P. Scotton. 1993. On the dynamic impact of a debris flow on structures, *Proc. of XXV IAHR Congress, Tokyo, Tech. Sess. B, III*, 203–210.
- Buchholtz, V. and T. Pöschel. 1998. Interaction of a granular stream with an obstacle. *Granular Matter*, **1**, 33–41.

- Chehata D., R. Zenit and C. R. Wassgren. 2003. Dense granular flow around an immersed cylinder. *Phys. of Fluids*, **15**(6), 1622–1631.
- Daido, A. 1993. Impact force of mud debris flows on structures. *Proc. of XXV IAHR Congress, Tokyo, Tech. Sess. B, III*, 211–218.
- Gauer, P., D. Issler, K. Lied, K. Kristensen, H. Iwe, E. Lied, L. Rammer and H. Schreiber. submitted. On full-scale avalanche measurements at the Ryggfonn test site, Norway. *Cold Reg. Sci. Technol.*, this issue.
- Gómez-Gesteira, M. and R. A. Dalrymple. 2004. Using a three-dimensional smoothed particle hydrodynamics method for wave impact on a tall structure. *J. of Waterway, Port, Coastal and ocean Eng.*, **130**(2), 63–69.
- Hákonardóttir, K. M., A. J. Hogg, T. Jóhannesson, G. G. Tómasson. 2003. A laboratory study of the retarding effects of braking mounds on snow avalanches. *Journal of Glaciology*, **49**(165), 191–200.
- Hákonardóttir, K. M. 2004. *The Interaction Between Snow Avalanches and Dams*. PhD thesis, School of Mathematics, University of Bristol.
- Holzinger, G., J. Hübl, M. Bacher, M. Friedrich, P. Mayr, R. Mayr, K. Platzer, R. Svaton and F. Zott. 2003. *Kleinmaßstäbliche Modellversuche zur Wirkung von Murbrechern*. Wien, Universität für Bodenkultur Wien, report no. 50.
- Holzinger, G. and Hübl, J. 2004. Belastung eines Murbrechers—Abgeleitet aus Laborversuchen [Impact forces on a debris flow breaker—Derived from laboratory experiments]. In Mikos, M. and D. Gutknecht, eds., *10. Kongress Interpraevent 2004, 24.–27. Mai 2004*, Riva del Garda, Trient, **3**, 131–139.
- Hungr, O., G. C. Morgan, and R. Kellrehals. 1984. Quantitative analysis of debris torrent hazard for design of remedial measures. *Can. Geotech. J.*, **21**, 663–667.
- Issler, D. 2003. Experimental information on the dynamics of dry-snow avalanches. In Hutter K. and N. Kirchner, eds., *Dynamic Response of Granular and Porous Materials Under Large and Catastrophic Deformations*. Lecture Notes in Applied and Computational Me-

- chanics, **11**, Berlin, Springer, 109–160.
- Larsen, J. O. 1996. *Ryggfonn-prosjektet. Skredlaster på konstruksjoner*. Oslo, Norwegian Geotechnical Institute, internal report.
- Lichtenhahn, C. 1973. Die Berechnung von Sperren in Beton und Eisenbeton. Kolloquium über Wildbachsperren. *Mitteilungen der Forstlichen Bundesversuchsanstalt, Wien*, **102**, 91–127.
- Norem, H. 1990. *Ryggfonn prosjektet; Forslag til beregning av dimensionerende snøskredlast mot mastekonstruksjoner*. Oslo, Norwegian Geotechnical Institute, Rapport nr. 581200-16.
- Scotton, P. and Deganutti, A. M. (1997). Phreatic line and dynamic impact in laboratory debris flow experiments. In Cheng-lung Chen, ed., *Debris-Flow Hazards Mitigation: Mechanics, Prediction, and Assessment (Proc. of 1st Int. Conf. held in San Francisco, California, August 7–9, 1997)*, 777–786.
- SLF. 1990. *Berechnung von Fliesslawinen - eine Anleitung für Praktiker mit Beispielen*. Davos, SLF-Mitteilung Nr. 47.
- Wassgren, C. R., J. A. Cordova, R. Zenit and A. Karion. 2003. Dilute granular flow around an immersed cylinder. *Phys. of Fluids*, **15**(11), 3318–3330.
- Wieghardt, K. 1974. Forces in granular flow. *Mech. Res. Commun.*, **1**, 3–7.
- Wieghardt, K. 1975. Experiments in granular flow. *Annu. Rev. Fluid Mech.* **7**, 89–114.

Tables

Exp. #	type of obst.	B (cm)	H (cm)	H_r (cm)	H_f (cm)	L (N)	L_{\max} (N)	C_D (1)
10	b	8	34.0	13	21	8.9	9.3	0.84
7	b	4	32.0	14	21	4.2	4.3	0.80
1	b	4	8.0	(31)	31	3.9	4.1	0.74
4	b	4	4.0	—	—	3.7	3.9	0.69
2	b	4	2.0	—	—	2.1	2.2	0.40
8	b	2	26.5	18	23	2.0	2.1	0.75
12	b	1	23.5	17	27	—	—	—
11	c	8	34.2	19	26	—	—	—
6	c	4	8.0	(28)	29	2.6	2.8	0.49
5	c	4	4.0	—	—	2.6	2.8	0.49
3	c	4	2.0	—	—	1.4	1.5	0.27
9	c	2	19.0	19	27	1.5	1.5	0.56

Table 1: Experiments to determine total load on mast-like obstacles. Type “b” means a rectangular block and “c” a cylinder, B is the width of the obstacle, H is the height of the obstacle, H_r and H_f are the height of the run-up of the flow on the front side of the obstacle and the maximum bed-perpendicular height of the fan that is thrown sideways and upward from the obstacle, respectively (see Fig. 9), L and L_{\max} are the median load during the near-steady flow phase and the maximum load near the end of this phase in N, and the last column C_D gives the computed dynamic drag coefficient $C_D = L / (B h_s 0.5 \rho_f \bar{u}_s^2)$, where $h_s = 11.4$ mm and $\bar{u}_s = 4.1$ ms⁻¹ are the estimated thickness and the depth-averaged velocity of the near-steady part of the flow, and $\rho_f = 1380$ kgm⁻³. The load was not measured in experiments 11 and 12 due to equipment failure, and the run-up and throw height are not tabulated for experiments 2–4 because the flow over the obstacle was affected by the bracket protecting the load cell in these experiments. The H_r values in are enclosed in parentheses for experiments 1 and 6 because the obstacle is lower than the run-up in these experiments.

Figures

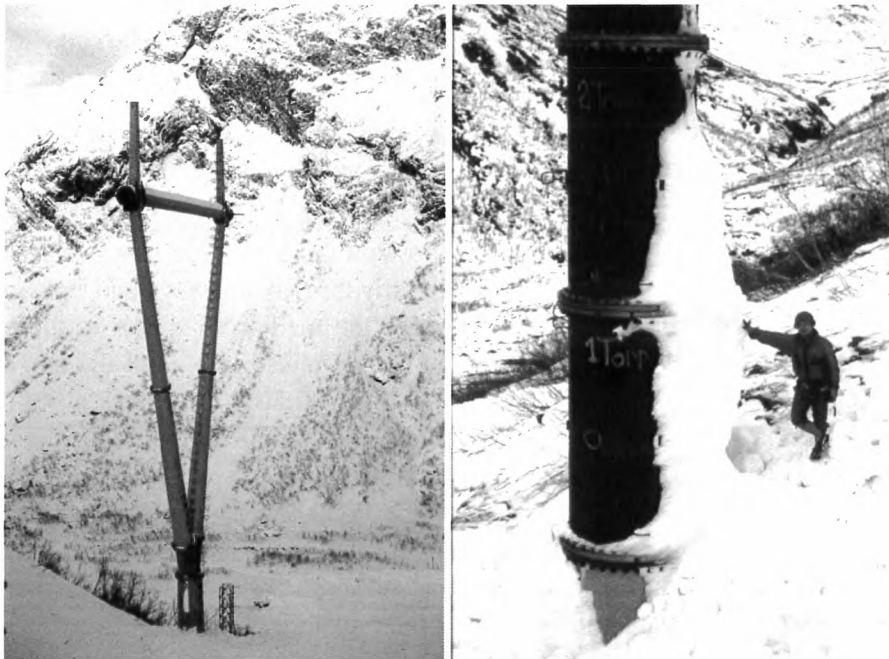


Figure 1: A mast built for studying impact forces on electrical power lines (left), and an instrument tower (right) that has just been hit by an avalanche in the Ryggfonna avalanche path in western Norway (photographs from Norwegian Geotechnical Institute). The mast was partly destroyed by an avalanche in 1991 and the lower part was rebuilt to construct the instrument tower at the same location.



Figure 2: The 7.5 m long experimental chute with an attached plywood plate for the mounting of deflecting dams. A wedge with a 60° top angle and a deflecting dam with a 20° deflecting angle are mounted on the chute. The masts were mounted about 20 cm above the lower end of the chute.

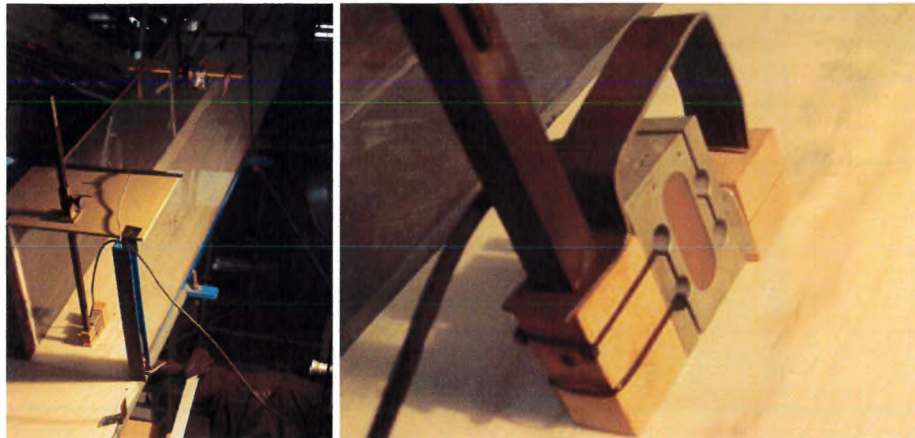


Figure 3: The setup of the experiments with mast-like obstacles seen from behind (left) and a close-up of a 4 cm high obstacle where the upper part of the load cell was shielded from impact with the flow with a metal bracket (right).

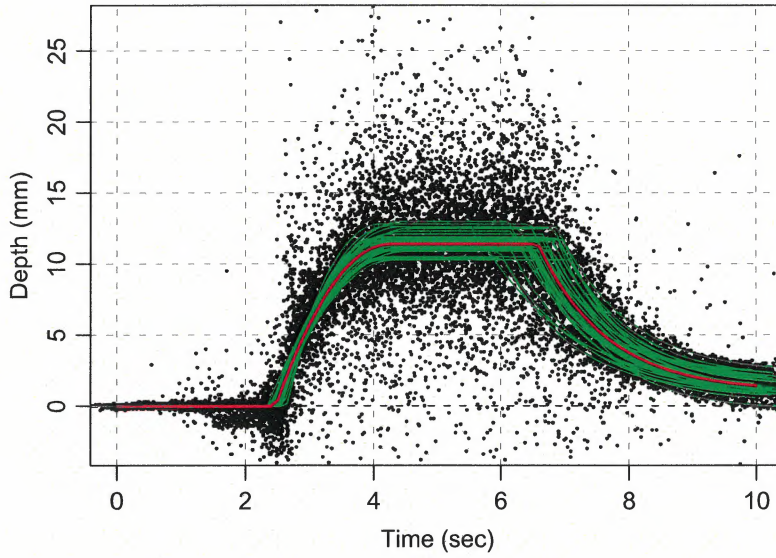


Figure 4: Flow depth measurements (symbols) that have been synchronised in time by making continuous curves fitted to the data from each experiment (thin curves) coincide at the points where they reach $0.5h_s$ near the front. Also shown is the continuous curve determined from all the points simultaneously (thick curve).

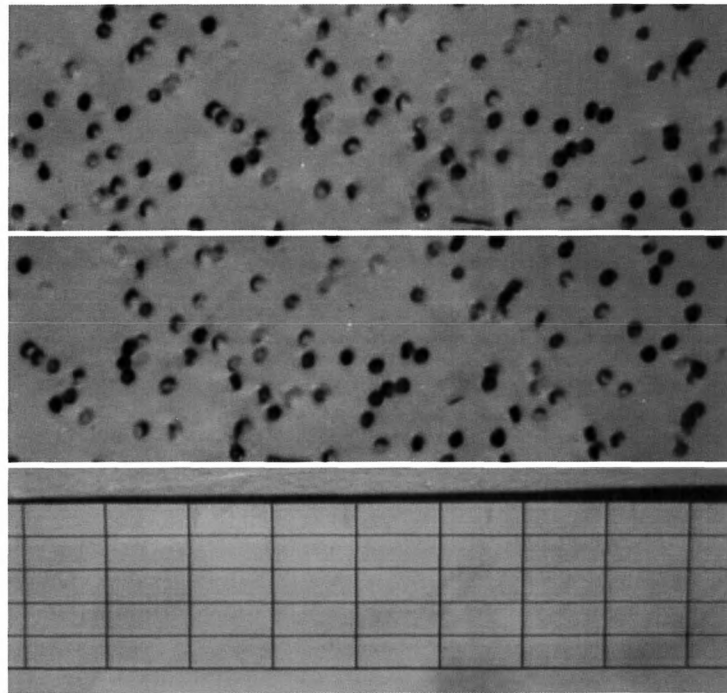


Figure 5: Top two panels: Two frames from the high speed video camera taken from above the flow during the near-steady flow phase of the datum experiment carried out at the end of the last day of experiments. The lower frame is $3/240$ sec. after the upper frame. The flow direction is from the right to left. Bottom panel: A 2.5×1 cm grid on the bottom of the chute with the high speed camera in the same position as in the experiment corresponding to the two upper frames. It is easily seen that the configuration of dark tracer particles in the second frame is shifted downstream with respect to the configuration of the particles in the first frame by somewhat more than two grid spacings (5 cm) in the bottom panel.

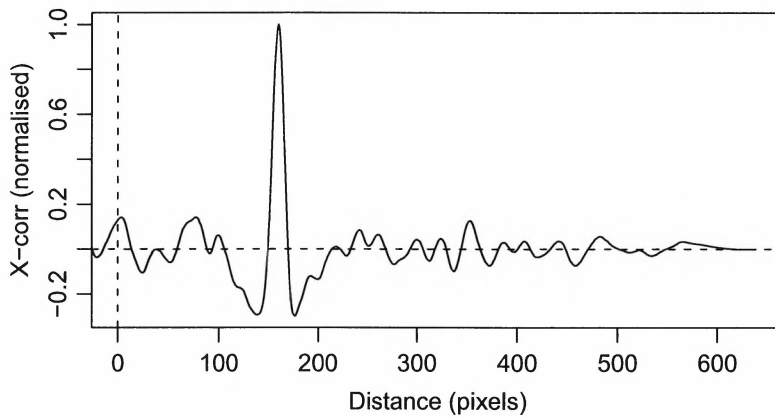


Figure 6: The cross-correlation function in the downstream direction corresponding to the two photos in Fig. 5 (accumulated in the direction transverse to the flow as described in the text). The cross-correlation function is only shown for positive (downstream) lags of the first (upper) photograph with respect to the second (lower) photograph.

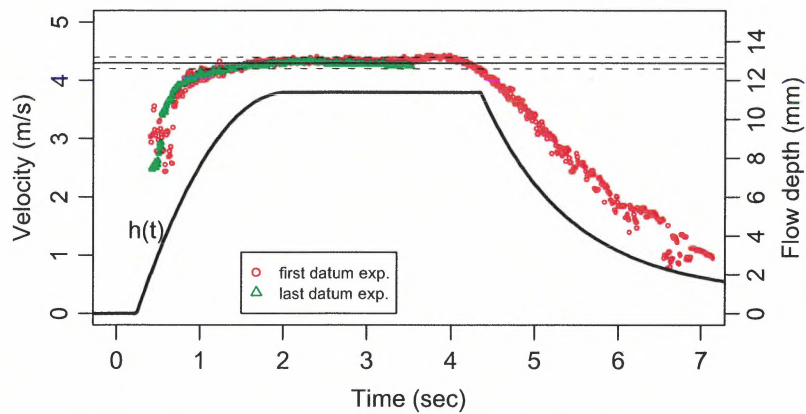


Figure 7: Surface flow velocity as a function of time for two datum experiments that were carried out on the first and last day of the experiments (symbols). The solid horizontal line shows the velocity 4.3 ms^{-1} and the dashed lines are 0.1 ms^{-1} above and below this value. The continuous curve shows the estimated flow depth as a function of time (the thick curve from Fig. 4, scale on the right of the figure).

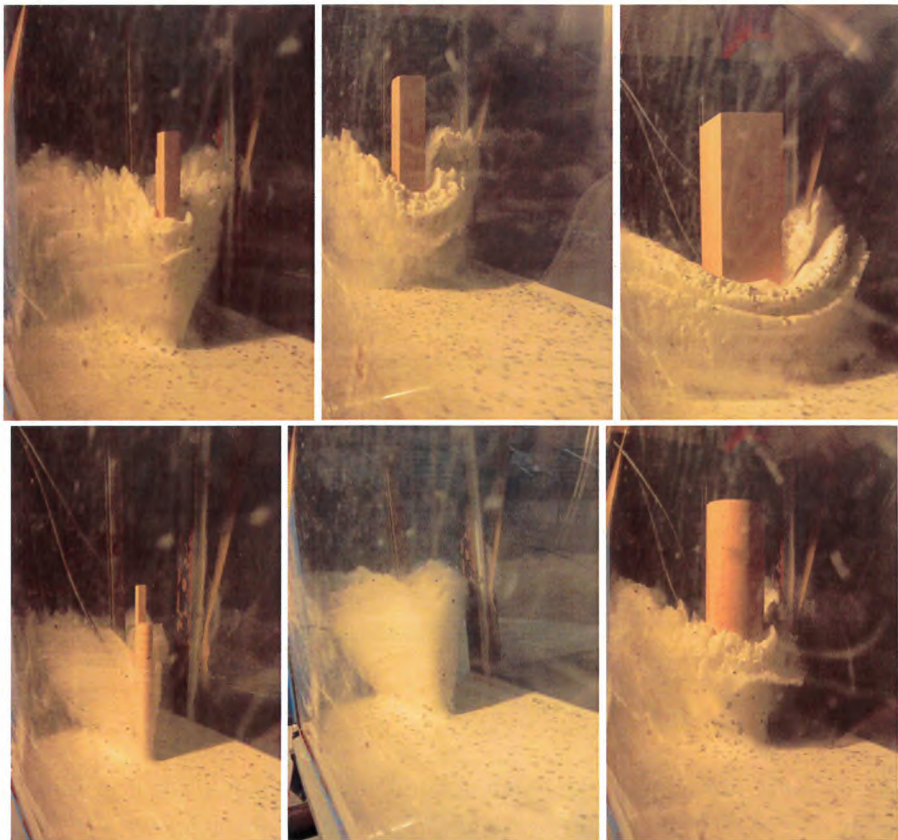


Figure 8: Photographs from the near-steady flow phase of six experiments with mast-like obstacles. Top row from left to right: blocks with width/heights of 2/26.5, 4/32 and 8/34 cm. Bottom row from left to right: cylinders with width/heights of 2/19, 4/8 and 8/34.2 cm. The cylinder in middle of the lower row did not extend through the flow.

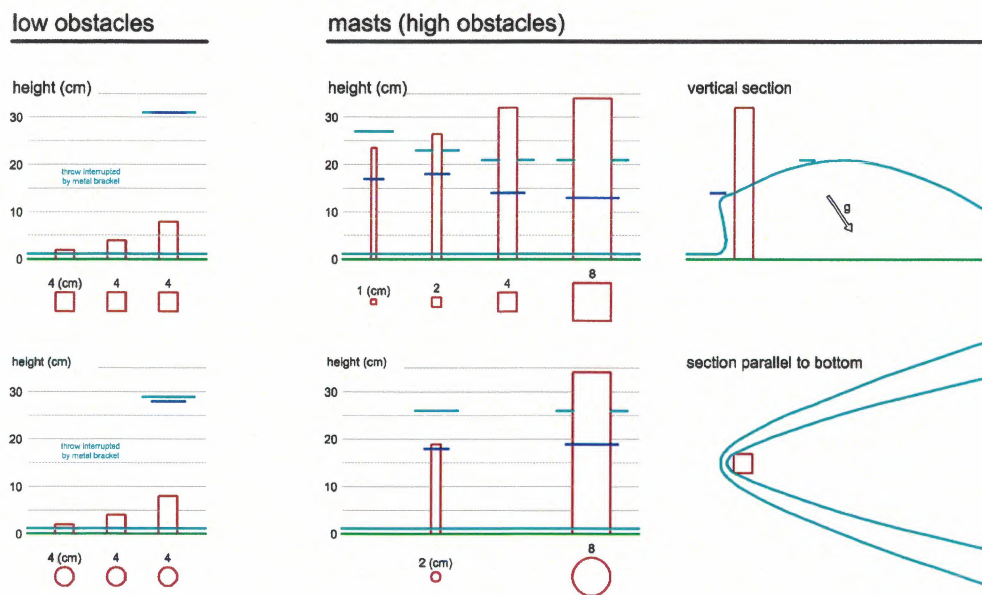


Figure 9: A qualitative drawing of the fan generated in the impact of the flow with the obstacle (right), and the run-up, H_r , and the throw height, H_f , for high obstacles with $H > 8$ cm (center) and low obstacles with $H \leq 8$ cm (left). The definitions of H_r and H_f are indicated on the top right drawing. H_r and H_f are not shown for obstacles with $H < 8$ cm because the flow over the obstacle is disturbed by the bracket protecting the load cell in that case.

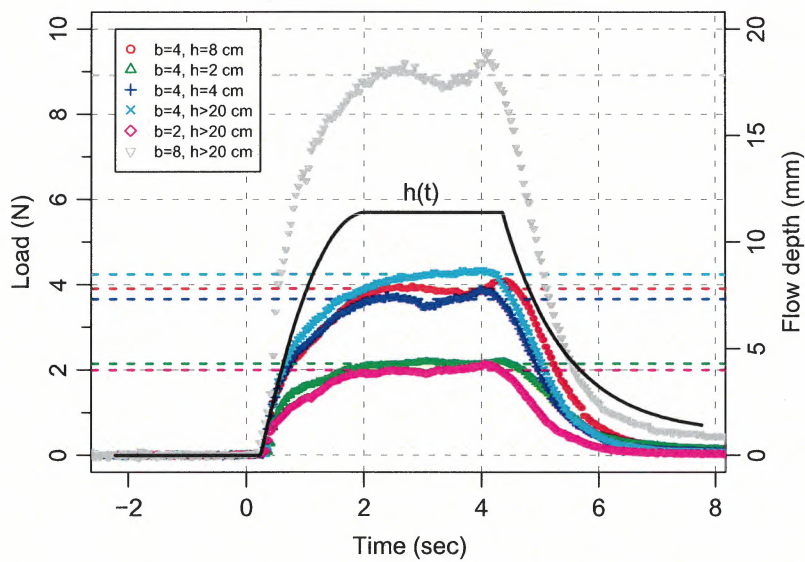


Figure 10: Measured load on rectangular blocks of varying width, B , and height, H . The estimated median load during the near-steady flow phase of each experiment is shown with dashed lines. The estimated flow thickness, $h(t)$, from Figure 4, is also shown (continuous curve).

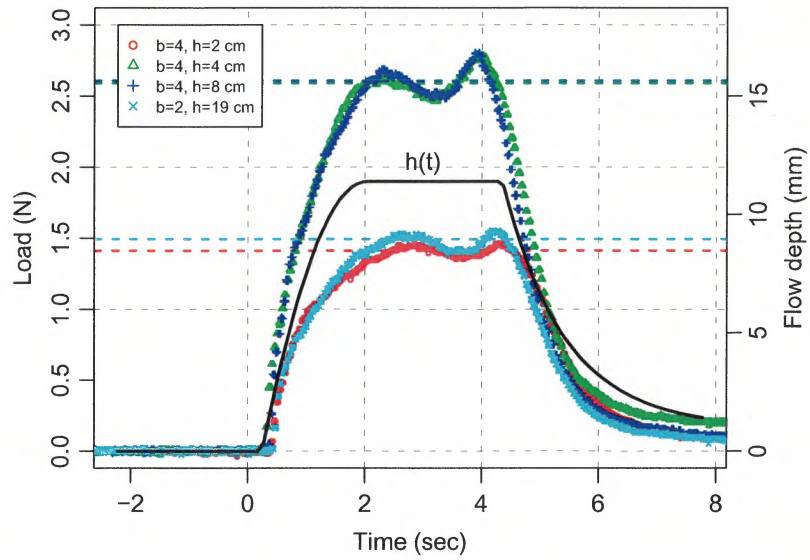


Figure 11: Measured load on cylinders of varying width/diameter, B , and height, H . The estimated median load during the near-steady flow phase of each experiment is shown with dashed lines. The estimated flow thickness, $h(t)$, from Figure 4, is also shown (continuous curve).

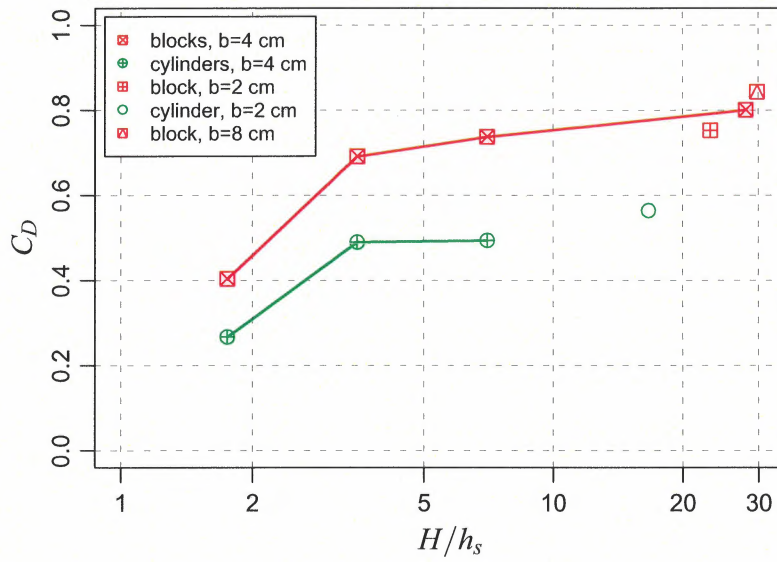


Figure 12: The dynamic drag coefficient, C_D , as tabulated in Table 1 as a function of the mast height, H , normalised with the flow depth, h_s , for blocks and cylinders. Data points corresponding to obstacles with the width $B = 4$ cm are connected with straight lines.

A.7 Paper Submitted to Peer-Reviewed Journal (3)

Keylock, C. J. 2005. Constrained surrogate time series with preservation of the mean and variance structure. Submitted to *Physical Review E*.

Title

Constrained surrogate time series with preservation of the mean and variance structure

Author

C.J. Keylock

Earth and Biosphere Institute, University of Leeds, Woodhouse Lane, Leeds, LS2 9JT,
U.K.

Received 6 August 2005

PACS numbers 05.45.Tp 02.50.Ey 05.40.Ca 89.75.-k

Abstract

A method is presented for generating surrogates that are constrained realizations of a time series but which preserve the local mean and variance of the original signal. The method is based on the popular iterated amplitude adjusted Fourier transform method but makes use of a wavelet transform to constrain behavior in the time domain. Using this new method it is possible to test for local changes in the nonlinear properties of the signal. We present an example for a change in Hurst exponent in a time series produced by fractional Brownian motion.

Distinguishing between linear and nonlinear processes from a time series of system outputs plays an integral role in the detection of deterministic chaos in physical systems. One approach is to formulate a null hypothesis for a specific class of processes and compare the system output to this hypothesis. The surrogate data method is a popular way to establish such a null hypothesis [1] and can be undertaken in two distinct ways: *Typical realizations* are Monte-Carlo generated surrogates from a model that provides a good fit to the data; *Constrained realizations* are surrogates generated from the data values to conform to certain properties of the data (such as its autocorrelative structure). This latter approach is more suitable for hypothesis testing as it does not require the definition of a pivotal test statistic [2]. In order to test the null hypothesis at a level of significance α with a two-tailed test, one can generate $2/\alpha-1$ surrogates which, together with the original data leads to an appropriate number of realizations of the data. If all the surrogates are either greater or less than the original data, the null hypothesis may be rejected at the level α .

An early method for generating constrained realizations conforming to a linear Gaussian, stochastic process [1] that has subsequently seen several applications [3] has been termed the Amplitude Adjusted Fourier Transform (AAFT) method [4]. An AAFT surrogate for a time series $\{x_i\}$, $i = 1, \dots, N$ is found by generating white noise data $\{w_i\}$ and manipulating it so that the sequential order of the ranked values matches that for $\{x_i\}$. The phases of this ordered white-noise sequence are then randomized in the Fourier domain and again rank ordered with respect to the original data. Some limitations with this method due to finite sample sizes and preservation of the Gaussian distribution [5] led [6] to propose an enhanced method known as the Iterated AAFT (IAAFT), which has

proven popular [7]. The squared amplitudes of $\{x_i\}$ are stored and then a random sort of the values in $\{x_i\}$ takes place. The Fourier transform of the random sort is taken and the squared amplitudes are replaced by those for $\{x_i\}$, with the complex phases retained. The Fourier transform is then inverted and rank-ordering is used to map values in this surrogate series to those in $\{x_i\}$. The modification to the spectral behaviour that results from this rank-ordering adjustment is dealt with by iterating this procedure until no further re-ordering occurs. The IAAFT method's popularity is due to its elegance, computational efficiency and ability to discriminate effectively between linear and nonlinear phenomena [4]. In a subsequent paper, a more general approach for constructing constrained surrogate data was proposed [8]. However, the computational time associated with the simulated annealing procedure for this algorithm has meant that it has not been as popular as the original IAAFT method.

More recently, a method for producing typical realizations has been proposed for cyclic data based on time-delay embedding [9]. This is known as the pseudoperiodic surrogates (PPS) method and for this case, the appropriate null hypothesis is that the data have been produced by periodic behavior driven by white noise. Although the surrogates are only typical realizations, the authors argue that their correlation dimension test statistic [10] is pivotal for the hypothesis of periodic behavior and the method seems to work well for this hypothesis. However, as shown in Fig. 1, this approach cannot be used successfully for testing the more common null hypothesis that the data are from a stationary, linear process, where nonlinearity is assessed using the asymmetry [2]

$A(\lambda) = \frac{\langle (x_i - x_{i-\lambda})^3 \rangle}{\langle (x_i - x_{i-\lambda})^2 \rangle^{\frac{3}{2}}}$ where the angled braces indicate ensemble averaging. The IAAFT and our proposed algorithms both accept the null hypothesis for

the stationary case and reject it at the 5 % significance level for the nonlinear process. These results are not surprising because the PPS method is designed to test a different null hypothesis. Because it generates typical realizations, the PPS algorithm is also not constrained to the values in the original dataset and gives a weaker match to the original spectrum than the other methods as is clear in Fig. 2. In particular, note that at low frequencies there has been a significant enhancement of the energy for the two examples based on the Rössler attractor using the PPS method. This problem has been previously noted for AAFT surrogates [6].

Our approach to surrogate generation uses a wavelet transform to preserve local values in the time domain. It has been previously proposed to use wavelets to generate surrogate data [11] but that method was based on a randomisation of the wavelet detail coefficients at a particular dyadic scale. The potential advantage of the wavelet approach is that behavior in the time-frequency plane can be preserved. Hence, randomisation of the coefficients on the time axis offers no clear advantage over the IAAFT, at least for univariate time series. Our method for generating surrogates is wavelet based, but overcomes this deficiency and preserves the patterns in the mean and variance while randomising nonlinear properties of the signal such as the Hurst exponent.

Our algorithm for generating a single surrogate time series proceeds as follows:

- (a) Take the stationary or maximal overlap discrete wavelet transform (MODWT) of the signal over dyadic scales 2^{j-1} $j = 1, \dots, J$. This will produce J sets of detail coefficients $\{D_i^j\}$ each containing N values (because the MODWT is an undecimated transform) and a set of approximation coefficients $\{A_i^j\}$ representing the unresolved scales. In this study we have analysed signals with a length 2^J so that all information (beyond a

constant) is contained in the detail coefficients. The MODWT has the additional useful properties that it is well-defined for any N (not restricted to a multiple of 2^J), and produces detail coefficients and spectra unaffected by circularly shifting the data (i.e. the coefficients are robust to the time at which one breaks into the signal). The variance of the detail coefficients at each level is equivalent to the Fourier spectrum of the signal [12]. The choice of wavelet basis function affects the time-frequency properties of the wavelet decomposition. In order to deal with non stationary signals it is advantageous to use a wavelet with a high number of vanishing moments [12]. The results in Fig. 1 to 4 all use a Daubechies wavelet with 16 vanishing moments [13].

- (b) Obtain a constrained realization of the detail coefficients at each level by applying the IAAFT algorithm (i.e. apply the IAAFT as if each set of detail coefficients was a time series in its own right) to yield surrogate detail coefficients $\{D_i^j(surr)\}$, $i = 1, \dots, N$; $j = 1, \dots, J$. Because this is a constrained realization method the values of the detail coefficients are preserved. Because the frequency behavior of these coefficients is retained, this method eliminates the randomization problem associated with [11]. We then have a surrogate for the detail coefficients at a particular level. In addition, we produce the mirror image of this surrogate $\{D_i^j(mirror)\} = \{D_k^j(surr)\}$, $i = 1, \dots, N$; $k = N, N - 1, \dots, 1$.
- (c) Match the surrogate and its mirror image to the original detail coefficients at a particular level by circularly rotating the values until an appropriate error function is minimized. Retain either the surrogate or the mirror image according to the lowest value for the error function. This locates the energy peaks at the appropriate locations in the signal, preserving the temporal structure. We have found that there is little

advantage to using more than a simple least-squares function at this stage.

- (d) Perform the inverse MODWT on the chosen surrogate detail coefficients for each level and the original approximation coefficients to produce a surrogate of the original time-series and use the rank-ordering method from the standard IAAFT algorithm to recover the values of the original time series.
- (e) As with the IAAFT algorithm, the rank-ordering has degraded the accuracy of our spectral representation of the signal. Hence, we require an iterative procedure to obtain convergence. We have found it best to implement these subsequent iterations in exactly the same manner as the IAAFT due to the relative speeds of the wavelet and Fourier transforms and the degree to which our wavelet-based first stage to the algorithm approximates a local minimum.

Figures 1 and 2 show that our algorithm is able to generate surrogates that discriminate between linear and non-linear processes and provide as good a match to the power spectrum of the data as other algorithms. Figure 3 shows properties of the surrogates for a time series consisting of 2048 values for fractional Brownian motion with a Hurst exponent (H) of 0.4 for the first half of the record and a change to $H = 0.65$ for the second half. Figure 4a illustrates the localization properties of the new algorithm. The surrogates (in gray) retain the positions of the major maxima and minima of the original series (black). Hence, they have the nice property that they “look like” the original data. The next two rows of Fig. 3 show various properties of both the signal and 39 surrogates generated by our method (middle) and the IAAFT (bottom). Our algorithm preserves the local mean and variance structure while randomizing the nonlinear aspects

of the signal. The latter is assessed by estimating H using a second derivative method [14] for 16 blocks of 128 consecutive values. The mean values were determined for the same blocks, while the wavelet variance was calculated using [15].

The advantage of producing surrogates that “look like” the data is not merely aesthetic. This property allows us to formulate further hypotheses that cannot be tackled successfully with standard IAAFT surrogates. For example, consider the case of fractional Brownian motion B defined by

$$\begin{aligned} B(0) &= 0 \\ \langle |B(t) - B(t - \Delta)|^2 \rangle &= \sigma^2 |\Delta|^{2H} \end{aligned} \quad (1)$$

If one considers the whole of the time series in Fig. 3 then the surrogates from IAAFT and our algorithm yield a similar average H (Fig. 4). However, specific segments of IAAFT surrogates do not preserve the local value for σ^2 , meaning that variability in both the local variance and the time series increments will contribute to the local estimate of H . Figure 3 shows that this will not be the case for our surrogates, meaning that, from (1), the variability in H for the surrogates is merely due to differences in the increments. This provides a means for detecting changes in H as the surrogates will retain an average measure of H (defined over the whole time series) while the data will reflect the local value. Figure 4c and 4d show example estimates of H for the final 256 values of the time series in Fig 3 determined for $\Delta = 1, \dots, 64$, and Fig. 4e and 4f give the probability of H based on the data plus surrogates for all eight windows of 256 values across the dataset. The transition between the values for the first and last halves of the data is clear in the case of our surrogates, but much more confused for IAAFT surrogates. Hence, our

surrogates have correctly found the transition from $H = 0.4$ to $H = 0.65$. The higher value for H for the data compared to the surrogates for the final increment is clear from Fig. 4c.

Given the range of phenomena that may be described by fractional Brownian motion or related fractal noises that are stationary in the increments, the new surrogate algorithm proposed in this paper may have application in a number of areas where one is concerned with changes in the properties of a signal through time. Our conceptually simple alteration to the highly effective IAAFT approach permits this surrogate generation method to be extended to consider a wider class of null hypotheses.

- [1] J. Theiler, S. Eubank, A. Longtin, B. Galdrikian, and J.D. Farmer, *Physica* **58D**, 77 (1992).
- [2] J. Theiler, D. Prichard, *Physica* **94D**, 221 (1996).
- [3] D. Prichard, C. P. Price, *Geophys. Res. Lett.* **20**, 2817 (1993); J. Theiler, P. E. Rapp, *Electroencephalogr. Clin. Neurophysiol.* **98**, 213 (1996).
- [4] D. Kugiumtzis, *Phys. Rev. E* **60**, 2808 (1999).
- [5] D. K. Ivanov, H. A. Pösch, and C. Stumpf, *Chaos* **6**, 243 (1996).
- [6] T. Schreiber, A. Schmitz, *Phys. Rev. Lett.* **77**, 635 (1996).
- [7] T. Schreiber, A. Schmitz, *Physica* **142D**, 346 (2000); K. Lehnertz *et al.*, *J. Clin. Neurophysiol.* **18**, 209, 2001; C. Rieke *et al.*, *IEEE T. BioMed. Eng* **50**, 634 (2003); D. Poggi *et al.*, *Geophys. Res. Lett.* **31**, L05102, doi:10.1029/2003GL018611 (2004).
- [8] T. Schreiber, *Phys. Rev. Lett.* **80**, 2105-2108 (1998).
- [9] M. Small, D. Yu, R.G. Harrison, *Phys. Rev. Lett.* **87**, 188101, 2001; M. Small, C.K. Tse, *Physica* **164D**, 187, 2002.

- [10] K. Judd, *Physica* **56D**, 216, 1992; **71D**, 421, 1994; M. Small, K. Judd, *Physica* **120D**, 386, 1998.
- [11] M. Breakspear, M. Brammer, P. A. Robinson, *Physica* **182D**, 1, 2003.
- [12] D. B. Percival, A. T. Walden, *Wavelet Methods for Times Series Analysis*, Cambridge University Press, 2000.
- [13] I. Daubechies, *Ten Lectures on Wavelets*, SIAM, 1992.
- [14] J. Istas, G. Lang, *Ann. Inst. Poincaré*, **33**, 407, 1994.
- [15] B. Whitcher, S. D. Byers, P. Guttorp, D. B. Percival, *Water Resour. Res.* **38**, 10.1029/2001WR000509, 2002. Algorithms for implementing this method can be found at <http://lib.stat.cmu.edu>.

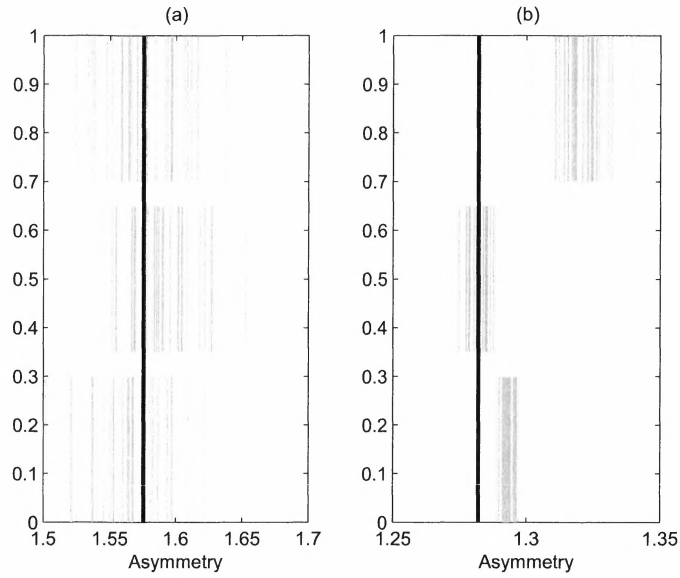


Figure 1. The asymmetry measure $A(\lambda=3)$ for a second-order autocorrelative process (a) and a chaotic path from the Rössler attractor (b). In each case the long black line records the asymmetry for the original data and the short gray lines the values for 39 surrogates. The surrogates are displayed at 0.7 – 1.0 (IAAFT), 0.35 – 0.65 (PPS with $d_e = 3$, $\tau = 8$, $\rho = 0.005$) and 0.0 – 0.30 (the new algorithm). The autocorrelative process is given by $x_i = 0.8x_{i-1} - 0.25x_{i-2} + 0.2\varepsilon$ where ε is a zero mean, unit variance Gaussian distribution. The Rössler equations are $\dot{q} = -(r + s)$, $\dot{r} = q + \alpha r$, $\dot{s} = 2 + t(q - 4)$ where, following [9], we choose $\alpha = 0.398$ to obtain a chaotic response. These equations were integrated for 20480 time steps of 0.1 units and values for r extracted. The first 10240 values were then discarded and one in every ten of the remainder were regularly sampled.

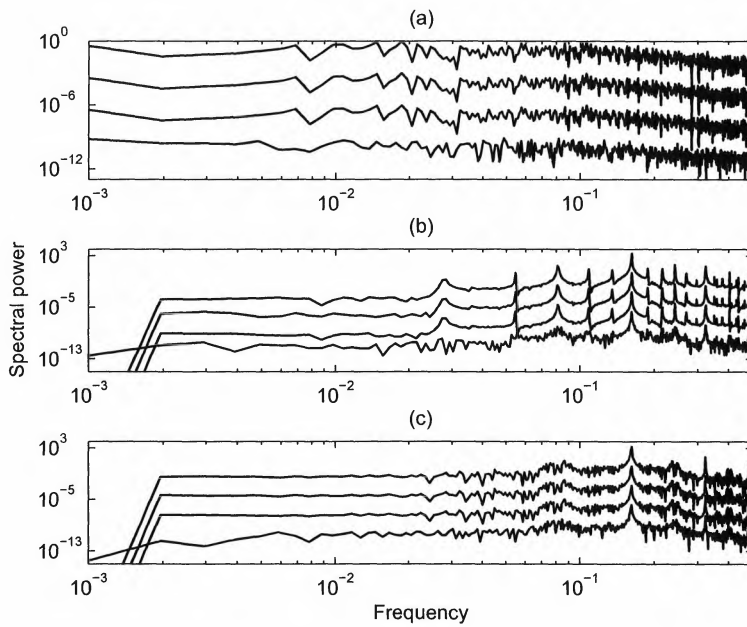


Figure 2. Power spectra for a second order autocorrelative process (a) a path on a periodic Rössler attractor (b) and a chaotic Rössler attractor (c). Each plot shows four spectra displaced from each other by 10^3 for clarity. The upper is the spectrum for the original data, the second is an IAAFT surrogate, the third is for a surrogate produced using our algorithm and the bottom for a PPS surrogate. The data in the middle figure were obtained from the Rössler equations in the same way as described in Fig. 1 except for α , which was altered to 0.3909 to give period 6 behavior [9].

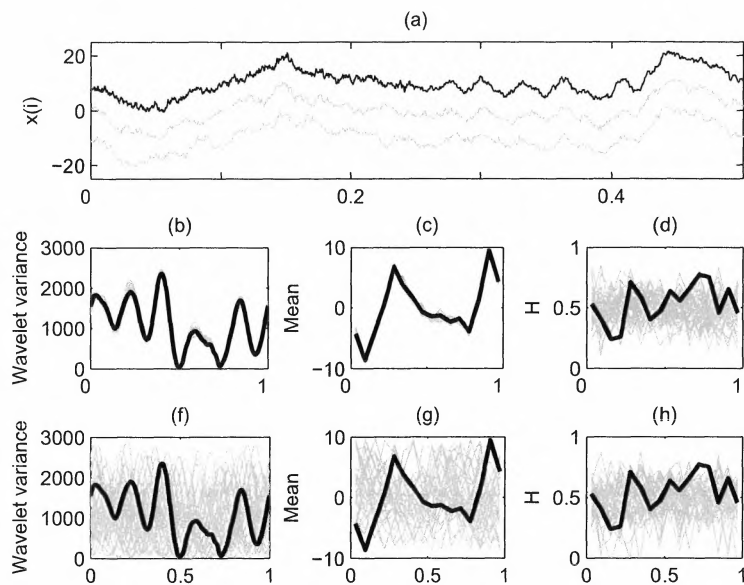


Figure 3. Time series and surrogate analysis for fractional Brownian motion with a change in H from 0.4 to 0.65 at the mid point. The time series (black) and two surrogates using the new algorithm (gray) are shown in the top panel, with vertical displacements to aid visibility. The second row shows properties of the original signal (black) and surrogates (gray) for our method and the third row shows similar information for IAAFT surrogates.

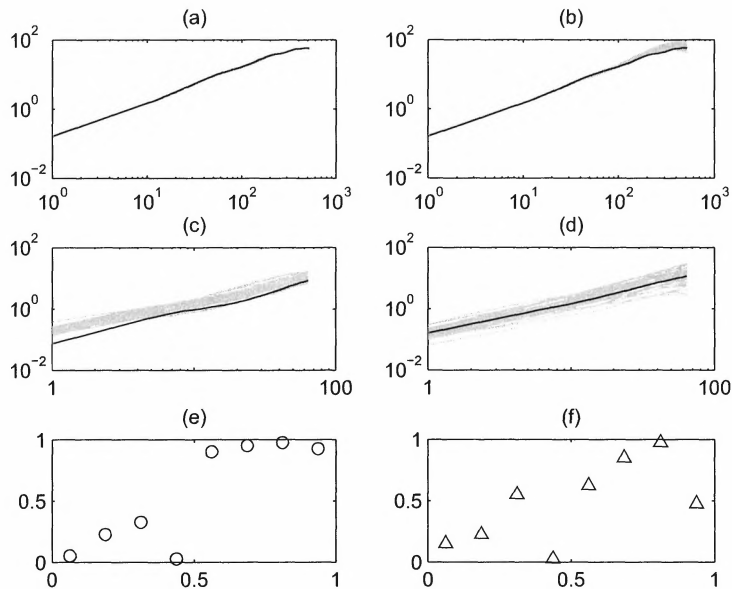


Figure 4. Hurst exponent properties for the time-series in Fig. 3. The plot on the left are for our surrogates and those on the right are for the IAAFT method. Fig. 4a and 4b show a plot of $\log \left\langle \left| B(t) - B(t - \Delta) \right|^2 \right\rangle$ vs $\log |\Delta|$ over the whole time series for $\Delta = 1, \dots, 512$. Hence, from (1) the gradient is $2H$. Fig 4c and 4d have the same axes but the calculation is undertaken over the last 256 values in the time series for $\Delta = 1, \dots, 64$. Fig. 4e and 4f give the probability of obtaining a particular value for H for the data (estimated from the slope of the line from plots similar to the above figure) as a function of the values for H of the 39 surrogates based on eight blocks of 256 values.

A.8 Manuscript to Be Submitted to Peer-Reviewed Journal (1)

Eglit, M. E. 2005. Impact of a snow avalanche against an obstacle. Formation of shock waves.
To be submitted.

Impact of a snow avalanche against an obstacle. Formation of shock waves

M.E. Eglit

August 29, 2005

Abstract

A brief review of the papers containing consideration of shock waves created in an avalanche flow at the impact against an obstacle is given. Theoretical and empirical formulae for the forces acting on obstacles in the impact are analyzed and some corrections are proposed. Data of calculations the pressure and density behind the shock are presented.

1 Introduction

Two types of shock waves can appear in the process of an interaction of snow avalanches with obstacles.

1. Shocks of the first type are observed in flows having an open (free) upper surface. They are just a sudden increase of the flow depth. One example is a hydraulic jump in a water flow. If the flow suddenly meets, e.g., a high wall that prevents it from going ahead then the fluid splashes up along the wall and stops (because of gravity). The subsequent parts of the flow in turn meet the stopped material in front of them and also pile up, so the zone of increased depth propagates upstream. The depth behind the shock may be significantly larger than the depth in front of it.

“Hydraulic” jumps can occur in flows of various media, both compressible and incompressible. Compressibility does not play a great role in the phenomenon: if possible the fluid prefers to pile up instead of being compressed.

2. Shocks of the second type are connected with the compressibility of the flowing material. If the material meets an obstacle and cannot escape anywhere, then it is forced to be compressed. The boundary between a compressed material and the undisturbed flow is a shock wave. The density and the pressure behind a strong shock can be much larger than those in front of it. Such shocks are called compression shocks in this paper.

For a weak compression shock the impact pressure may be estimated by the formula

$$p_c = \rho v a$$

where ρ , v and a are the flow density, relative velocity component along the normal to the shock, and sound speed in front of the shock, respectively; p_c is the lower limit of the pressure behind a compression shock in a flow with given density and velocity.

At open surfaces of the flow the pressure is maintained to be atmospheric. When a compression shock wave propagating from the obstacle meets an open surface and it is reflected as a rarefaction wave decreasing the flow density and pressure. That is why the time interval Δt during which the obstacle feels the large pressure is usually short. It equals the time needed for the compression wave to reach an open surface plus the time for the rarefaction wave to come back to the obstacle. The value Δt depends on the depth and width of the flow, and on the relative speed of propagation of the shock. The latter is always larger than the sound velocity a .

When the rarefaction wave reaches the obstacle, it is again reflected by it as a rarefaction wave and the pressure at the obstacle becomes lower than the pressure in the flow before the impact. This new rarefaction wave is reflected by open surfaces of the flow as a compression wave, and so on. Due to the process of subsequent reflections of waves the pressure at the obstacle is oscillating, decreasing due to interactions and energy dissipation.

In this review we discuss compression shocks in avalanche flows and do not speak about "hydraulic" jumps. Some of the results we are speaking about, can be found in the book by Bozhinskiy and Losev (1987). The aim of this review is to formulate the basic assumptions more clearly and explicitly to find the ways to overcome the shortcomings of the theory. We do not follow the texts and notations of the reviewed papers literally, speaking mainly about basic assumptions and equations.

2 Compression shocks. Theory

A system of shocks can appear at the impact of an avalanche against an obstacle due to compressibility of the avalanche snow. The shock that appears at the moment of the impact is adjacent to the obstacle. The pressure behind this shock determines the force on the obstacle at the instant of the impact. This is the maximum value of the force.

Two problems of calculating the pressure behind a shock wave have been studied analytically and experimentally:

1. The obstacle is a wall, that is perpendicular to the velocity of the avalanche flow (Shurova and Yakimov, 1969, 1970; Isaenko, Marin and Yadroshnikov, 1970, Shurova, 1984; Gonor and Pik-Pichak, 1983). This can be a model for estimating the maximum pressure at a catching dam.

2. The wall is inclined to the flow. The snow is not stopped by the obstacle (Briukhanov et al., 1967, Shurova, 1984). This can be a model for a deflecting dam.

2.1 Interaction with a catching dam

Consider first the interaction between an avalanche and a catching dam. Let the upstream face of the dam be perpendicular to the velocity of the avalanche flow. Assume that

- a) the flow velocity profile is homogeneous,
- b) the influence of the bottom and the free boundary of the flow can be neglected. This means that we consider a layer, that is not close to the bottom and to the free surface, and the time period during which the reflected waves created by the interaction of the

shock wave with the flow boundaries do not reach the studied part of the dam surface yet.

Then the flow is one-dimensional, and the shock wave that appears at the moment of the impact is parallel to the wall and propagates upstream. The snow velocity in the domain between the shock and the obstacle equals zero.

The relations that follow from the mass and momentum conservation across the shock are

$$\rho(v + D) = \rho_1 D, \quad (1)$$

$$\rho(v + D)^2 = \rho_1 D^2 + \sigma_{xx} - \sigma_{xx1}.$$

Here ρ , v , σ_{xx} are the flow density, velocity and the component of the stress tensor in front of the shock, x -axis is directed to the dam along the normal to the shock front; the parameters behind the shock are marked by "1", so that ρ_1 , σ_{xx1} are the density and the stress behind the shock; D is the velocity of the shock. The absolute value of the force acting on a unit area of the obstacle is equal to $|\sigma_{xx1}|$.

The state of the flow ahead of the shock, i.e., ρ , v , σ_{xx} , is supposed to be known. Then the two relations (1) contain three unknown parameters D , ρ_1 , σ_{xx1} , so additional equations are needed to calculate σ_{xx1} .

Eliminating the unknown ρ_1 we can obtain the following formula for σ_{xx1}

$$\sigma_{xx1} = \sigma_{xx} - \rho v(v + D), \quad (2)$$

while eliminating the unknown D we will have

$$\sigma_{xx1} = \sigma_{xx} - \frac{\rho \rho_1}{\rho_1 - \rho} v^2 \quad (3)$$

If the value of the density behind the shock ρ_1 could be found from certain additional equations, or if the value of the relative shock velocity $v + D$ could be estimated by some physical assumptions then we could calculate σ_{xx1} and therefore the impact force.

The first step in formulating the needed additional relations is to specify constitutive equations for avalanching snow.

Shurova and Yakimov proposed two models concerning the stresses in front of and behind a shock. The flowing material was considered as a mixture of air and ice. In the first model (let us call it the "SI gas model") they disregarded all the stresses except the pressure in the interstitial air (Briukhanov et al., 1967; Shurova, 1984). In the second model (let's call it "SI solid model") the normal stress was assumed to be a sum of the air pressure and certain stress caused by the interaction of ice particles (Shurova and Yakimov, 1969, 1970; Shurova, 1984).

A model for behavior of a high density snow-air mixture interacting with an obstacle was proposed by Gonor and Pik-Pichak (1983). In their paper a numerical solution of the problem is described, without explicit consideration of shock waves.

2.1.1 The SI gas model for avalanching snow

Assume that ice particles do not have contact with each other, the snow-air mixture behaves like a gas, so that the stresses are described by a pressure (viscosity can be

neglected in the narrow zone around a shock wave). Noting that by definition pressures correspond to negative stresses we write

$$\sigma_{xx} = -p, \quad \sigma_{xx1} = -p_1. \quad (4)$$

The mixture density ρ is

$$\rho = \frac{m+1}{\frac{m}{\rho_a} + \frac{1}{\rho_i}}. \quad (5)$$

Here subscripts a and i indicate air and ice, so that ρ_a, ρ_i are the air and ice densities, and m is the ratio of air and ice mass concentrations in the mixture, i.e.

$$m = \frac{1-\phi}{\phi},$$

where ϕ is ice particle mass concentration, and the gas mass concentration is $1-\phi$. The relation between ϕ, ρ, ρ_a and ρ_i is:

$$\phi = \frac{1 - \frac{\rho_a}{\rho}}{1 - \frac{\rho_a}{\rho_i}}.$$

The following two important assumptions are further made.

A₁). The pressure p in a mixture is just the interstitial air pressure p_a :

$$p = p_a, \quad p_1 = p_{a1}.$$

A₂). Velocities and temperatures of both air and ice components do not differ from each other (an equilibrium flow).

The relation for a perfect gas

$$p_a = R\rho_a T_a \quad (6)$$

is supposed to hold for air. The formula relating p, ρ and T follows from (5) and (6)

$$p = \frac{RT\rho}{1 + \frac{1}{m} - \frac{\rho}{m\rho_i}} \quad (7)$$

where p_a, T_a are denoted by p, T . The equation (7) is an equation of state for a mixture.

For parameters behind the shock we can write

$$p_1 = \frac{RT_1\rho_1}{1 + \frac{1}{m} - \frac{\rho_1}{m\rho_i}} \quad (8)$$

Relations (7) and (8) introduce the temperatures T and T_1 . The temperature T in front of the shock is supposed to be known in advance, but the air temperature behind the shock T_1 is unknown. So still some additional relations are to be found.

A common approach in continuum mechanics is to consider the energy equation. But the authors of the papers in discussion do not follow this way. Instead they suggest that

A₃). The air temperature does not change in a shock wave

$$T_1 = T \quad (9)$$

As an alternative to this condition they suggest that

A_4). The air temperature ratio across the shock is linked to the pressure ratio by the Poisson adiabat

$$T_1 = T \left(\frac{p_1}{p} \right)^{\frac{\gamma-1}{\gamma}} \quad (10)$$

where $\gamma = 1.4$ is the ratio of the specific heats for an air.

The relation (9), or (10) together with (4), (7) and (8) close the system of jump conditions (1). Now it is possible to calculate the pressure behind the shock, and, therefore, the force acting on the obstacle. The results can be found in (Shurova, 1984).

Discussion

1. Assumption A_1 is reasonable if the particles are not too small, their diameter being larger than a few hundredth of μm (Rudinger, 1980). The latter is true for snow avalanches.

2. Assumption A_2 needs to be discussed. First, the vertical velocities of air and particles are different due to sedimentation of particles. Second, the flow just behind a shock is always nonequilibrium: contrary to the air particles, solid particles cross the shock front with negligible change in their velocity because the time in which a particle crosses the shock wave is much smaller than the relaxation time needed to change the velocity substantially (Rudinger, 1980). Some distance is required for particles to achieve a new equilibrium with the moving air. However, if we include this distance into the shock wave, and neglect sedimentation in this rather narrow zone, then we can regard the flow at both sides of the shock as being equilibrium.

3. The equation (7) is usually simplified in dynamics of multiphase flows. The denominator can be transformed in the following way

$$1 + \frac{1}{m} - \frac{\rho_1}{m\rho_i} = \frac{1+m}{m}(1-\zeta) = \frac{1-\zeta}{1-\phi}$$

where

$$\zeta = \frac{\rho}{(1+m)\rho_i} = \phi \frac{\rho}{\rho_i}$$

is the volume concentration of particles in the mixture. If $\zeta \ll 1$, then the equation of state can be approximated by

$$p = R_M T \rho \quad (11)$$

where

$$R_M = \frac{Rm}{1+m} = (1-\phi)R \quad (12)$$

In this approach the mixture behaves as a gas with R_M as the gas constant. Typically for powder avalanches $\frac{\rho}{\rho_i} \sim 0.01 \ll 1$, $\phi \sim 0.9$, $\zeta \sim 10^{-2} \ll 1$. Even for dense dry avalanche $\frac{\rho}{\rho_i} \sim 0.1 \ll 1$, $\phi \sim 0.99$, $\zeta \sim 10^{-1} \ll 1$. So the equation (11) is often applicable. However the authors of the papers in discussion use the original equation (7) in their calculations.

4) It is well known that the assumption A_3 is not valid for gas flows without particles even if shocks are weak and the temperature variations are small (acoustic waves). It gives a wrong value for the sound speed ($\sqrt{\gamma}$ times less than the correct value). The reason is that the process of the particle's passage through a shock is very fast while the heat transfer that could equalize the gas temperature is slow; therefore the process is better thought to be adiabatic than isothermal.

However a particle-laden flow can often be treated as isothermal. This can be done if the particle mass concentration is large so that the heat capacity of the particles is much larger than the heat capacity of air inside the mixture. Then the temperature changes in air caused by compression can be compensated by heat transfer from the particles without significantly affecting the temperature of the latter (Rudinger, 1980). Of course, it is not the case just behind the shock front, but it is true for temperature in the end of the shock zone (including the relaxation distance).

5) The assumption A_4 is not valid. The correct relation for a gas flow (called the Rankine-Hugoniot adiabat) is derived using the equation of energy across the shock. It is definitely different from the relation following from (A_4) though the difference is not large for weak shocks (with a small pressure ratio), see Figs 1, 2. For solid-gas mixtures the Rankine-Hugoniot adiabat for the gas component is valid at the front of the shock, but not valid for parameters behind the shock zone since the energy exchange between air and ice particles occurs there.

The right way to obtain the needed additional relation across a shock is to take into account the equation of energy. To follow this way the internal energy of air-ice mixture should be specified based on certain physical assumptions.

One possibility is to assume that there is no interaction between ice particles and air. Then for the air we could use the Rankine-Hugoniot adiabat instead of the Poisson adiabat to obtain a more correct closed system of jump conditions. This situation we have immediately behind the shock front. However, interaction between ice particles and air does take place in a flow behind the shock front, and to calculate the flow parameters at the end of the shock zone we need an expression for the internal energy of the mixture.

The equation of state and the expression for the mixture internal energy for low density flows can be found in (Rudinger, 1980), and those for high density flows - in (Gonor and Pik-Pichak, 1983).

If the volume concentration can be neglected, and an equilibrium between gas and particles exists ($T_a = T_i = T$), then the mixture behaves as a perfect gas with the gas constant R_M . The internal energy per unit mass E is

$$E = (1 - \phi)c_V T + \phi c_i T$$

Here c_V is specific heat at constant volume for air, and c_i is specific heat for ice. The specific heats ratio Γ for a mixture at the condition $\zeta \ll 1$ is

$$\Gamma = \gamma \frac{\delta + m}{\delta\gamma + m} = \gamma \frac{1 + \delta\phi/(1 - \phi)}{1 + \gamma\delta\phi/(1 - \phi)},$$

where $\gamma = c_p/c_V$ is the specific heats ratio for air, and $\delta = c_i/c_p$ is the ratio of specific heats of particles and air. For a mixture of ice and air $\delta \sim 2$. If $\phi = 0.8$ then $\Gamma = 1.02$. Values of Γ for ice-air mixtures with $\phi > 0.8$ are very close to 1 (see Table 1). It means that the assumption A_2 is justified for such mixtures.

Table 1: Typical ϕ and Γ values.

ρ	10 ρ_a	20 ρ_a	30 ρ_a	40 ρ_a	50 ρ_a
ϕ	0.90123	0.95130	0.96799	0.97633	0.98134
Γ	1.01399	1.00666	1.00433	1.00318	1.00250

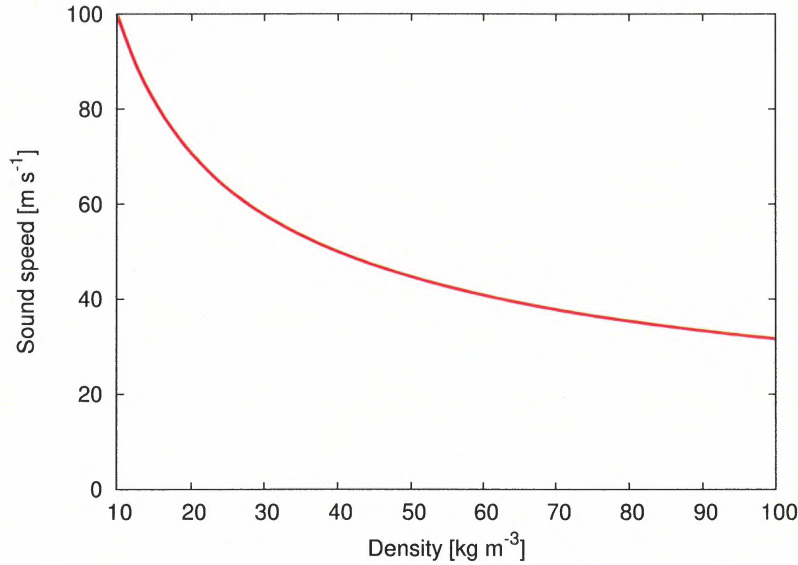


Figure 1: The sound speed in avalanching snow; $p = 100\text{KPa}$

The following formula for the equilibrium speed of sound is valid

$$a = \sqrt{\left(\frac{\partial p}{\partial \rho}\right)_{s=\text{const}}} = \sqrt{\Gamma \frac{p}{\rho}}.$$

It can be seen from this formula that the equilibrium sound speed in mixtures is always less than that in gas at the same value of the pressure since $\Gamma < \gamma$ and $\rho > \rho_a$, see Figure 1.

Figures 2-4 show the dependencies of the density ratio ρ_1/ρ , pressure ratio p_1/p , and nondimensional speed of the shock wave D/a on the Mach number $M = v/a$ of the flow. The curves were obtained by use of Rankine-Hugoniot adiabat for the mixture. The formula for the pressure behind a shock is

$$\frac{p_1}{p} = 1 + \frac{\Gamma(\Gamma + 1)M^2}{4} \left(1 + \sqrt{1 + \frac{16}{(\Gamma + 1)^2 M^2}}\right)$$

The following values of the air and ice parameters were used in calculations

$$\rho_a = 1.25 \text{ kg m}^{-3}, \rho_i = 916.7 \text{ kg m}^{-3}, \gamma = 1.4,$$

$$c_p = 1005 \text{ J kg}^{-1} \text{ K}^{-1}, c = 2170 \text{ J kg}^{-1} \text{ K}^{-1}, \delta = 2.16.$$

Calculations were made for the values of the flow density ρ , particle mass concentration ϕ and specific heats ratio Γ in front of the shock that are written in the Table 1.

In Figures 5, 6 the dependencies of the pressure behind the shock on the flow density at fixed values of the initial pressure and initial flow velocity in front of the shock are plotted.

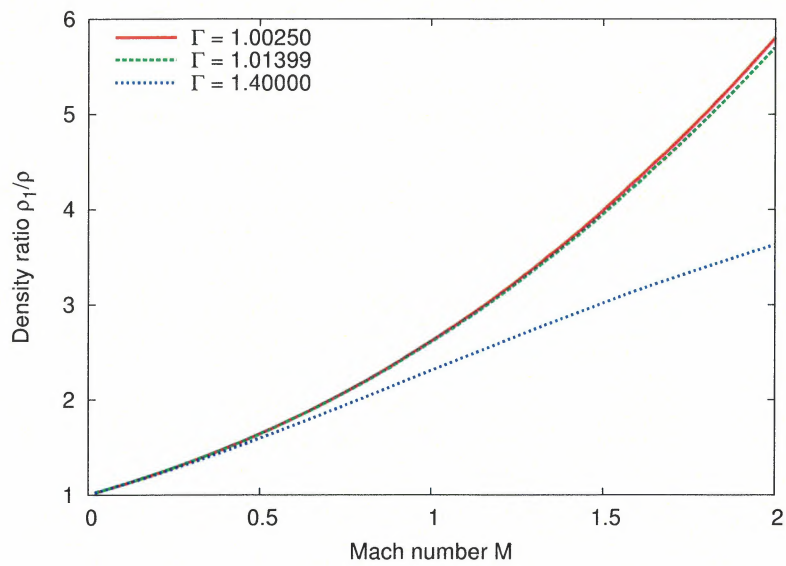


Figure 2: The ratio of the densities behind and in front of a shock. Dashed line - pure air.

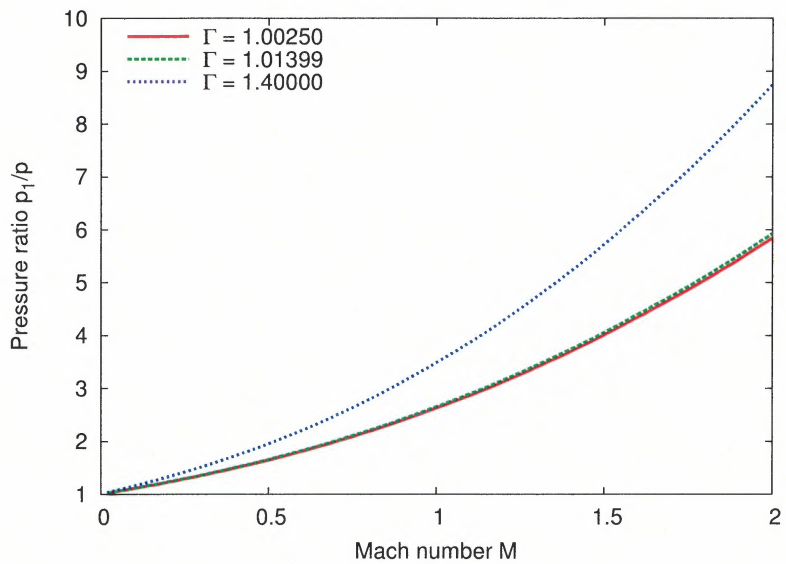


Figure 3: The ratio of the pressures behind and in front of a shock. Dashed line - pure air.

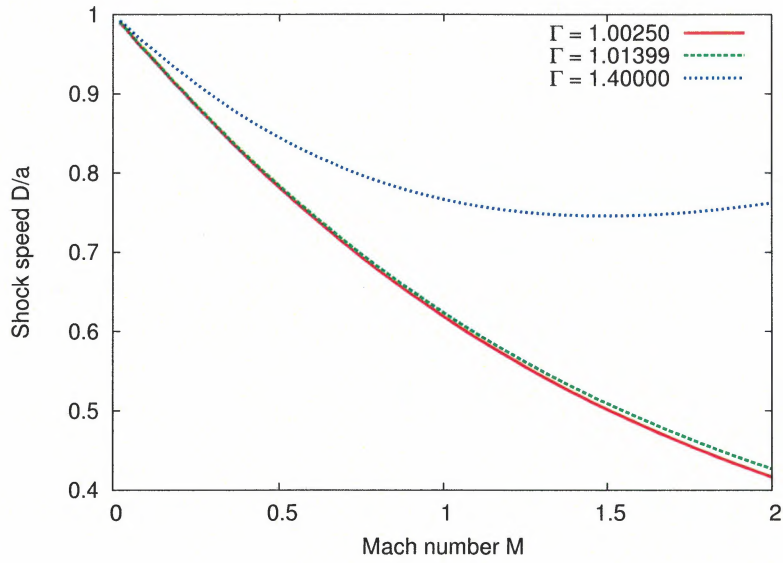


Figure 4: The shock speed relative to the obstacle. Dashed line - pure air.

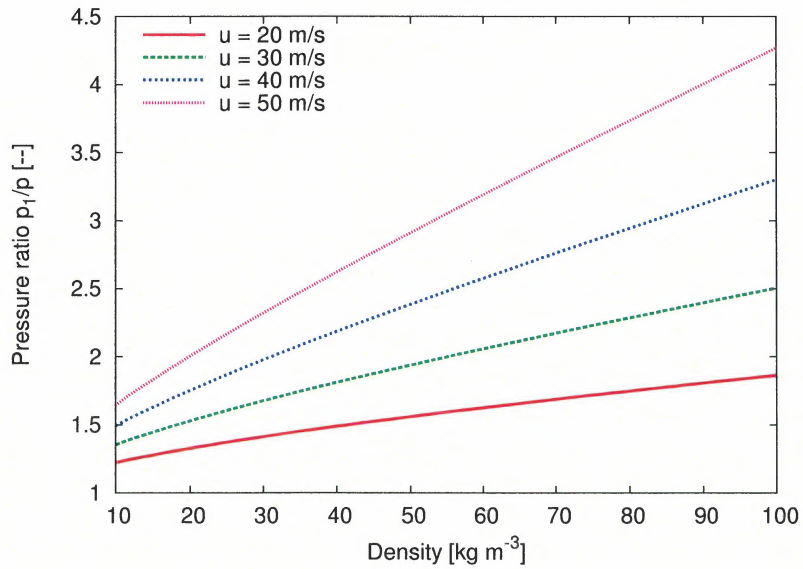


Figure 5: Pressure $p_1 \times 10^{-2} KPa$ behind a shock versus flow density ρ ; $v = 30m/s$, $p = 100KPa$

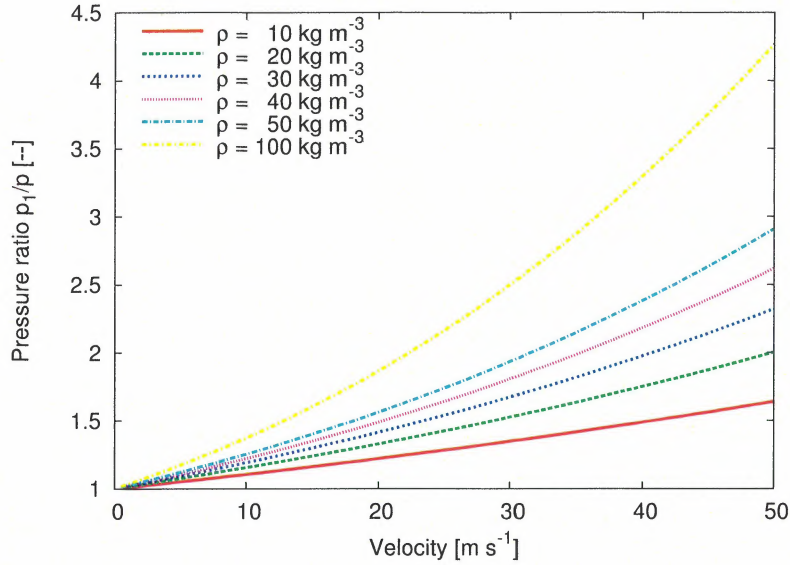


Figure 6: Pressure $p_1 \times 10^{-2} KPa$ behind a shock versus flow density ρ ; $v = 30m/s$, $p = 100KPa$

2.1.2 Account of ice particles interactions. SI gas-solid model

To take into account the stresses due to interaction of ice particles Shurova and Yakimov (1969, 1970) supposed that the total normal stress is $\sigma_{xx} = -(p + \sigma)$, where p is the interstitial air pressure and σ presents the stress in the ice. Then the relations (1) are replaced by

$$\rho(v + D) = \rho_1 D, \quad (13)$$

$$\rho(v + D)^2 = \rho_1 D^2 - (p + \sigma) + (p_1 + \sigma_1).$$

The relation (3) is replaced by

$$\bar{p}_1 = p + \frac{\rho \rho_1}{\rho_1 - \rho} v^2 + \sigma, \quad (14)$$

where $\bar{p}_1 \equiv p_1 + \sigma_1$ determines the force on the obstacle. Relation (8) is assumed to be valid for p_1 . To have a full system of equations one should specify σ and σ_1 . It is supposed that 1) they are maximum possible values of stresses (i.e., the compression strength) for an ice structure in front of and behind the shock, 2) these maximum values are known functions of the density and temperature, 3) $\sigma = 0$ if the flow density is low, namely $\rho \leq \rho^*$, $\rho^* \sim 0.2\rho_i$.

Consider first low density avalanche flows with $\rho \ll \rho^*$. In this case $\sigma = 0$. If the shock is weak ($\rho_1/\rho < \rho^*/\rho$), then $\sigma_1 = 0$, so gas models described in the previous subsection can be used. For strong shocks ($\rho_1 > \rho^* \gg \rho$) the authors recommend to use an approximate equality

$$\frac{\rho_1}{\rho_1 - \rho} \approx 1 \quad (15)$$

to obtain the following simple formula for calculating the force \bar{p}_1 per unit area of the obstacle:

$$\bar{p}_1 = p + \rho v^2 \quad (16)$$

This formula is just the formula (3) with the condition $\rho_1 \gg \rho$.

Discussion.

The way to calculate the pressure behind the shock is developed in the above papers only for the low density avalanche flow, $\rho \ll \rho^*$ and only for "weak" and "strong" shocks. But even for such flows the solution is not complete: to know whether the shock is "weak" or "strong" we should know the function $\sigma(\rho, T)$. This function is not specified in (Shurova and Yakimov, 1969, 1970). Experiments are needed to determine it.

2.1.3 Compression shocks in dense avalanches

A model to describe compression shocks in dense avalanches has been proposed by Gonor and Pik-Pichak (1983). They consider the snow as an ideal compressible fluid when studying the process of impact. The equation of state is suggested in the form

$$p = p_0 f\left(\frac{\rho}{\rho_0}\right) + c\rho E \quad (17)$$

where

$$f = d + a\left(\frac{\rho}{\rho_0} - 1\right) + b\left(\frac{\rho}{\rho_0} - 1\right)^2,$$

ρ , ρ_0 are the mixture density and its initial value, E is the mixture internal energy density, a, b, c, d are empirical constants. The formula for E is

$$E = c_V T - \frac{p}{V^c} \int_{V_0}^V V^c f dV \quad (18)$$

where $V = 1/\rho$, T is the mixture absolute temperature, and c_V is its specific heat capacity. This formula can be derived in the following way. Consider the thermodynamical Gibbs' identity

$$dE + pdV = Tds \quad (19)$$

where s and $V = 1/\rho$ are the entropy and volume per unit mass, respectively. The relation (19) is valid both for ideal and viscous fluids, and for ideal fluids it is just a combination of the first and the second laws of thermodynamics. Assume that $E = E(V, T)$, $p = p(V, T)$. Then we may rewrite the relation (19) as

$$ds = \frac{1}{T} \left(\frac{\partial E}{\partial V} + pdV \right) dV + \frac{1}{T} \frac{\partial E}{\partial T} dT$$

Since ds is a total differential of s , the following relation should hold

$$\frac{\partial}{\partial V} \left(\frac{1}{T} \frac{\partial E}{\partial T} \right) = \frac{\partial}{\partial T} \left(\frac{1}{T} \left(\frac{\partial E}{\partial V} + p \right) \right)$$

or

$$p + T \frac{\partial p}{\partial T} + \frac{\partial E}{\partial V} = 0 \quad (20)$$

Since p does not depend on t according to equation (17) we obtain the differential equation

$$\frac{\partial E}{\partial V} = -p$$

Solving this equation and assuming that c_V does not depend on the temperature we come to (18).

The following values of a, b, c, d were found from the experimental results presented in (Isaenko, Yadroshnikov, 1972)

$$a = 0.1845, \quad b = 125.0, \quad c = 0.0406, \quad d = -6.830$$

The authors used this model for numerical solution of the problem of the impact. They considered a homogeneous flow with a given depth, density and velocity that suddenly meet a wall located normally to the flow. The height of the wall was assumed to be much larger than the initial flow depth, and the gravity was neglected. This can be done if we are interested in the first stage of the process only. The unsteady motion of the fluid was studied. In particular, the variation of the open surface of the flow with time, and the distributions of pressure at the wall for various instants were calculated. The numerical scheme did not include an explicit study of shock waves though the obtained distribution of the pressure in the avalanche body contains zones with the sharp variation of p (shock waves).

2.2 Interaction with a deflecting dam

Shocks due to compressibility of the flow have been considered for stationary flow near an inclined obstacle. An analytical solution can be easily obtained under the following conditions: 1) all stresses except the pressure p can be neglected so that the mixture in the process of impact can be regarded as an ideal gas; 2) the flow is supersonic, 3) the inclination angle of the dam is not too large, 4) the influence of the flow boundaries is neglected, 5) gravity is neglected.

In (Briukhanov et al., 1967; Shurova, 1984) an analytical solution is constructed for an infinitely wide catching dam with an inclined face. But since the authors neglect gravity, their solution can be applied to a case of deflecting dams after slight modification.

The authors first calculate an isothermal sound speed c being defined as $c = \sqrt{\frac{\partial p}{\partial \rho}}$ (a derivative at $T = const$) using the equation of state (7). It is

$$c = \sqrt{\frac{m(1+m)RT}{(m+1 - \frac{\rho}{\rho_i})^2}}$$

Since the ratio of mass concentrations of air and ice m is usually small (typical value $m \sim 5 \cdot 10^{-3}$ at $\rho/\rho_i = 0.2$, i.e. for dense avalanches), then the sound velocity is much less than that in the air and in the ice. Calculations show that $c \sim 30m/s$ at $\rho/\rho_i = 0.2$ and $p = p_{at}$.

The analytical solution is constructed for an avalanche flow with $v > c$. Qualitatively it is similar to the corresponding well known solution in gas dynamics. The difference is in another form of the equation of state: equation (7) instead of the Clapeyron equation.

Discussion.

1. The authors again assume that the temperature does not change across the shock instead of considering the energy equation. That is why their solution needs some corrections.



Figure 7: Left: a moving cart with a snow sample; right: a tables with an obstacle. Photos from (Yakimov et.al, 1971)

2. The authors consider a steady flow. But at the very beginning of the process of impact it is unsteady. This phase is not studied.

3 Formulae for the pressure at the obstacle derived from data of experiments

A device to measure forces acting on obstacles had been constructed at Elbrus High Mountain Glacioecological station of Moscow State University. A view of the device is shown in Fig.7. A cart with snow sample on it descends along the rails that are placed on a mountain slope. At the end of the way the cart meets a table with a knife in its front part and an obstacle installed on the table. The cart is going under the table while the snow sample is cut by the knife and moves over the table surface to meet the obstacle. Sensors located on the obstacle measure the forces acting on it.

The advantages of this device comparatively to chutes, where the snow is moving naturally over the bottom, are the following. The density and the structure of the snow, the form and dimensions of the moving snow front zone, and the snow velocity at the moment of meeting the obstacle are known. They can be set in every desired manner, while for flows in chutes they depend on motion and can not be fixed in advance. A series of measurements has been done to study a process of impact and the possibilities for physical modeling of the impact of real avalanches. Obstacles of various shapes were tried including vertical walls, wedge-shaped obstacles, conical mounds, cylindrical rods (thick wire).

3.1 Interaction with a wedge-shaped obstacle

Experiments have been made to measure forces acting on a wedge-shaped obstacle located in an avalanche path (Yakimov et al, 1979). Wedges with the angles $\alpha = 60^\circ$, $\alpha = 90^\circ$, $\alpha = 120^\circ$, $\alpha = 150^\circ$ were used, the angle between the flow velocity and the wedge surfaces being 0.5α . The flow depth was equal to the height of the wedge H , or (in some experiments) larger than H . The normal component of the force on the surface was measured as a function of time. Dimensionless parameters were introduced

$$\text{Fr} = \frac{v_0}{\sqrt{gH}}, \quad \tau = \frac{v_0 t}{H}, \quad c_{x_{max}} = \frac{F_{max}}{\frac{1}{2}\rho_0 v_0^2 S_2}, \quad c_{x_\infty} = \frac{F_\infty}{\frac{1}{2}\rho_0 v_0^2 S_2},$$

where v_0 , ρ_0 are the flow velocity and density, S_2 is the area of the projection of the wedge to the plane perpendicular to the flow velocity, t is time, Fr is the Froude number, F_{max} is the maximum value of the force (observed at small values of τ), and F_∞ is the value of the force at large τ corresponding to a stationary flow along the wedge surface.

The following empirical formulae are proposed

$$c_{x_{max}} = 0.025\alpha; \quad c_{x_\infty} = 1.2 \quad \text{if} \quad \alpha > 90^\circ, \quad (21)$$

where α should be measured in degrees. According to these formulae $c_{x_{max}}$ and c_{x_∞} depend neither on the Froude number nor on the flow width.

Discussion.

Conditions, at which the formulae (21) are valid, are not written in (Yakimov et al., 1979). Moreover, the data are presented that show a dependence of the force on the width and depth of the flow: the maximum value of the force increases by 20% as the ratio of the flow width to the width of midel crossection of the obstacle increases by a factor 2. This dependence is not included in (21).

3.2 Impact against an inclined wall

Measurements of the maximum impact pressure P at the impact of a snow sample against an inclined wall were made by researchers of Siberian Technical University of Railways (Isaenko, Marin, and Yadroshnikov, 1970), (Isaenko, 1975). The measurements had been made in a chute, which was built at one of the slopes in Sakhalin Island. The length of the travel path of snow before meeting an obstacle was 98m. The width of the chute was 2 m., the height of the side walls was 1.5 m, and the slope angle was 38° . The bottom and the side walls were covered by smooth material. Snow velocities were up to 35 m/s at the moment of meeting the obstacle. One of the conclusions is that the maximum impact pressure depends on the snow velocity linearly. The dependence of P on the snow velocity and the angle α_1 between the snow velocity and the wall is approximated by the formula

$$P = A\rho v \sin \alpha_1 \quad (22)$$

where $A = \text{const}$. This formula can be regarded as an approximation of the equation (2) since the shock speed relatively

This formula is not in agreement with (21).

References

Bozhinskiy A.N. and Losev K.S., 1987. Osnovi lavinovedenija. Leningrad, Gidrometeoizdat, 280p. English translation: Bozhinskiy, A. N. and K. S. Losev, The Fundamentals of Avalanche Science, Eidg. Institut fur Schnee- und Lawinenforschung, 1998, CH-7260 Davos Dorf, Switzerland.

Briukhanov A.V., Grigorian S.S., Miagkov S.M., Plam M.Ya., Shurova I. Ya., Eglit M.E., Yakimov Yu.L. 1967. On some new approaches to the dynamics of snow avalanches. Physics of Snow and Ice. Proceedings of Int. Conf. on Low Temperat. Sci., Sapporo, Japan, 1967, pp. 1221-1241

Gonor, A.L., Pik-Pichak, E.G., 1983. Chislennoe modelirovanie udara snezhnoi lavini po tverdoi stenke (Numerical modeling of an impact of a snow avalanche against a solid wall). Izvestija Akademii nauk SSSR, Mekhanika zhidkosti i gaza, 6, 86-91

Isaenko, E.P., Marin, Yu.A. and V.I. Yadroshnikov, 1970. Modelirovanie udara lavini iz snezhnoi doski o nepodvizhnoe prepjatstvie. (Modeling of an impact of a snow slab avalanche against a fixed obstacle). Trudi Novosibirskogo Instituta inzhenerov zheleznodorozhnogo transporta, 101, 87-108.

Isaenko, E.P., 1975. Snow avalanche impact pressure on an obstacle. IAHS-AISH, Publ. 114.

Isaenko, E.P., V.I. Yadroshnikov, 1972. Issledovanie ob'emno-napriazhennogo sostojanija snega pri udarnih nagruzkah. (Study of a stress state in snow at impact). Trudy Novosibirskogo Instituta inzhenerov zheleznodorozhnogo transporta, 141, 85-92.

Shurova, I.E. and Yakimov, Yu.L., 1969. Opredelenie naprjazhenii za frontom udarnoi volni v pilevoi snezhnoi lavine s uchetom prochnosti tverdoi fazi (Calculation of stresses behind a shock wave in a powder snow avalanche with account of the strength of the solid phase). Prikladnaja mehanika i tekhnicheskaja fizika, 1, 100-101.

Shurova, I.E. and Yakimov, Yu.L., 1970. Issledovanie udara snega o nepodvizhnoe prepjatstvie (Study of the impact of snow against a fixed obstacle). Materiali Glaciologicheskikh Issledovanii, 16, 52-57.

Shurova, I.E., 1984. A mechanism of the interaction of a moving Snow Mass with a Fixed Obstacle. Glaciological Data, Report GD-16.

Rudinger, G., 1980. Fundamentals of gas-particle flow. Elsevier, Amsterdam, 142 p.

Yakimov Yu. L., Shurova I.E., 1971. Modelirovanie vzaimodeistviya snezhnoi lavini s prepjatstviem (Modelling of the interaction of a snow avalanche with an obstacle), Institute of Mechanics, Moscow State University, Report No.1201, 32 p.

Yakimov, Yu.L., Shurova, I.E., and Stavskii, Tz.I., 1979. Eksperimentalnoe issledovanie vzaimodeistviya snezhnogo potoka s klinovidnimi prepjatstviiami (Experimental study of an interaction of a snow flow with wedge-shaped obstacles). Institute of Mechanics, Moscow State University, Report No.2145, 62 p.

A.9 Unpublished Report(1)

Gauer, P. and K. Kristensen. 2005. Ryggfonn measurements. Winter 2004/2005. NGI Report 20021048-8. Norges Geotekniske Institutt, Oslo, Norway.

Avalanche Studies and Model Validation in Europe, SATSIE

Ryggfønn measurements Winter 2004/2005

20021048-8

1 December 2005

I henhold til NGIs kvalitetssikringssystem, kan NGI kun bli holdt ansvarlig for den signerte versjonen av dette dokumentet. Dette kan på anmodning ettersendes med ordinær post.

Dokumentet må ikke benyttes i utdrag eller til andre formål enn det dokumentet omhandler. Det må ikke leveres til tredjemann uten oppdragsgivers samtykke. Dokumentet må ikke reproduseres.

In accordance with NGIs quality assurance system, NGI can only be held responsible for the signed version of this document. On request, this can be sent by ordinary mail.

This document shall not be used in parts, nor for other purposes than the document deals with. The document shall not be given to a third party without the proprietor's (client's) consent. This document shall not be copied, in parts or in whole.



20021048-11



Avalanche Studies and Model Validation in Europe, SATSIE

Ryggfonn measurements Winter 2004/2005

20021048-8

1 December 2005

Client: **European Commission**

Contact person: Denis Peter
Contract reference: Contract of 18.10.02

For the Norwegian Geotechnical Institute

Project Manager: Karstein Lied

Report prepared by: Peter Gauer and Krister Kristensen

Reviewed by: Karstein Lied

Work also carried out by:



SUMMARY

This report presents data collected from the full-scale avalanche test site Ryggfonn during the Winter 2004/2005. The weather and snow conditions are described and when possible, the avalanches have been characterized according to the IAHS avalanche code and the deposit boundaries have been mapped.

Measurements obtained from the avalanche path include impact pressure readings from two load cells at a steel tower as well as impact pressures on three load cells fixed to a concrete structure. In addition, normal stress and shear stress were measured at two locations at a 16 m high dam. Six geophones, placed in the ground in the runout zone, have detected vibrations from some of the passing avalanches. When possible, for each avalanche the front speeds have been estimated. These estimates are based on pulsed Doppler radar measurements, seismic measurements, and the timing between impacts on the constructions. The pulsed Doppler radar provided also velocity measures from the avalanche body.

The measurements obtained are briefly discussed and presented in graphs.



Contents

1	Ryggfonn full-scale experiments (NGI)	5
1.1	Test site	5
1.2	Impact pressure measurements	6
1.3	Load plate measurements	7
1.4	Velocity estimates	9
2	Winter 2004/2005	11
2.1	General conditions in 2004/2005	11
2.2	Avalanche 20041207 17:00	15
2.3	Avalanche 20050107 04:16	18
2.4	Avalanche 20050416 15:00	29

LIST OF TABLES

2.1	Avalanche classification	13
2.2	Overview of archived measurements at Ryggfonn test site during winter season 2004/2005	13
2.3	Field observations/ measurements	32
A-1	Code for morphological avalanche classification	A1
A-2	Canadian snow avalanche size classification system	A2

**LIST OF FIGURES**

1.1	Overview of the Ryggfonn test site; location map	5
1.2	Profile line of main track at the Ryggfonn test site	6
1.3	Load plate measurements	8
2.1	Weather data from Ryggfonn test site 2004–2005	12
2.2	Map of all avalanche deposits recorded in winter season 2004/2005 .	14
2.3	Avalanche 20041207 17:00: Deposition/outline map	15
2.4	Avalanche 20041207 17:00: Load cell measurements	16
2.5	Avalanche 20041207 17:00: Deposition/outline map	17
2.6	Avalanche 20050107 04:16: Deposition/outline map	19
2.7	Avalanche 20050107 04:16: Timing	20
2.8	Avalanche 20050107 04:16: Timing	21
2.9	Avalanche 20050107 04:16: Load cell measurements (raw data) . . .	22
2.10	Avalanche 20050107 04:16: Load cell measurements	23
2.11	Avalanche 20050107 04:16: Fluctuation intensity vs. position within the avalanche	24
2.12	Avalanche 20050107 04:16:	25
2.13	Avalanche 20050107 04:16: Load plate measurements (raw data) . .	26
2.14	Avalanche 20050107 04:16: Load plate measurements; first surge . .	27
2.15	Avalanche 20050107 04:16: Load plate measurements; second surge	28
2.16	Avalanche 20050416 15:00: Snapshot from avalanche release	30
2.17	Avalanche 20050416 15:00: Snapshot from avalanche descent	31
2.18	Avalanche 20050416 15:00: Deposition/outline map	33
2.19	Avalanche 20050416 15:00: Track status	34
2.20	Avalanche 20050416 15:00: Snow depth profile at the dam before the event	34
2.21	Avalanche 20050416 15:00: Sensor status I	35
2.22	Avalanche 20050416 15:00: Sensor status II	36
2.23	Avalanche 20050416 15:00: Deposition/outline map	37
2.24	Avalanche 20050416 15:00: Total deposition in the runout area . . .	38
2.25	Avalanche 20050416 15:00: Timing	39
2.26	Avalanche 20050416 15:00: Front velocity and front acceleration vs. location along the lower track	40
2.27	Avalanche 20050416 15:00: Velocity vs. position within the avalanche.	41
2.28	Avalanche 20050416 15:00: Velocity and acceleration vs. position within the avalanche.	42
2.29	Avalanche 20050416 15:00: Velocity and acceleration vs. location along the lower track	43
2.30	Avalanche 20050416 15:00: Friction coefficients vs. location along the lower track	44
2.31	Avalanche 20050416 15:00: Load cell measurements (raw data) . . .	45
2.32	Avalanche 20050416 15:00: Load cell measurements	46



2.33	Avalanche 20050416 15:00: Fluctuation intensity vs. position within the avalanche	47
2.34	Avalanche 20050416 15:00: Fluctuation intensity vs. position within the avalanche	48
2.35	Avalanche 20050416 15:00: ρC_D vs. position within the avalanche .	49
2.36	Avalanche 20050416 15:00: Load plate measurements (raw data) . .	50
2.37	Avalanche 20050416 15:00: Load plate measurements	51
2.38	Avalanche 20050416 15:00: Snapshots from the avalanche descent I	52
2.39	Avalanche 20050416 15:00: Snapshots from the avalanche descent II	53
2.40	Snapshots from a subaqueous flume experiment	54
2.41	Avalanche 20050416 15:00: Snapshots from the track I	55
2.42	Avalanche 20050416 15:00: Snapshots from the track II	56
2.43	Avalanche 20050416 15:00: Snapshots from the lower track	57
2.44	Avalanche 20050416 15:00: Snapshots from the lower track (erosion I)	58
2.45	Avalanche 20050416 15:00: Snapshots from the lower track (erosion II)	59
2.46	Avalanche 20050416 15:00: Snapshots from the deposits	60

1 RYGGFONN FULL-SCALE EXPERIMENTS (NGI)

Task leader: Karstein Lied; participation of Krister Kristensen, Carl Harbitz, Peter Gauer, Arne Moe, Erik Lied and Harald Iwe, as well as the Department of Geology and Geophysics, University of Barcelona, the Icelandic Meteorological Office - Avalanche section and Austrian Institute for Avalanche and Torrent Research

1.1 Test site

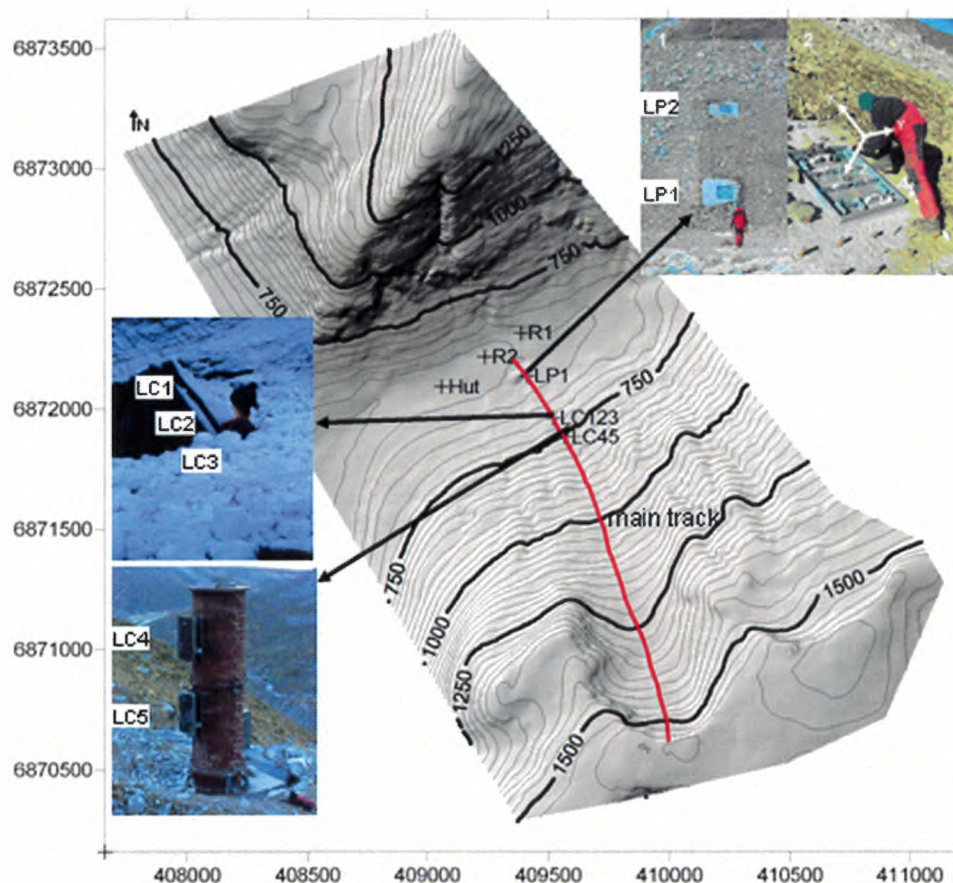


Figure 1.1: Overview of the Ryggfonn test site (UTM coordinates in m). The view shows the line of the main track and the locations of the load cells (LC45 and LC123) and the placement of the load plates in the dam (LP1 and LP2). In addition, two Doppler radar positions are indicated (R1 and R2).

The Ryggfonn full-scale avalanche test site has been in operation since 1980. The test site has a vertical drop of about 900 m and a horizontal length of 2100 m. Typical avalanche

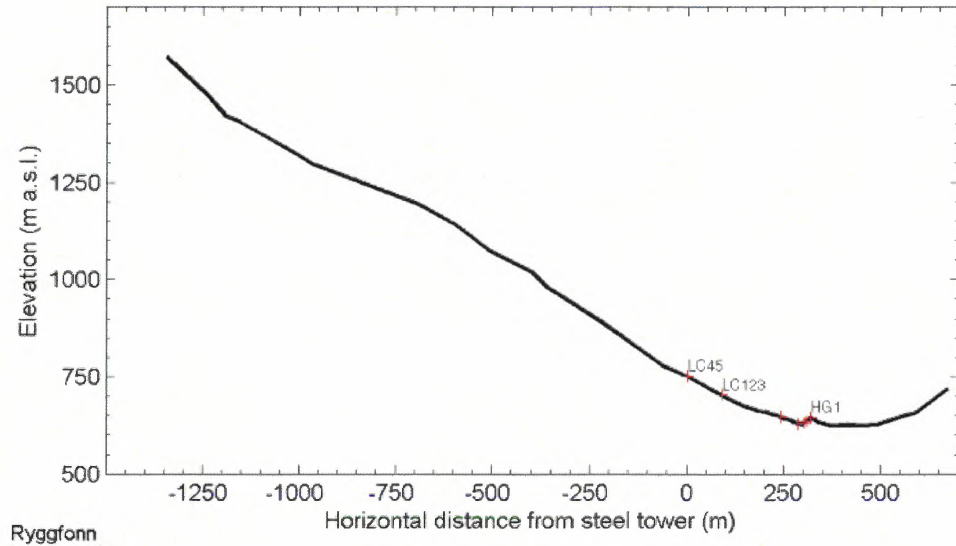


Figure 1.2: Profile line of main track at the Ryggfonn test site. The horizontal distance is measured relative to the steel tower. Sensor positions are indicated

size ranges between 2 (mass of 0.1 Gg) and 4 (mass of 10 Gg) according to the Canadian snow avalanche size classification (McClung and Schaerer, 1993); they may even reach class 5 (mass of 100 Gg). Maximum velocity can reach up to 60 m s^{-1} . Figure 1.1 shows a location map of the main sensors used during the winter season 2004/2005 and Figure 1.2 gives an impression of the profile of the main track.

1.2 Impact pressure measurements

The steel tower has a diameter 1.3 m and is equipped with 2 load plates, each with an area, A_m , of $1.2 \text{ m} \times 0.6 \text{ m}$. The concrete structure is instrumented with 3 load plates identical to those at the steel tower.

The interpretation of load cell measurements is not straightforward. Commonly, the drag force, F_D , due to a flow around a slender obstacle is expressed in terms of a dimensionless drag factor C_D , i.e.

$$F_D = \frac{1}{2} \rho C_D A_a U_\infty^2 \quad (1.1)$$

Here, ρ is the density of the fluid, U_∞ the upstream flow velocity, and A_a is the projected area of the obstacle that is affected. If A_a is less A_m then the pressure measurements have to be corrected by a (unknown) factor A_m/A_a . This can cause an uncertainty. Reasons for $A_a < A_m$ can be that the flow height of the avalanche is smaller than the height of the plate or the plate is already buried from deposits. The drag factor itself is a function of the



flow regime and depends on factors like the Reynolds number, Re , Froude number, Fr , and the geometry of the obstacle. If one considers a granular flow, C_D might also depend on the particle concentration, size, and restitution coefficient. Depending on the flow regime, C_D can vary by several orders of magnitude. Despite this, the value used for a rectangular cross section in dry flow avalanches is commonly set to 2, cf. (Mellor, 1968). This holds true for the powder part as well as for the dense part, even if not explicitly stated. In (Norem, 1990), Norem proposed a value of 2.5 for dry snow avalanches and 6.3 for wet snow avalanches based on impact pressure measurements from the Ryggfonn test site. Salm and others (1990) recommend a C_D equals 2 and a density of 300 kg m^{-3} . Due to the large size of the sensors, the measured impact forces represent average values. Single impacts might exceed these values by an order of magnitude. The averaging effect of the large size also causes a damping of the fluctuation intensity, defined as

$$I_F = \left| \frac{\widetilde{LC} - LC}{\widetilde{LC}} \right| \approx \left| \frac{2u'}{U} + \frac{\rho'}{\rho} \right| \quad (1.2)$$

LC is the measured pressure by the load cell and \widetilde{LC} is a running mean taken either over 0.5 s (approximately between 5 m to 15 m spatial resolution) or 5 m. Temporal averaging has the disadvantage that the spatial resolution might change during time. On the other side, spatial averaging seems only reasonable, if at least a rough estimate of the velocity distribution along the flow direction is available. For a better comparison, the plots of the turbulent intensity are restricted to a maximum value of one, even if partly this value is exceeded. This can occur mainly in the tail shortly before the avalanche stops and single blocks hit the sensor. In this case the average value is close to zero but the single impact is noticeable.

1.3 Load plate measurements

On the uphill side of the dam, two 1 m^2 large load plates are placed at heights 2 and 8 m above the dam base. The plates are constructed to measure the three stress components: (z) normal to the slope, (x) shear pointing towards the dam crown and (y) shear pointing at a right angle. Each load plate has a maximum measuring range of 400 kPa in the normal direction and 200 kPa for the shear components. A detailed description can be found in (SATSIE, 2003).

In general, an avalanche transmits stresses due to normal pressure, p , and tangential traction, q , at the contact surface. Thus, any stress within a snowpack is a combination of both contributions, and forces measured by a load plate can be written as

$$\begin{aligned} LP_z &= f_z(p, q_x, q_y, \alpha) \\ LP_x &= f_x(p, q_x, q_y, \alpha) \\ LP_y &= f_y(p, q_x, q_y, \alpha) \end{aligned} \quad (1.3)$$

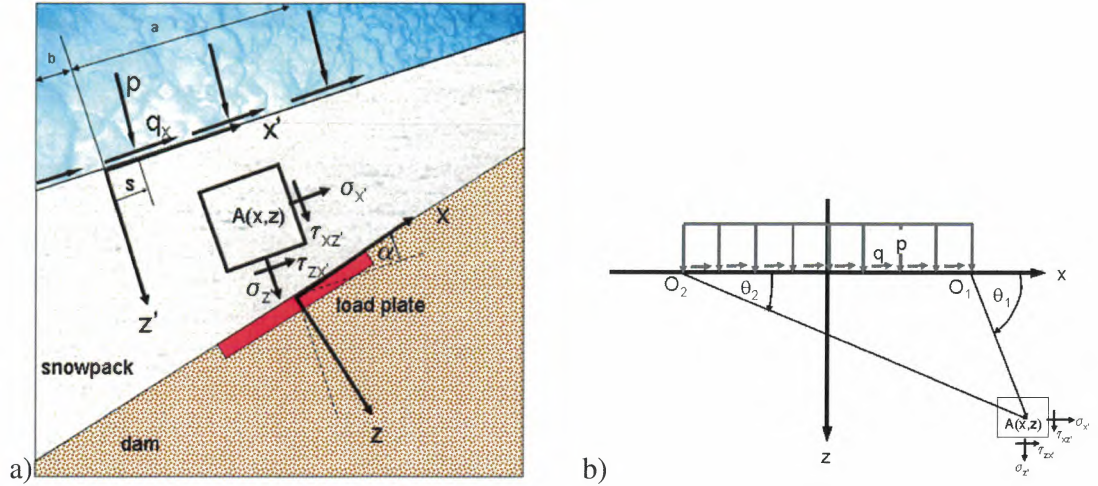


Figure 1.3: Load plate measurements: schematic illustrating the relation between the coordinate systems adapted to the ground and the snow surface, respectively.

where α is the angle between the sliding surface and the plane of the load plate. The functions f_x , f_y , and f_z might be defined using the superposition of the Boussinesq solutions for a point load normal and tangential to the contact surface with an elastic, isotropic and semi infinite medium and their integration over the loaded area. If one assumes, for simplicity, the avalanche as an uniform rectangular load, the measured force can then be used to back-calculate the normal stress, p , and the tangential components, q_x and q_y . Assuming an infinitely wide avalanche hitting the dam and a Poisson ratio ν equal to 0.5, the stresses at a point with coordinates (x, z) (see Fig. 1.3) within the snow pack read

$$\sigma'_x = -\frac{2z}{\pi} \int_{-b}^a \frac{p(s)(x-s)^2 ds}{((x-s)^2 + z^2)^2} - \frac{2}{\pi} \int_{-b}^a \frac{q_x(s)(x-s)^3 ds}{((x-s)^2 + z^2)^2} \quad (1.4a)$$

$$\sigma'_z = -\frac{2z^3}{\pi} \int_{-b}^a \frac{p(s) ds}{((x-s)^2 + z^2)^2} - \frac{2z^2}{\pi} \int_{-b}^a \frac{q_x(s)(x-s) ds}{((x-s)^2 + z^2)^2} \quad (1.4b)$$

$$\tau'_{xz} = -\frac{2z^2}{\pi} \int_{-b}^a \frac{p(s)(x-s) ds}{((x-s)^2 + z^2)^2} - \frac{2z}{\pi} \int_{-b}^a \frac{q_x(s)(x-s)^2 ds}{((x-s)^2 + z^2)^2} \quad (1.4c)$$

The stresses in the system of the load plates are then given by

$$\begin{pmatrix} \sigma_x & \tau_{pxz} \\ \tau_{xz} & \sigma_z \end{pmatrix} = \begin{pmatrix} \cos \alpha & -\sin \alpha \\ \sin \alpha & \cos \alpha \end{pmatrix} \cdot \begin{pmatrix} \sigma'_x & \tau'_{pxz} \\ \tau'_{xz} & \sigma'_z \end{pmatrix} \cdot \begin{pmatrix} \cos \alpha & -\sin \alpha \\ \sin \alpha & \cos \alpha \end{pmatrix}^T \quad (1.5)$$

The angle, α , measure between the dam surface and the surface of the snowpack, depends on the snow distribution in front of the dam. For definition of the load functions in three



dimensions we refer to, e.g., (Johnson, 2001, Chapter 3.2 and 3.6). Due to the motion of the avalanche, the load functions vary with time. Only those parts of the avalanche in proximity to the sensors contribute much as the influence of a distributed load decreases with distance. Shortcomings in the approximations above are: 1) the Poisson ratio, ν , for a real snowpack is less than 0.5; 2) one should consider a layered system consisting of a soft snowpack and a stiffer ground.

1.4 Velocity estimates

Estimates of the avalanche front speed are based on pulsed Doppler radar (DR) measurements by NGI, seismic measurements by the Department of Geology and Geophysics (DGG) at the University of Barcelona, and the timing between impacts on the constructions. In the plot for time series, the zero time is taken as the time when the avalanche hits the first sensor. In the Winter 2004/2005 the first sensor was the steel tower.

Pulsed Doppler radar measurements

In one successful avalanche releases during the season, pulsed Doppler radar systems were used to measure the avalanche velocity. The pulsed Doppler radar emits short pulses and samples the echo in distinct time intervals, corresponding to distance intervals (range gates). Frequency analysis of the echo signals, exploiting the the Doppler effect, yields the velocity distribution within the width of a range gate. Thus, it is possible to gain information on the front speed along the track and information on the velocity versus time at a specific location (Schreiber and others, 2001).

From this information it is also possible to approximately transform times series of measurements at a specific location into a spatial distributions of the same quantity along the avalanche body as it passes the sensor (neglecting any change of the quantity downstream). This allows one to get a glimpse of the spatial structure of the avalanche. The position within the avalanche, x_{pwa} , is a measure of distance behind the front as it is measured by the sensor after a given time. The position can be calculated by

$$x_{pwa} = \int_{t_0}^t u(t) dt \quad (1.6)$$

where t_0 is the arrival time of the front at the specific location. x_{pwa} is comparable to the wind run used in meteorology.

In addition to the velocity, information on accelerations can be derived. To this end, the velocities of a pair of adjoining range gates, having a width Δx are compared. Starting with a first guess of the average velocity, \bar{u} , between both range gates (either the upstream velocity, $u_1(t_1)$, or another suitable estimate) the required travel time, $\Delta t = \Delta x / \bar{u}$, between the range gates can be calculated. Then, the velocity of the downhill range gate $u_2(t_1 + \Delta t)$ is used to recalculate $\bar{u} = (u_1(t_1) + u_2(t_1 + \Delta t)) / 2$. In this way, the average velocity can be found iteratively. The estimated acceleration is calculated by



$$a = \frac{(u_1(t_1) - u_2(t_1 + \Delta t))}{\Delta t} \quad (1.7)$$

However, one should keep in mind that the measured velocities are actually only a weighted average speed within the width of the range gate. In the experiments, range gate widths of 25 m, were used.

Commonly used model equations for avalanches base the balance between driving force due to gravity and the resisting force due to dry friction (no velocity dependency) and friction which is linear and quadratic in the velocity (cf. Mellor (1968)). This can be written by

$$a = g \sin \phi - (a_0 \cos \phi + a_1 u + a_2 u^2) \quad (1.8)$$

Using the calculated acceleration (deceleration) values from (1.7), it is possible to fit these according to (1.8) and so gain some idea of the friction coefficients. It should be noted that a_1 and a_2 in this representation are function of the flow height. Not included in this approximation are effects due to the gradient of the normal pressure appearing in models based on continuum mechanics.



2 WINTER 2004/2005

2.1 General conditions in 2004/2005

The first part of the 2004-2005 was fairly stormy with comparatively large amounts of snow. By the end of January the total snow height at 930 m a.s.l. was 340 cm, corresponding to more than 200% of the median for this month. The winds in this period had a slightly more westerly component than normal, which resulted in a rather unusual snow deposition pattern, and as an effect of this, avalanche releases at unusual locations. This is reflected in the release pattern of the winter's largest avalanche in Ryggfonn in early January.

The snow was nevertheless mostly stable during the winter, except for a depth hoar layer near the ground that had been established in December. This situation caused unexpected avalanching in some paths, but the January avalanche in Ryggfonn resolved the situation in this starting zone.

Due to the loss of the meteorological station at Fonnbu by fire, no monthly climate data are available. However, Fig. 2.1 shows weather measurements from stations close to the avalanche site. Red line graphs indicate measurements made in the runout zone at 600 m a.s.l., blue graphs indicate measurements made at a ridge station close to the starting zone at 1400 m a.s.l. The precipitation is measured at a valley station (Sindre, Stryn). The vertical lines are the avalanche occurrences in the Ryggfonn path.

The following avalanches were observed in the Ryggfonn path this winter:

- December 7 2004 at 17:00 h: naturally released small avalanche
- January 7 2005 at 04:16 h: naturally released wet snow avalanche; this avalanche consisted mostly likely of two distinguish surges of which the first surge was a dry mixed avalanche and the second more wet.
- April 15 2005: naturally released small dry snow avalanche
- April 16 2005 at 15:00 h: artificially released dry snow avalanche

A classification is given in Tab. 2.1 and an overview of the available measurements in Tab. 2.2. Figure 2.2 plots the outlines of the two major avalanches at Ryggfonn in Winter 2004/2005.

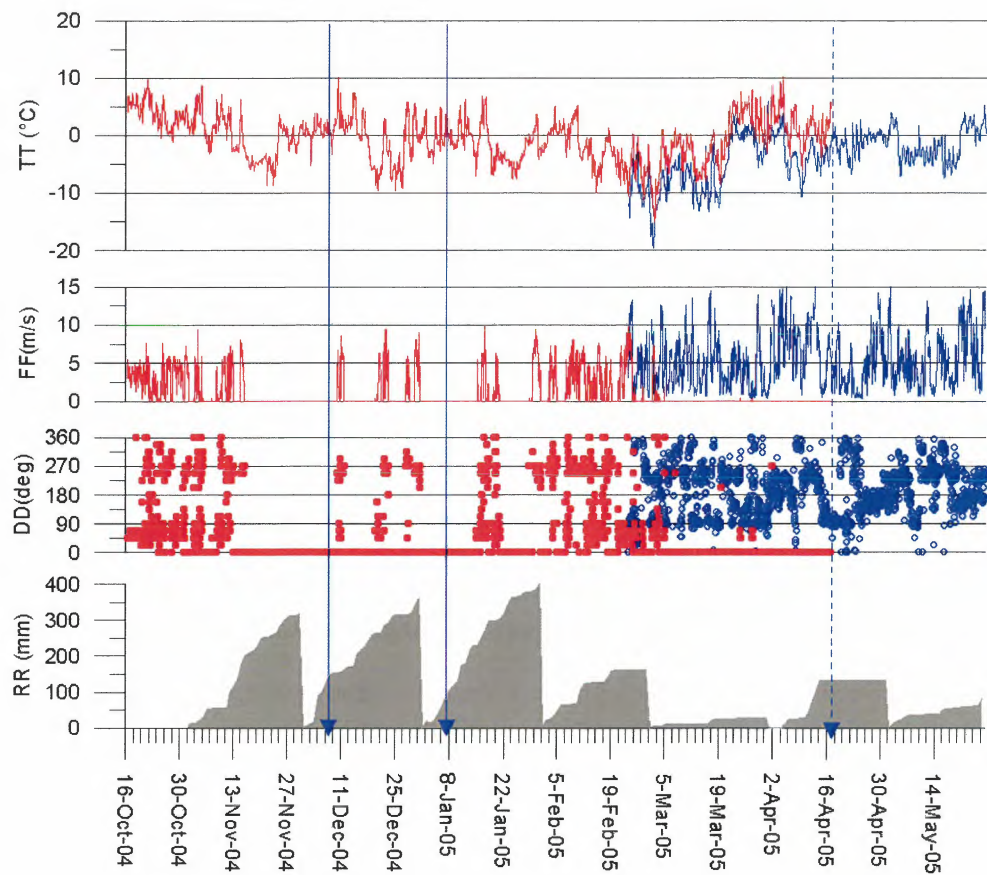


Figure 2.1: Weather data from Rygghonn test site. Red line graphs indicate measurements made in the runout zone at 600 m a.s.l., blue graphs indicate measurements made at a ridge station close to the starting zone at 1400 m a.s.l. The snow height and the unfilled accumulated precipitation graphs is based on data from the DNMI-station 58880 Sindre, 118 m a.s.l. Vertical lines with arrows indicate avalanches in Rygghonn (solid=natural, dotted=artificial avalanche)



Table 2.1: Avalanche classification

Date yyyymmdd hh:mm	Size ¹	Deposit (10 ³ m ³)	Classification (ICSI) ²										Speed (m s ⁻¹)	
			A	B	C	D	E	F	G	H	J	LC4-LC1 ³ 101 m	LC1-LP1 ⁴ 218 m	
20041207 17:00	NA	NA	3	2	1	2	7	3	2	1	1	NA	NA	
20050107 04:16	4	NA	3	2	1	1	7	3	2	1	1	30	17	
20050107 04:16 b	4	NA	3	2	1	1	2	3	2	1	1	NA	5	
20050415	NA	NA	7	/	1	2	/	/	1	1	1	NA	NA	
20050416 15:00	4	NA	4	7	1	2	7(2)	2	7	3	4	30	5	

¹According to Canadian avalanche size classification, cf. (McClung and Schaerer, 1993)

²According to International Avalanche Classification (Avalanche Atlas (UNESCO, 1981), also in (McClung and Schaerer, 1993))

³The estimated average speeds are calculated between the steel tower and the concrete structure,

⁴and between the concrete structure and the foot of the dam, respectively.

Table 2.2: Overview of archived measurements at Ryggfonn test site during winter season 2004/2005

Date yyyymmdd hh:mm	geophone (GF)1 2 3 4 5 6 H1	load cell (LC)4 5 1 2 3	load plate (LP)1 2	radar P-DR	field obs.	maps
20041207 17:00	X O O O O O O	U X O O O	O O	-	-	X
20050107 04:16	X X X X X X X	X X X X X	X X	-	-	X
20050107 04:16 b						
20050415	- - - - - - -	- - - - -	- -	-	-	X
20050416 15:00	X X X X X X X	B X X X X	X X	X	X	X

Codes: X -data; P -sensor partly buried; B -sensor buried; O -data, but no measured signal (did not reach sensor); - -no data; U sensor status unknown

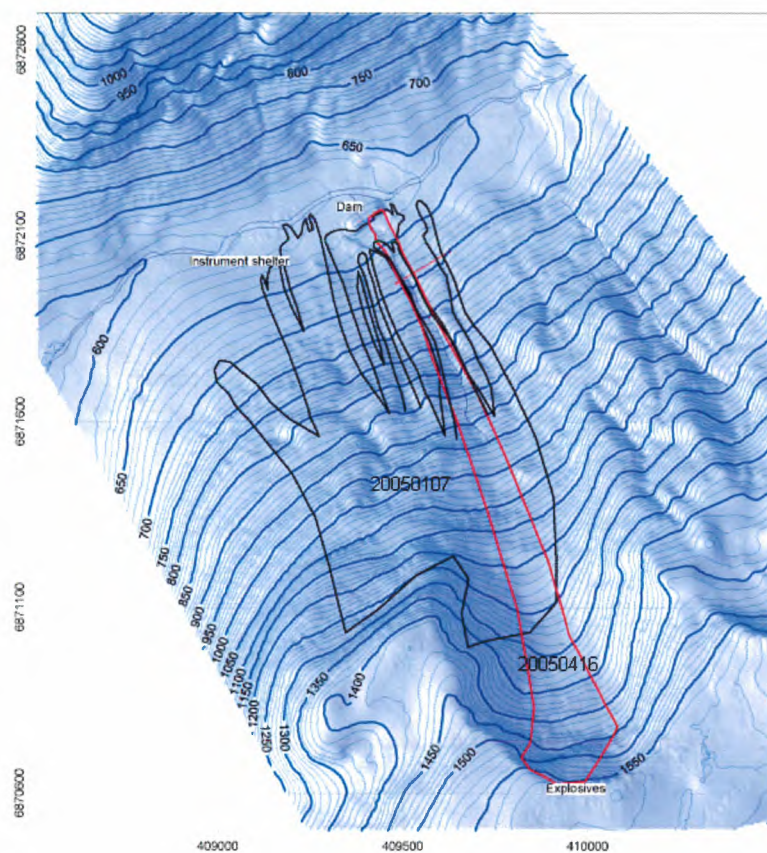


Figure 2.2: Map of the Ryggfonn test site with the all avalanche deposits recorded in Winter 2004/2005. The black line indicates the natural avalanches, while the red solid line represents an artificially released avalanche on 20050416 15:00

2.2 Avalanche 20041207 17:00

Avalanche code (UNESCO/IAHS 1981): A3, B2, C1, D2, E7, F3, G2, H1, J1.

Weather and avalanche summary At 930 m a.s.l., the air temperature was -0.7°C , with high temperatures of 4.0°C the preceding 24 hours. At the time of the avalanche release there were SSW-wind of 6 m s^{-1} , with gusts up to 12 m s^{-1} . In the runout zone at 600 m a.s.l. the temperature was 2.7°C , which was also the highest in the preceding 24 hour period.

Results

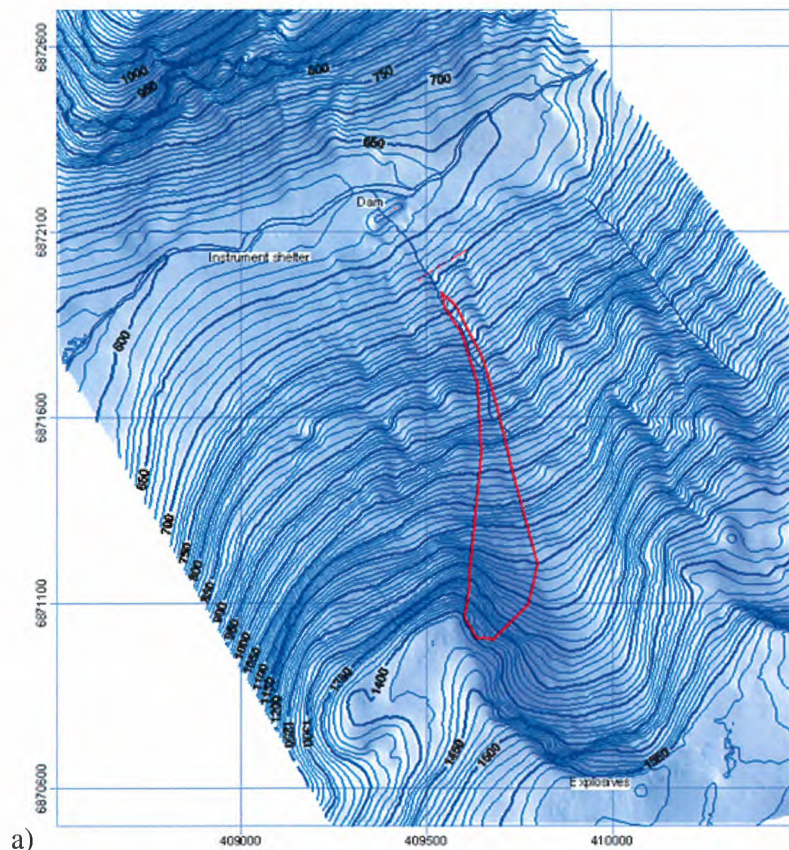


Figure 2.3: Avalanche 20041207 17:00: Deposition/outline map.

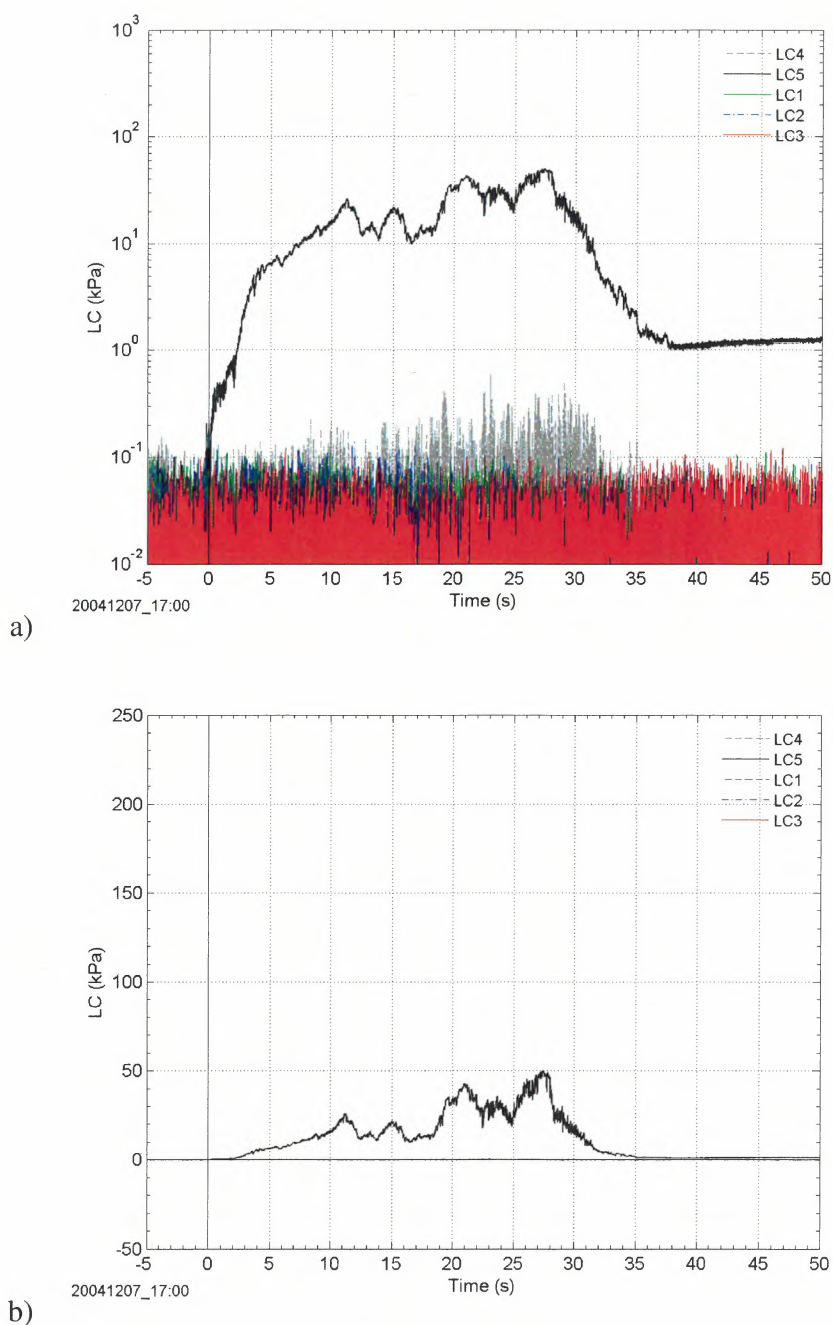
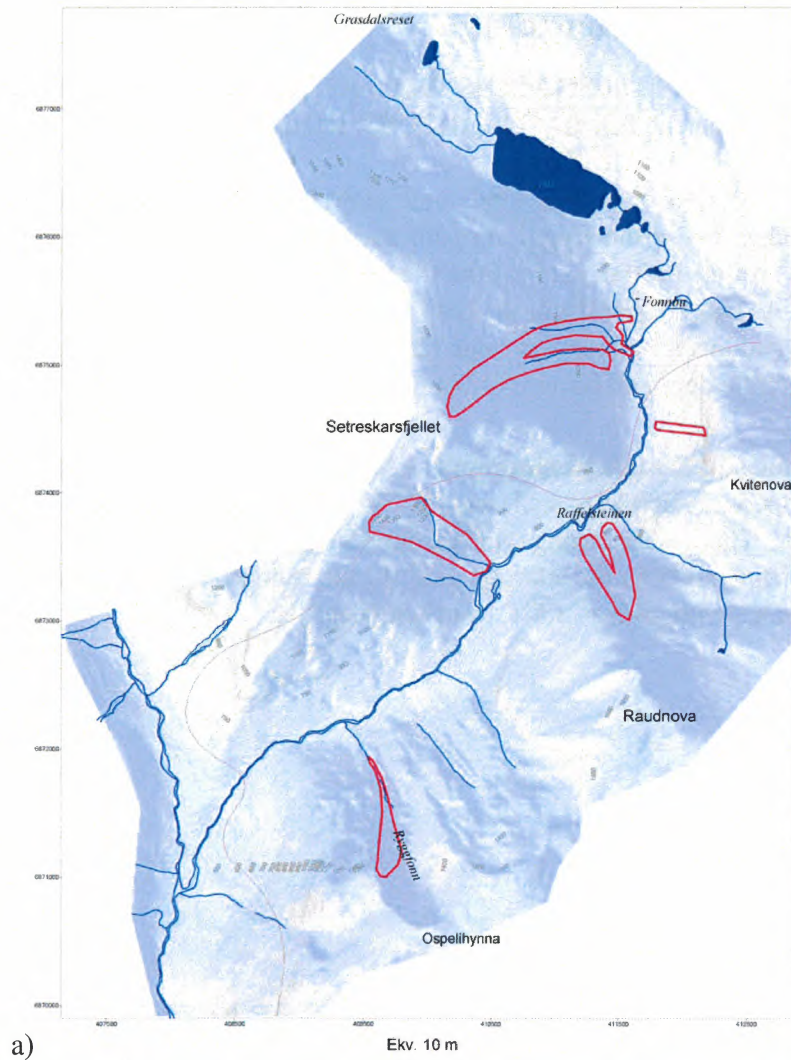


Figure 2.4: Avalanche 20041207 17:00: Load cell measurements: pressure vs. time; a) logarithmic and b) linear presentation.



b)

Figure 2.5: Avalanche 20041207 17:00: Deposition/outline map in the Ryggfonn area (upper panel); Avalanche deposit in the Fonnbu area around the same time (lower panel).



2.3 Avalanche 20050107 04:16

Avalanche code (UNESCO/IAHS 1981): A3, B2, C1, D1(2), E7, F3, G2, H1, J1.
(second avalanche A3, B2, C1, D1(2), E2, F3, G2, H1, J1).

During a period of strong winds and snow in the first part of January, several natural avalanches ran in the Rygghonn path and the adjacent area. Because the 0°C isotherm was at around 1000 m a.s.l. at the time of release, the avalanche consisted of partly wet snow. As can be seen from the map, the avalanche originated from the west side of the cirque and lower on the west ridge. Bad visibility and irregular terrain made it difficult to estimate the depth and extent of the initial fracture.

Weather and avalanche summary At the time of the avalanche release at 04:16 h, the air temperature at 930 m a.s.l. was -0.1°C, with high temperatures of 0.8°C the preceding 5 hours. There were strong winds from SSW, with gusts up to 19 m s⁻¹, heavy snowfall and drifting snow in the starting zone. In the runout zone at 600 m a.s.l. the temperature was 0.4°C, with high as 3.5°C, four hours earlier.

Results

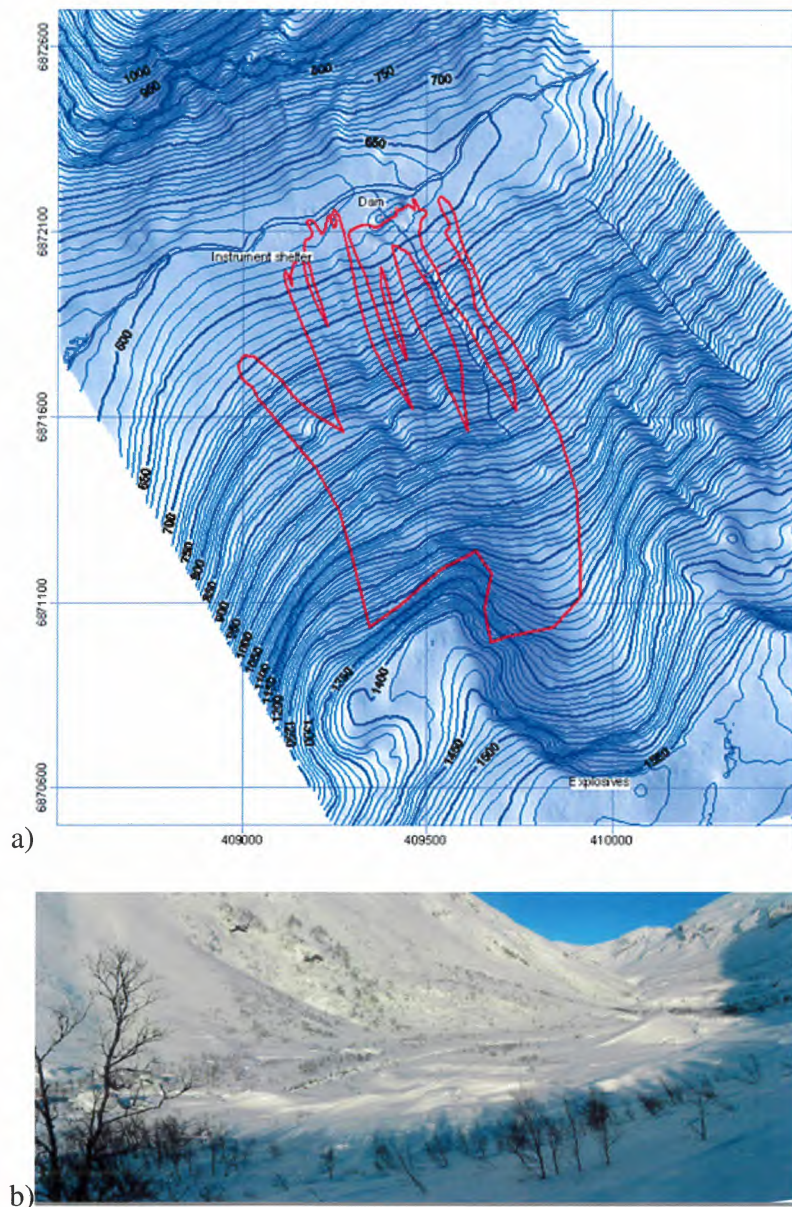


Figure 2.6: Avalanche 20050107 04:16: Deposition/outline map (upper panel); area of the dam after the avalanche.

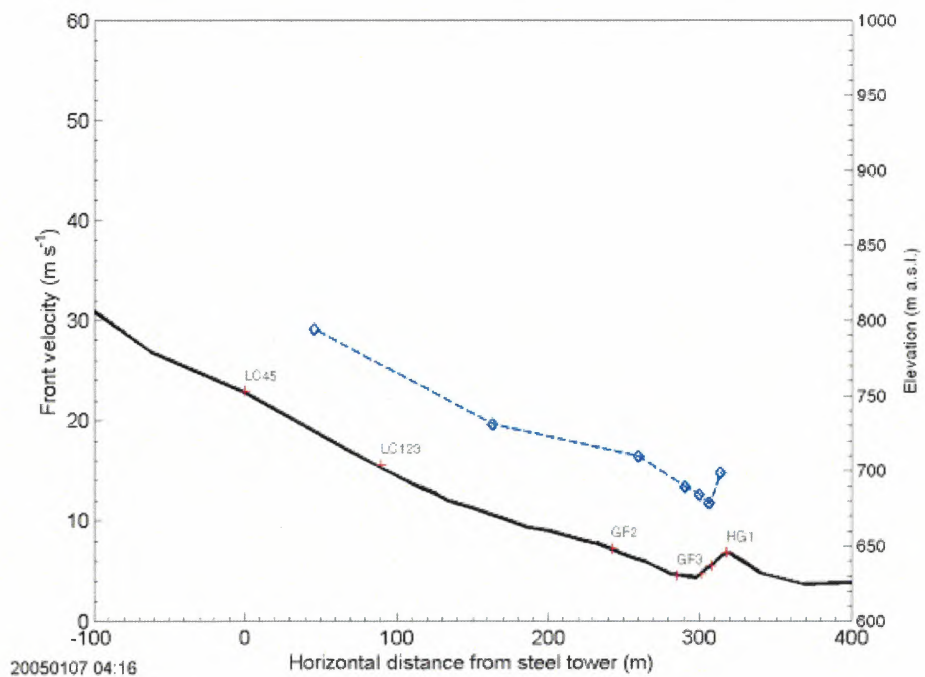
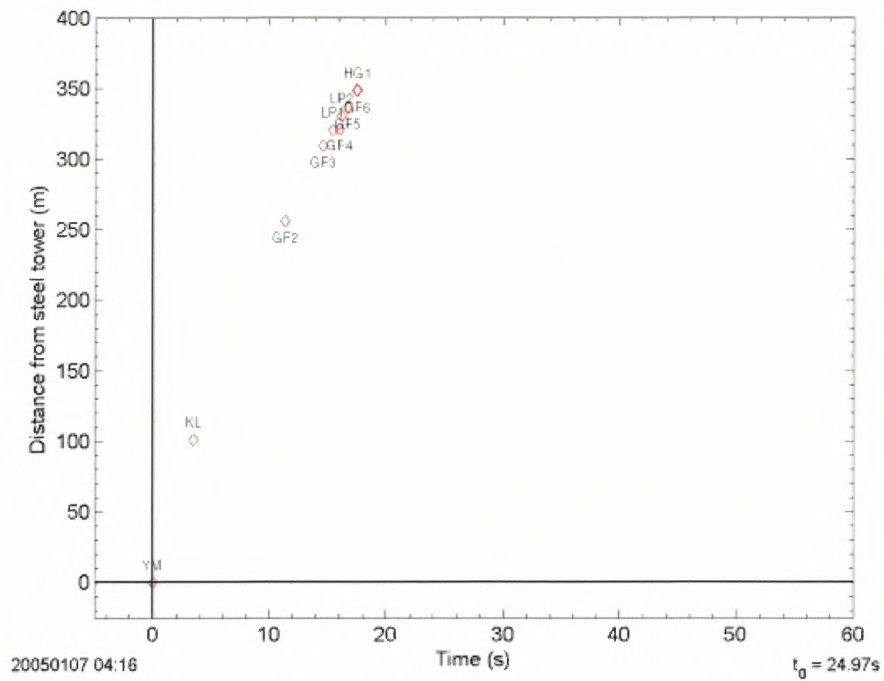


Figure 2.7: Avalanche 20050107 04:16: Timing of the first surge; Distance vs. time (top); Front velocity vs. horizontal distance (bottom). Shown are estimates based on the arrival times at various sensor locations.

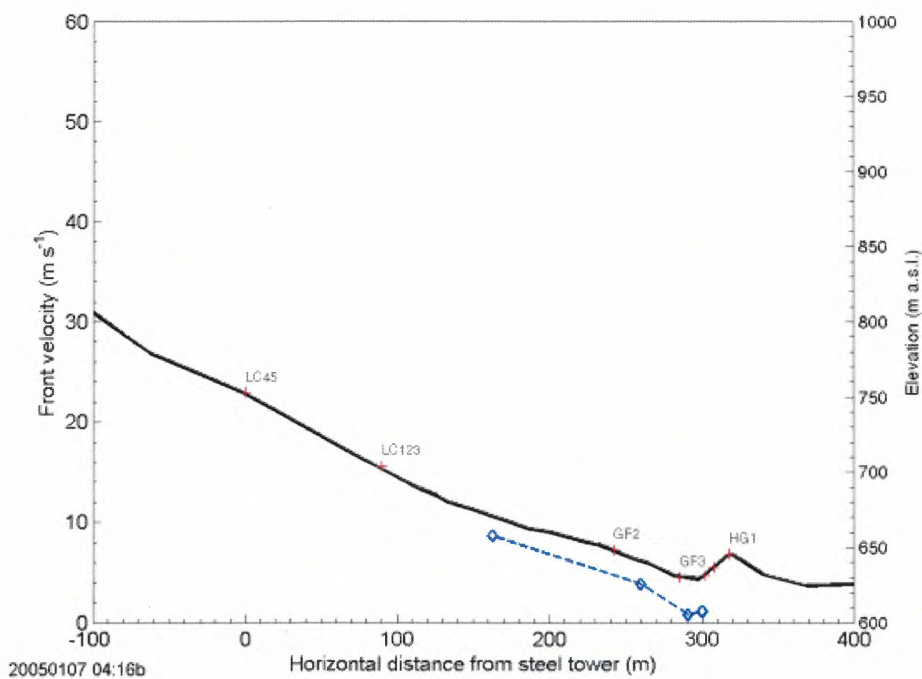
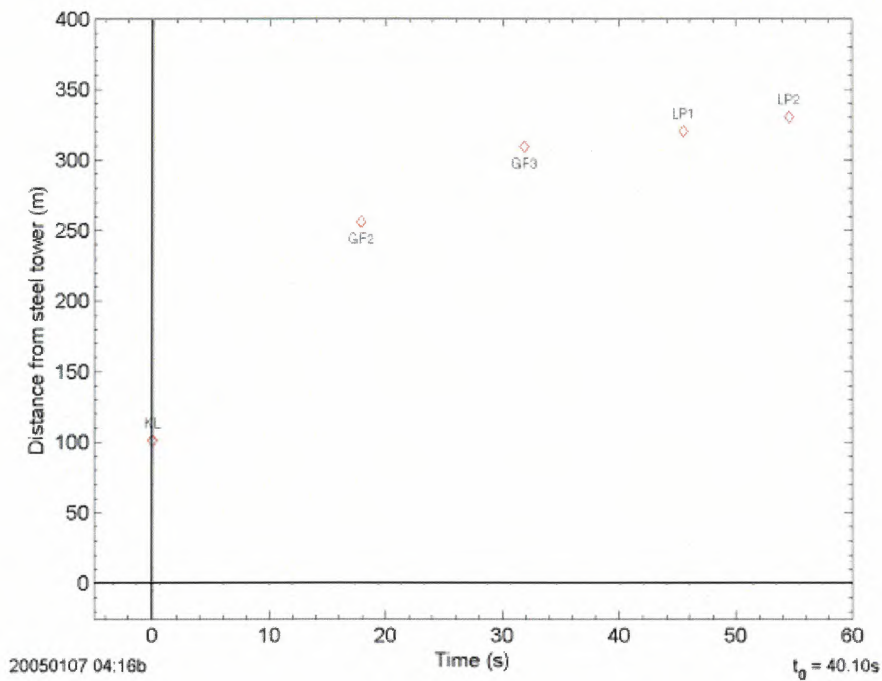
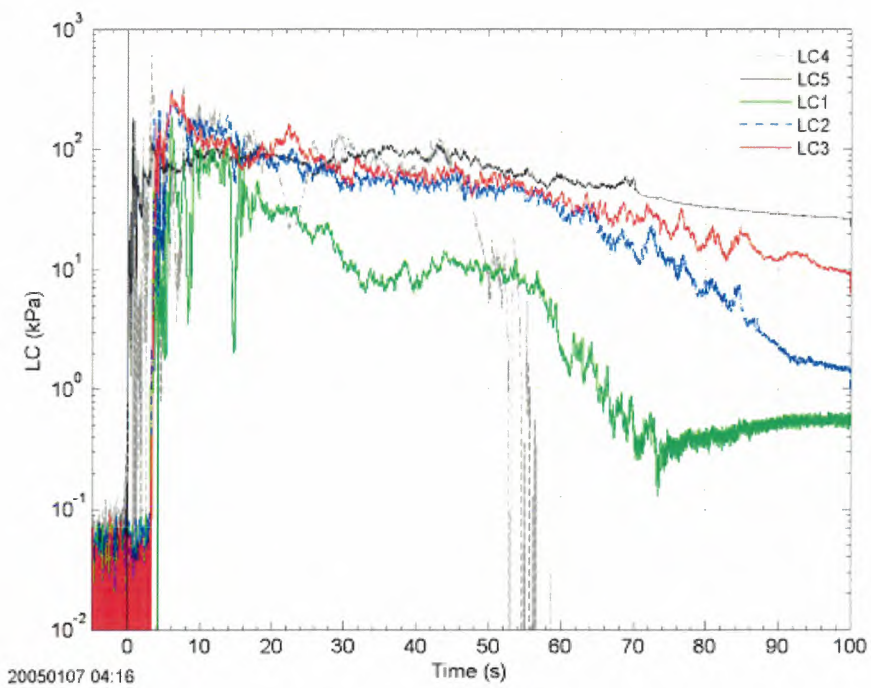
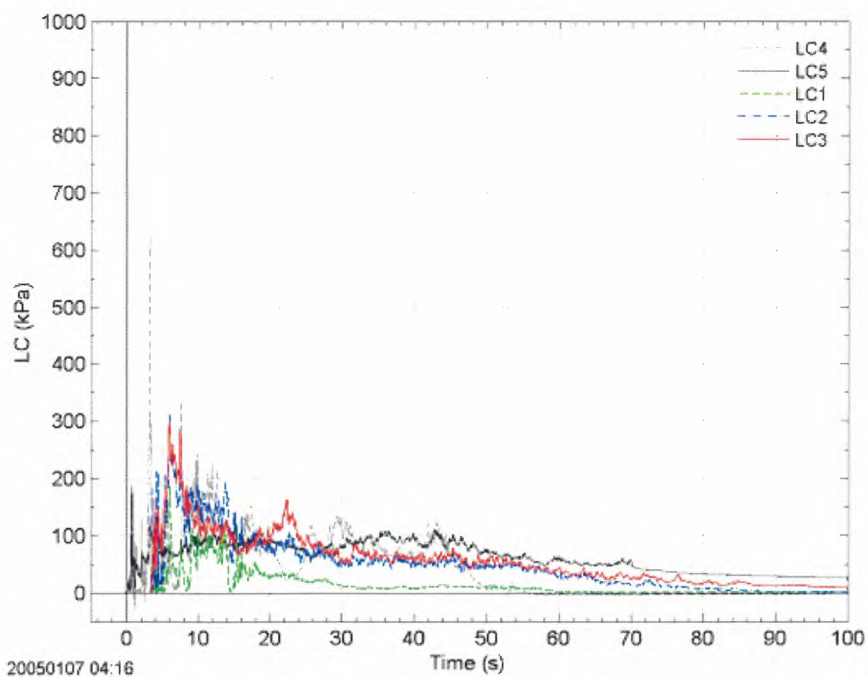


Figure 2.8: Avalanche 20050107 04:16: Timing of the first surge; Distance vs. time (top); Front velocity vs. horizontal distance (bottom). Shown are estimates based on the arrival times at various sensor locations.

20021048-11



a)



b)

Figure 2.9: Avalanche 20050107 04:16: Load cell measurements (raw data): pressure vs. time; a) logarithmic and b) linear presentation.

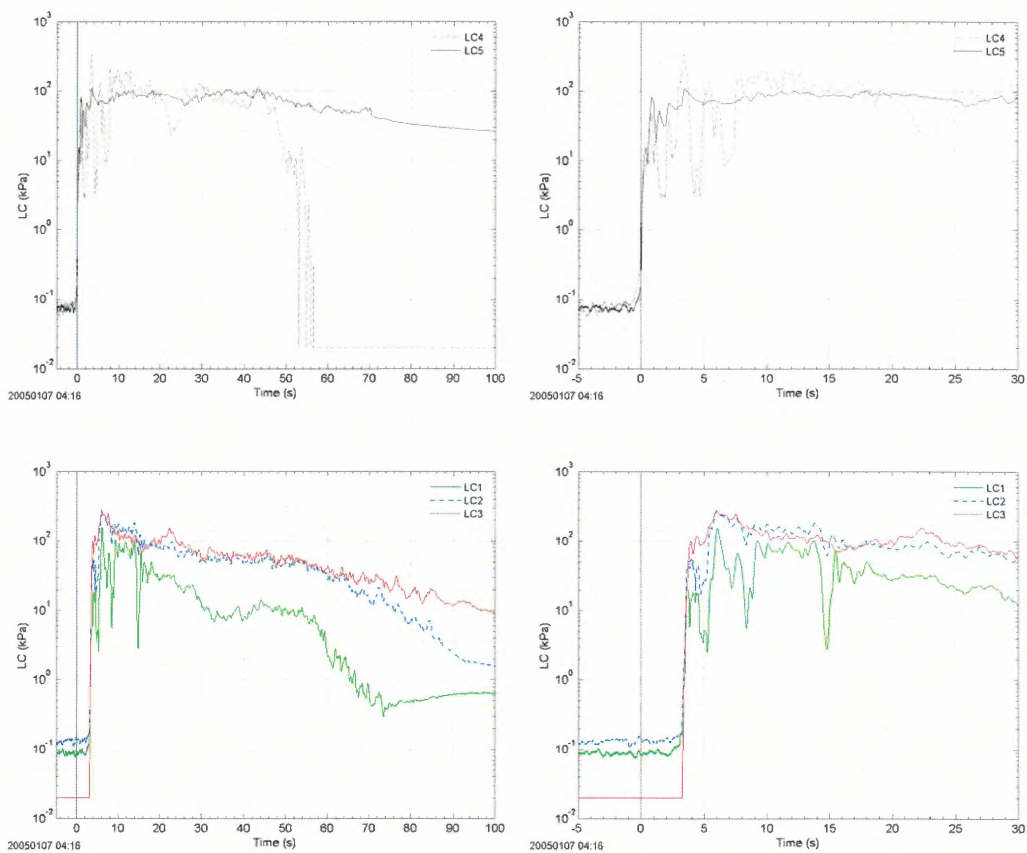


Figure 2.10: Avalanche 20050107 04:16: Load cell measurements: pressure vs. time; top) at the steel tower; and bottom) at the concrete wedge. Data are running means over 0.25 s. Right hand shows an enlargement of the first 30 s.

20021048-11

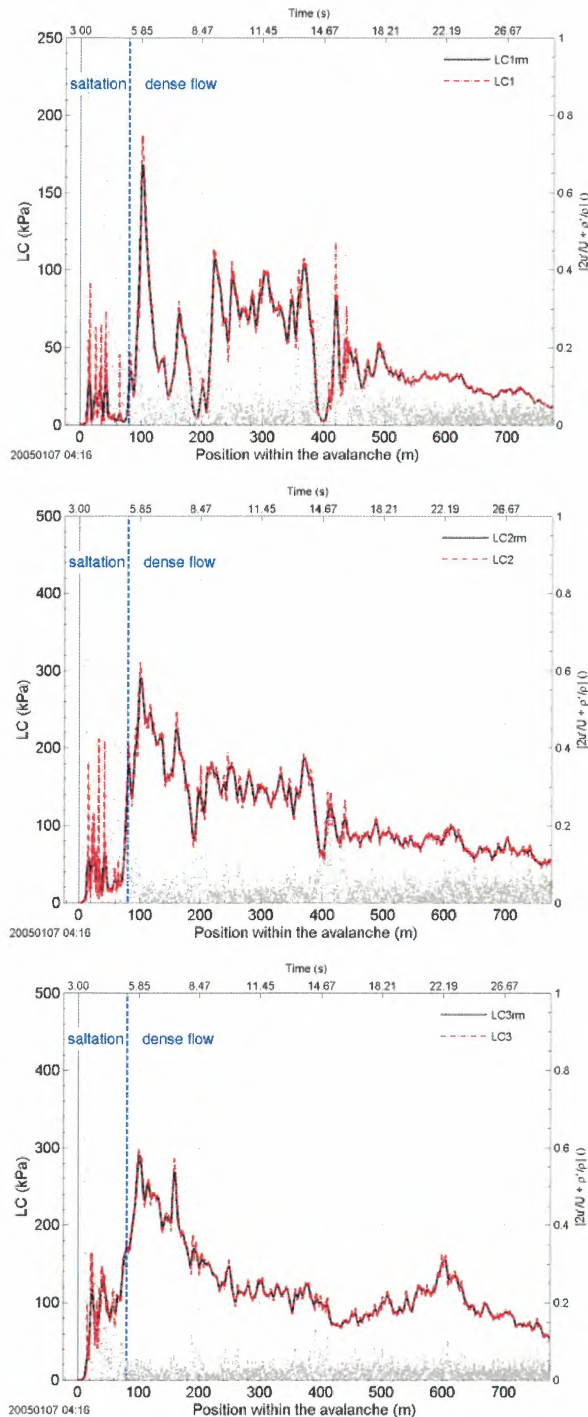


Figure 2.11: Avalanche 20050107 04:16: Fluctuation intensity vs. position within the avalanche. The lines present the measured impact pressure (dashed line) and the running mean (full line) taken over 5 m, respectively (left axis), at the concrete wedge. The fluctuation intensity is marked with dots (right axis). The underlying velocity profile is based on correlation between pressure measurements at the steel tower and the concrete wedge and should be regarded as a rough estimate. Top: LC1; middle: LC2; bottom LC3.

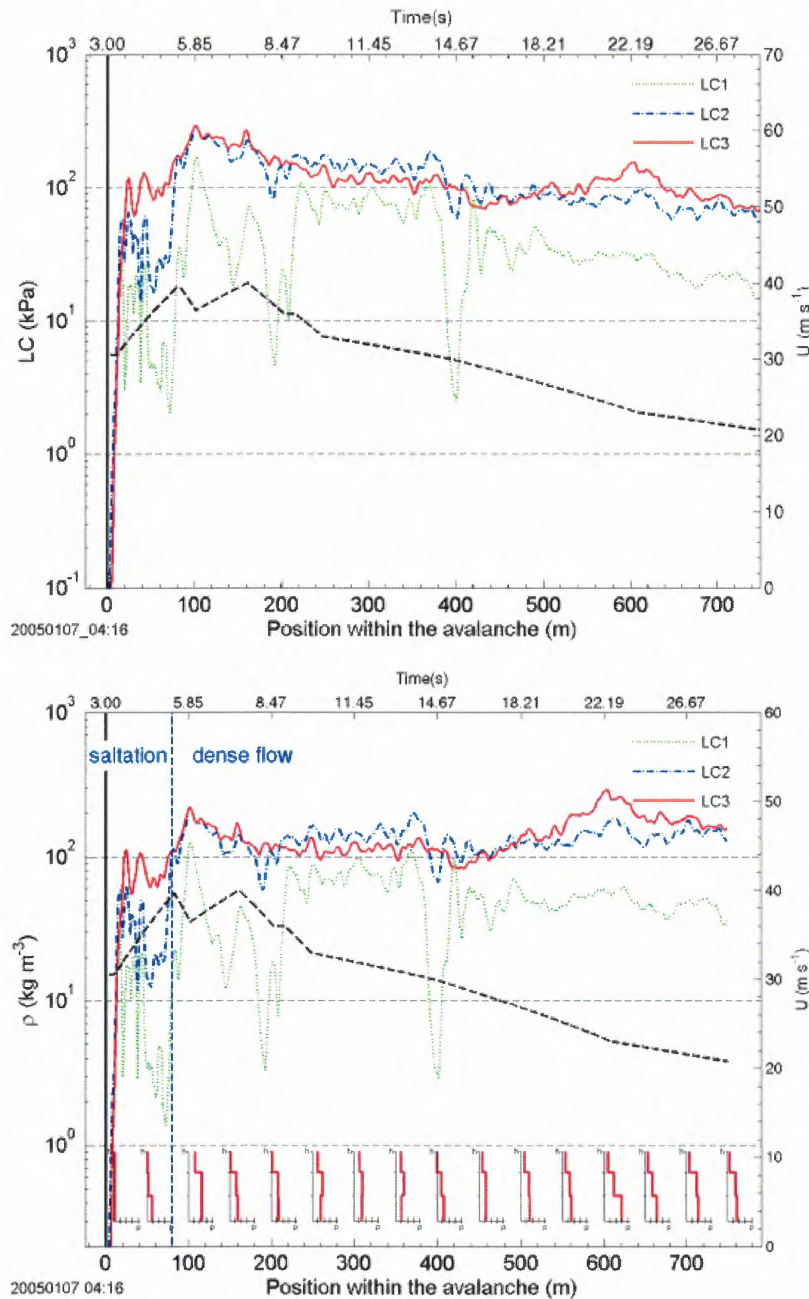


Figure 2.12: Avalanche 20050107 04:16: Impact Pressure vs. position within the avalanche (top). Estimated density vs. position within the avalanche assuming $C_D \approx 2$ (bottom). Data are running means taken over 5 m. Note the logarithmic scaling of the left ordinate and the different horizontal scaling. The small inset profiles indicate the vertical density distribution showing the mean density over the height of individual plates (ticks mark density steps by 100 kg m^{-3}). The black line shows the corresponding velocity profile (right axis). The underlying velocity profile is based on correlation between pressure measurements at the steel tower and the concrete wedge and should be regarded as a rough estimate. Correlation between LC4 and LC1 might indicate higher velocity in the frontal part.

20021048 - 11

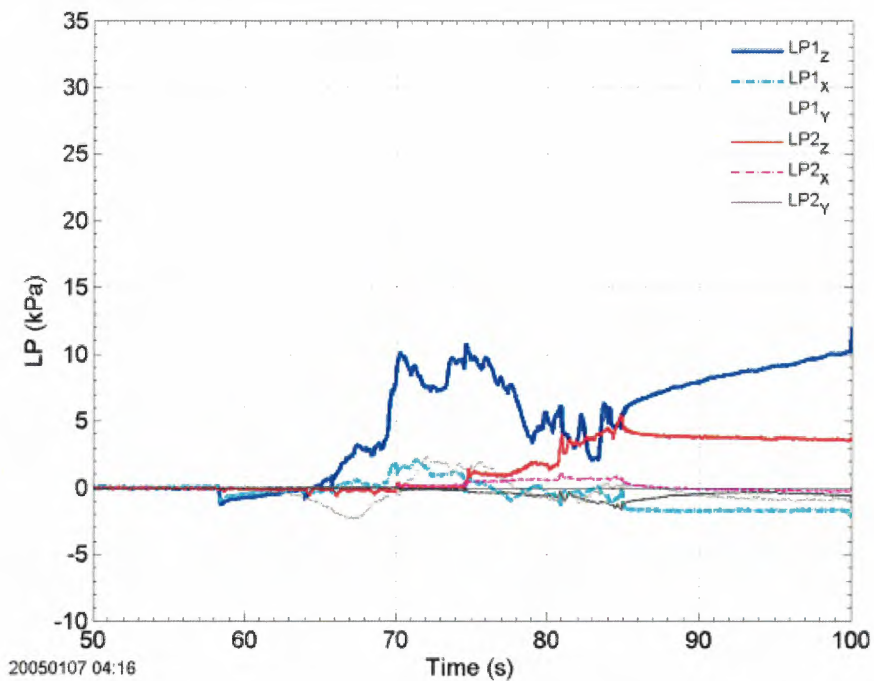
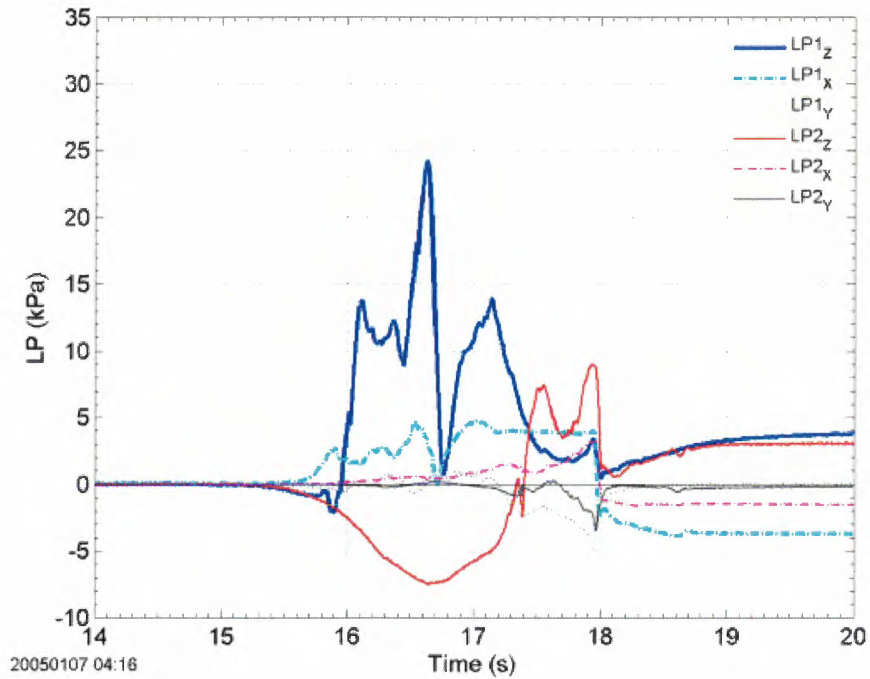


Figure 2.13: Avalanche 20050107 04:16: Load plate measurements: LP (raw data) vs. time. Top: first surge; bottom: second surge

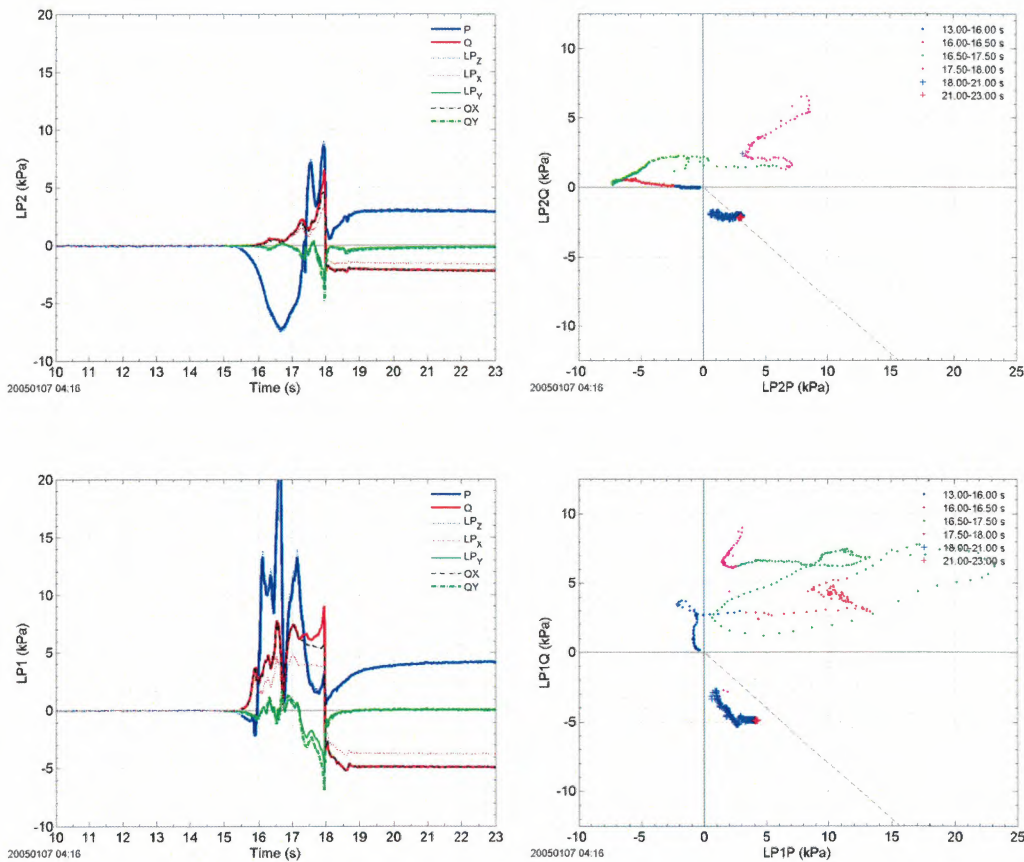


Figure 2.14: Avalanche 20050107 04:16: Load plate measurements; first surge: Stresses vs. time (left hand side) and shear stress vs. normal stress at the sliding plane (surface of the snowpack) along the dam slope (right hand side). The upper panel shows LP2 and the lower one LP1. LP_z and LP_x mark the measured stresses. P and Q are the calculated stresses according to (1.3). The dashed line in right panels corresponds to the ratio between shear and normal stress in the case of static loading ($-\tan 20^\circ$ or $-\tan 40^\circ$).

20021048-11

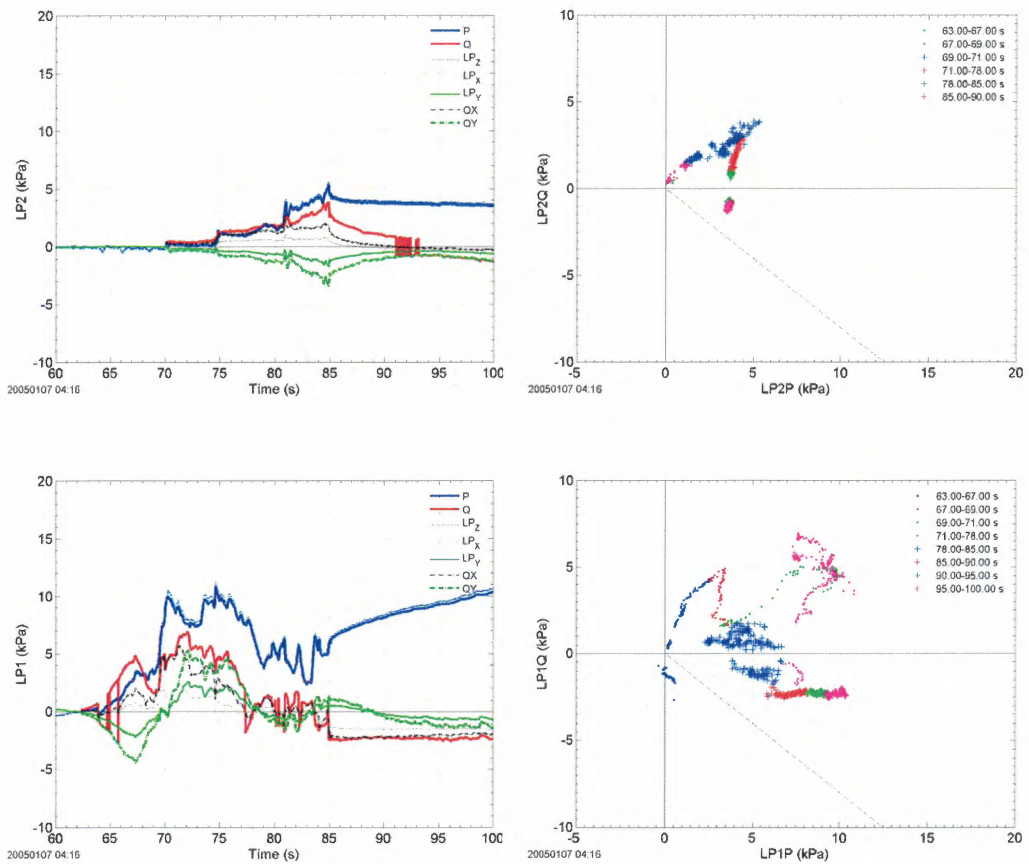


Figure 2.15: Avalanche 20050107 04:16: Load plate measurements; second surge: Stresses vs. time (left hand side) and shear stress vs. normal stress at the sliding plane (surface of the snowpack) along the dam slope (right hand side). The upper panel shows LP2 and the lower one LP1. LP_z and LP_x mark the measured stresses. P, and Q are the calculated stresses according to (1.3). The dashed line in right panels corresponds to the ratio between shear and normal stress in the case of static loading ($-\tan 40^\circ$).



2.4 Avalanche 20050416 15:00

Avalanche code (UNESCO/IAHS 1981): A4, B2, C1, D2, E7(2), F3, G7, H3, J4.

After nearly two months of stable weather and snow conditions there was a period of snowfall and SW winds in the first part of April. It was decided to attempt a blasting of Ryggfonn when the weather cleared around the 15th. Before the blasting could be done however, a small avalanche ran in the lower path as a result of afternoon sunshine on the 15th. On the 16th the main Ryggfonn avalanche was released by detonating 150 kg of explosives buried in the top cornice

Weather and avalanche summary Sunny and calm with 25 cm fresh snow deposition from previous days. At 1420 m a.s.l the air temperature was -2.5°C , with high temperatures of -1.5°C the preceding 24 hours. SW-wind of 2 m s^{-1} , with gusts up to 5 m s^{-1} . In the runout zone the temperature was 5.1°C at the time of release.

Results



Figure 2.16: Avalanche 20050416 15:00: Snapshot from the avalanche release (photo by L. Rammer).

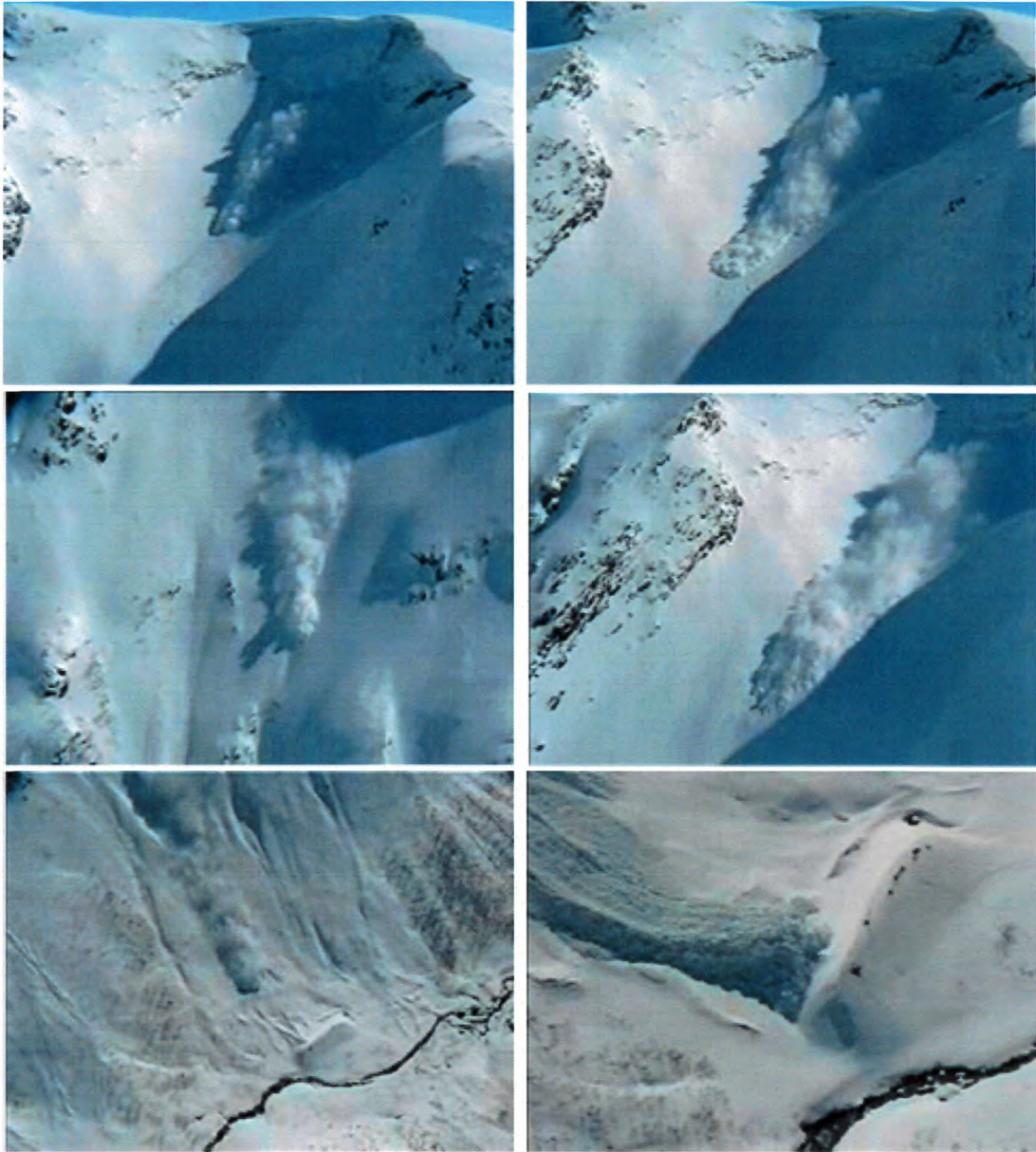


Figure 2.17: Avalanche 20050416 15:00: Snapshot from avalanche descent taken from the video by K. Kristensen.



Table 2.3: Field observations/measurements

location	clod density (kg m ⁻³)	snow temperature (°C)	water content	comments
by the dam	450 530	-5		
by the dam	450 450 650 670 650 450 600	0 0 -5 0 0 -4 0	wet dry wet wet dry wet	surrounding snowpack
50 m above the dam	450 450 350 380 570	-5 -5 -5 -5 0	dry dry dry dry wet	within shear plane
75 m above the dam	500	-5	dry	
at the concrete wedge	400 500	0 0	wet wet	shear plane 25 m west shear plan 10 m west 1 1/2 plates visible, wedge of avalanche snow in front of the plates 40 cm edge length west 70 cm edge length east
at the steel tower	600 670 690 400 660 630	0 0 0 0 0 0		at the plate wedge of avalanche snow in front of the plates 80 cm edge length west 5 m length; 2–3 m width clod size: 0.1–0.5 m

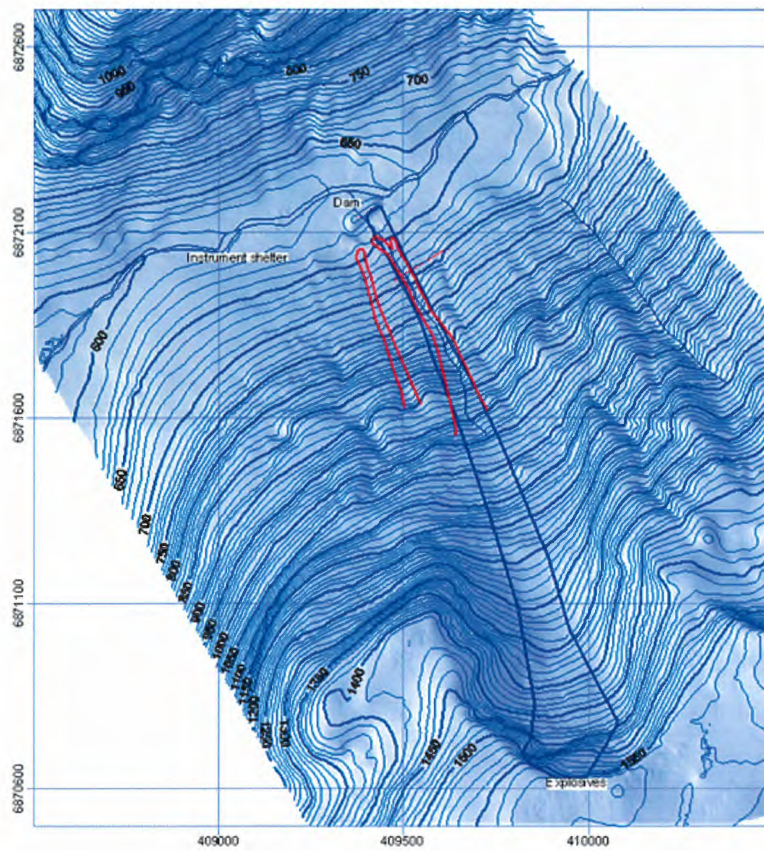


Figure 2.18: Avalanche 20050416 15:00: Deposition/outline map. Red lines events 20050415; blue line 20050416 15:00



Figure 2.19: Avalanche 20050416 15:00: Track status before the event. (Photos by Arne Moe)

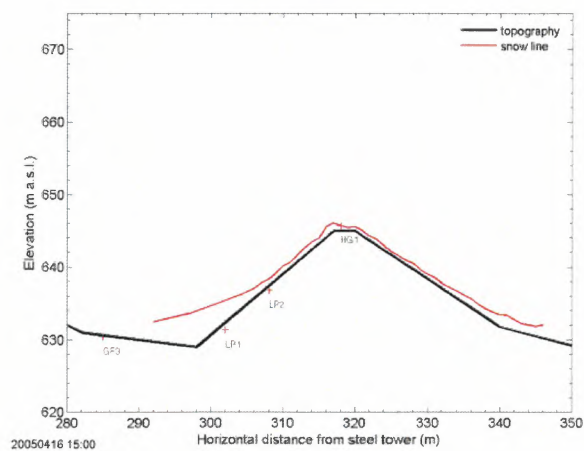
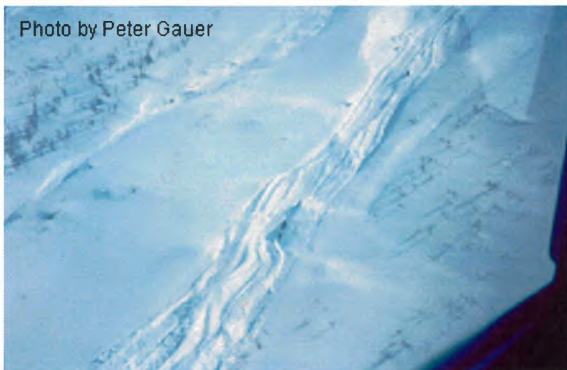


Figure 2.20: Avalanche 20050416 15:00: Snow depth profile at the dam before the event.

before



Photo by Peter Gauer



after



Photos by
Karstein Lied

Figure 2.21: Avalanche 20050416 15:00: Sensor status before and after the event. Top: load cells at the steel tower; bottom at the concrete wedge. (Photos by Karstein Lied and Peter Gauer)



Figure 2.22: Avalanche 20050416 15:00: Sensor status after the event; the width of concrete wedge is about 0.6 m. (Photo by Krister Kristensen)

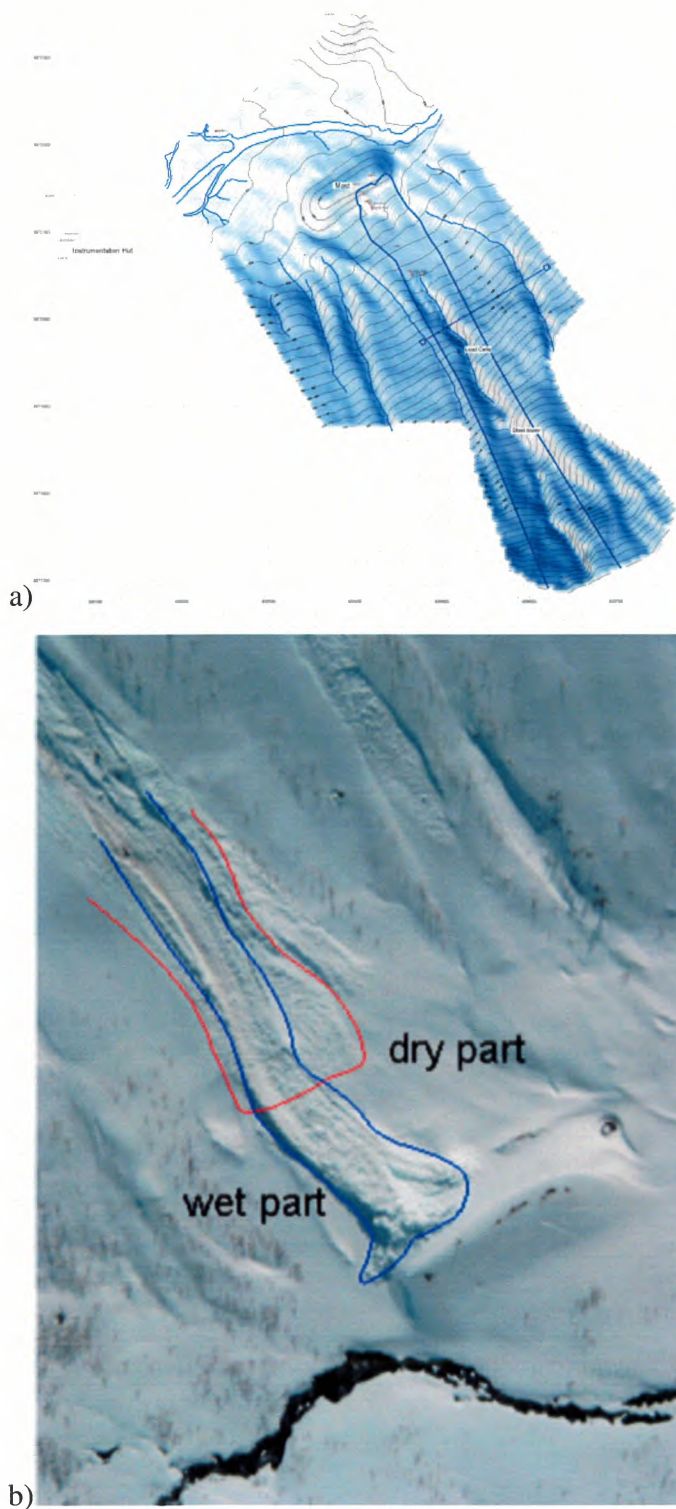


Figure 2.23: Avalanche 20050416 15:00: Deposition/outline map in the Ryggfonn area (upper panel); Avalanche deposit (lower panel; photo by Arne Moe taken from the ridge) The deposits on the right hand side and the outreach pointing to the right origin from previous events.

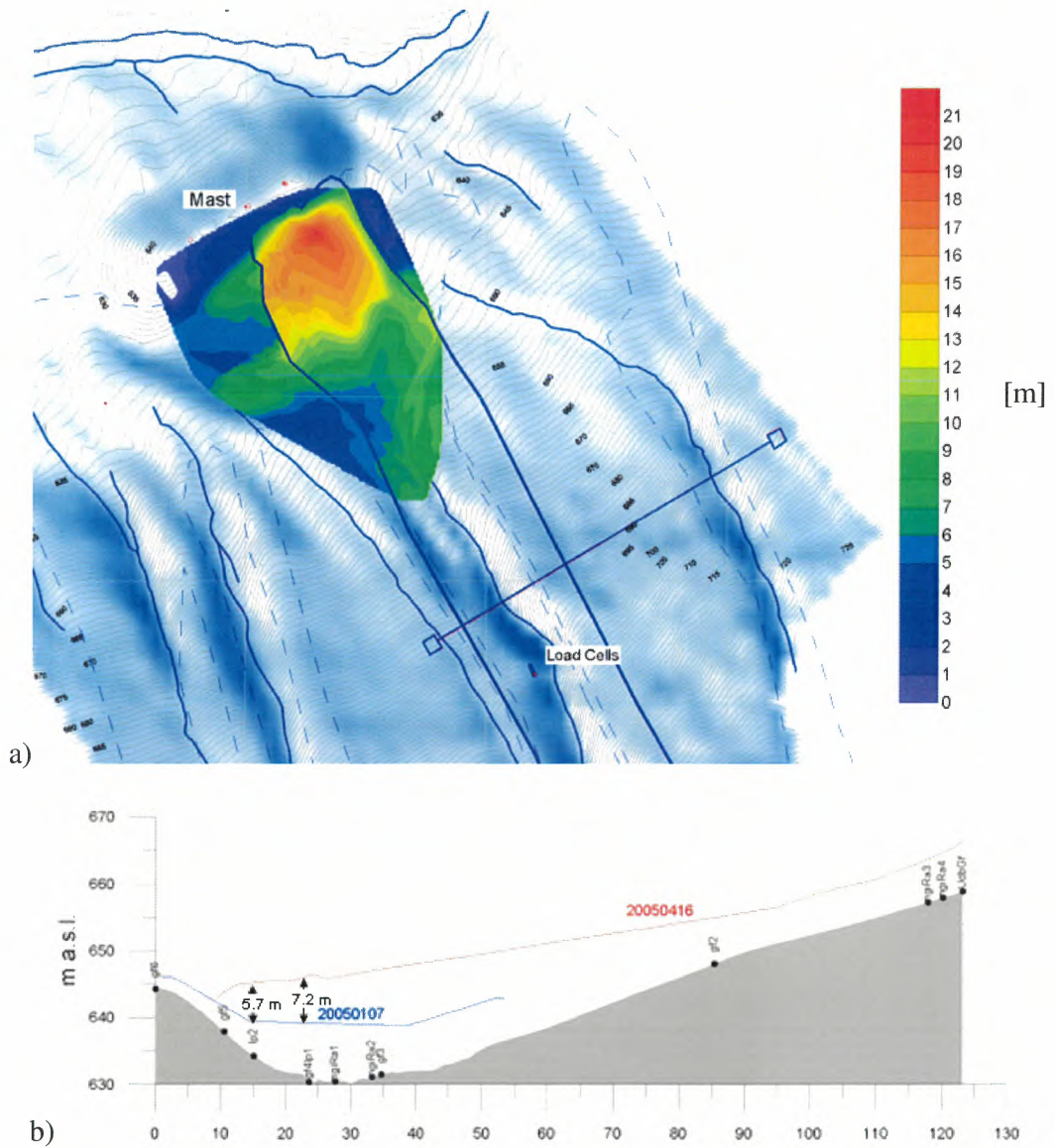


Figure 2.24: Avalanche 20050416 15:00: a) Total deposition in the runout area; b) cross section along the line connecting the load plates

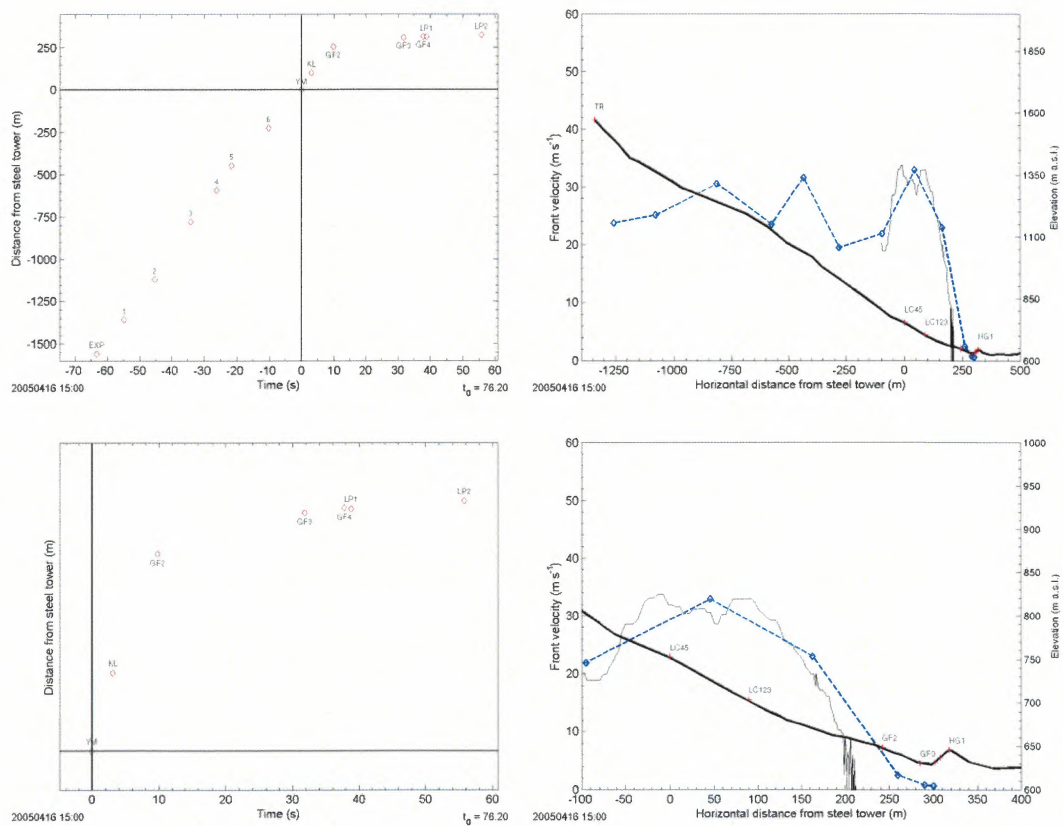


Figure 2.25: Avalanche 20050416 15:00: Timing; Distance vs. time (left); Front velocity vs. horizontal distance (right). Shown are estimates based on the arrival times at various sensor locations and on video analysis. In addition, the thin black line (right side) shows the front velocity measured by the pulsed Doppler radar. Top row shows the whole track whereas the bottom row is an enlargement of the runout area.

20021048-11

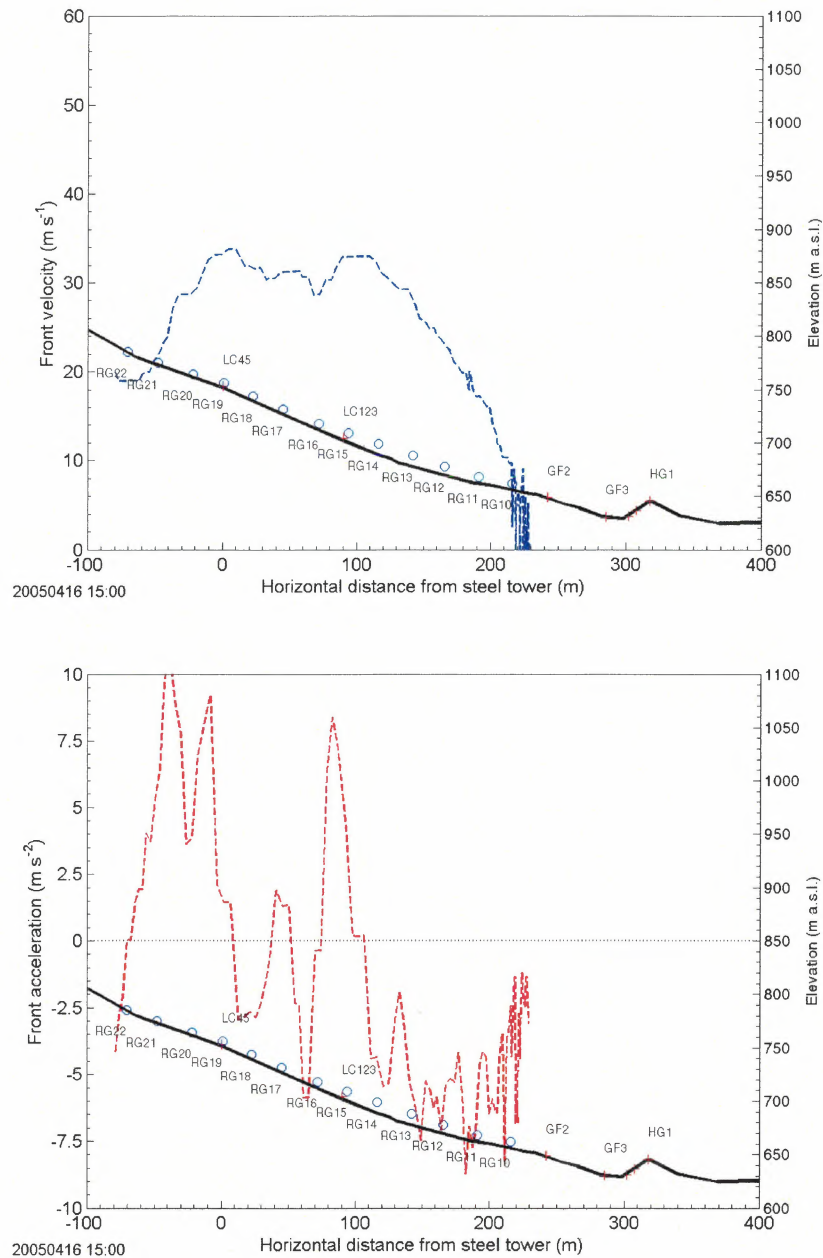


Figure 2.26: Avalanche 20050416 15:00: Front velocity and front acceleration vs. location along the lower track. The upper panel shows the velocity and the lower panel the acceleration derived from the front velocity readings. The thick solid line gives the path profile in the lower part of the track. \circ s indicate the approximated midpoint of the range gate.



Ryggfonn measurements

Winter 2004/2005

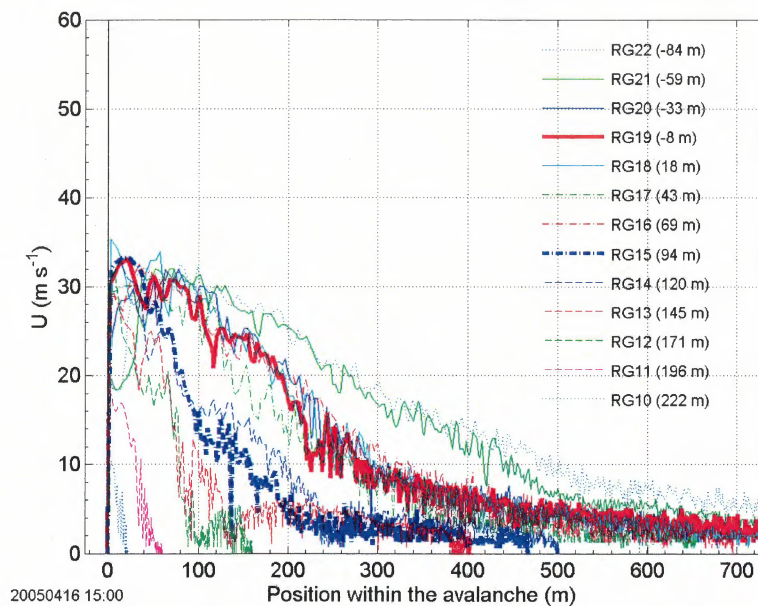


Figure 2.27: Avalanche 20050416 15:00: Velocity vs. position within the avalanche. Shown are all available range gate data.

20021048-11

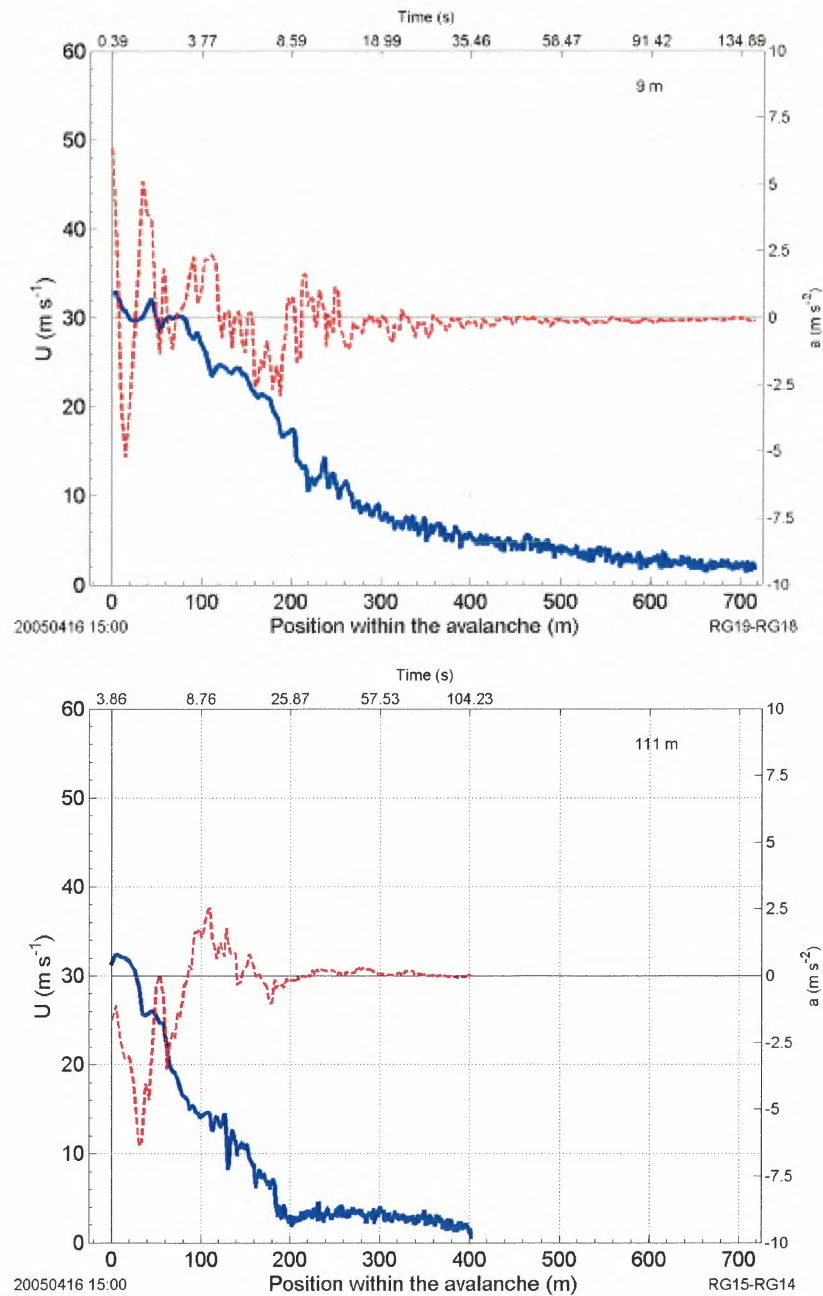


Figure 2.28: Avalanche 20050416 15:00: Velocity (solid line; left ordinate) and acceleration (dashed line; right ordinate) vs. position within the avalanche. Top) values are calculated for a location approximately 9 m below the steel tower (between RG19 and RG18); bottom) values given a point around the concrete wedge (between RG15 and RG14). The mean slope angle at the steel tower is approximately 30° and at the concrete wedge about 26°.

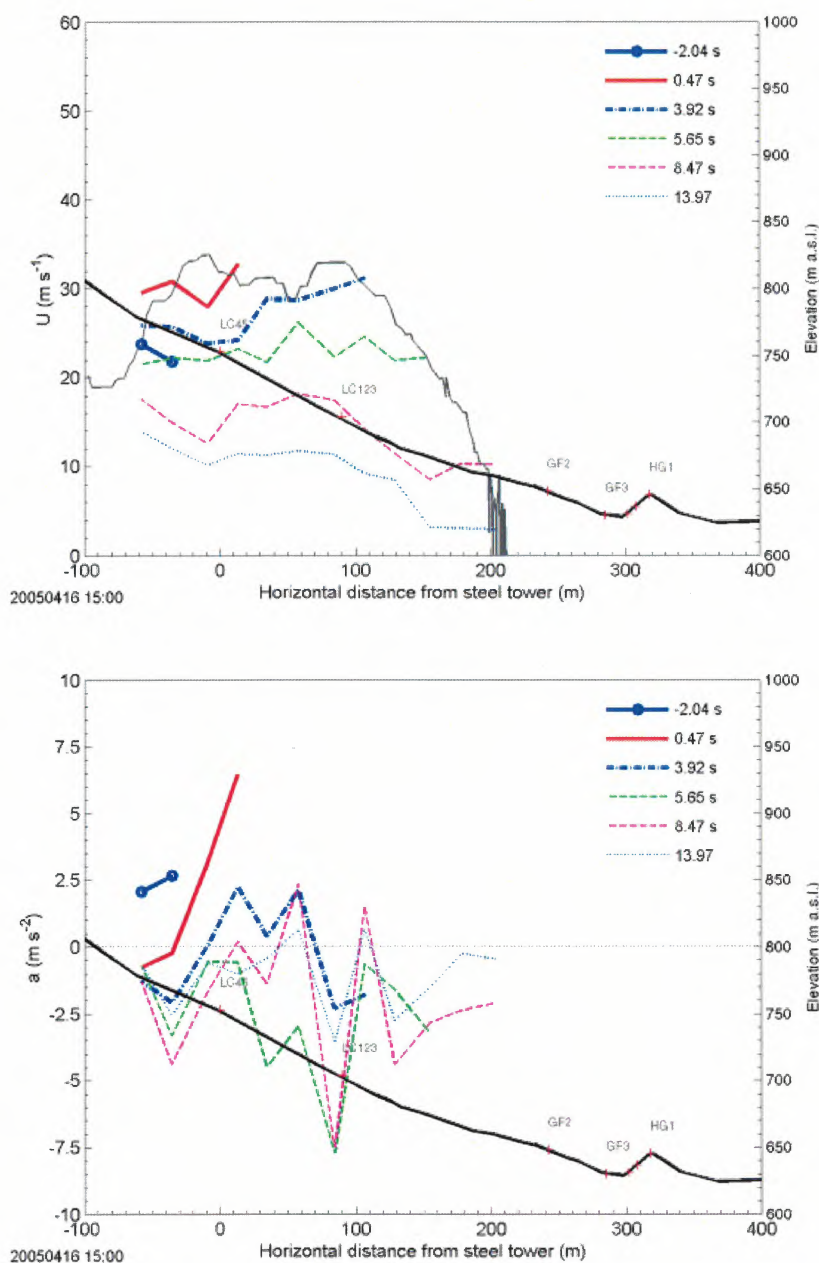


Figure 2.29: Avalanche 20050416 15:00: Velocity and acceleration vs. location along the lower track for six instants in time. The upper panel shows the averaged velocity and the lower panel the acceleration derived from the respective pair of adjoining range gates of the Doppler radar. In addition, the thin solid line in the upper panel shows the front velocity. The thick solid line gives the path profile in the lower part of the track.

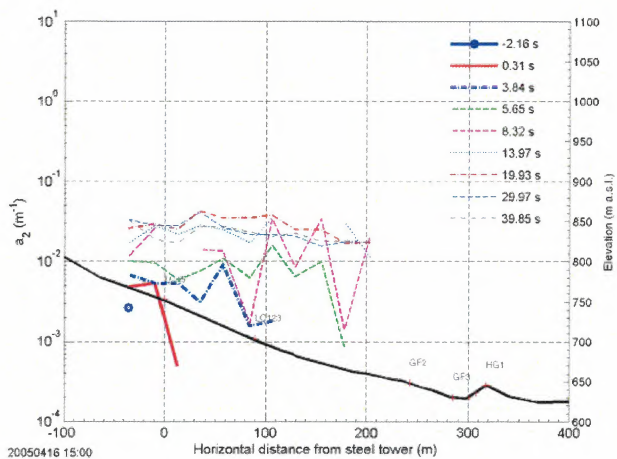
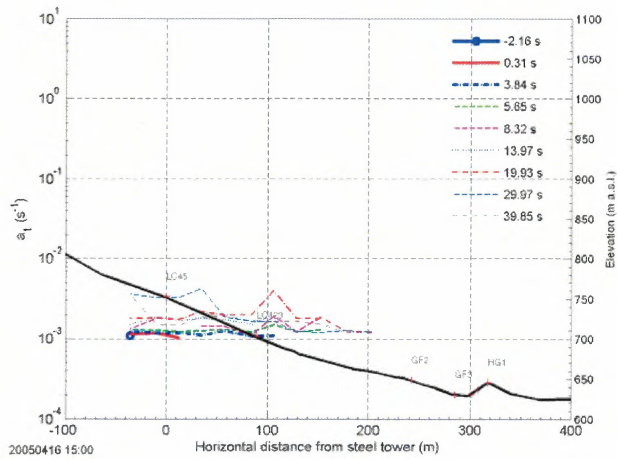
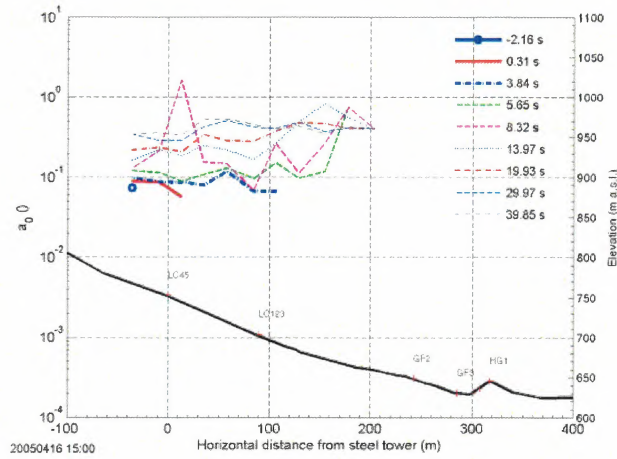
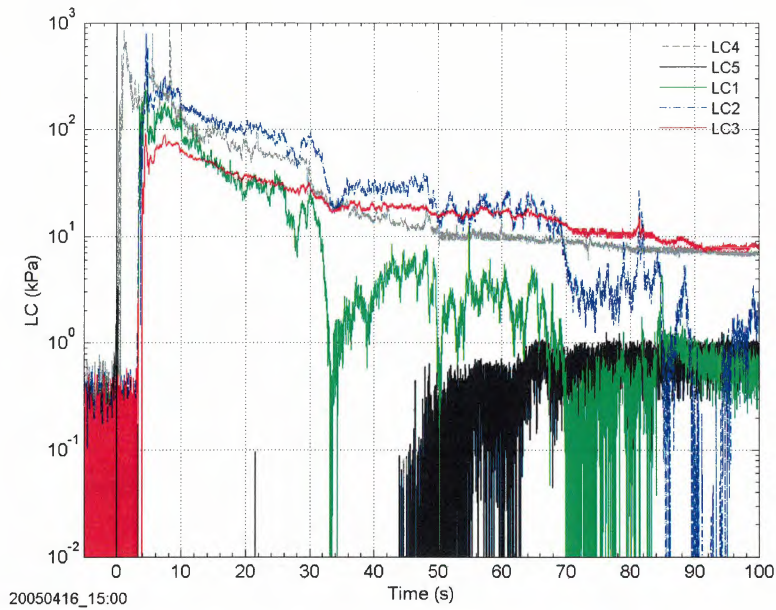
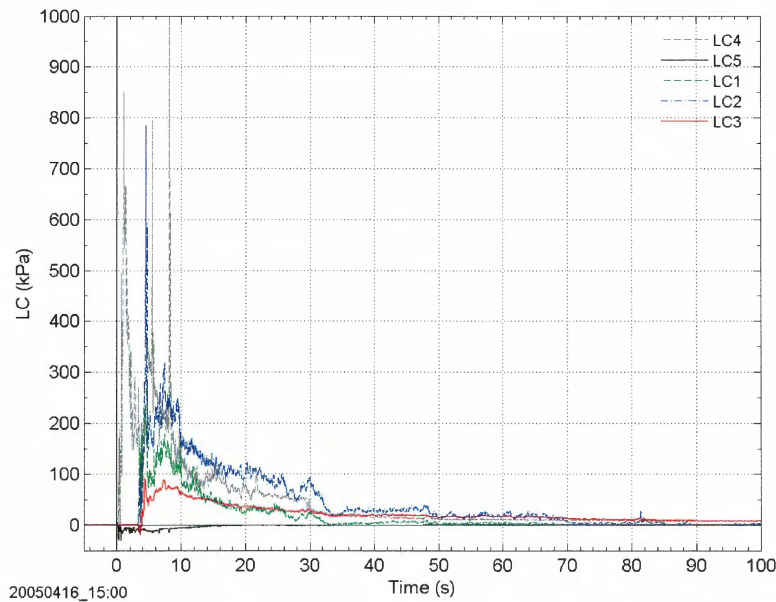


Figure 2.30: Avalanche 20050416 15:00: Friction coefficients (according to (1.8)) vs. location along the lower track for nine instants in time. The thick solid line gives the path profile in the lower part of the track.



a)



b)

Figure 2.31: Avalanche 20050416 15:00: Load cell measurements: pressure vs. time (raw data; offset corrected); a) logarithmic and b) linear presentation.

20021048-11

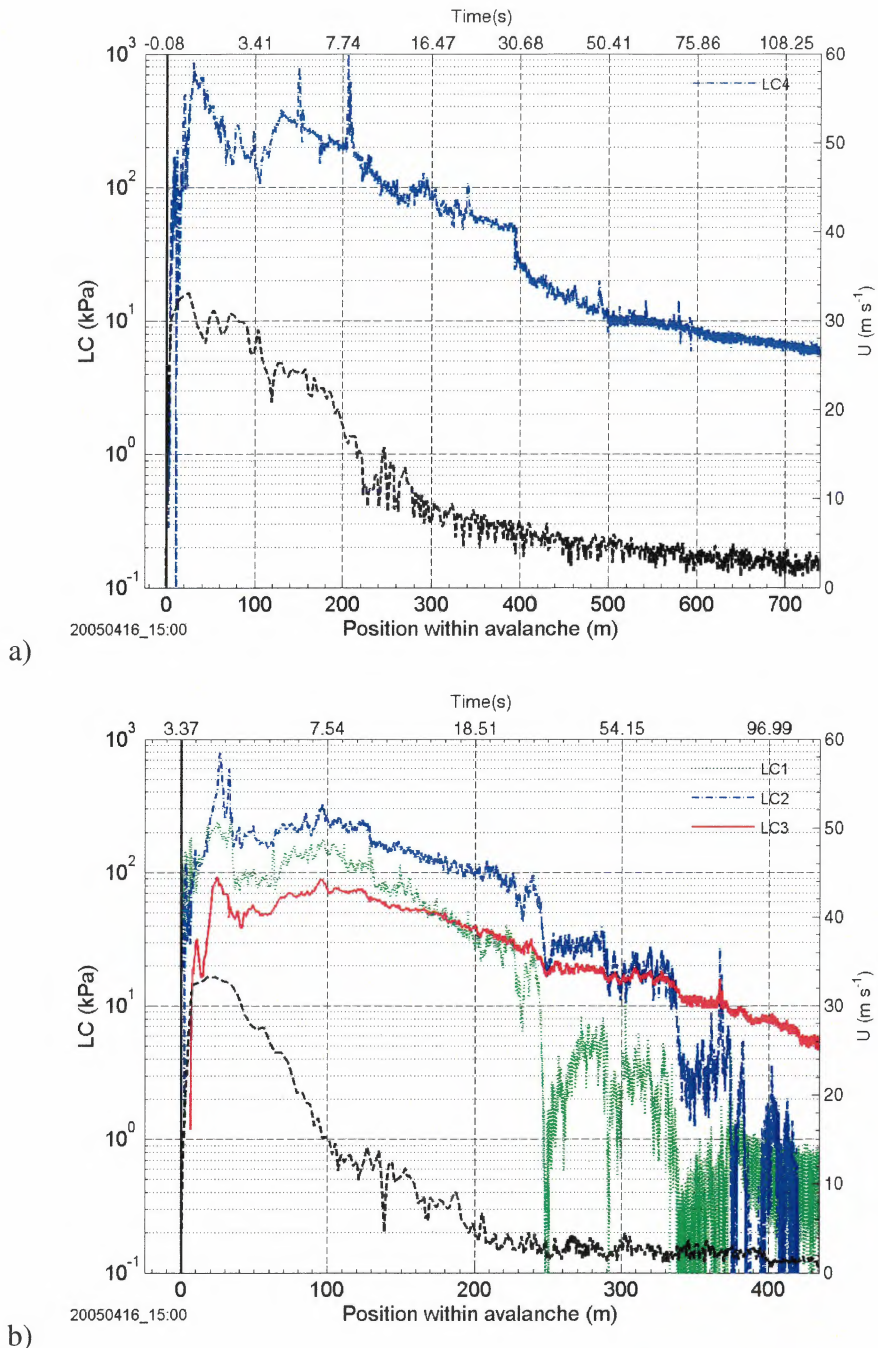


Figure 2.32: Avalanche 20050416 15:00: Load cell measurements: pressure vs. position within the avalanche; a) at steel tower and b) at the concrete wedge. Note the logarithmic scaling of the left ordinate and the different horizontal scaling. The black dashed lines show the corresponding velocity profiles.

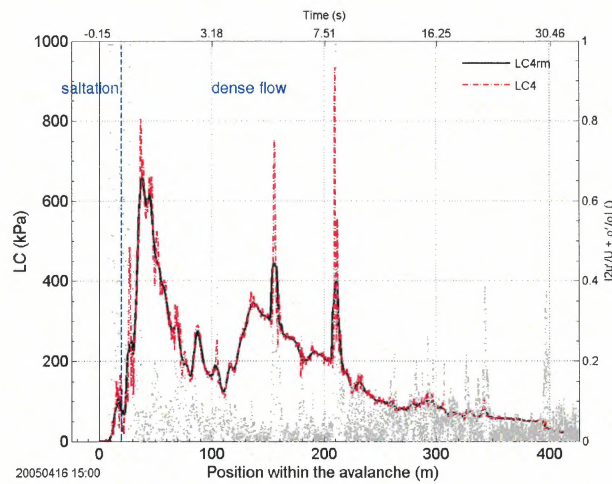


Figure 2.33: Avalanche 20050416 15:00: Fluctuation intensity vs. position within the avalanche. The lines present the measured impact pressure (dashed line) and the running mean (full line) taken over 5 m, respectively (left axis), at the concrete wedge. The fluctuation intensity is marked with dots (right axis). LC4 (LC5 was partly buried at the time).

20021048-11

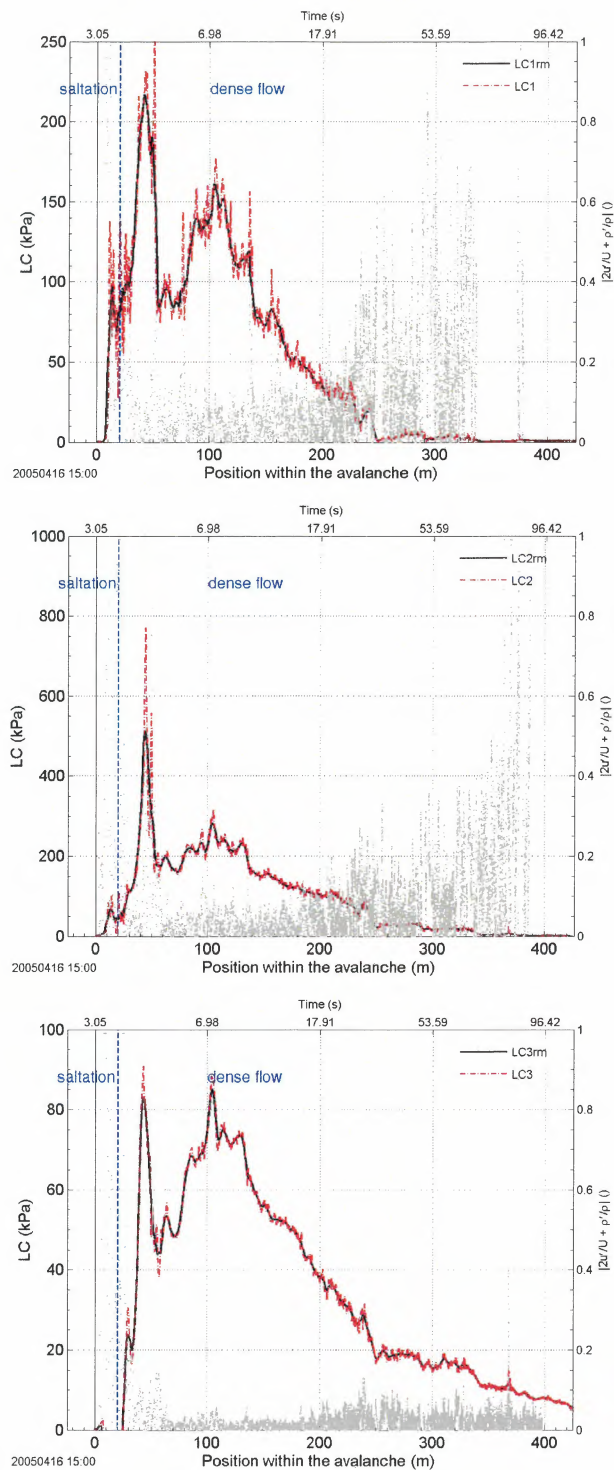


Figure 2.34: Avalanche 20050416 15:00: Fluctuation intensity vs. position within the avalanche. The lines present the measured impact pressures (dashed line) and the running means (full line) taken over 5 m, respectively (left axis), at the concrete wedge. The fluctuation intensities is marked with dots (right axis). Top: LC1; middle: LC2; bottom LC3 (partly buried at the time).

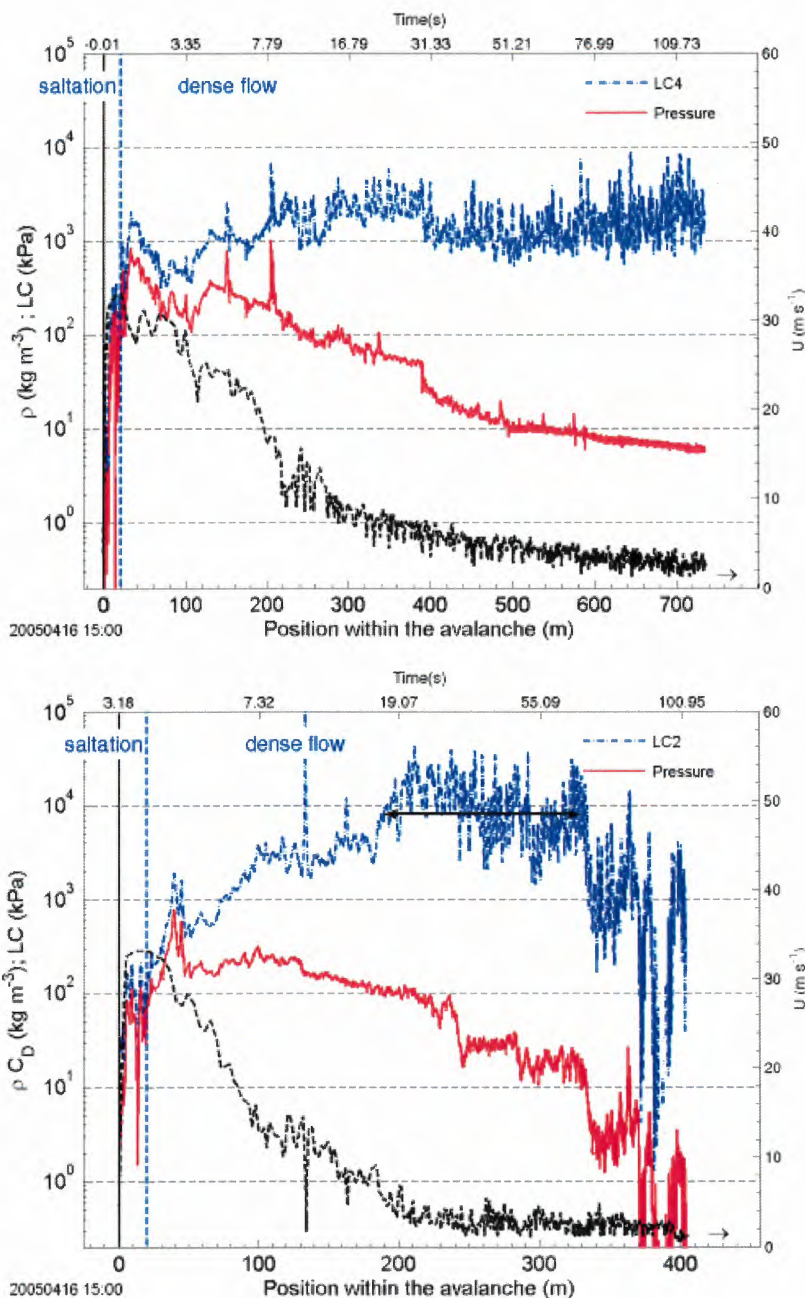


Figure 2.35: Avalanche 20050416 15:00: ρC_D vs. position within the avalanche (dash-dotted line). The full lines represent the measured impact pressure as the running mean taken over 5 m. Note the logarithmic scaling of the left ordinate and the different horizontal scaling. The black dashed lines show the corresponding velocity profiles. Upper panel gives measurements from the steel tower (LC4) and the lower panel from the concrete wedge (LC2).

20021048-11

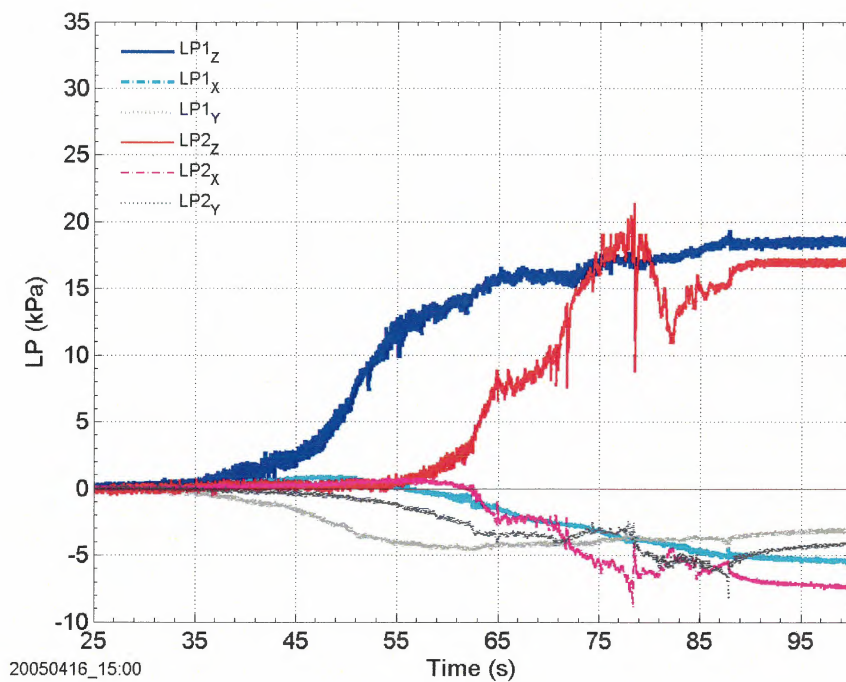


Figure 2.36: Avalanche 20050416 15:00: Load plate measurements: LP (raw data) vs. time.

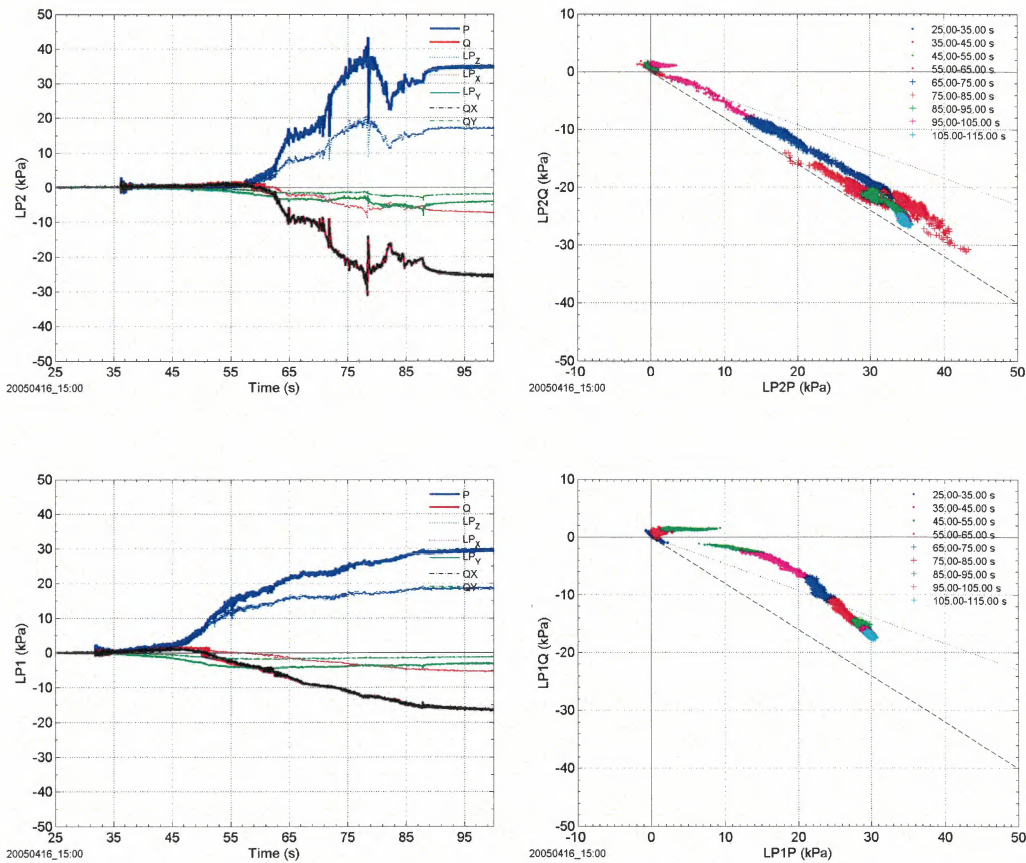


Figure 2.37: Avalanche 20050416 15:00: Load plate measurements: Stresses vs. time (left hand side) and shear stress vs. normal stress at the sliding plane (surface of the snowpack) along the dam slope (right hand side). The upper panel shows LP2 and the lower one LP1. LP_z , LP_x , and LP_y mark the measured stresses. P , Q_x , and Q_y are the calculated stresses according to (1.3). Q is the total traction. The dashed line in the right panels corresponds to the ratio between shear and normal stress in the case of static loading ($-\tan 40^\circ$ or $-\tan 20^\circ$).

20021048-11

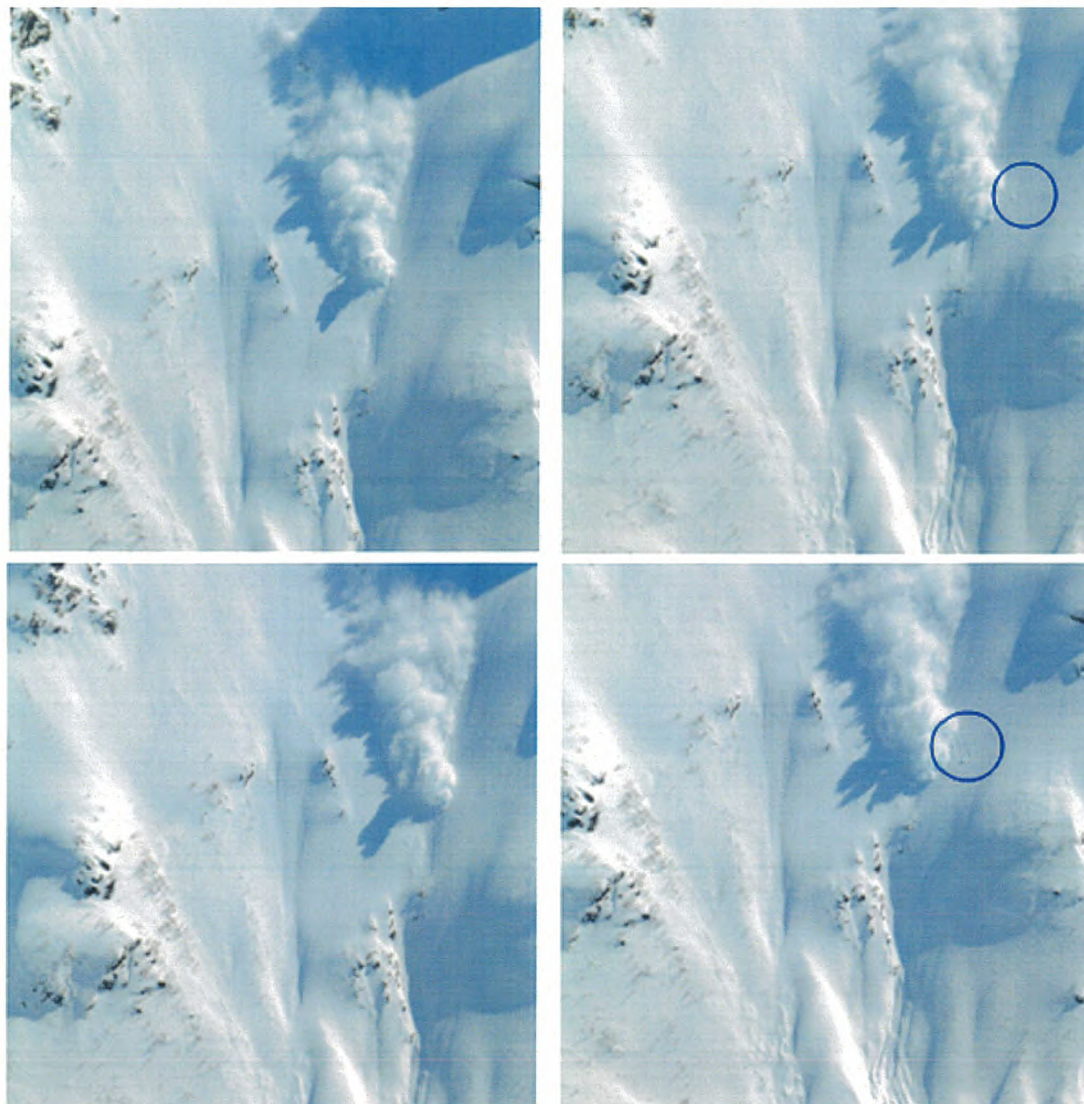


Figure 2.38: Avalanche 20050416 15:00: Series of snapshots from the avalanche descent I. Circles indicate flying snow clods.(Photos by Arne Moe)

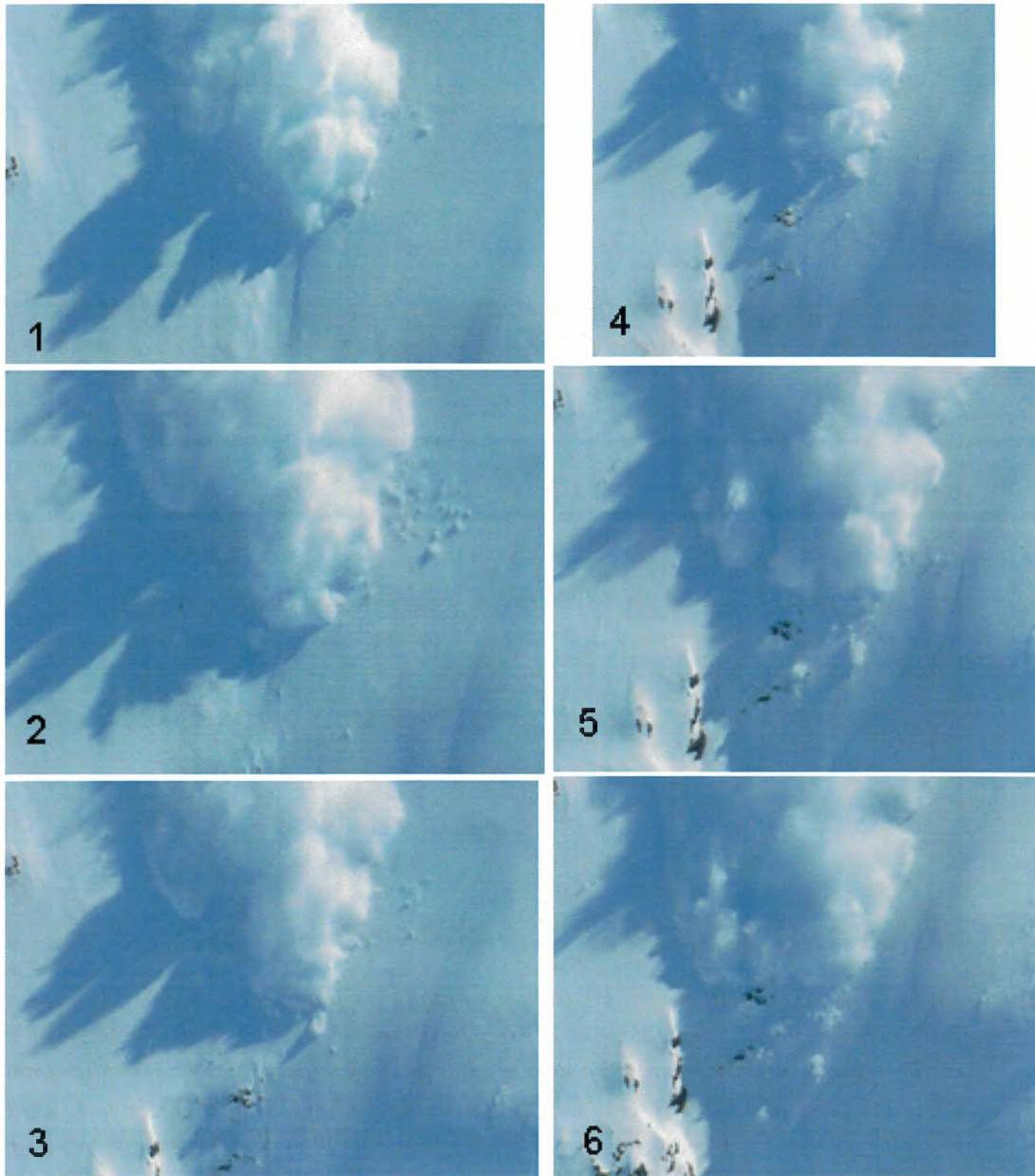


Figure 2.39: Avalanche 20050416 15:00: Series of snapshots from the avalanche descent II. Photos are taken approximately every 1 s. Obvious are the impacts of clods around the front; some are difficult to see due to the shadow of the cloud. The impinging clods seem to erode the snowpack and to through small clod up into the air. The clods were not obvious until the track steepened beyond the upper plateau. If one combines this observation with observation from flume experiments (see Fig. 2.40) one might get an idea of possible erosion and entrainment mechanisms at the front of the saltation layer. (Photos by Arne Moe)

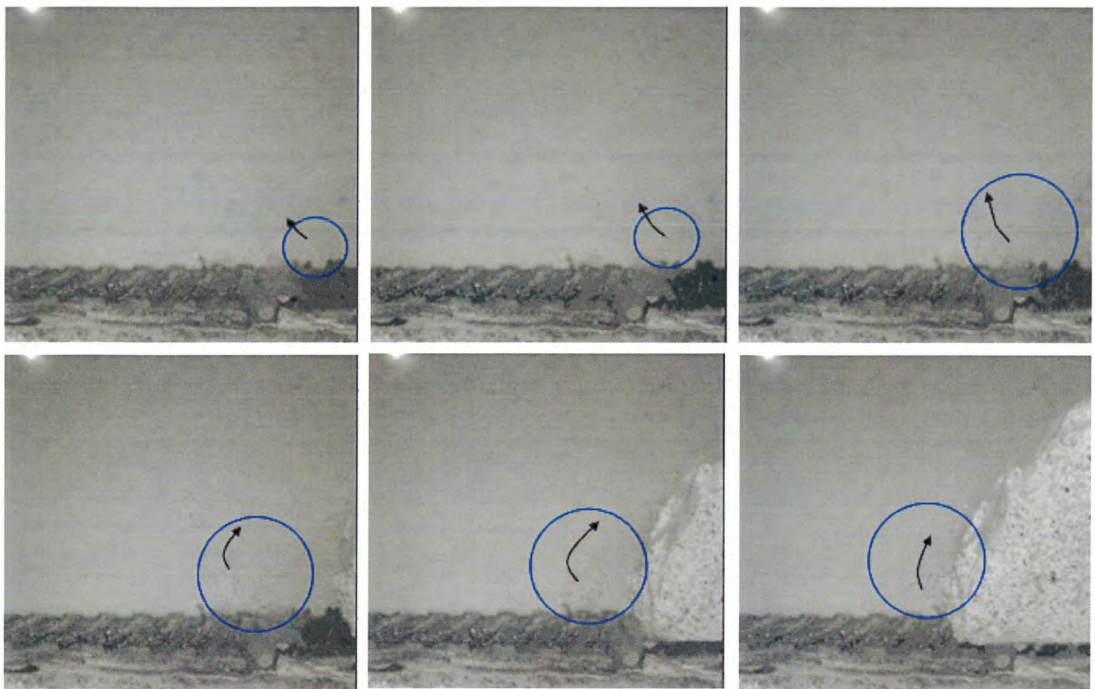


Figure 2.40: Series of snapshots from a subaqueous flume experiment. Photos extracted from a high speed video taken at a fixed position. In this case, the water flow in front of the slide erodes remaining sand and clay particles from a previous experiment. The particles are lifted up (direction indicated by the arrows) and finally incorporated into the slide (video by Trygve Ilstad). The series is included to give an idea of How snow might be incorporated into the flow.



Figure 2.41: Avalanche 20050416 15:00: Snapshots from the track I. Left hand side: during the descent of the avalanche; right hand side after the event (similar location). Obviously, the avalanche eroded during the descent. Scratch marks remind one at erosion/abrasion due to (saltating) particles.(Photos by Arne Moe)

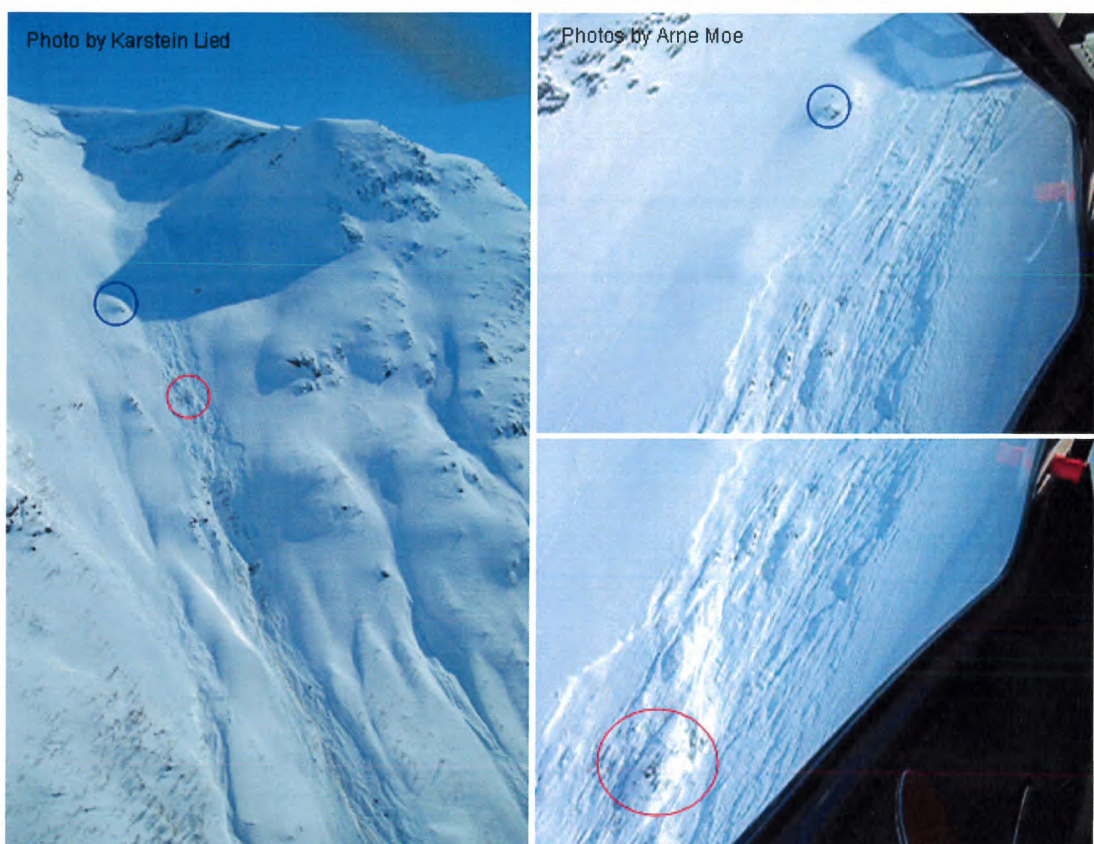


Figure 2.42: Avalanche 20050416 15:00: Snapshots from the track II. Left hand side: Overview; right hand side after the event (Circles indicate similar locations). Obviously, the avalanche eroded during the descent. Scratch marks remind one at erosion/abrasion due to (saltating) particles.(Photos by Karstein lied and Arne Moe)



Figure 2.43: Avalanche 20050416 15:00: Snapshots from the lower track. Line indicates the boundary of the erosion. Inset shows the situation before the release. (Photos by Karstein Lied and Peter Gauer)



Figure 2.44: Avalanche 20050416 15:00: Snapshots from the lower track (erosion I). One can see a brownish strip indicating erosion of soil. (Photo by Krister Kristensen)

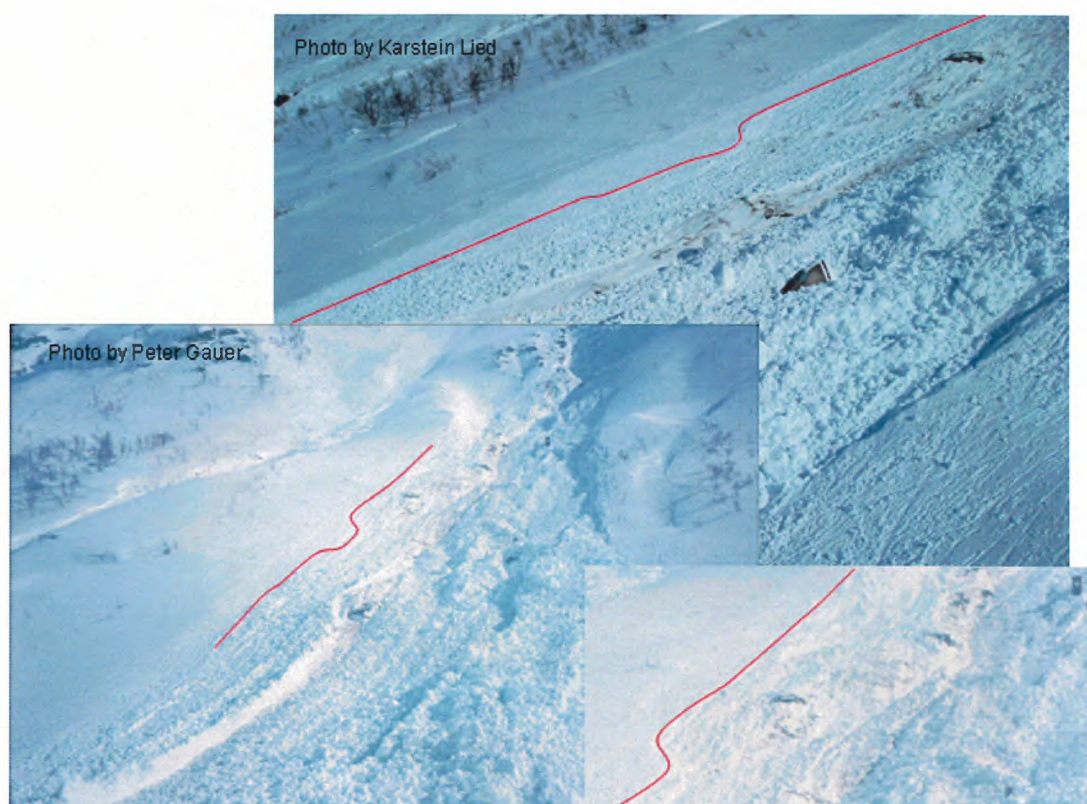


Figure 2.45: Avalanche 20050416 15:00: Snapshots from the lower track (erosion II). Lines indicate the boundary of the erosion. (Photos by Karstein Lied and Peter Gauer)

20021048-11



Figure 2.46: Avalanche 20050416 15:00: Snapshots from the deposits. (Photos by Arne Moe)



References

- Johnson, K. L. 2001. *Contact Mechanics*. Cambridge, U.K., Cambridge University Press.
- McClung, D. and P. Schaerer. 1993. *The Avalanche Handbook*. 1011 SW Klickitat Way, Seattle, Washington 98134, The Mountaineers.
- Mellor, M. 1968. Cold regions science and engineering. Part III: Engineering, Section A3: Snow Technology Avalanches. Hanover, New Hampshire, Cold Regions Research & Engineering Laboratory.
- Norem, H. 1990. Ryggfonn-prosjektet. NGI Report 581200-16. Sognsveien 72, N-0860 Oslo, Norwegian Geotechnical Institute. (in Norwegian).
- Salm, B., A. Burkhard, and H. U. Gubler. 1990. Berechnung von Fliesslawinen. eine Anleitung für Praktiker mit Beispielen. Mitt. Eidgenöss. Inst. Schnee- Lawinenforsch. 47. SLF, Davos, Switzerland, 37 pages.
- SATSIE, . 2003. *Avalanche Studies and Model Validation in Europe EU: Management Progress Report*. Coordinator: Norwegian Geotechnical Institute, available from <http://www.leeds.ac.uk/satsie> edition.
- Schreiber, H., W. L. Randeu, H. Schaffhauser, and L. Rammer. 2001. Avalanche dynamics measurement by pulsed Doppler radar. *Annals of Glaciology*, **32**, 275–280.
- UNESCO, . 1981. *Avalanche Atlas*. International Commission on Snow and Ice of the International Association of Hydrological Sciences, IAHS.



Table A-1: Code for morphological avalanche classification (1981, *Avalanche Atlas/UNESCO*)

Criterion Characteristics	Criterion	Symbols	
		Characteristics	
		pure	mixed
Manner of starting	A		
Loose snow avalanche		1	} 7
Slab avalanche		2	
Slab avalanche soft		3	
Slab avalanche hard		4	
Position of sliding surface	B		
Surface-layer avalanche (general)		1	} 8
Surface-layer avalanche, new snow fracture		2	
Surface-layer avalanche, old snow fracture		3	
Full-depth avalanche		4	
Liquid Water in snow fracture	C		
Absent: dry-snow avalanche		1	} 7
Present: wet-snow avalanche		2	
Form of Path	D		
Unconfined avalanche		1	} 7
Channelled avalanche		2	
Form of movement	E		
Powder avalanche (dominant)		1	} 7
Flow avalanche (dominant)		2	
Surface roughness of deposit	F		
Coarse deposit (general)		1	} 7
Coarse deposit angular blocks		2	
Coarse deposit rounded clods		3	
Fine deposit		4	
Liquid water in deposit	G		
Absent: dry-deposit		1	} 7
Present: wet-deposit		2	
Contamination of deposit	H		
Clean deposit		1	} 8
Contaminated deposit (general)		2	
Contaminated by rocks, debris, soil		3	
Contaminated by branches, trees		4	
Contaminated by debris of structures		5	
Triggering mechanism ¹	J		
Natural release		1	
Human release (general)		2	
Human release, accidental		3	
Human release, intentional		4	

¹This criterion is an element of the genetic classification. since the triggering mechanism within the given alternatives is known most cases and is important for many problems, it is added to the morphological code.



Table A-2: Canadian snow avalanche size classification system and typical factors (McClung and Schaerer, 1993)

Size	Description	Typical mass (Mg)	Typical path length (m)	Typical impact pressure (kPa)
1	Relative harmless to people	< 10	10	1
2	Could bury, injure or kill a person	10 ²	100	10
3	Could bury a car, destroy a small building, or break a few trees	10 ³	1000	100
4	Could destroy a railway car, large truck, several buildings, or a forest with an area up to 4 hectares	10 ⁴	2000	500
5	Largest snow avalanche known; could destroy a village or a forest of 40 hectares	10 ⁵	3000	1000

Kontroll- og referanseside/ Review and reference page



Oppdragsgiver/Client European Commission Kontraksreferanse/ Contract of 18.10.02 Contract reference	Dokument nr/Document No. 20021048-8 Dato/Date 2005-12-01
Dokumenttittel/Document title Ryggfonn measurements Prosjektleder/Project Manager Karstein Lied Utarbeidet av/Prepared by Peter Gauer and Krister Kristensen	Distribusjon/Distribution <input type="checkbox"/> Fri/Unlimited <input checked="" type="checkbox"/> Begrenset/Limited <input type="checkbox"/> Ingen/None
Emneord/Keywords	
Land, fylke/Country, County Norway, Kommune/Municipality Stryn Sted/Location Grasdalen, Ryggfonn Kartblad/Map 1418 IV, Lodalskåpa UTM-koordinater/UTM-coordinates 32VMP094725	Havområde/Offshore area Felt navn/Field name Sted/Location Felt, blokknr./Field, Block No.

Kvalitetssikring i henhold til/Quality assurance according to NS-EN ISO9001								
Kontrollert av/ Reviewed by	Kontrolltype/ Type of review	Dokument/Document		Revisjon 1/Revision 1		Revisjon 2/Revision 2		
		Kontrollert/Reviewed		Kontrollert/Reviewed		Kontrollert/Reviewed		
		Dato/Date	Sign.	Dato/Date	Sign.	Dato/Date	Sign.	
	Helhetsvurdering/ General Evaluation *							
	Språk/Style							
	Teknisk/Technical - Skjønn/Intelligence - Total/Extensive - Tverrfaglig/ Interdisciplinary							
	Utforming/Layout							
	Slutt/Final							
	Kopiering/Copy quality							
* Gjennomlesning av hele rapporten og skjønnsmessig vurdering av innhold og presentasjonsform/ On the basis of an overall evaluation of the report, its technical content and form of presentation								
Dokument godkjent for utsendelse/ Document approved for release			Dato/Date			Sign.		

A.10 Unpublished Report(2)

Gauer, P. and K. Kristensen. 2005a. Ryggfonn measurements. Overview and dam interaction. NGI Report 20021048-10. Norges Geotekniske Institutt, Oslo, Norway.

20021048-11

Avalanche Studies and Model Validation in Europe, SATSIE

Ryggfonn measurements Overview and dam interaction

20021048-10

1 December 2005

Client: **European Commission**

Contact person: Denis Peter

Contract reference: Contract of 18.10.02

For the Norwegian Geotechnical Institute

Project Manager: Karstein Lied

Report prepared by: Peter Gauer and Krister Kristensen

Reviewed by: Karstein Lied

Work also carried out by:



SUMMARY

This report presents an overview of avalanche data collected at the full-scale avalanche test site Ryggfonn, Norway. The avalanches have been characterized according to the IAHS avalanche code and the deposit boundaries have been mapped.

Measurements obtained from the avalanche path include impact pressure readings from two load cells at a steel tower as well as impact pressures on three load cells fixed to a concrete structure. In addition, normal stress and shear stress were measured at two locations at a 16 high dam. Six geophones, placed on the ground in the runout zone, have detected vibrations from some of the passing avalanches. When possible, for each avalanche the front speeds have been estimated. The estimates are based on pulsed Doppler radar measurements, seismic measurements, and the timing between impacts on the constructions.

Impact pressure, deposition maps, estimated arrival time of the avalanche front at the different sensor location are presented for the period from 1998–2005. In addition the corresponding mean front velocity is shown together with estimates on the averaged acceleration of the front. If possible, values for ρc_D are derived for a period of 2 s at the front of the avalanche.

Deposition map and information on the runout distance combined with estimated front velocity data and freeboard height of about 21 avalanches are used to provide a relation for the effect of the catching dam for dry snow avalanches. The normalized overrun length, l_{ovr} (measured from the top of the dam), is expressed by a linear relation of the normalized kinetic energy,

$$\frac{l_{ovr}}{h_{fb}} \approx 2.57 \frac{u_b^2}{2g h_{fb}} - 1.2 \quad (0.1)$$

where h_{fb} is the effective free board height, u_b the front velocity at the "base" of the dam and g is the gravitational acceleration.

The mass distribution ratio might be estimated by

$$m_r \approx 0.055 \frac{u_b^2}{2g h_{fb}} - 0.031. \quad (0.2)$$

m_r is defined as the estimated fraction of the total deposit mass that surpassed the downstream foot of the dam.



10	Effect of the catching dam	103
10.1	Overrun length	103
10.2	Mass distribution ratio	110
10.3	Spreading ratio	111
10.4	Comparison to chute (granular) experiments	112
10.5	What are open questions?	118

LIST OF TABLES

1.1	Avalanche characterization I	12
1.2	Avalanche characterization II	13
1.3	Timing	14
10.1	Analyzed avalanches with respect to the dam interaction.	106
A-1	Code for morphological avalanche classification	A1
A-2	Canadian snow avalanche size classification system	A2

20021048-11



6.5	Avalanche 20020101 08:11: impact pressure and timing	46
6.6	Avalanche 20020101 08:11: front velocity and acceleration (runout area)	47
6.7	Avalanche 20020101 08:11: estimated ρC_D values	48
7.1	Avalanche 20030114 03:30: impact pressure and timing	49
7.2	Avalanche 20030114 03:30: front velocity and acceleration (runout area)	50
7.3	Avalanche 20030114 05:40: impact pressure and timing	51
7.4	Avalanche 20030114 05:40: front velocity and acceleration (runout area)	52
7.5	Avalanche 20030115 13:27: map of the deposit	53
7.6	Avalanche 20030115 13:27: impact pressure and timing	54
7.7	Avalanche 20030115 13:27: front velocity and acceleration (runout area)	55
7.8	Avalanche 20030118 15:14: impact pressure and timing	56
7.9	Avalanche 20030118 15:14: front velocity and acceleration (runout area)	57
7.10	Avalanche 20030406 13:06: map of the deposit	58
7.11	Avalanche 20030406 13:06: impact pressure and timing	59
7.12	Avalanche 20030406 13:06: front velocity and acceleration	60
7.13	Avalanche 20030406 13:06: front velocity and acceleration (runout area)	61
7.14	Avalanche 20030406 13:06: estimated ρC_D values	62
8.1	Avalanche 20031215 16:40: map of the deposit	63
8.2	Avalanche 20031215 16:40: impact pressure and timing	64
8.3	Avalanche 20031215 16:40: front velocity and acceleration (runout area)	65
8.4	Avalanche 20031215 16:40: estimated ρC_D values	66
8.5	Avalanche 20031217 03:24: map of the deposit	67
8.6	Avalanche 20031217 03:24: impact pressure and timing	68
8.7	Avalanche 20031217 03:24: front velocity and acceleration (runout area)	69
8.8	Avalanche 20031217 03:24: estimated ρC_D values	70
8.9	Avalanche 20040204 06:10: map of the deposit	71
8.10	Avalanche 20040204 06:10: impact pressure and timing	72
8.11	Avalanche 20040204 06:10: front velocity and acceleration (runout area)	73
8.12	Avalanche 20040204 06:10: estimated ρC_D values	74
8.13	Avalanche 20040204 06:10 2nd surge	75
8.14	Avalanche 20040204 06:10 2nd surge: front velocity and acceleration (runout area)	76
8.15	Avalanche 20040204 06:10: estimated ρC_D values	77
8.16	Avalanche 20040224 08:50: map of the deposit	78



10.22 Spread-out ratio vs. normalized kinetic energy 111
10.23 Normalized runout ratio vs. normalized kinetic energy 113
10.24 Normalized runout ratio vs. normalized kinetic energy: comparison
between various experiments 115
10.25 Effective deceleration vs. normalized kinetic energy: comparison be-
tween various experiments 116
10.26 Effective deceleration vs. normalized kinetic energy: comparison be-
tween various experiments 117

20021048-11

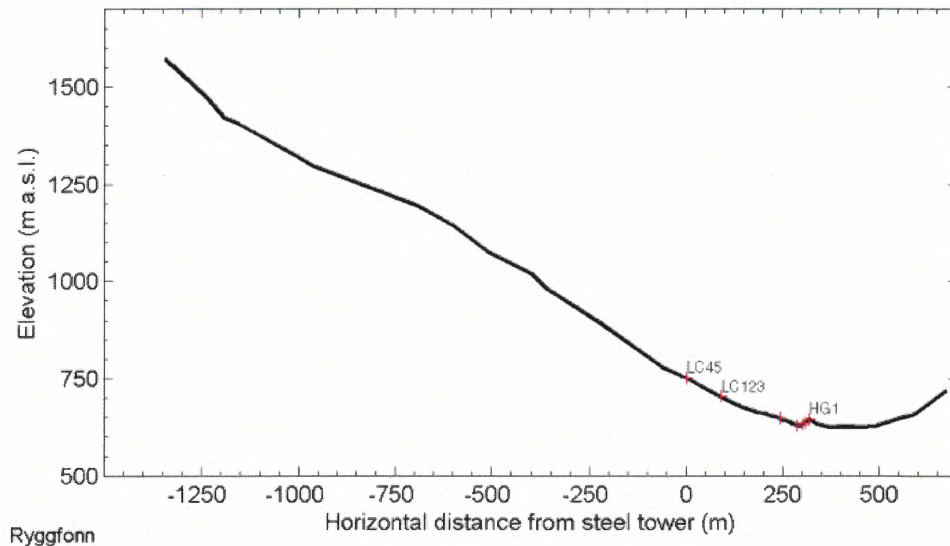


Figure 1.2: Profile line of main track at the Ryggfonn test site. The horizontal distance is measured relative to the steel tower. Sensor positions are indicated

Harsh conditions within an avalanche make measurements a difficult task. Accessibility to the avalanche path prior to a release is usually limited. Sensors have to be placed a long time before an event and might be buried by the time due to previous avalanches. The knowledge of the sensor status is important, a fact that limits the reliability of automatic measurements. This has to be kept in mind reading the following presentation of the avalanche data.

To gain information on the flow behavior, information from different measurements and observations must be combined. This is not always straightforward and might need some subjective interpretation, which also leaves some uncertainty.

The following report presents an overview of impact pressure, deposition maps, estimated arrival time of the avalanche front at the different sensor location are presented for the period from 1998–2005. If available videos were used to gain additional information. In addition the corresponding mean front velocity is also shown and estimates on averaged acceleration of the front.

Note that there is a degree of uncertainty in some velocity measurements: The sensitivity of the strain gauges at the tower (used before 2001) differs from that of the load plates in the concrete structure so that the first signals recorded at the two locations may correspond to the passage of different parts of the avalanche. Furthermore, the concrete structure is located slightly to the side and above the main gully; when the gully is not yet filled with snow, the front of small avalanches may not reach the sensors and the inferred front ve-



$$a_f = \frac{v_f(s_{v_i})^2 - v_f(s_{v_{i-1}})^2}{2(s_{v_i} - s_{v_{i-1}})} \quad (1.4)$$

There is an uncertainty in this procedure, however it can give some idea of the effective accelerations.



Table 1.2: Avalanche characterization II: Maximum impact pressures and estimated front velocities. As the sensor status is not know in all cases some of the pressure readings must be read with some precaution. Parentheses are used to mark questionable values, there are also some uncertainties left by the others.

Date ¹ yyyymmdd hh:mm	LC4 (kPa)	LC5 (kPa)	LC1 (kPa)	LC2 (kPa)	LC3 (kPa)	Speed (ms ⁻¹)		dam foot ⁴
						LC4-LC1 ²	LC1-LP1 ³	
19930327 14:30	NaN	NaN	NaN	0.0	0.0	42.8	33.2	33.0
19970417 14:00	NaN	NaN	(21.7)	109.6	69.2	33.8	3.0	0.7
19990122 06:03	NaN	NaN	5.8	11.1	66.0	20.3	11.5	2.5
19990131 16:05	NaN	NaN	(0.2)	(0.2)	(0.1)	NaN	NaN	NaN
19990215 12:28	NaN	NaN	12.1	76.3	40.3	25.3	15.5	NaN
20000111 05:53	NaN	NaN	203.3	428.0	255.3	30.4	28.6	26.0
20000217 13:55	NaN	NaN	391.5	311.2	(44.6)	49.8	37.8	30.0
20011115 03:15	(0.5)	(16.4)	(0.1)	(128.6)	(0.1)	NaN	NaN	(DNR)
20011115 03:30b	(7.2)	(14.4)	(0.1)	(157.0)	(0.1)	NaN	NaN	(DNR)
20011115 04:03c	(2.1)	(13.4)	(7.1)	(117.1)	(77.3)	16.1	NaN	DNR
20020101 01:42	(3.9)	(0.3)	(3.1)	(64.2)	(55.9)	25.3	NaN	(DNR)
20020101 08:11b	(33.6)	(3.4)	(13.7)	(35.4)	(14.5)	24.6	14.2	2.3
20030114 03:30	NaN	NaN	29.0	93.7	131.5	NaN	2.9	0.0
20030114 05:40a	NaN	NaN	58.4	91.1	126.9	NaN	3.8	DNR
20030115 13:27	NaN	NaN	242.4	191.8	149.9	NaN	34.0	19.5
20030118 15:14	NaN	NaN	76.2	113.0	100.2	NaN	4.8	1.0
20030406 13:06	NaN	NaN	2.4	17.0	9.0	11.7	NaN	DNR
20031215 16:40	13.0	10.0	7.6	16.2	61.7	25.4	22.6	22
20031217 03:24	94.9	73.0	4.3	34.5	115.1	27.5	12.6	6.0
20040204 06:10	351.6	270.4	57.2	91.9	28.8	28.5	2.6	0.5
20040204 06:10b	329.9	253.7	53.0	69.0	17.7	6.9	2.9	0.5
20040224 08:50a	65.8	50.6	(15.3)	(1.8)	(1.4)	25.4	NaN	NaN
20040224 22:30	264.4	203.4	(18.2)	(5.2)	(3.6)	32.9	25.4	12
20040224 22:30b	253.6	195.1	(16.9)	(3.7)	(2.7)	31.5	28.1	22
20040228 15:30	145.1	111.6	(11.4)	(3.7)	(2.7)	37.5	21.8	15.0
20041207 17:00	0.0	48.9	0.0	0.0	0.0	NaN	NaN	DNR
20050107 04:16	342.8	109.6	154.6	279.8	281.6	29.0	18.2	14.3
20050107 04:16b	211.3	(21.1)	77.9	126.6	165.4	NaN	4.8	1.2
20050416 15:00	636.1	(2.1)	209.7	458.7	(86.7)	32.8	6.1	1.0

¹The avalanches are also documented in (Gauer and Kristensen, 2005, 2004, Kristensen, 1996, 1997, 2001).

²The estimated average speeds are calculated between the steel tower and the concrete structure,

³and between the concrete structure and the foot of the dam, respectively. For avalanches prior to 2002, the arrival time at the dam is derived from geophone data. In addition video were used if available.

⁴Estimated front velocity at the uphill foot of the dam.

NaN remark values which are not available and DNR mark avalanche which did not reach the dam.

20021048-11



2 COMPARISON

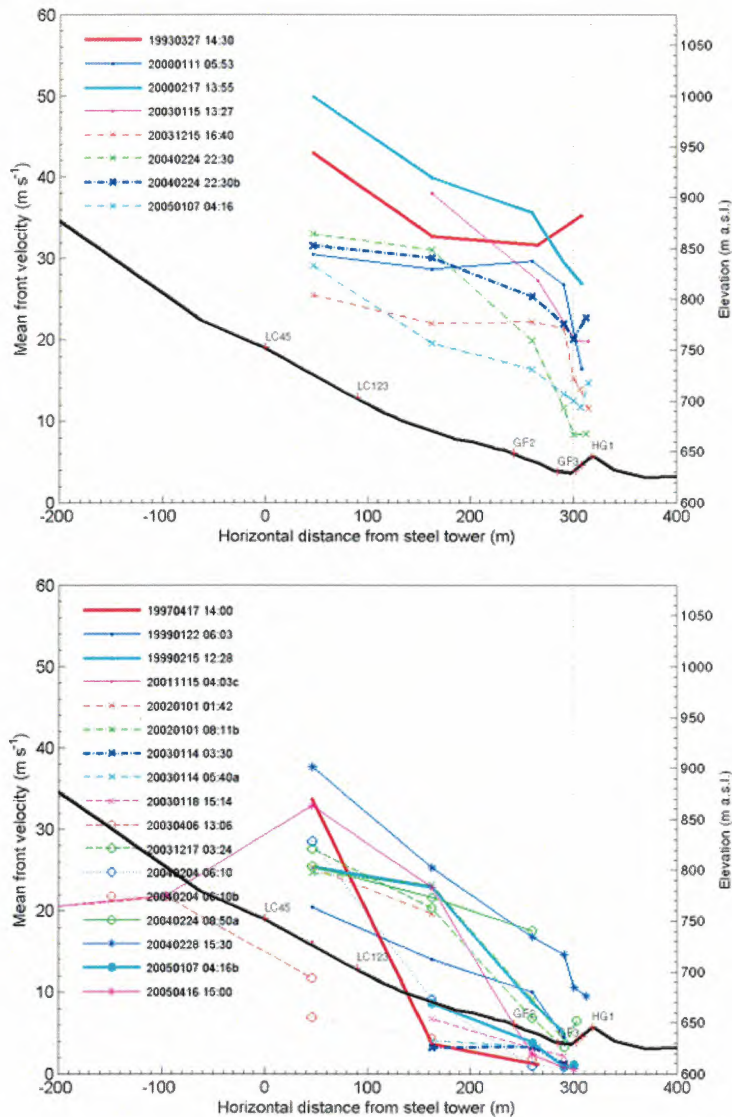


Figure 2.3: Comparison of the mean front velocity vs. horizontal distance. Shown are estimates based on the arrival times at various sensor locations. The top panel shows all avalanches surpassing the dam in the period from 1998/1999 until 2004/2005. The lower panel shows a collection of avalanches which stopped at or before the dam for the same period. The dotted vertical line indicates the foot of the dam

20021048-11

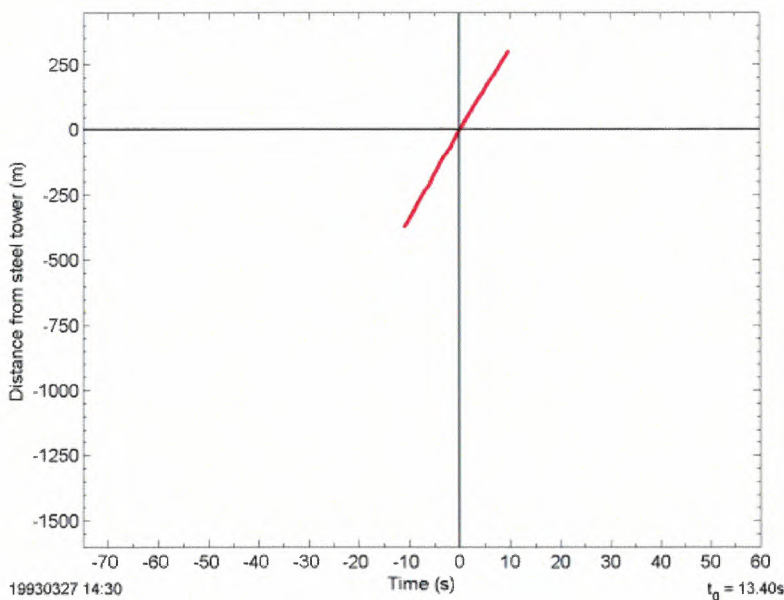
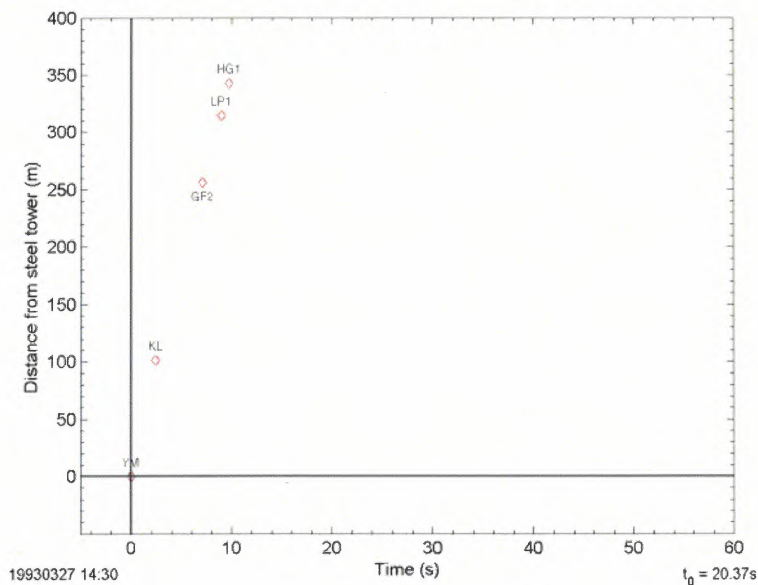


Figure 3.2: Avalanche 19930327 14:00: Timing (Distance vs. time; top); Shown are estimates based on the arrival times at various sensor locations (top) and timing based on video analysis by J. McElwaine (bottom).

20021048-11

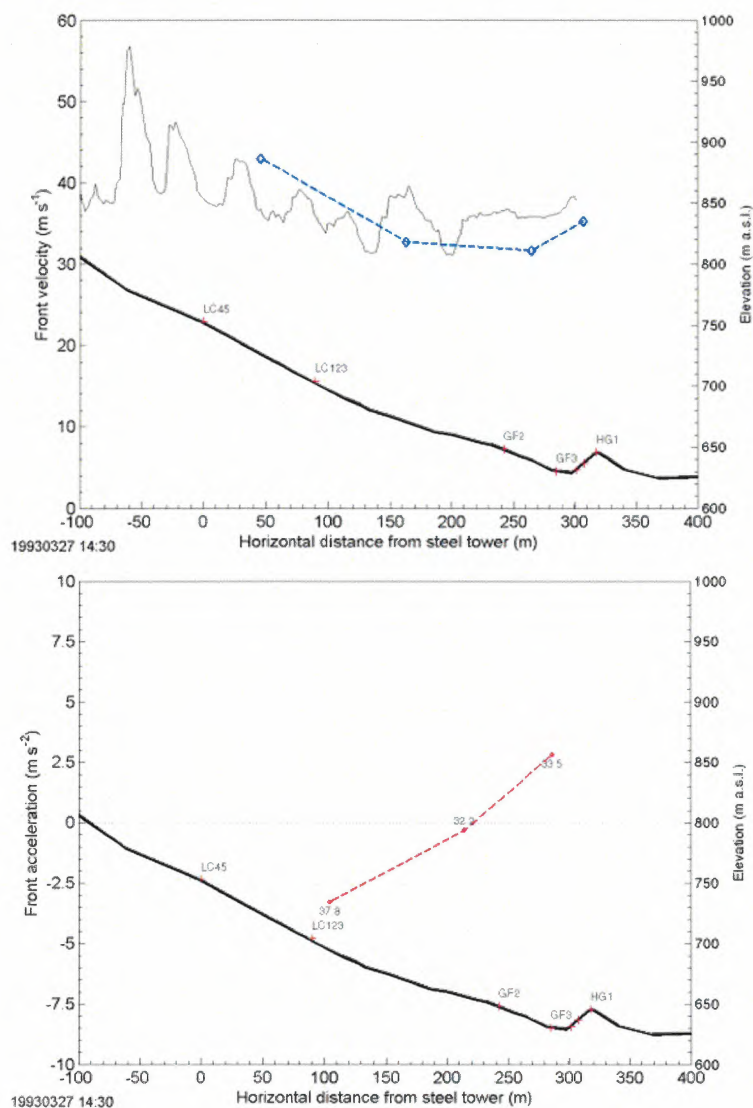


Figure 3.4: Avalanche 19930327 14:00: Mean front velocity vs. horizontal distance (top); corresponding accelerations (bottom; values are the corresponding velocities in $m s^{-1}$). Shown are estimates based on the arrival times at various sensor locations complemented with data based on video analysis by J. McElwaine in the runout area.

20021048-10

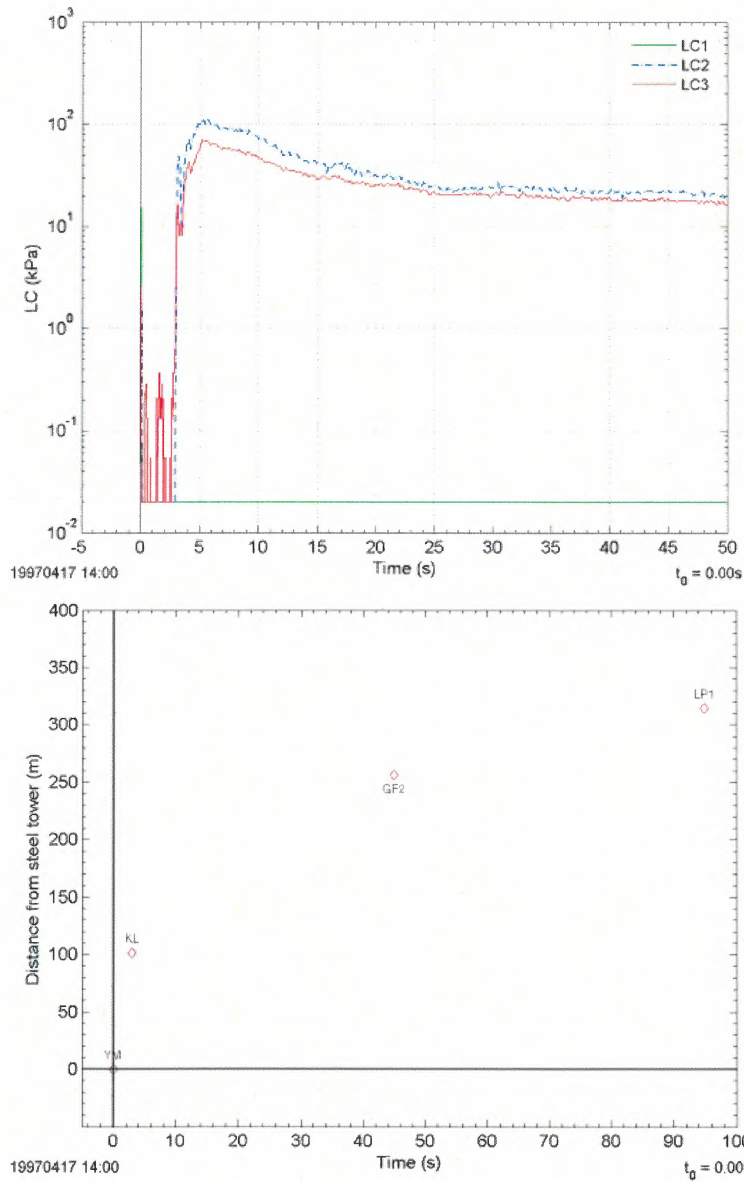


Figure 3.6: Avalanche 19970417 14:00: Impact pressure vs. time (top); Timing (Distance vs. time; bottom).

20021048-11

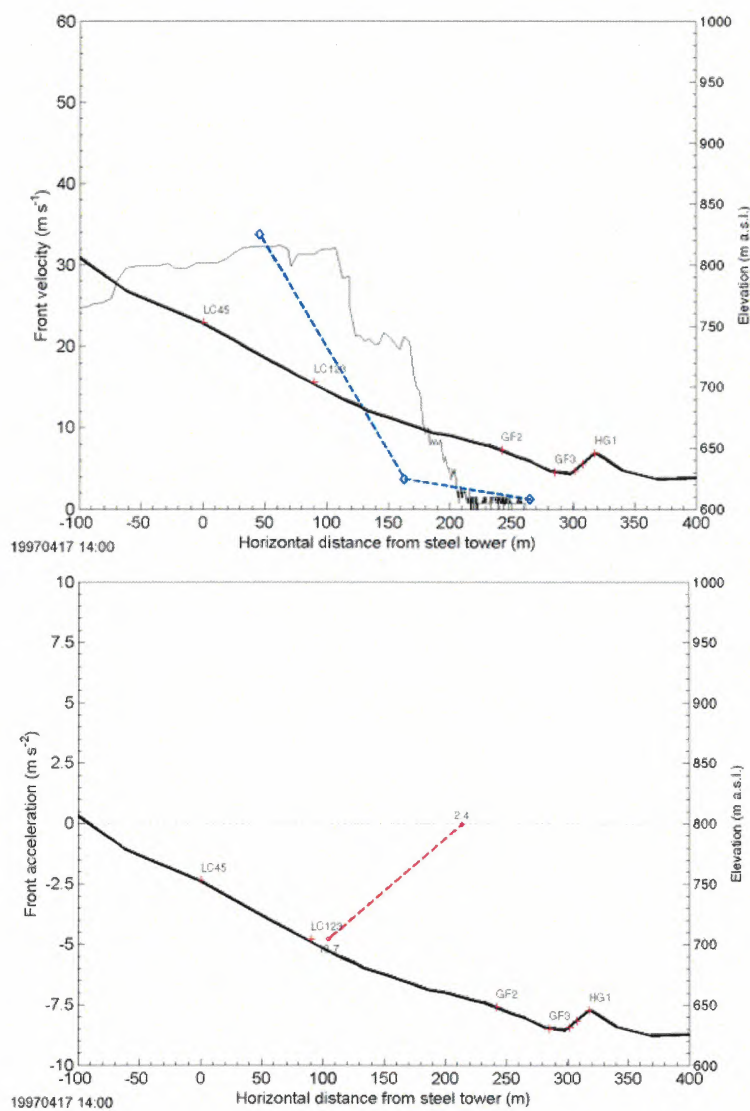


Figure 3.8: Avalanche 19970417 14:00: Mean front velocity vs. horizontal distance (top); corresponding accelerations (bottom; values are the corresponding velocities in $m s^{-1}$). Shown are estimates based on the arrival times at various sensor locations complemented with data from Doppler radar measurements by AIATR in the runout area.

20021048-11

4 WINTER 1998/1999

4.1 Avalanche 19990122 06:03

Avalanche code (UNESCO/IAHS 1981): A3, B3, C1, D2, E1, F4, G1, H4, J1.

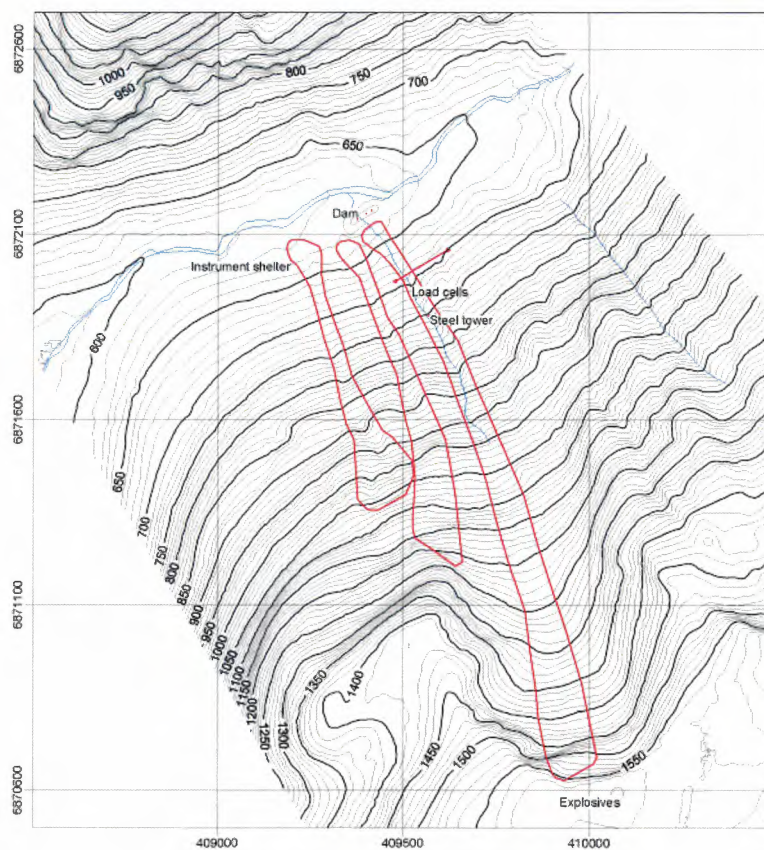


Figure 4.1: Avalanche 19990122 06:03: Map of the deposit.

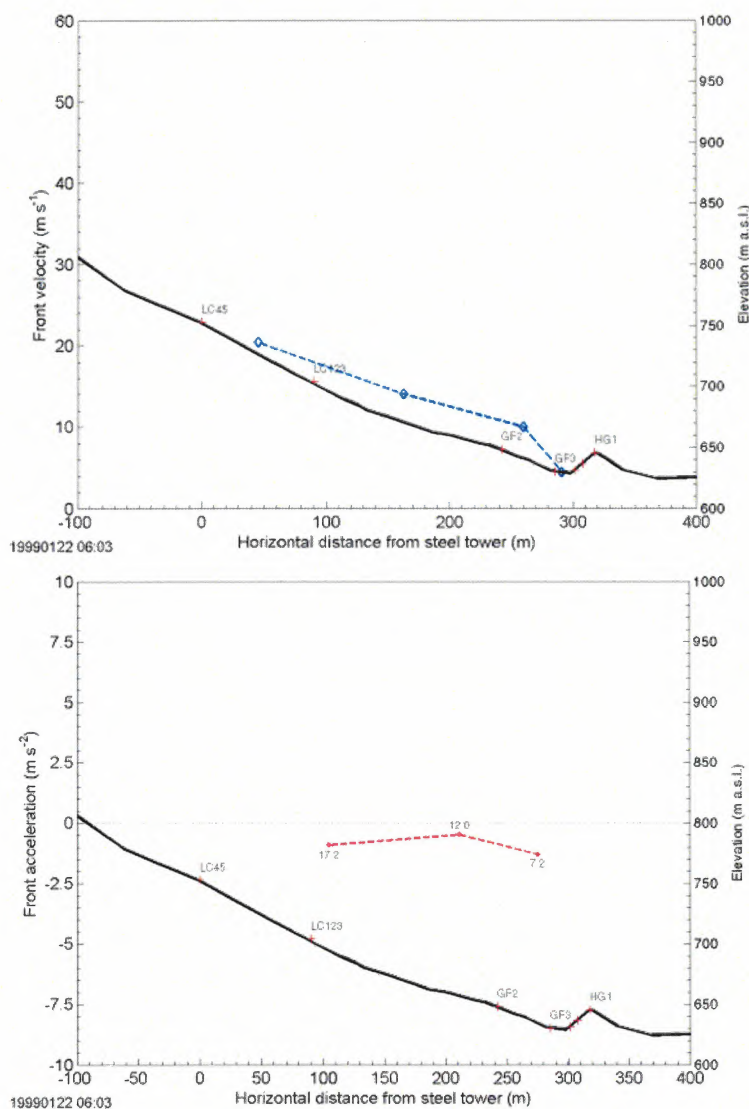


Figure 4.3: Avalanche 19990122 06:03: Mean front velocity vs. horizontal distance (top); corresponding accelerations (bottom; values are the corresponding velocities in $m s^{-1}$). Shown are estimates based on the arrival times at various sensor locations in the runout area.

20021048-11

4.2 Avalanche 19990131 16:05

Avalanche code (UNESCO/IAHS 1981): A3, B3, C1, D2, E1, F4, G1, H4, J1.

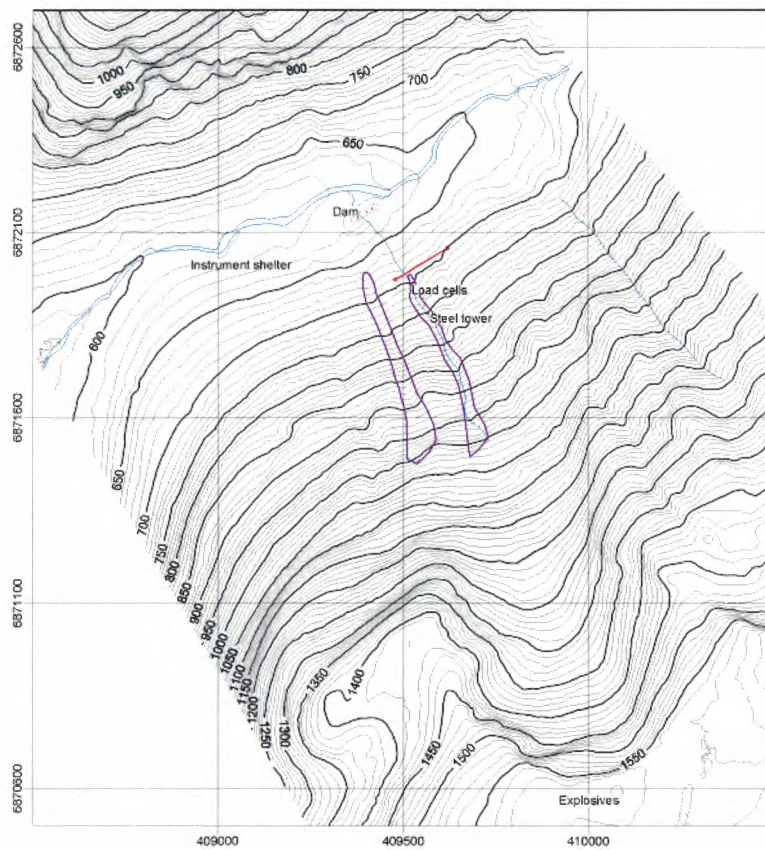


Figure 4.5: Avalanche 19990131 16:05: Map of the deposit.

4.3 Avalanche 19990215 12:28

Avalanche code (UNESCO/IAHS 1981): A3, B3, C1, D2, E1, F4, G2, H4, J1.

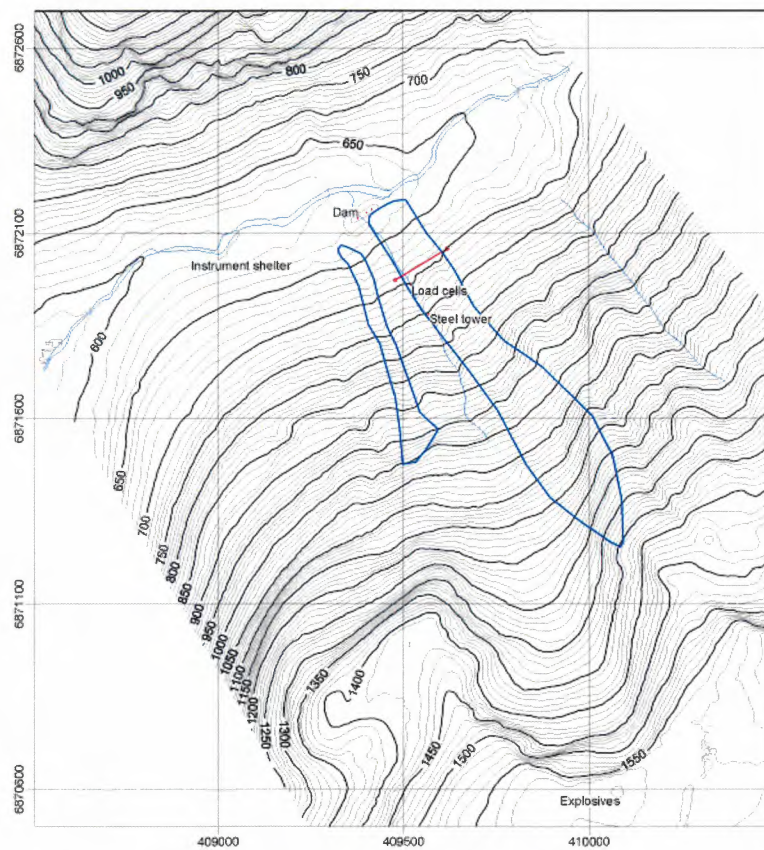


Figure 4.7: Avalanche 19990215 12:28: Map of the deposit.

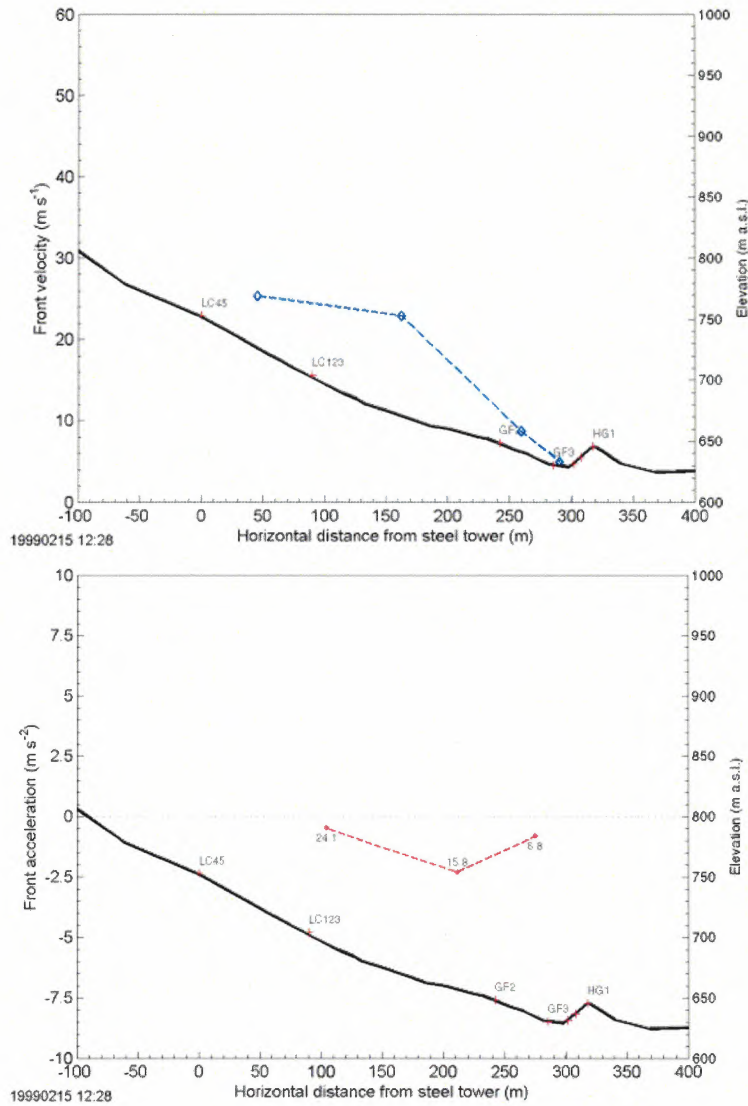


Figure 4.9: Avalanche 19990215 12:28: Mean front velocity vs. horizontal distance (top); corresponding accelerations (bottom; values are the corresponding velocities in $m s^{-1}$). Shown are estimates based on the arrival times at various sensor locations in the runout area.

20021048-11

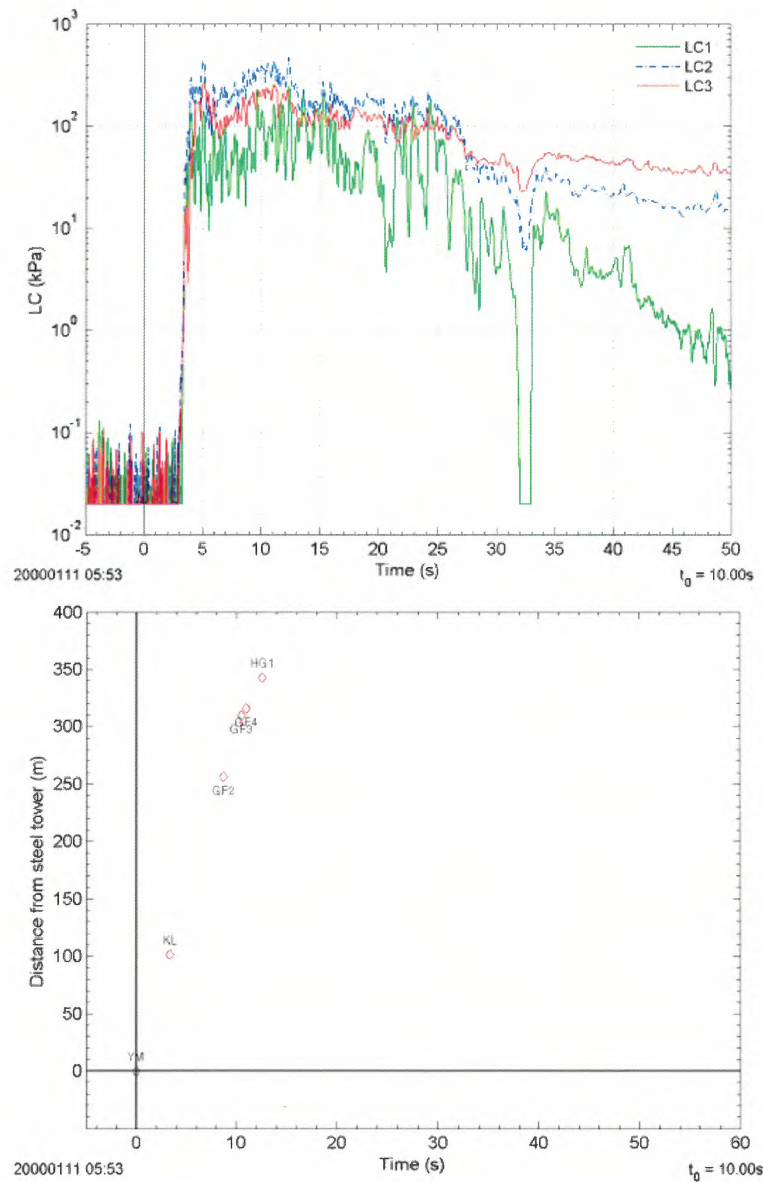


Figure 5.2: Avalanche 20000111 05:53: Impact pressure vs. time (center); Timing (Distance vs. time; bottom).

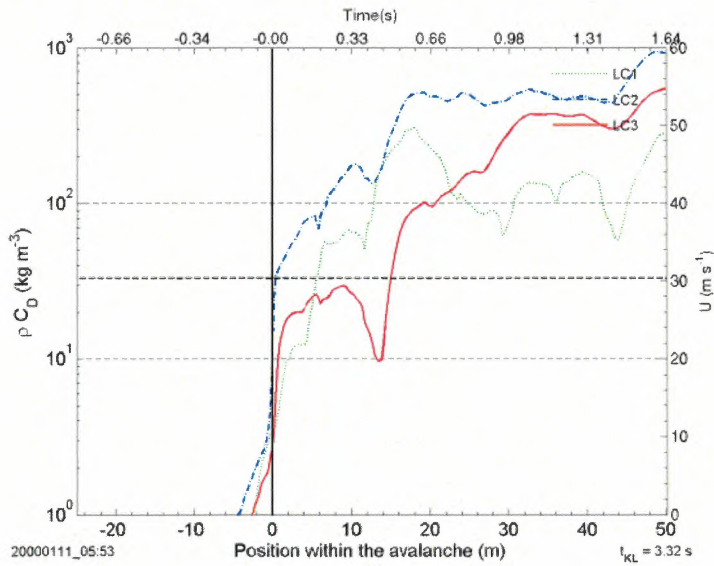


Figure 5.4: Avalanche 20000111 05:53: Estimated ρC_D values for the first approximately 2 s of impact at the concrete structure. Values are based on the estimated mean front velocity indicated by the thick dashed line; the velocity is taken to be constant over the period.

20021048-11

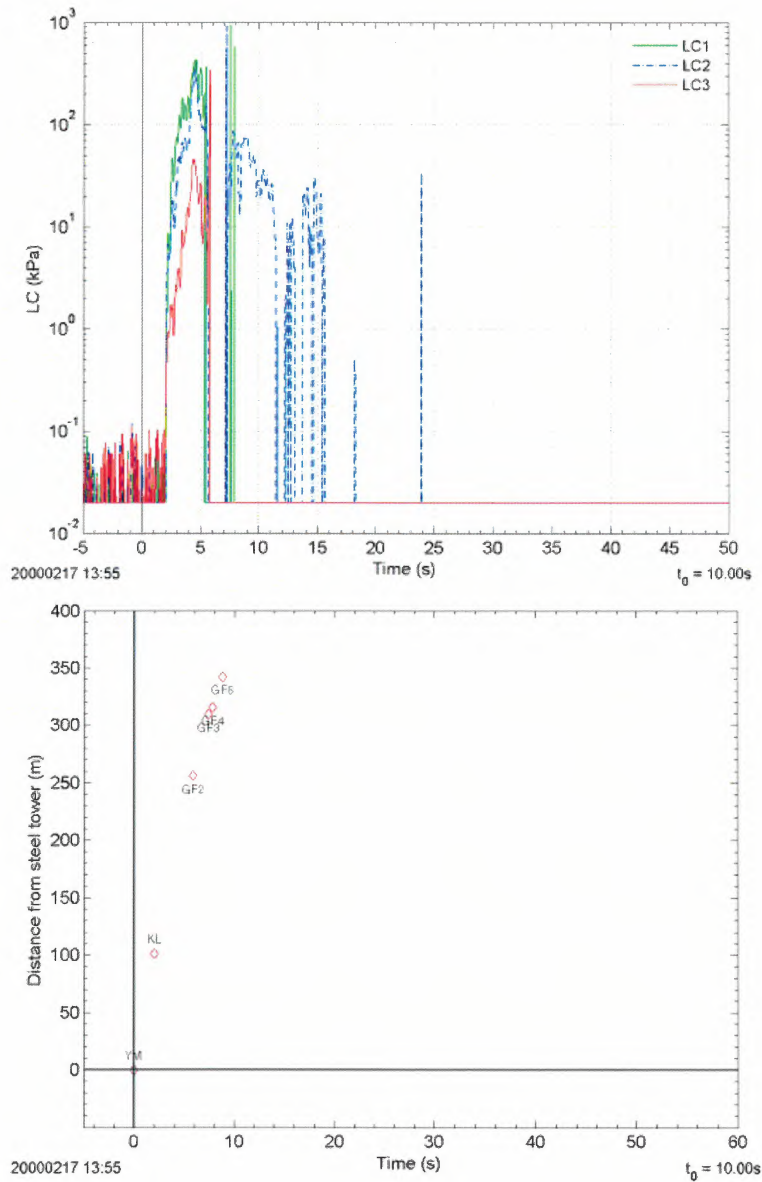


Figure 5.6: Avalanche 20000217 13:55: Impact pressure vs. time (top); Timing (Distance vs. time; bottom).

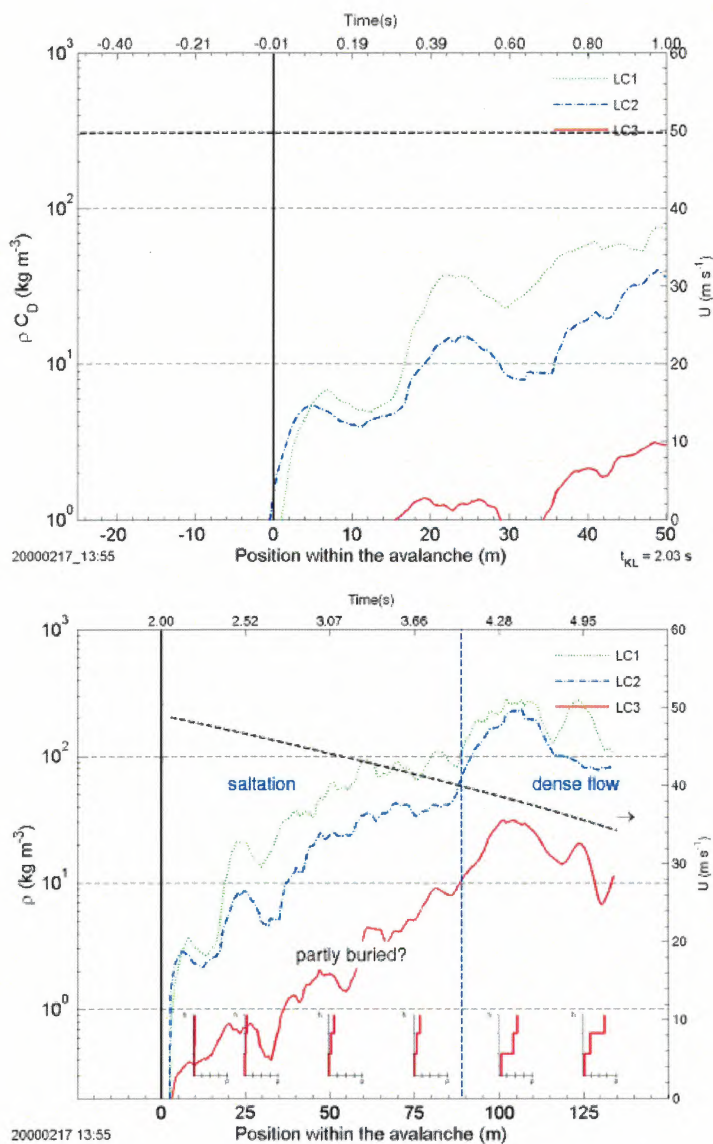


Figure 5.8: Avalanche 20000217 13:55: Estimated ρC_D values for the first approximately 2 s of impact at the concrete structure. Values are based on the estimated mean front velocity indicated by the thick dashed line; the velocity is taken to be constant over the period (Top panel). For comparison, bottom panel shows the calculated density using $C_D = 2$ based on the best approximation of the velocity distribution over time. Inset give an impression of the density profile with height.

20021048-11



6.2 Avalanche 20020101 01:42

Avalanche code (UNESCO/IAHS 1981): A/, B/, C/, D2, E/, F/, G/, H/, J1.

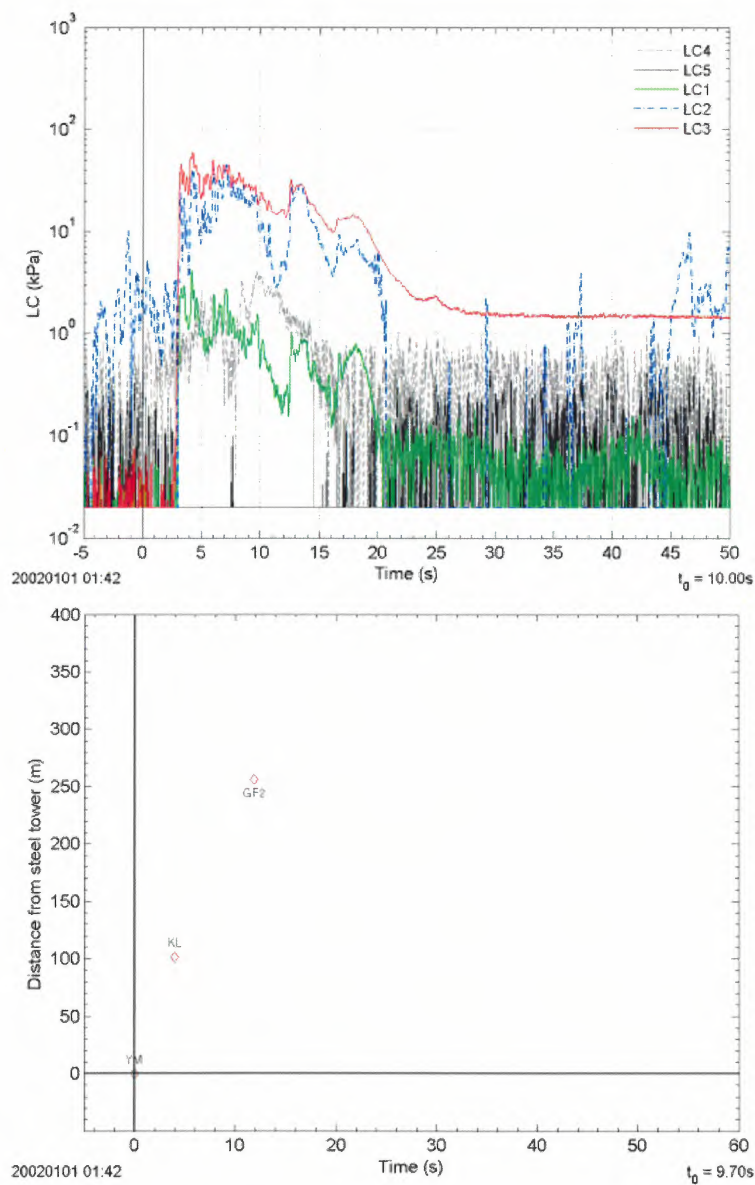


Figure 6.2: Avalanche 20020101 01:42: Impact pressure vs. time (top); Timing (Distance vs. time; bottom);

20021048-11

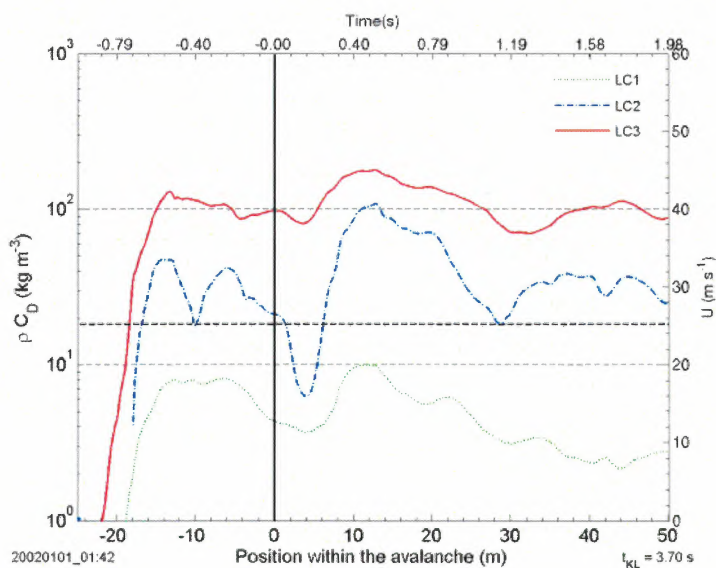


Figure 6.4: Avalanche 20020101 01:42: Estimated ρC_D values for the first approximately 2 s of impact at the concrete structure. Values are based on the estimated mean front velocity indicated by the thick dashed line; the velocity is taken to be constant over the period.

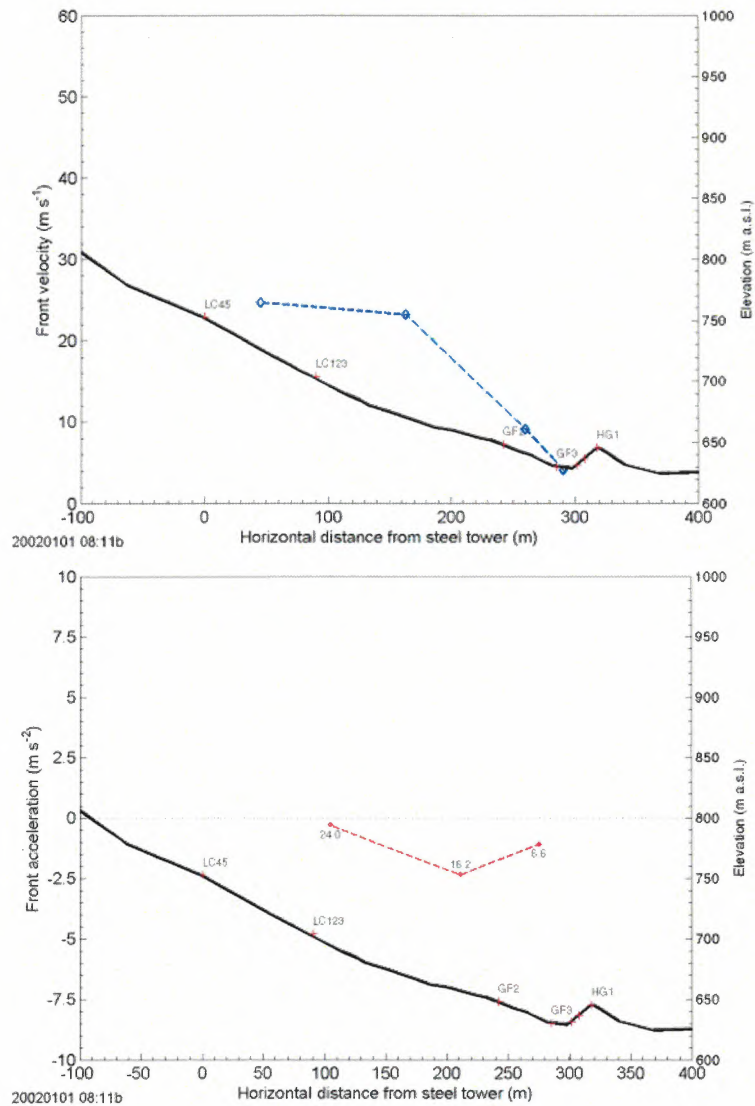


Figure 6.6: Avalanche 2002101 08:11: Mean front velocity vs. horizontal distance (top); corresponding accelerations (bottom; values are the corresponding velocities in $m s^{-1}$). Shown are estimates based on the arrival times at various sensor locations in the runout area.

20021048-11



7 WINTER 2002/2003

7.1 Avalanche 20030114 03:30

Avalanche code (UNESCO/IAHS 1981): A/, B/, C1, D2, E/, F/, G/, H/, J1.

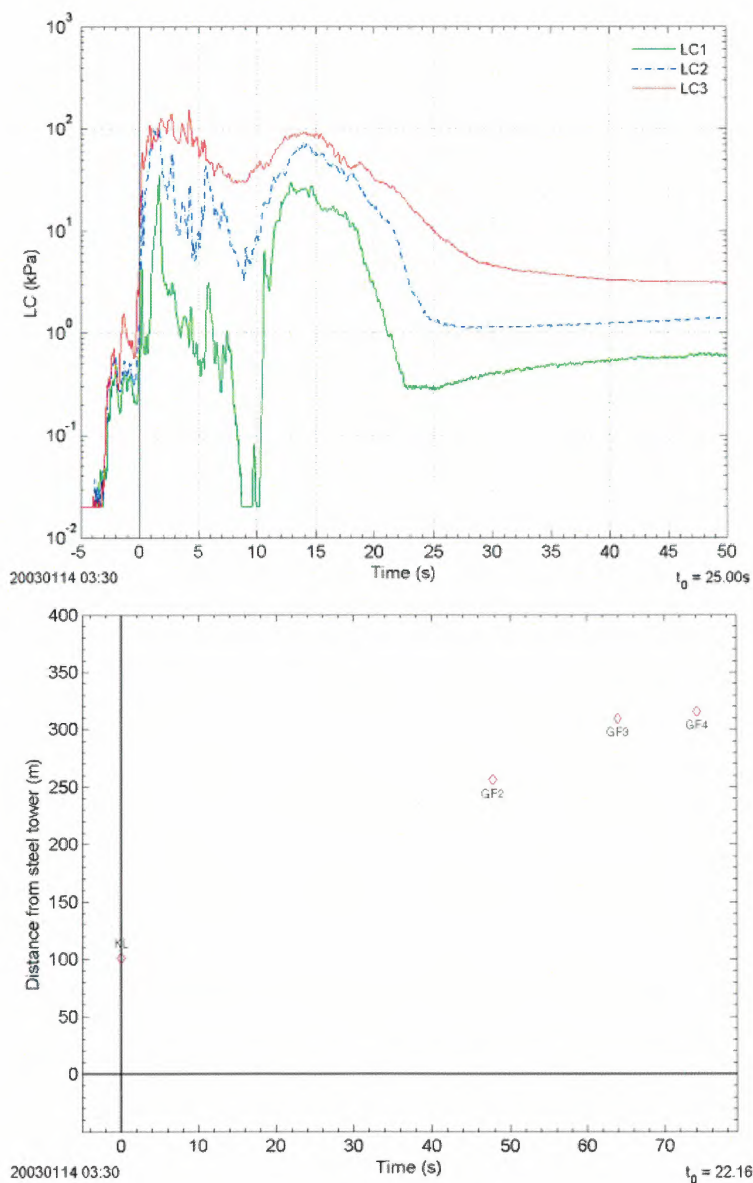


Figure 7.1: Avalanche 20030114 03:30: Impact pressure vs. time (top); Timing (Distance vs. time; bottom);

20021048-11

7.2 Avalanche 20030114 05:40

Avalanche code (UNESCO/IAHS 1981): A/, B/, C1, D2, E/, F/, G/, H/, J1.

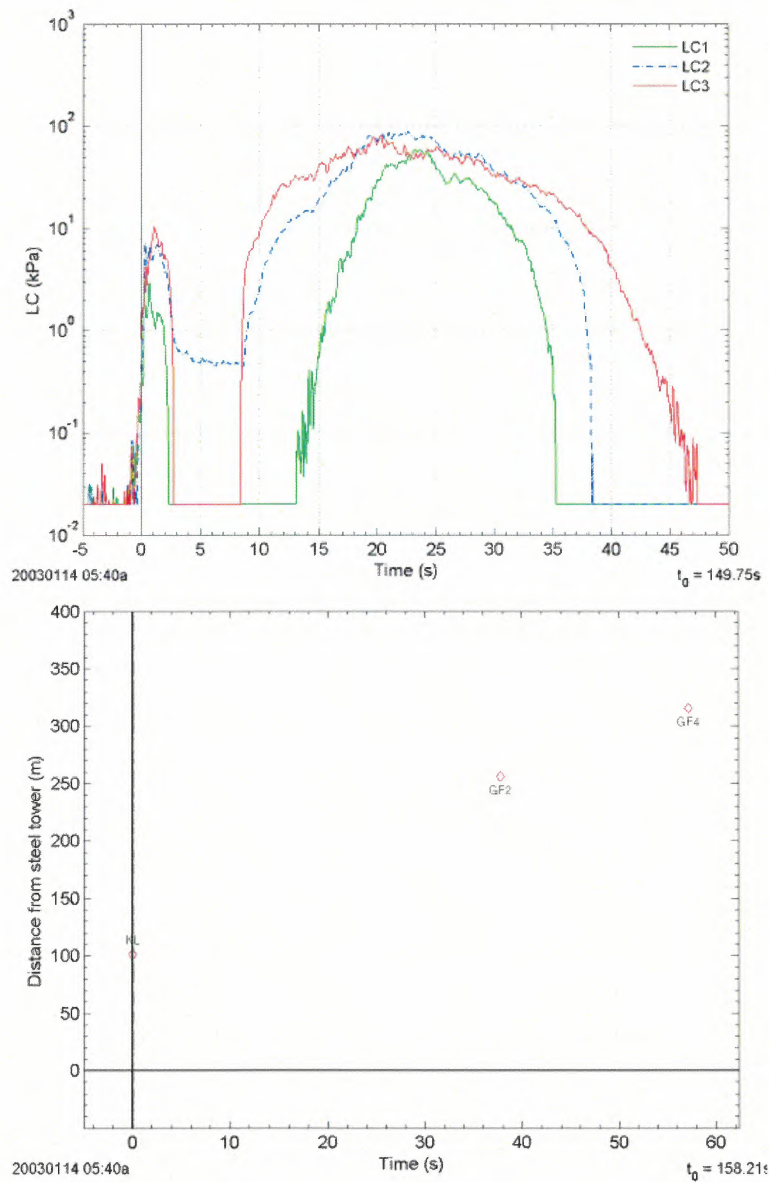


Figure 7.3: Avalanche 20030114 05:40: Impact pressure vs. time (top); Timing (Distance vs. time; bottom);

20021048-11

7.3 Avalanche 20030115 13:27

Avalanche code (UNESCO/IAHS 1981): A2, B/, C7, D2, E/, F3, G/, H/, J1.

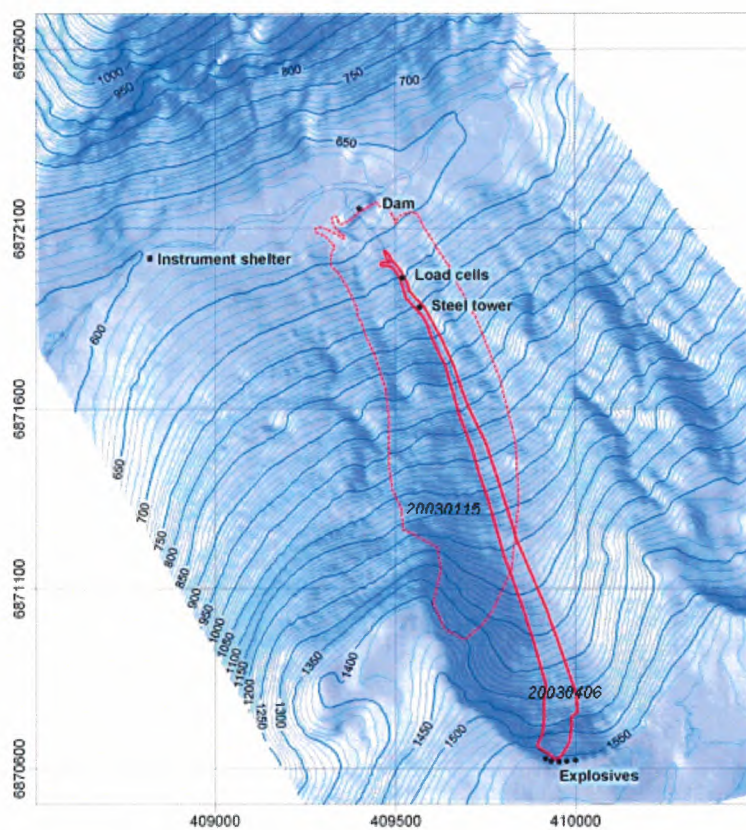


Figure 7.5: Avalanche 20030115 13:27: Map of the deposit.

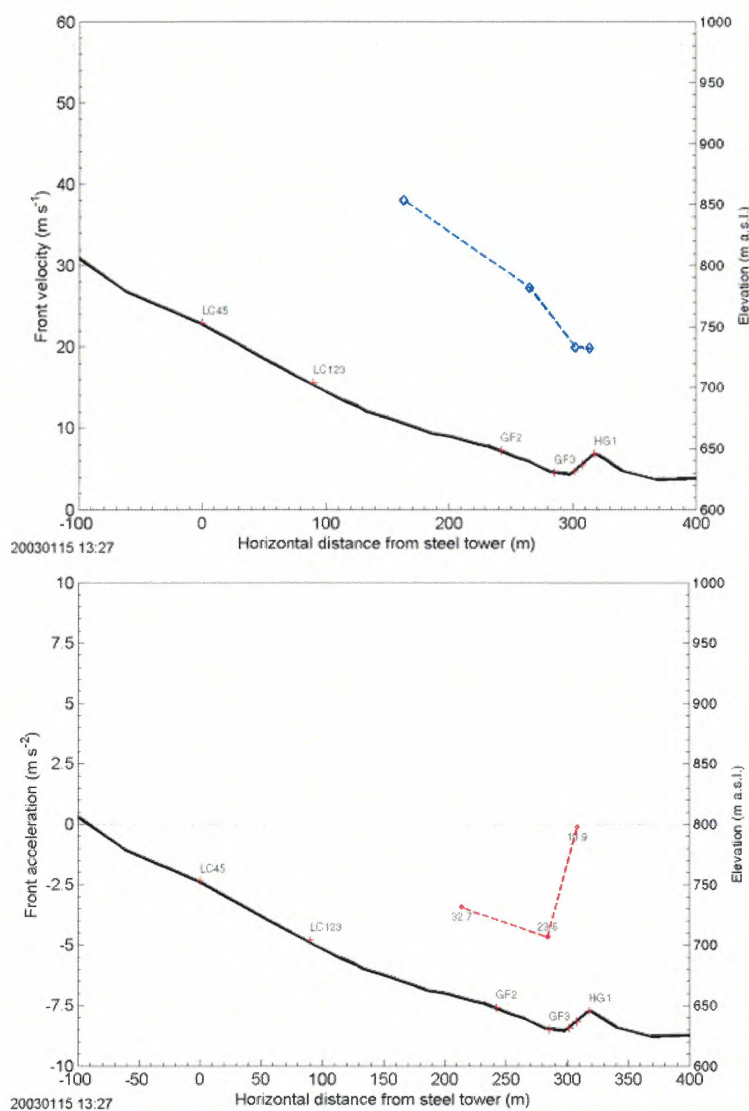


Figure 7.7: Avalanche 20030115 13:27: Mean front velocity vs. horizontal distance (top); corresponding accelerations (bottom; values are the corresponding velocities in $m s^{-1}$). Shown are estimates based on the arrival times at various sensor locations in the runout area.

20021048-11

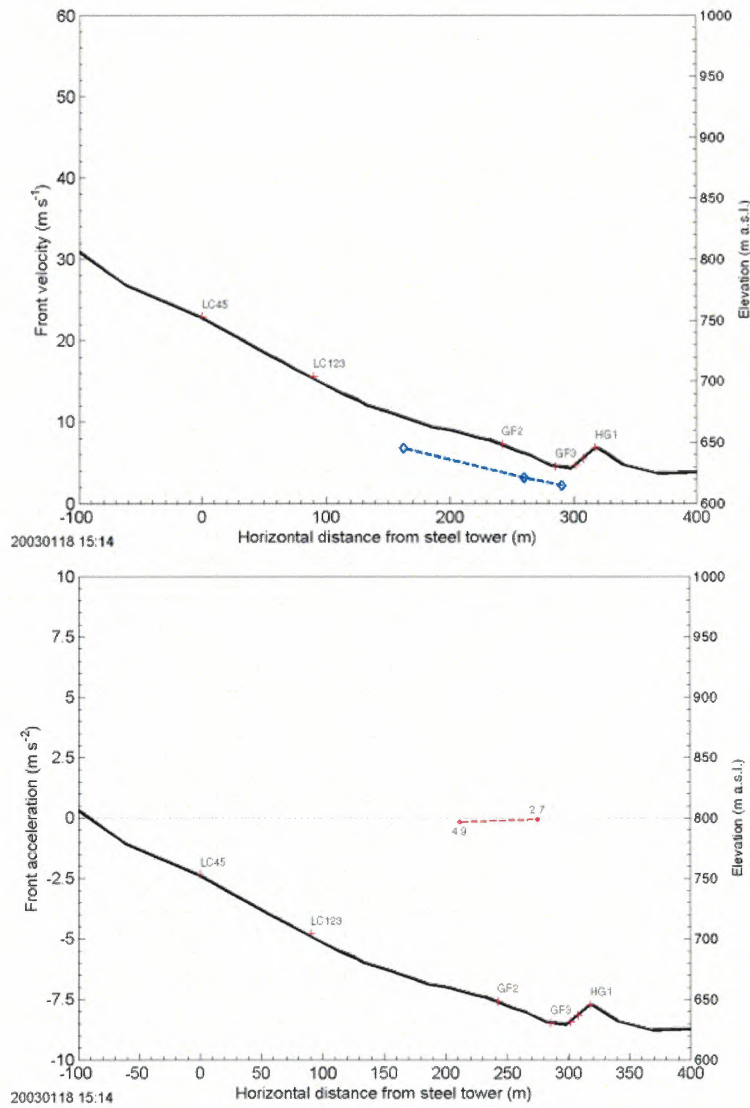


Figure 7.9: Avalanche 20030118 15:14: Mean front velocity vs. horizontal distance (top); corresponding accelerations (bottom; values are the corresponding velocities in $m s^{-1}$). Shown are estimates based on the arrival times at various sensor locations in the runout area.

20021048-11

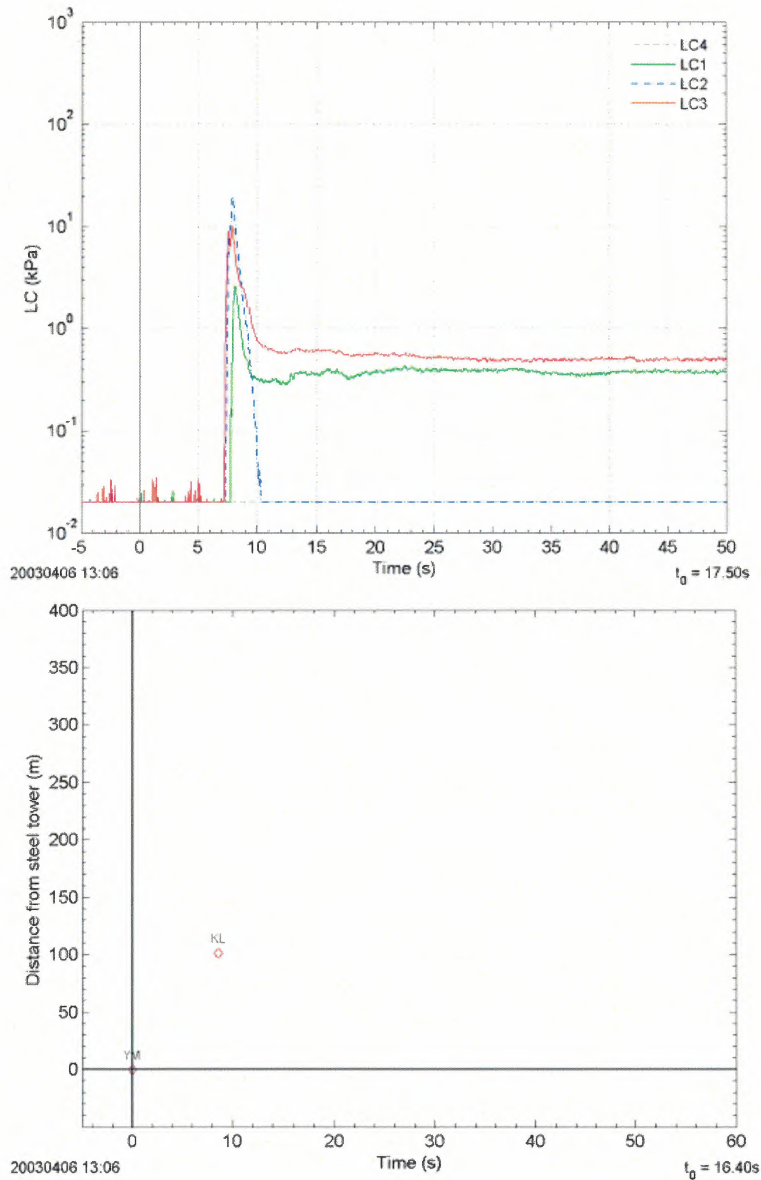


Figure 7.11: Avalanche 20030406 13:06: Impact pressure vs. time (top); Timing (Distance vs. time; bottom).

20021048-11

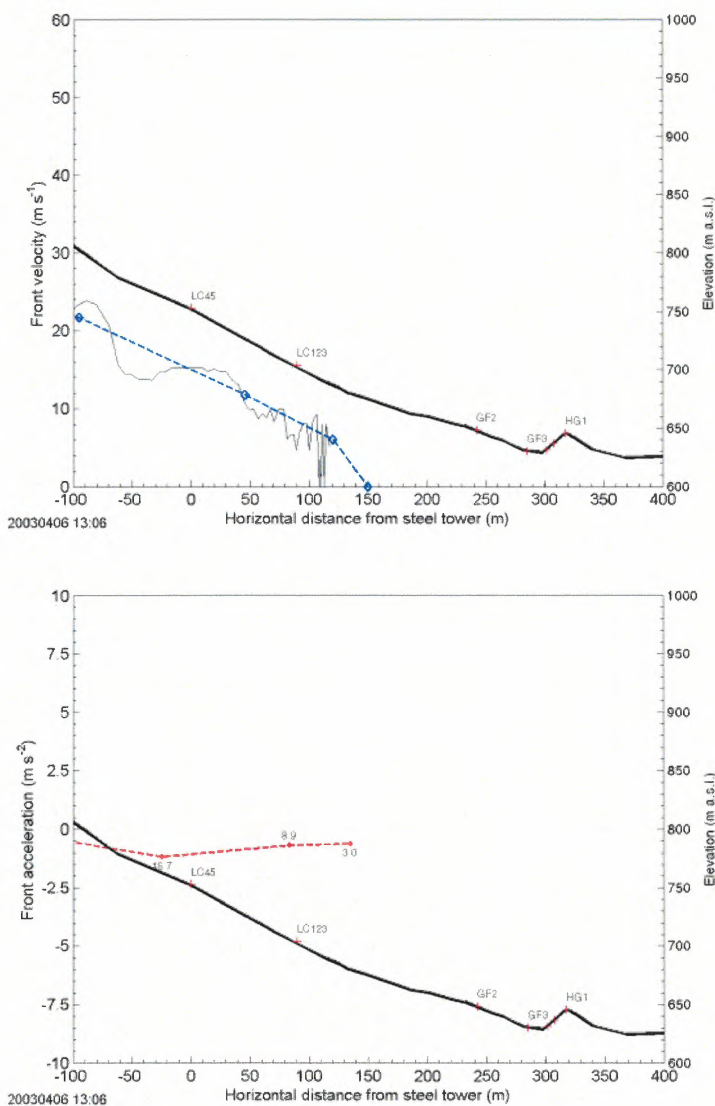


Figure 7.13: Avalanche 20030406 13:06: Mean front velocity vs. horizontal distance (top); corresponding accelerations (bottom; values are the corresponding velocities in $m s^{-1}$). Shown are estimates based on the arrival times at various sensor locations and on video analysis in the runout area. In addition, the thin black line (right side) shows the front velocity measured by pulsed Doppler radar (range gate width 50 m).

8 WINTER 2003/2004

8.1 Avalanche 20031215 16:40

Avalanche code (UNESCO/IAHS 1981): A1, B2, C1, D2, E7, F4, G1, H1, J1.

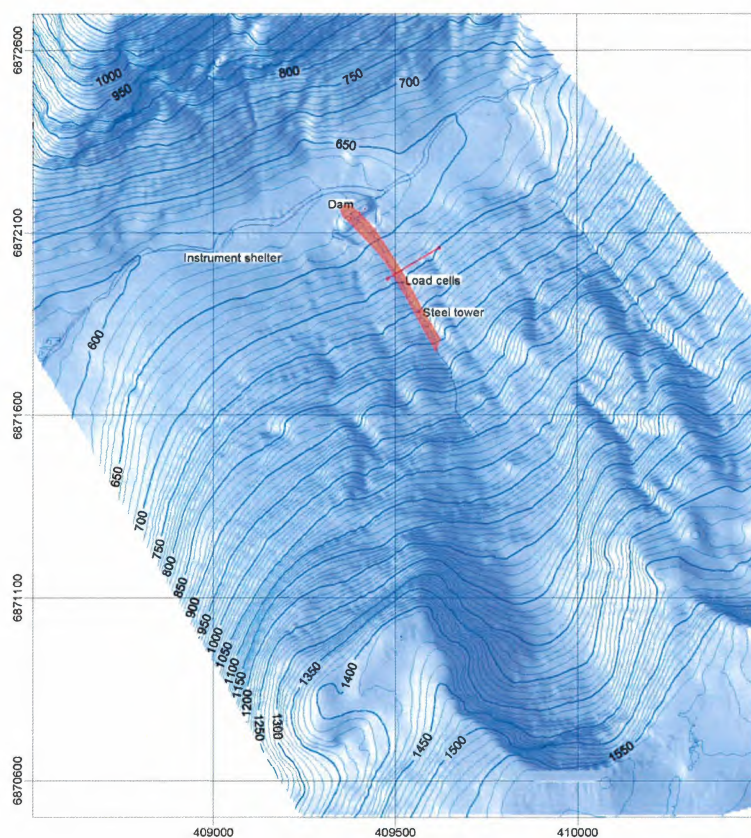


Figure 8.1: Avalanche 20031215 16:40: Map of the deposit (20031215 and 20031217).;

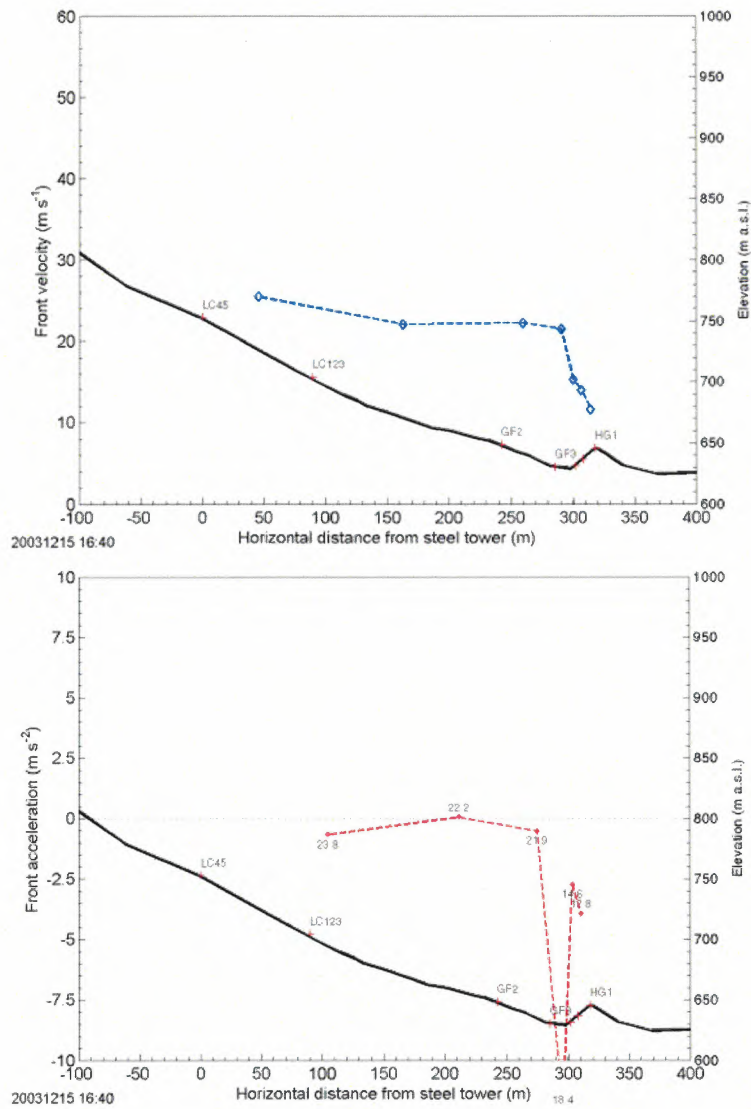


Figure 8.3: Avalanche 20031215 16:40: Mean front velocity vs. horizontal distance (top); corresponding accelerations (bottom; values are the corresponding velocities in $m s^{-1}$). Shown are estimates based on the arrival times at various sensor locations in the runout area.

20021048-11

8.2 Avalanche 20031217 03:24

Avalanche code (UNESCO/IAHS 1981): A1, B2, C1, D2, E7, F4, G7, H1, J1.

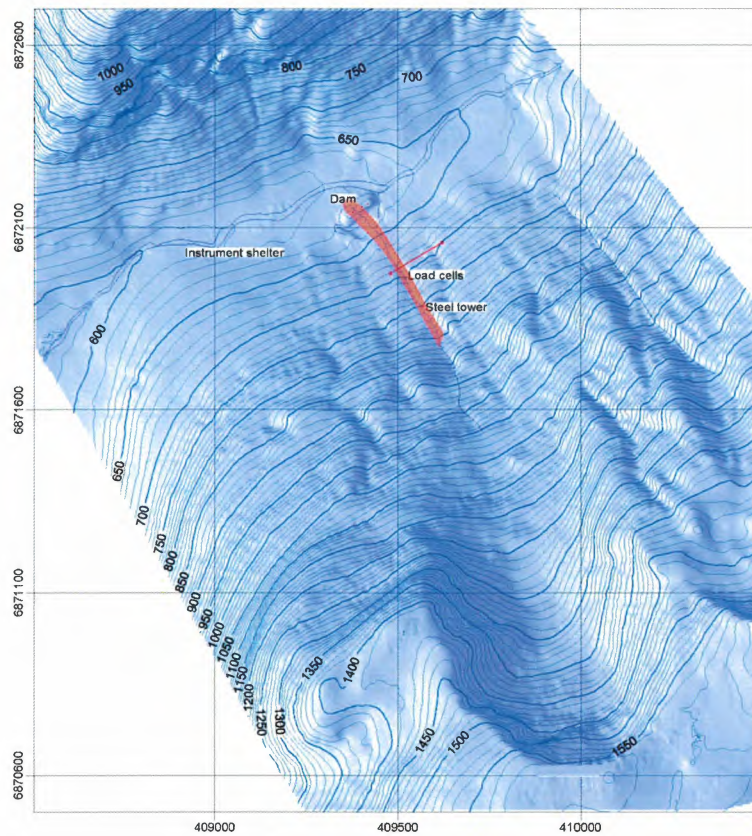


Figure 8.5: Avalanche 20031217 03:24: Map of the deposit (20031215 and 20031217);

20021048-11

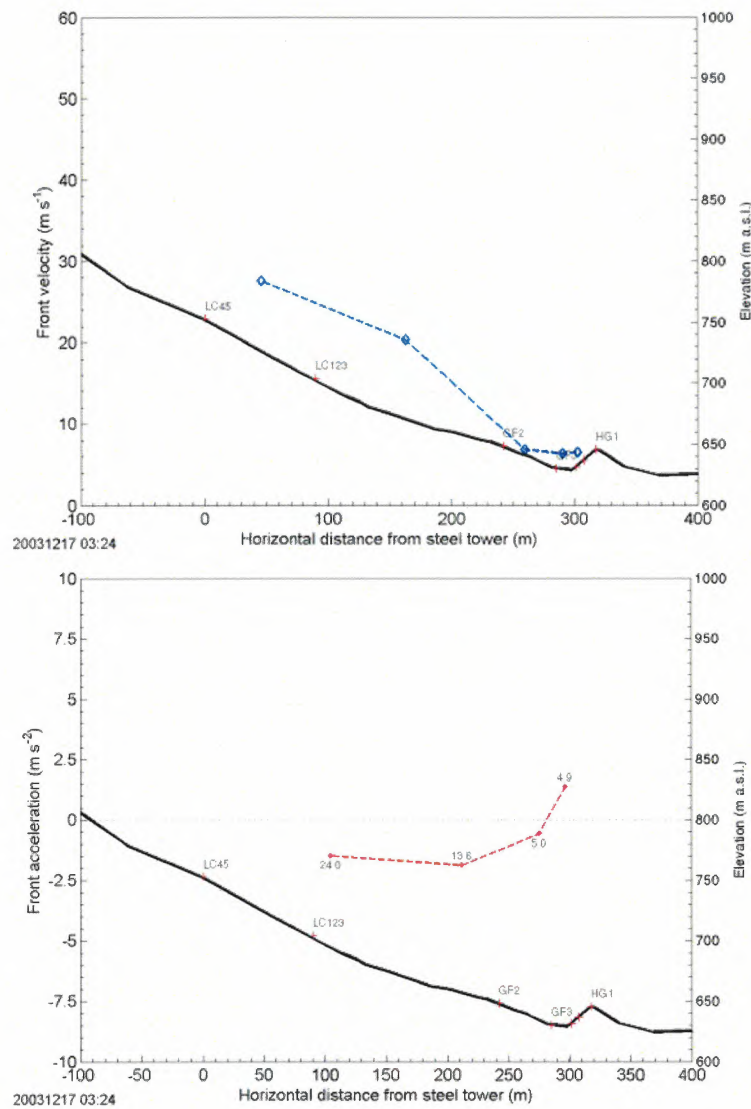


Figure 8.7: Avalanche 20031217 03:24: Mean front velocity vs. horizontal distance (top); corresponding accelerations (bottom; values are the corresponding velocities in $m s^{-1}$). Shown are estimates based on the arrival times at various sensor locations in the runout area.

20021048-11

8.3 Avalanche 20040204 06:10

Avalanche code (UNESCO/IAHS 1981): A1, B2, C7, D2, E7, F3, G2, H4, J1.

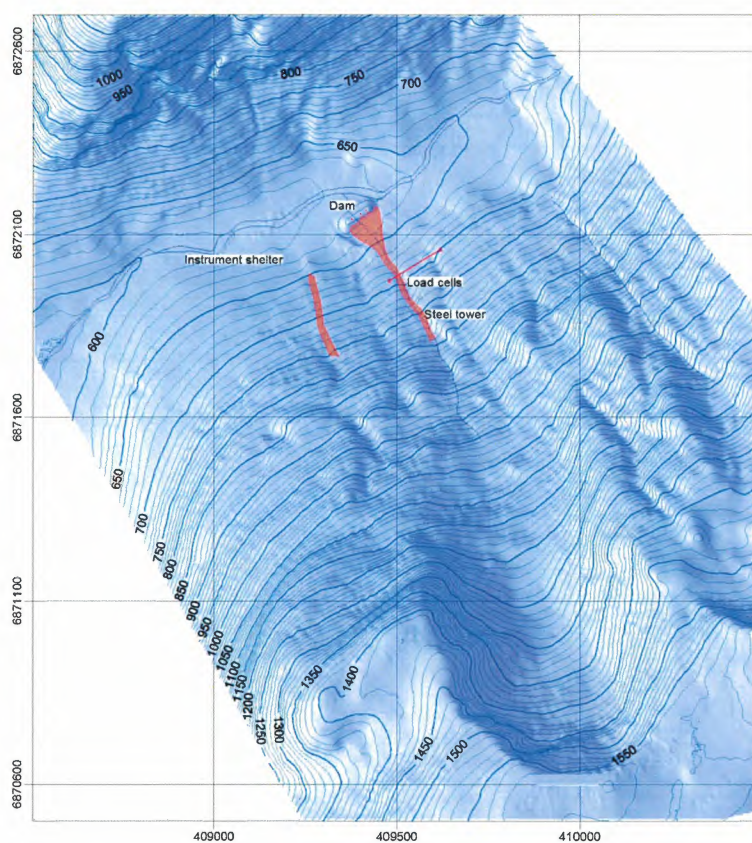


Figure 8.9: Avalanche 20040204 06:10: Map of the deposit (top).

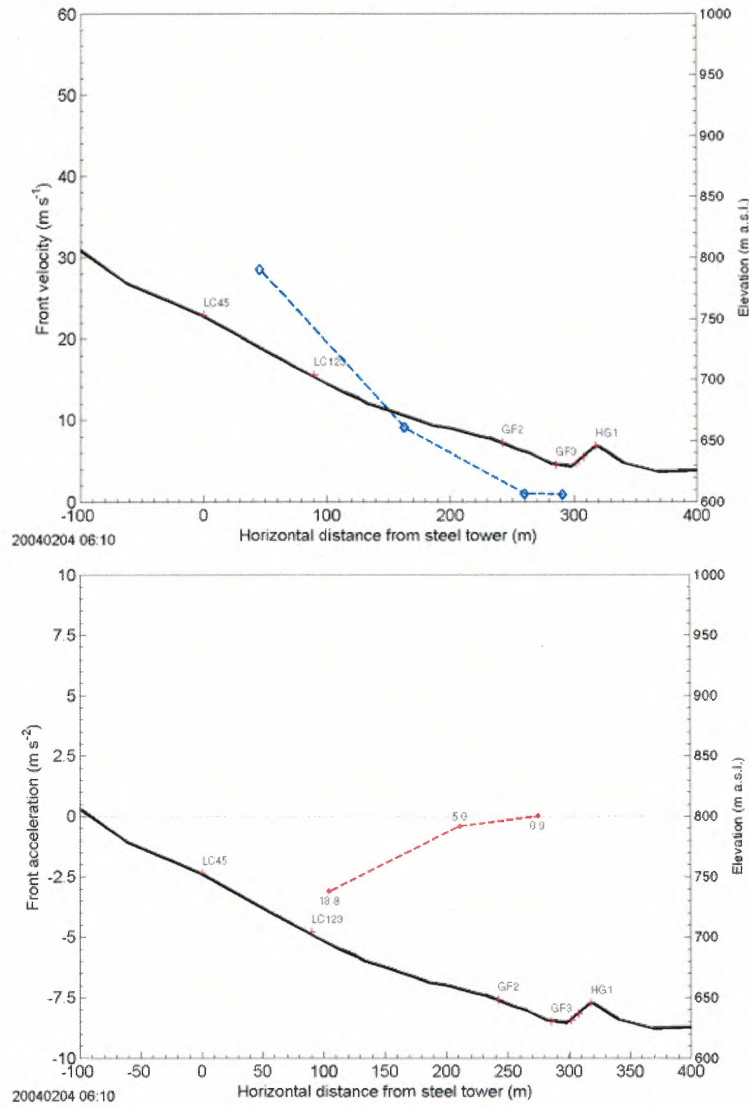


Figure 8.11: Avalanche 20040204 06:10: Mean front velocity vs. horizontal distance (top); corresponding accelerations (bottom; values are the corresponding velocities in $m s^{-1}$). Shown are estimates based on the arrival times at various sensor locations in the runout area.

20021048-11

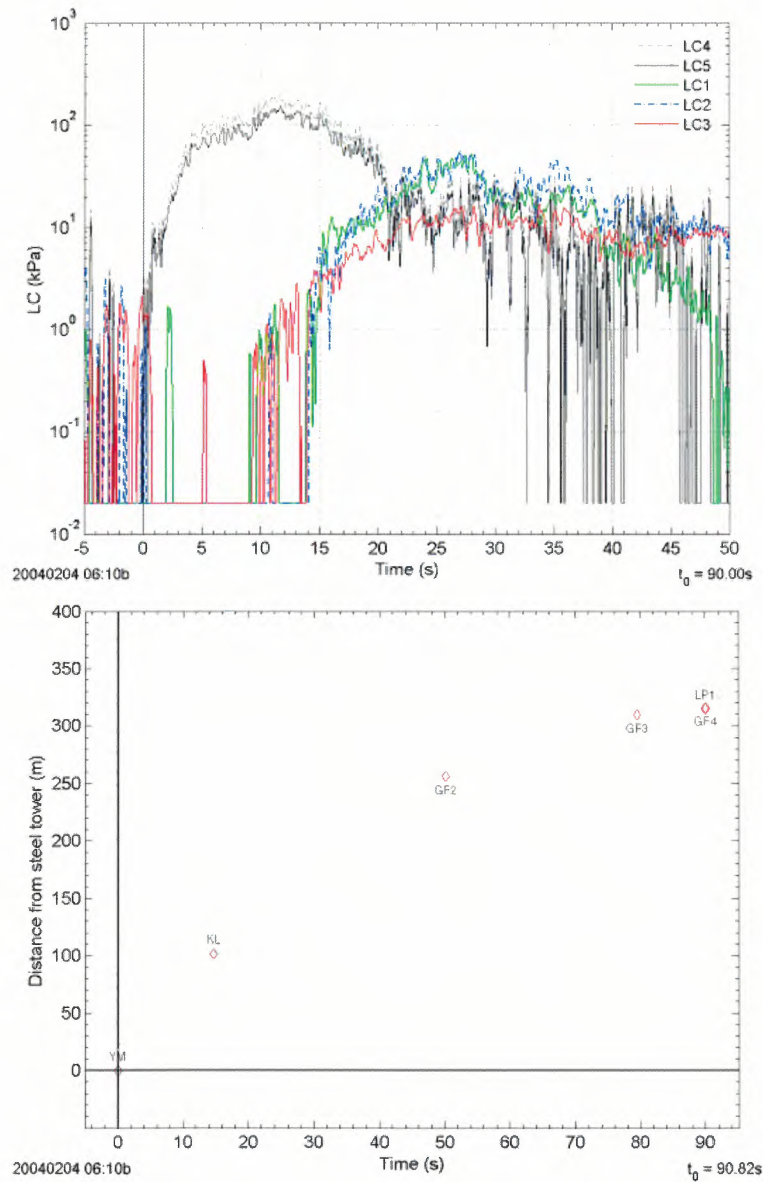


Figure 8.13: Avalanche 20040204 06:10 2nd surge: Impact pressure vs. time (center); Timing (Distance vs. time; bottom);

20021048-11

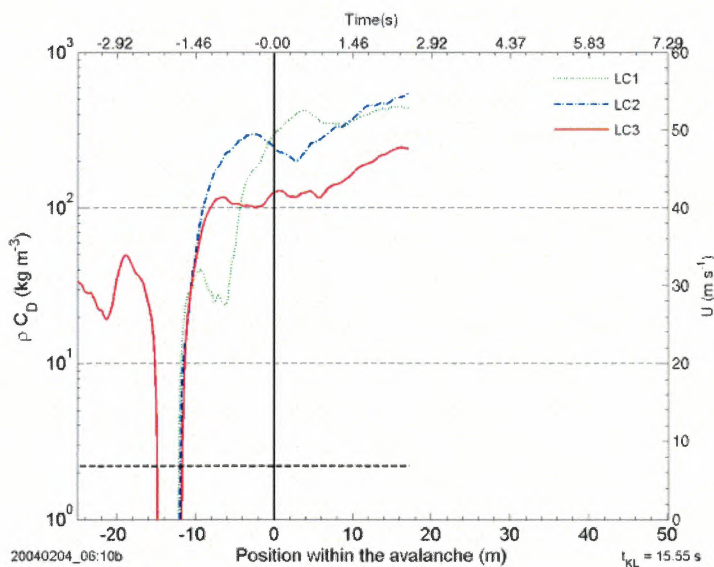


Figure 8.15: Avalanche 20040204 06:10: Estimated ρC_D values for the first approximately 2 s of impact at the concrete structure. Values are based on the estimated mean front velocity indicated by the thick dashed line; the velocity is taken to be constant over the period.

20021048-11

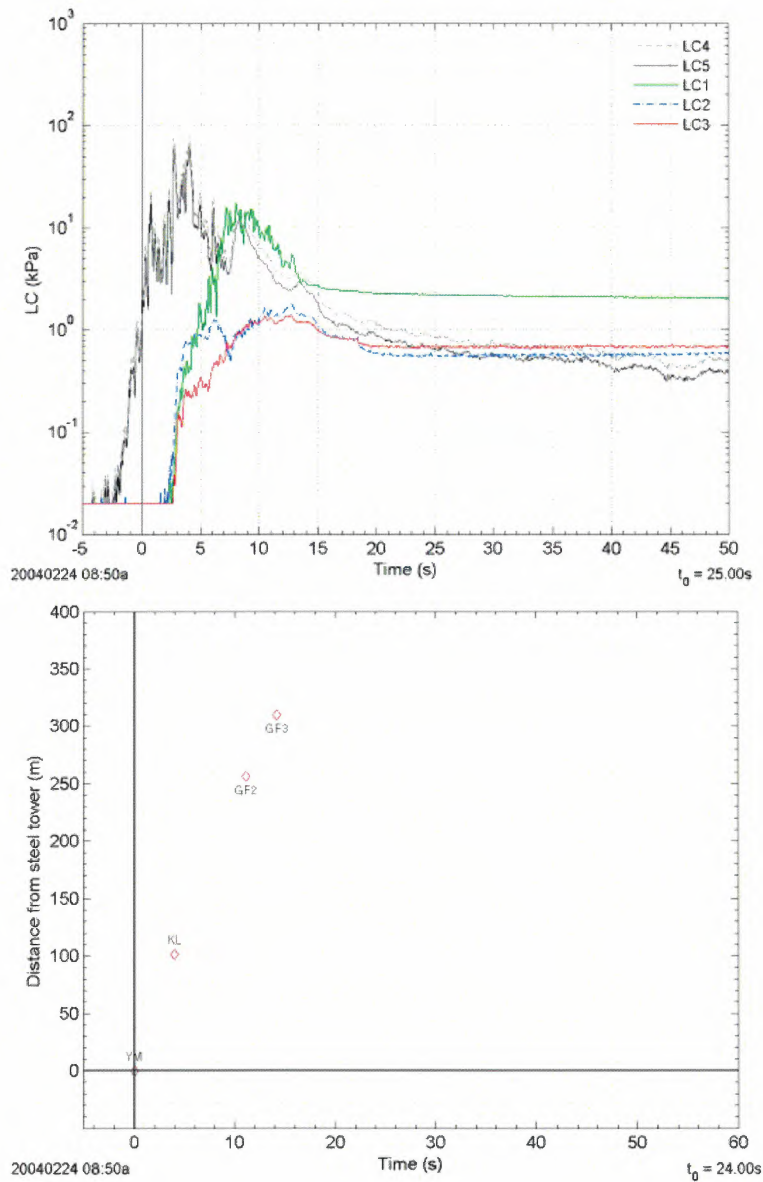


Figure 8.17: Avalanche 20040224 08:50: Impact pressure vs. time (top); Timing (Distance vs. time; bottom);

20021048-11

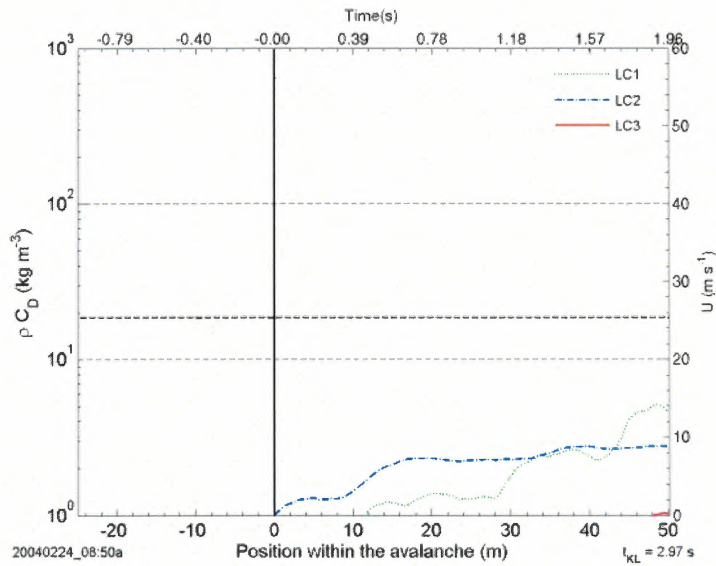


Figure 8.19: Avalanche 20040224 08:50: Estimated ρC_D values for the first approximately 2 s of impact at the concrete structure. Values are based on the estimated mean front velocity indicated by the thick dashed line; the velocity is taken to be constant over the period.

20021048-11

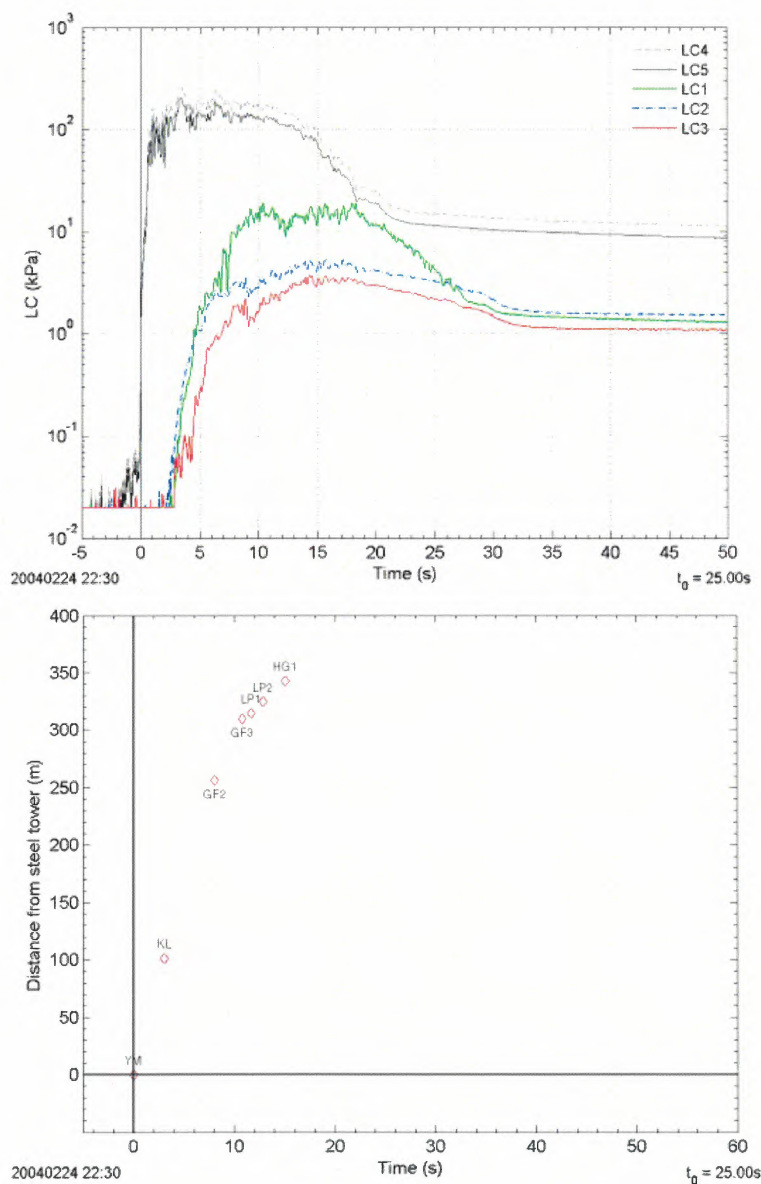


Figure 8.21: Avalanche 20040224 22:30: Impact pressure vs. time (center); Timing (Distance vs. time; bottom).

20021048-11

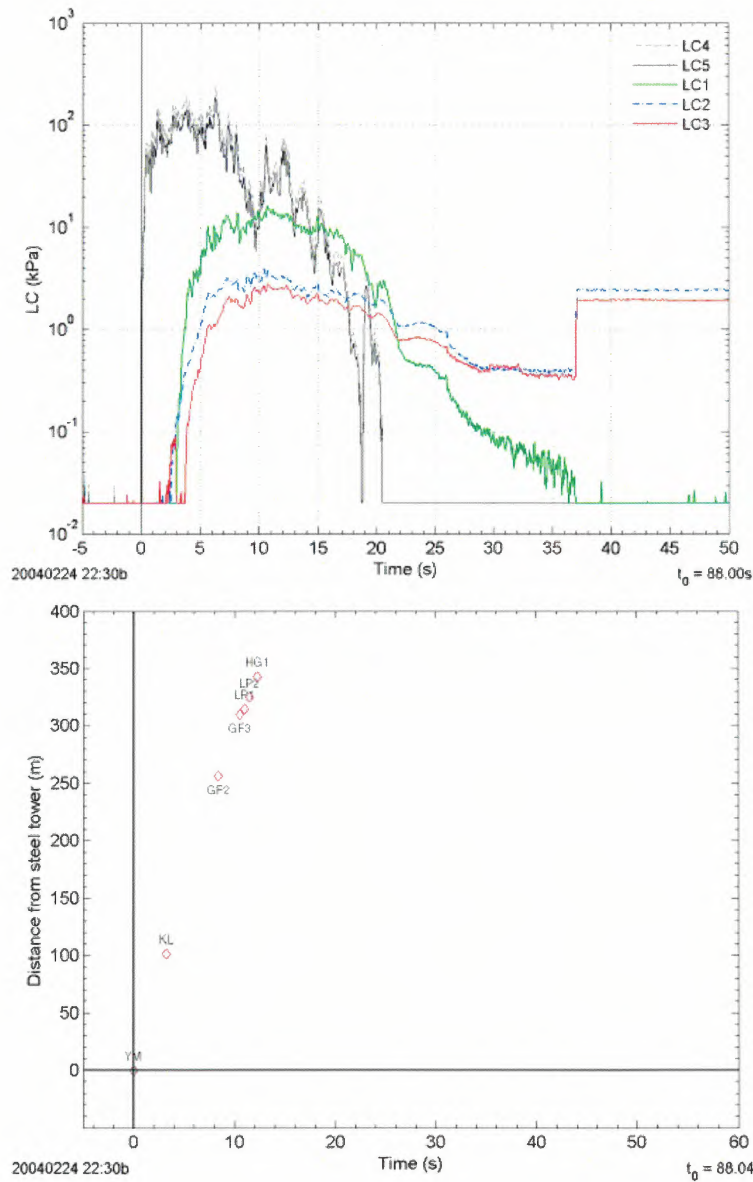


Figure 8.23: Avalanche 20040224 22:30 2nd avalanche (about 1 min later): Impact pressure vs. time (center); Timing (Distance vs. time; bottom);

20021048-11

8.6 Avalanche 20040228 15:30

Avalanche code (UNESCO/IAHS 1981): A1, B2, C1, D2, E7, F4, G2, H1, J4.

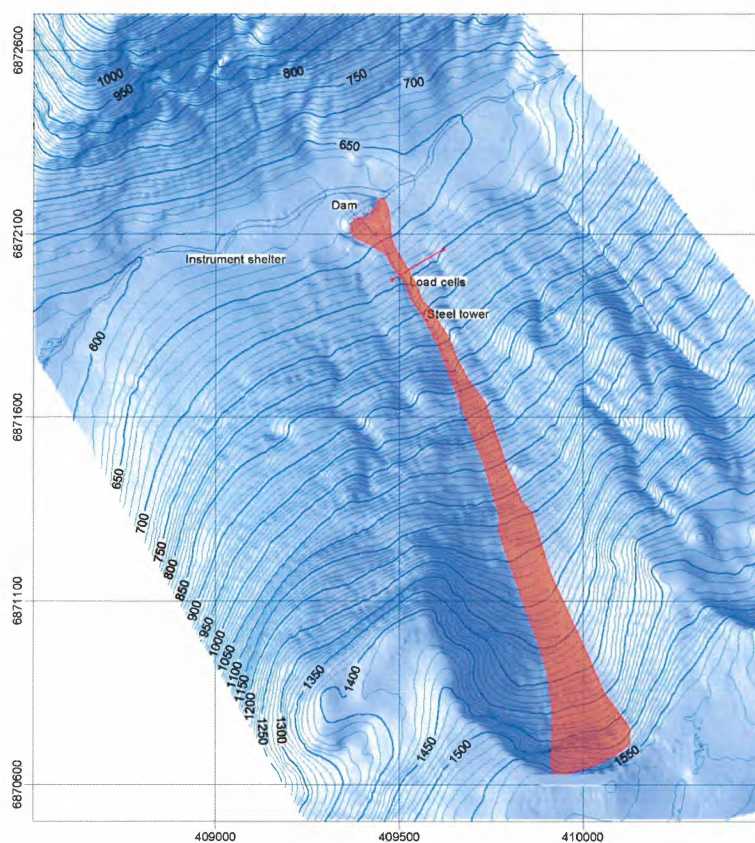


Figure 8.25: Avalanche 20040228 15:30: Map of the deposit.

20021048-11

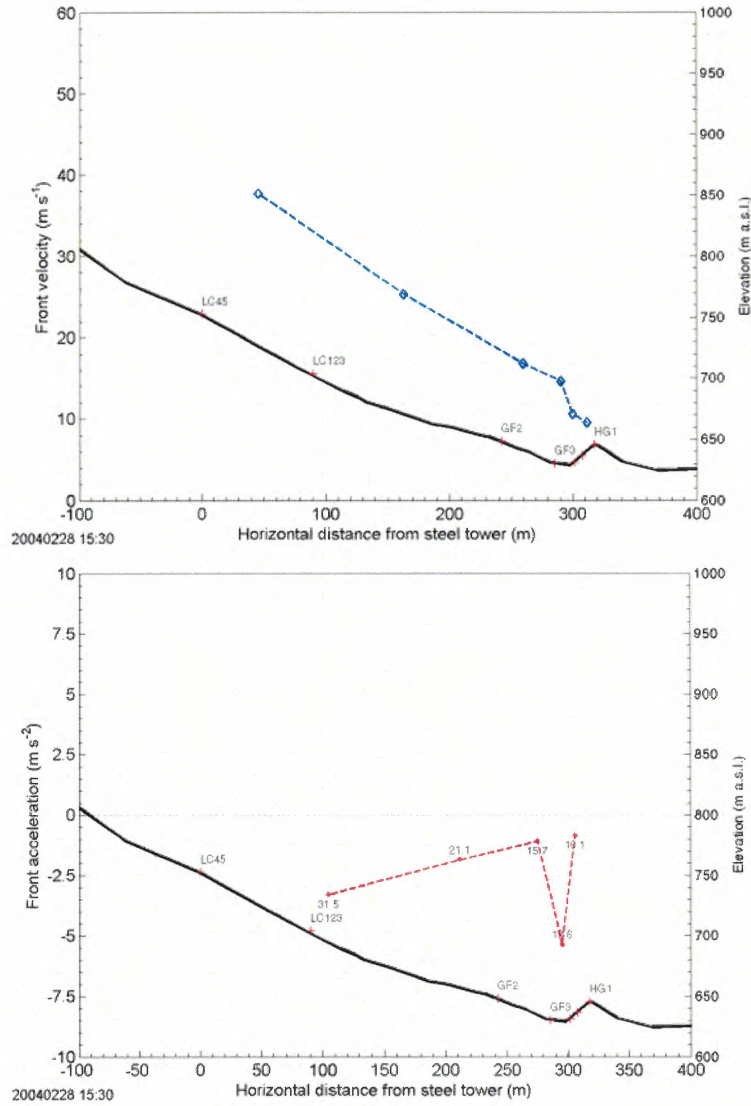


Figure 8.27: Avalanche 20040228 15:30: Mean front velocity vs. horizontal distance (top); corresponding accelerations (bottom; values are the corresponding velocities in $m s^{-1}$). Shown are estimates based on the arrival times at various sensor locations in the runout area.

20021048-11

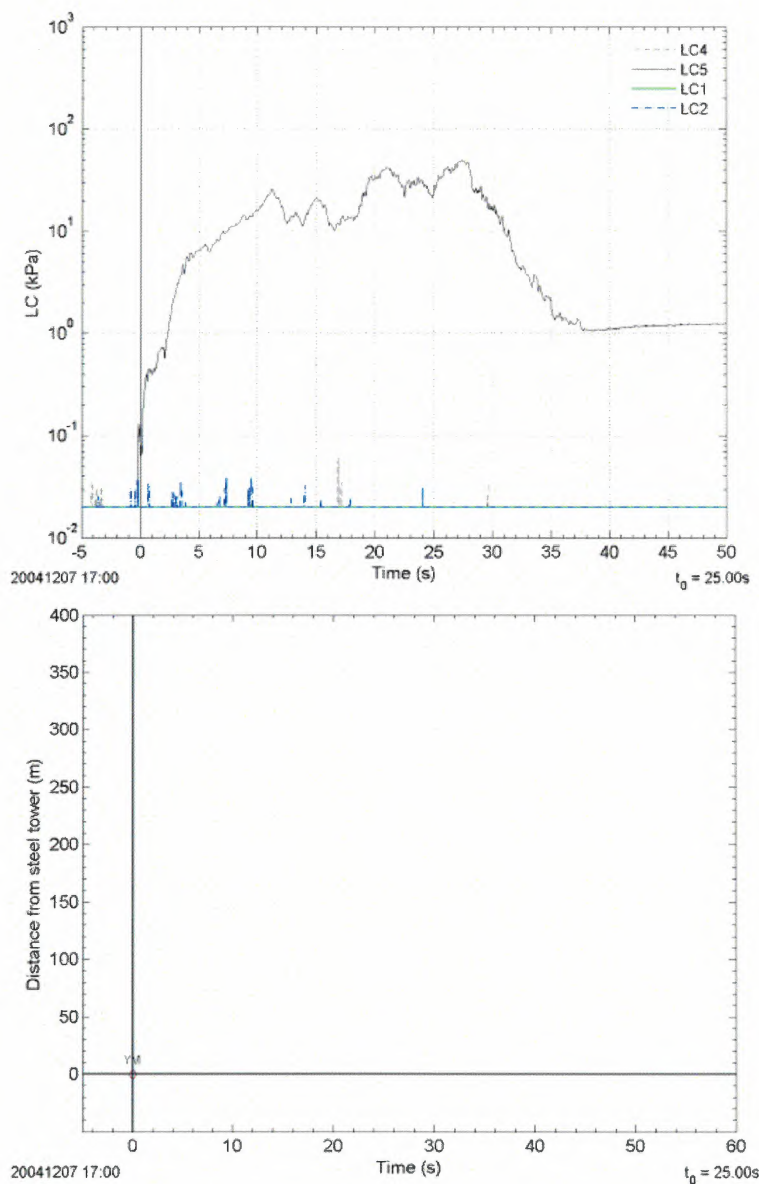


Figure 9.2: Avalanche 20041207 17:00: Impact pressure vs. time (top); Timing (Distance vs. time; bottom).

20021048-11

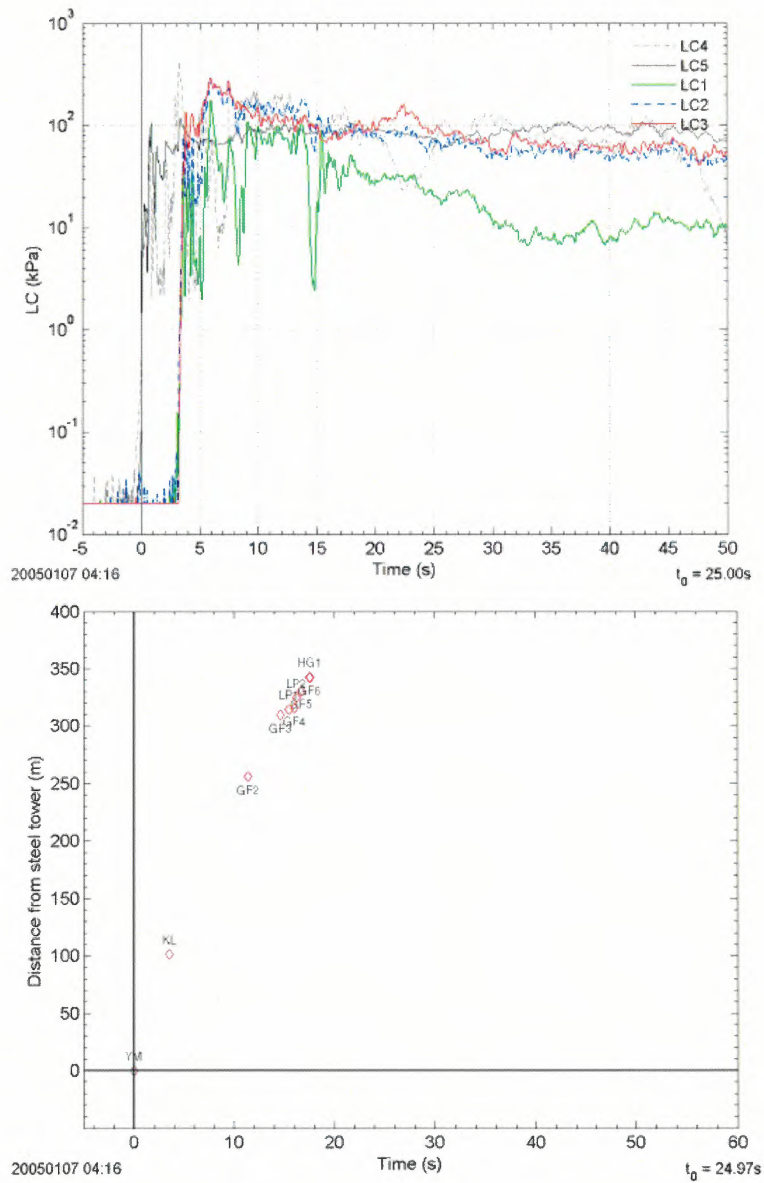


Figure 9.4: Avalanche 20050107 04:16: Impact pressure vs. time (top); Timing (Distance vs. time; bottom);

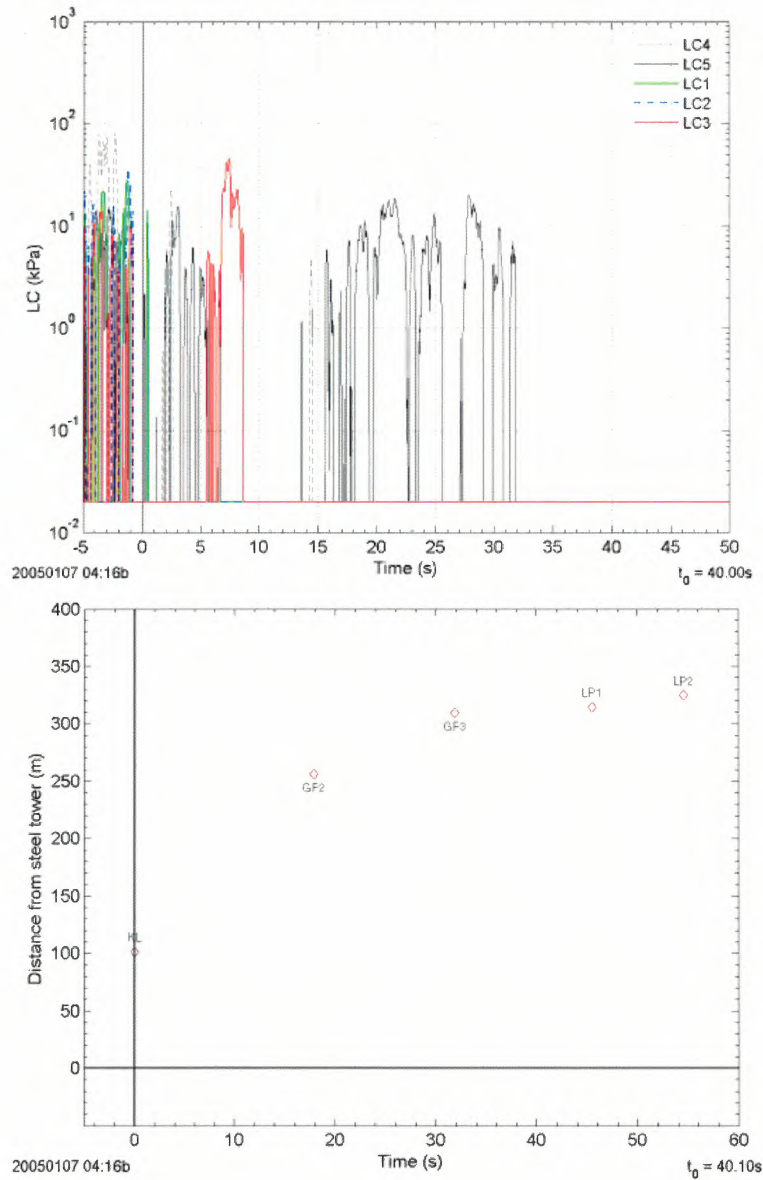


Figure 9.6: Avalanche 20050107 04:16 2nd surge: Impact pressure vs. time (center); Timing (Distance vs. time; bottom);

20021048-11

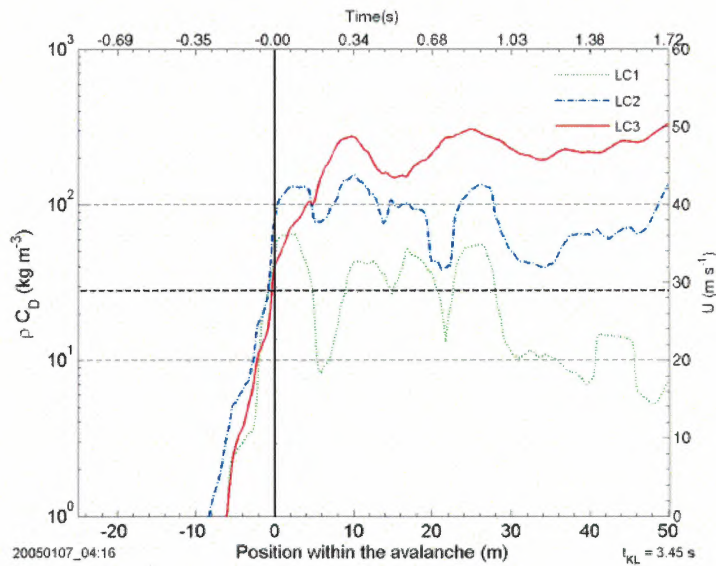


Figure 9.8: Avalanche 20050107 04:16: Estimated ρC_D values for the first approximately 2 s of impact at the concrete structure. Values are based on the estimated mean front velocity indicated by the thick dashed line; the velocity is taken to be constant over the period.

20021048 - 11

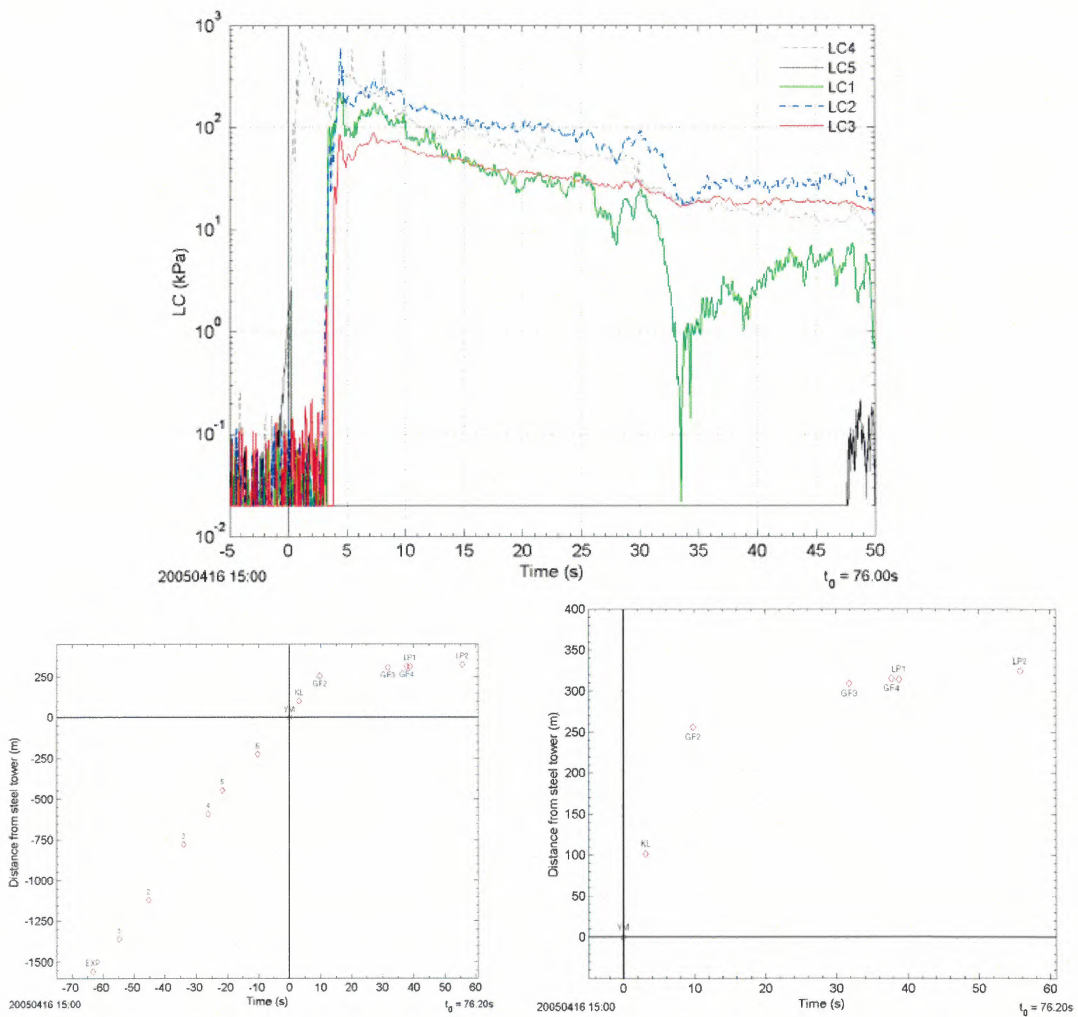


Figure 9.10: Avalanche 20050416 15:00: Map of the deposit (top; total for 2004/2005); Impact pressure vs. time (center); Timing (Distance vs. time; bottom);

20021048-11

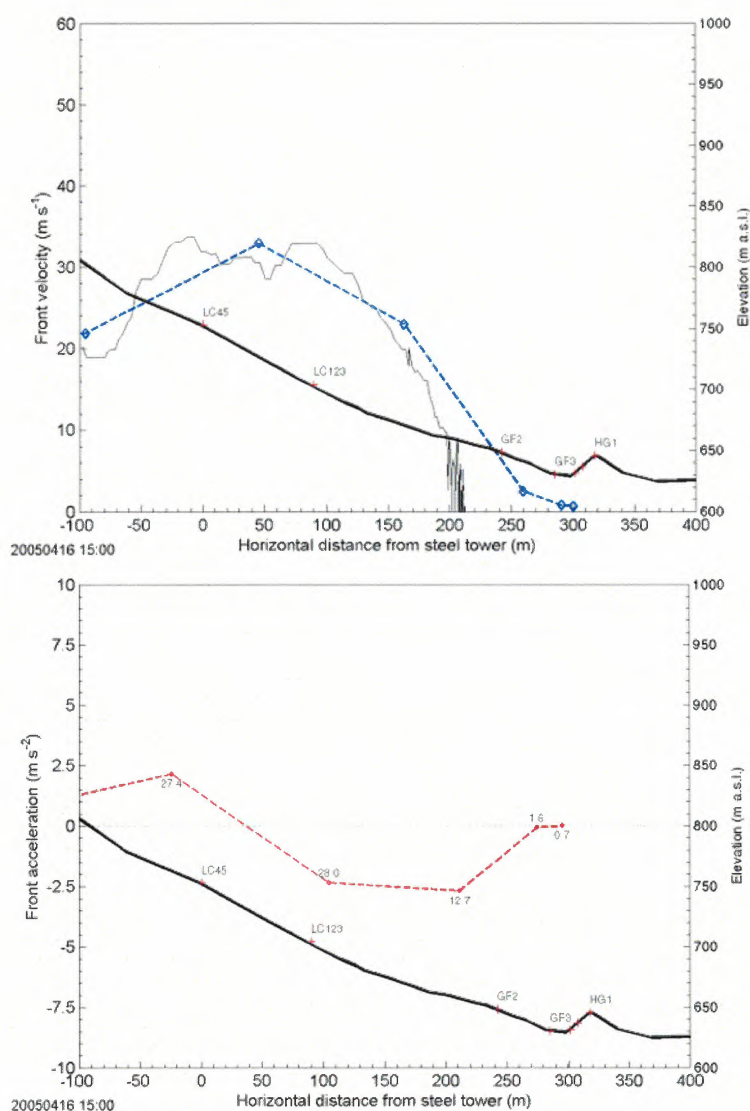


Figure 9.12: Avalanche 20050416 15:00: Mean front velocity vs. horizontal distance (top); corresponding accelerations (bottom; values are the corresponding velocities in $m s^{-1}$). Shown are estimates based on the arrival times at various sensor locations and on video analysis for the runout area. In addition, the thin black line (right side) shows the front velocity measured by pulsed Doppler radar (range gate width 25 m).

10 EFFECT OF THE CATCHING DAM



Figure 10.14: Avalanche ascending the dam

To study the effect of the catching dam 21 avalanches were reanalyzed with respect to the overrun length. The dam is about 16 m high and the slope angle is 40° . The surrounding ground is sloping at about $10 - 14^\circ$. Figure 10.15 shows a sketch of the dam profile. The evaluated avalanches are presented in Table 10.1. All investigated avalanches are regarded as dry flow or powder snow avalanches. Even if the most reliable data are used, there is still an uncertainty in the quality of the data.

10.1 Overrun length

Figure 10.17 shows the normalized overrun length vs. the normalized kinetic energy. The overrun length of all avalanches but the 20000217 14:00 that surpassed the dam can be fit by

$$\frac{l_{ovr}}{h_{fb}} \approx b_1 \frac{u_b^2}{2g h_{fb}} + b_0 \quad (10.1)$$

where l_{ovr} is the overrun length measured from the top of the dam, h_{fb} the free board height, u_b the front velocity at the "base" of the upstream foot of the dam and g is the gravitational acceleration. $u_b^2/(2g h_{fb})$ is the kinetic energy normalized by the potential energy (needed to climb up the effective dam height) also marked by E_n in the following. The parameter b_1 is approximately 2.5 and b_0 is -0.75. The fitting line is also shown. The correlation coefficient R^2 is close to 0.93.

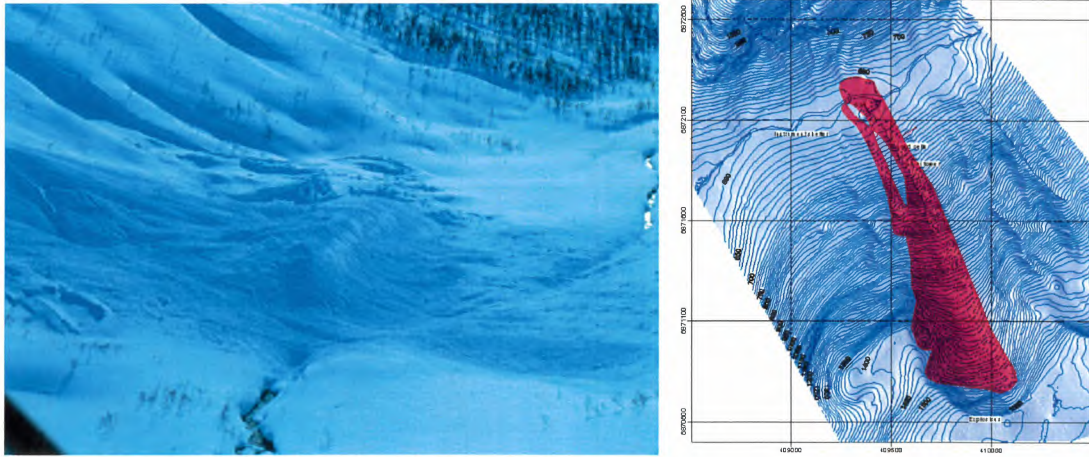


Figure 10.16: Deposition pattern of the 19970208 12:38 avalanche. Left side, image of the deposit and right side, map of the deposit

$$\frac{m u^2}{2} = m a_e l_s \quad (10.6)$$

where the left is the kinetic energy and the right hand side the work done during deceleration; m is the mass.

(10.1) can also be resolved with respect to an effective deceleration, a_{ef} ,

$$a_{ef} \approx \frac{g}{b_1 + 2 b_0 / \text{Fr}^2} = \frac{g}{b_1 + b_0 / E_n} \quad (10.7)$$

Figure 10.18 shows the comparison between the observed deceleration and the one based on the curve fitting.

Figures 10.19 and 10.20 show the similar plots as above, but using only those avalanche data that are thought to be most complete and again excluding the 20000217 14:00 one for the fitting. In this case, the fit parameters are $b_1 = 2.57$ and $b_0 = -1.2$. The correlation coefficient R^2 is 0.98. In this case, Fr_c is approximately 0.97.

According to equation (10.7), the effective deceleration reaches an asymptotic value for high Froude numbers (normalized energy values). The asymptotic value is

$$\lim_{\text{Fr} \rightarrow \infty} a_e = \frac{g}{b_1} \approx 4 \text{ m s}^{-2} \quad (10.8)$$

Similar values for the effective deceleration in the runout area were actually measured for the front of two mixed type avalanches above the dam by Doppler Radar measurements

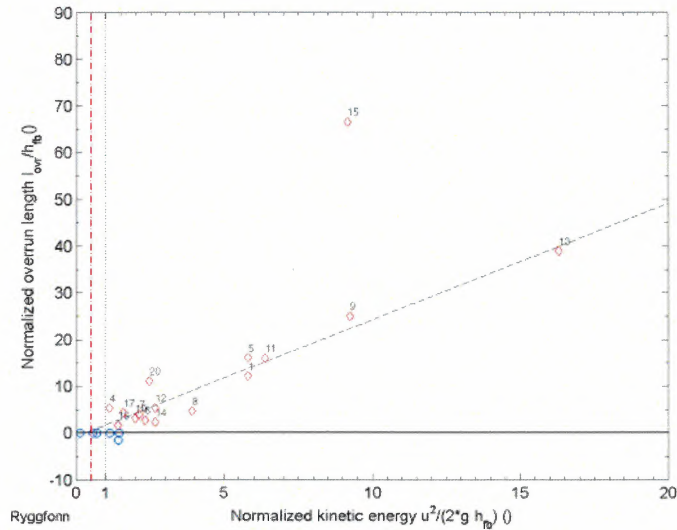


Figure 10.17: Correlation between normalized kinetic energy and normalized overrun length (all selected avalanches). \diamond mark all avalanches surpassing the dam crown and \circ those which stopped before. The line shows the fit according to (10.1) for all avalanches that surpassed the dam excluding the 20000217 14:00 one. The dash-dotted red line marks the critical energy E_c .

20021048-11

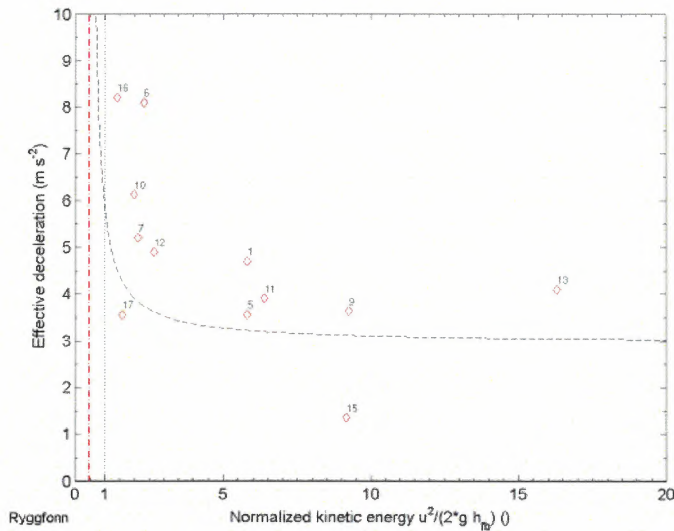


Figure 10.20: Effective deceleration vs. normalized kinetic energy (most complete observations). \diamond mark the calculated values according (10.5). Only the most complete data sets are used. The line indicates the corresponding fit according to (10.7). The dash-dotted red line marks the critical energy E_{nc} .

20021048-11

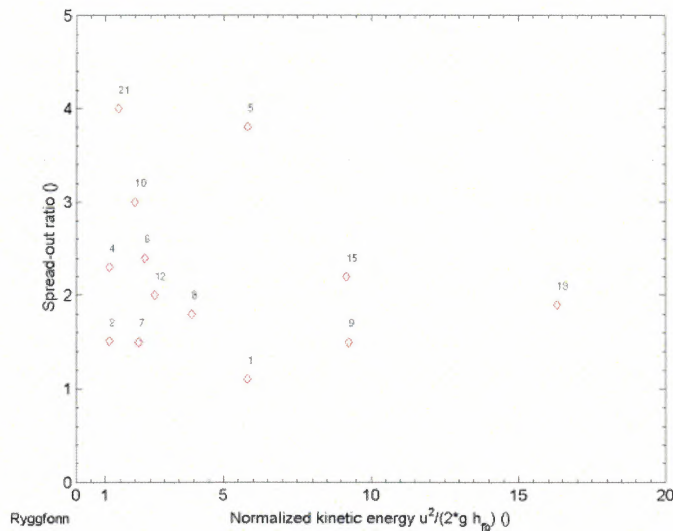


Figure 10.22: Spread-out ratio vs. normalized kinetic energy

10.3 Spreading ratio

Figure 10.22 shows the spread-out ratio vs. normalized kinetic energy ($0.5 Fr^2$). Here, the spreading ratio (spread-out ratio) is defined as the ratio of the maximum deposit width to the avalanche width 100 m before the dam. There is a slight tendency that the spread-out ratio increases with decreasing Froude number. This means with lower Froude number the tendency for the avalanche increases to flow around rather than to overtop the dam. A similar effect can be observed, e.g., in the atmosphere for air flowing over a mountain top/ridge (Stull, 1997, Ch. 14.2.3).

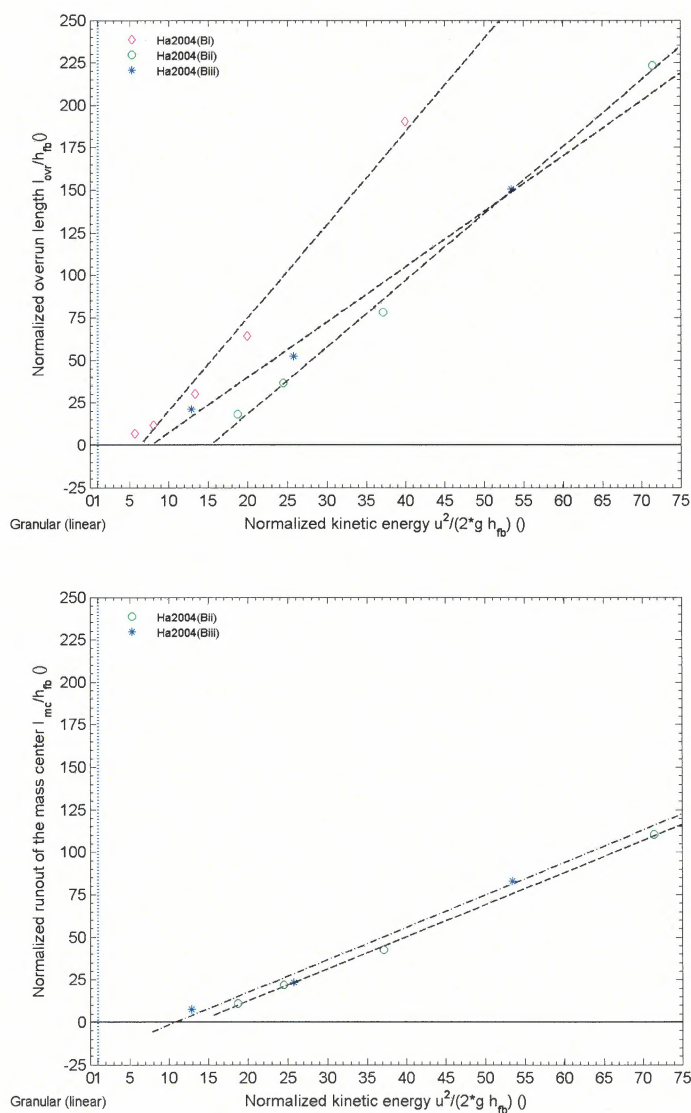


Figure 10.23: Normalized runout ratio vs. normalized kinetic energy: comparison between granular experiments. Top panel shows the linear fit for the overrun length ((Hákondottír, 2004)). The bottom panel shows the corresponding normalized runout length of the center of mass for two experiments. The dashed line indicate linear fits.

20021048-11

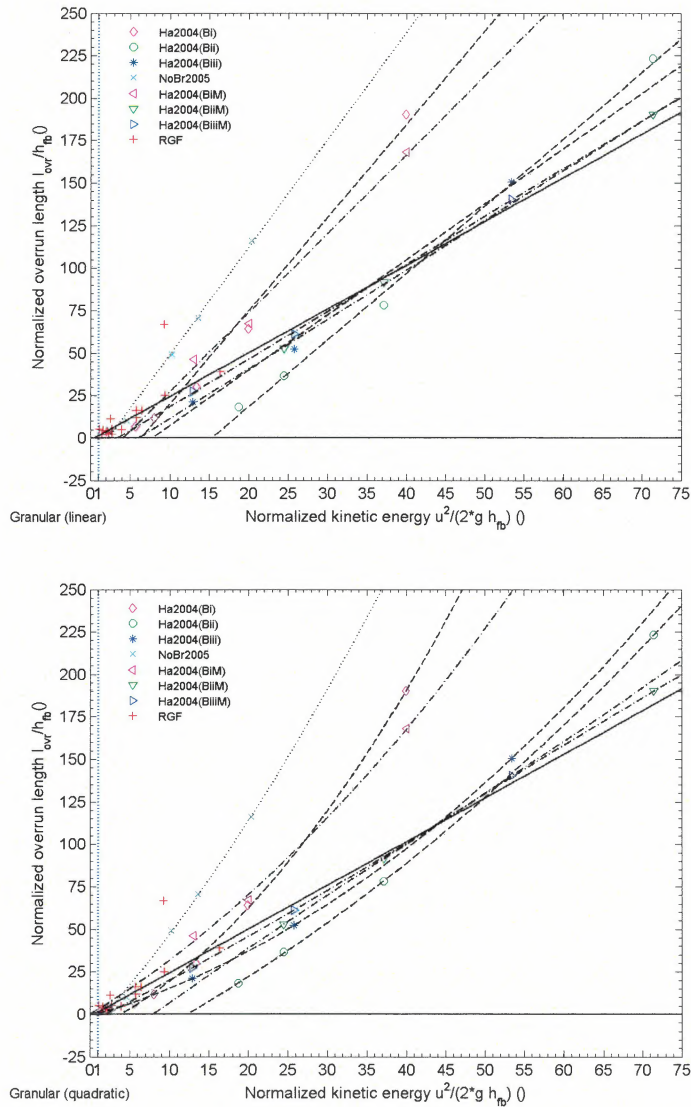


Figure 10.24: Normalized runout ratio vs. normalized kinetic energy: comparison between various experiments. Top panel show the linear fit for all experiments. In the bottom panel, a quadratic fit was used for the granular experiments. The Ryggfonn data are marked (+).

20021048-11

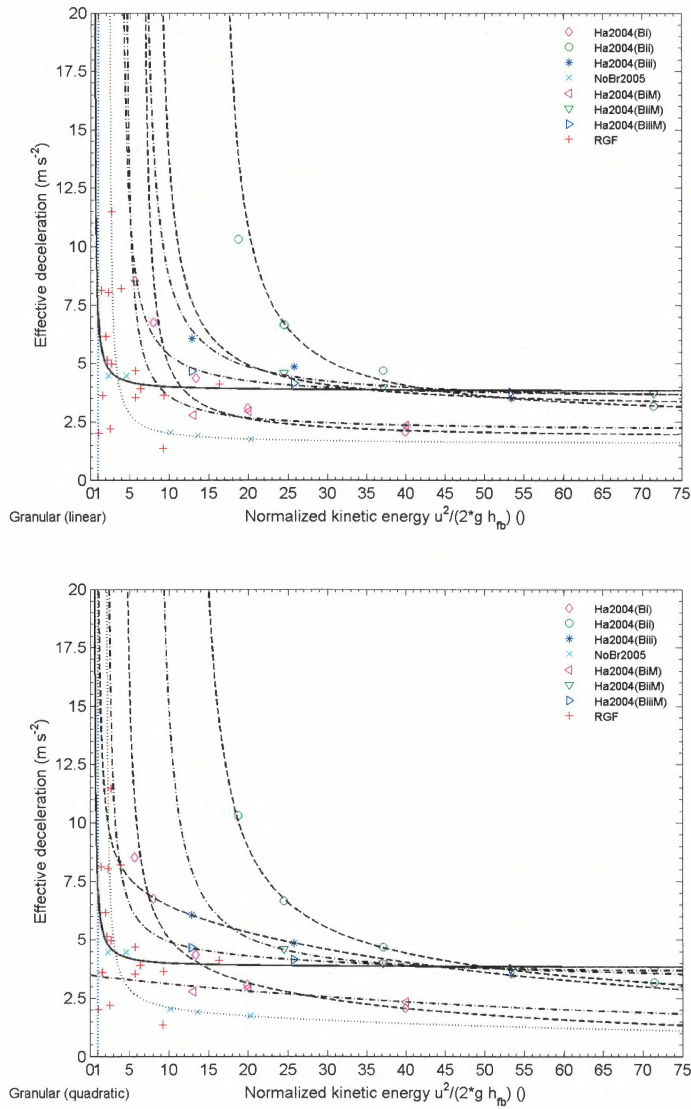


Figure 10.26: Effective deceleration vs. normalized kinetic energy: comparison between various experiments. Top panel show the based on linear fit for all experiments. In the bottom panel, based on a quadratic fit for the granular experiments. The Rygge data are marked (+).

20021048-11



References

Gauer, P., D. Issler, K. Lied, K. Kristensen, H. Iwe, E. Lied, L. Rammer, and H. Schreiber. submitted. On full-scale avalanche measurements at the Ryggfonn test site, Norway. *Cold Regions Science and Technology*, .

Gauer, P. and K. Kristensen. 2004. *Avalanche Studies and Model Validation in Europe, SATSIE: Ryggfonn measurements Winter 2002/2003 and 2003/2004*. NGI Report 20021048-5. Sognsveien 72, N-0806 Oslo, Norwegian Geotechnical Institute.

Gauer, P. and K. Kristensen. 2005. *Avalanche Studies and Model Validation in Europe, SATSIE: Ryggfonn measurements Winter 2004/2005*. NGI Report 20021048-8. Sognsveien 72, N-0806 Oslo, Norwegian Geotechnical Institute.

Hákonardóttir, K. M., T. Jóhannesson, A. J. Hogg, M. Kern, and F. Tiefenbacher. 2004. The interaction between rapid granular flows and braking mounds. ????, .

Hákonardóttir, Kristín Martha. 2004. *The Interaction Between Snow Avalanches and Dams*. Phd thesis, School of Mathematics, University of Bristol.

Issler, D., C. B. Harbitz, K. Kristensen, K. Lied, A. S. Moe, M. Barbolini, F. V. DeBlasio, G. Khazaradze, J. N. McElwaine, A. I. Mears, M. Naaim, and R. Sailer. submitted. A comparison of avalanche models with data from dry-snow avalanches at Ryggfonn, Norway. In *IFLC05*.

Kristensen, K. 1996. The Ryggfonn Project: Avalanche data from the Winters 1991/1992, 1992/1993, and 1993/1994. NGI Report 581200-31. Sognsveien 72, N-0806 Oslo, Norwegian Geotechnical Institute.

Kristensen, K. 1997. The Ryggfonn Project: Avalanche data from the Winters 1994/1995, 1995/1996. NGI Report 581200-32. Sognsveien 72, N-0806 Oslo, Norwegian Geotechnical Institute.

Kristensen, K. 2001. The Ryggfonn Project: Avalanche data from the Winters 1996/1997, 1997/1998, 1998/1999 and 1999/2000. NGI Report 581200-33. Sognsveien 72, N-0806 Oslo, Norwegian Geotechnical Institute.

Lied, K., A. Moe, K. Kristensen, and D. Issler. 2002. Snow Avalanche Research Programme SIP-6: Ryggfonn. Full scale avalanche test site and the effect of the catching



Table A-1: Code for morphological avalanche classification (1981, *Avalanche Atlas/UNESCO*)

Criterion Characteristics	Symbols		
	Criterion	Characteristics	
		pure	mixed
Manner of starting	A		
Loose snow avalanche		1	} 7
Slab avalanche		2	
Slab avalanche soft		3	
Slab avalanche hard		4	
Position of sliding surface	B		
Surface-layer avalanche (general)		1	} 8
Surface-layer avalanche, new snow fracture		2	
Surface-layer avalanche, old snow fracture		3	
Full-depth avalanche		4	
Liquid Water in snow fracture	C		
Absent: dry-snow avalanche		1	} 7
Present: wet-snow avalanche		2	
Form of Path	D		
Unconfined avalanche		1	} 7
Channelled avalanche		2	
From of movement	E		
Powder avalanche (dominant)		1	} 7
Flow avalanche (dominant)		2	
Surface roughness of deposit	F		
Coarse deposit (general)		1	} 7
Coarse deposit angular blocks		2	
Coarse deposit rounded clods		3	
Fine deposit		4	
Liquid water in deposit	G		
Absent: dry-deposit		1	} 7
Present: wet-deposit		2	
Contamination of deposit	H		
Clean deposit		1	} 7
Contaminated deposit (general)		2	
Contaminated by rocks, debris, soil		3	
Contaminated by branches, trees		4	
Contaminated by debris of structures		5	
Triggering mechanism ¹	J		
Natural release		1	
Human release (general)		2	
Human release, accidental		3	
Human release, intentional		4	

¹This criterion is an element of the genetic classification. since the triggering mechanism within the given alternatives is known most cases and is important for many problems, it is added to the morphological code.

Kontroll- og referanseside/ Review and reference page



Oppdragsgiver/Client European Commission Kontraksreferanse/ Contract reference EVG1-CT200200059	Dokument nr/Document No. 20021048-11 Dato/Date 1. December 2005
Dokumenttittel/Document title Avalanche Studies and modell Validation in Europe, SATSIE 3. Annual report Prosjektleder/Project Manager Karstein Lied Utarbeidet av/Prepared by Dieter Issler	Distribusjon/Distribution <input type="checkbox"/> Fri/Unlimited <input checked="" type="checkbox"/> Begrenset/Limited <input type="checkbox"/> Ingen/None
Emneord/Keywords Avalanches, dynamics, fullscale, smallscale tests	
Land, fylke/Country, County Kommune/Municipality Sted/Location Kartblad/Map UTM-kordinater/UTM-coordinates	Havområde/Offshore area Felt navn/Field name Sted/Location Felt, blokknr./Field, Block No.

Kvalitetssikring i henhold til/Quality assurance according to NS-EN ISO9001							
Kon-trollert av/Reviewed by	Kontrolltype/Type of review	Dokument/Document		Revisjon 1/Revision 1		Revisjon 2/Revision 2	
		Kontrollert/Reviewed		Kontrollert/Reviewed		Kontrollert/Reviewed	
		Dato/Date	Sign.	Dato/Date	Sign.	Dato/Date	Sign.
KL	Helhetsvurdering/General Evaluation *	1/12-05	kl				
KL	Språk/Style	1/12-05	kl				
KL	Teknisk/Technical - Skjønn/Intelligence	1/12-05	kl				
	- Total/Extensive						
	- Tverrfaglig/Interdisciplinary						
	Utforming/Layout						
	Slutt/Final						
	Kopiering/Copy quality						

* Gjennomlesning av hele rapporten og skjønnsmessig vurdering av innhold og presentasjonsform/
On the basis of an overall evaluation of the report, its technical content and form of presentation

Dokument godkjent for utsendelse/ Document approved for release	Dato/Date 01.12.2005	Sign.
------------------------------------------------------------------------	--------------------------------	------------------